NONLINEAR ANALYSIS OF CONCRETE STRUCTURES BASED ON A 3D SHEAR-BEAM ELEMENT FORMULATION

by

Jan G. Teigen

THESIS
Presented for the Degree of

DOCTOR PHILOSOPHIAE

UNIVERSITY OF OSLO
Department of Mathematics
Mechanics Division

February 1994

Abstract

The present work deals with the development of an analysis-model applicable to large scale 3D beam structures of reinforced and prestressed concrete. The model is based on the finite element method and allows for large displacements through the Corotated Lagrangian description of motion and a variety of material nonlinearities in the short-time as well as the long-time regime. The loading may be both unidirectional and corotational. By relating all changes in loads, prescribed displacements, temperature, time and static system to a common history parameter, the response of a structure may be traced from the very start of construction to its completion, throughout the service life and finally into the ultimate load range.

The key ingredient of the analysis-model is the new 3D shear-beam element formulation. It can handle the response of reinforced and prestressed concrete in each one and combinations of the axial, bending, shear and torsion modes.

Acknowledgements

The author would like to thank Professor Jostein Hellesland at the University of Oslo (UiO) for providing a lot of interesting reports of great importance for this study. Also his advices on certain subjects related to time dependent concrete behavior are highly appreciated. The same appreciation is expressed to Professor Magne Nygård at UiO for his comments on finite element related subjects. I would also like to thank my good friend Professor Kurt Gerstle at the University of Colorado for all his attention and constant encouragements throughout the course of the work.

This study was made possible by research grants from the Royal Norwegian Council for Scientific and Industrial Research (NTNF) and from Det Norske Veritas (DNV). These contributions are gratefully acknowledged. Also the financial support from UiO in the final stage of the work, as well as the excellent office facilities provided, are recognized with gratitude.

I feel privileged to have got this opportunity.

Addendum:
The defense of this thesis was held in late May 1994 with Professor Carlos A. Felippa at the University of Colorado and Professor Svein I. Sørensen at the Norwegian Institute of Technology (NTH) as opponents. I would like to thank them both for their careful review of the work and their interesting comments.

Contents

List of Figures

List of Tables

List of Symbols

Symbols are in general defined on first appearance and often also later. For easy reference, however, those most commonly used are briefly explained below in alphabetic order with the Greek symbols listed last.

$\boldsymbol{A}_m$	–	strain transformation matrix, from (x, y, z)-system to (x, m)-system
$\boldsymbol{A}_{cm}$	–	strain transformation matrix, from (x, m)-system to principal $(1, 2)$-system
$\boldsymbol{a}_t$	–	strain transformation vector, from (x, y, z)-system to tangential tendon or pbar direction
$\boldsymbol{a}_{tm}$	–	strain transformation vector, from (x, m)-system to bar direction in question
A_o	–	cross section area in undeformed configuration
A_s	–	effective shear area (Chap. 3)
A_s, A_p	–	individual rebar and tendon cross section areas
A_2, A_3	–	quantities in the tension stiffening formulation
$a_s(a_x), a_b$	–	rebar and pbar cross section areas per unit length normal to the bar axis
$\boldsymbol{B}$	–	strain-displacement matrix
$\mathcal{B}_{cc}, \mathcal{B}_{ct}$	–	aging functions
$\mathcal{B}_T$	–	temperature function
$\mathcal{B}_\sigma, \mathcal{B}_{sus}$	–	sustained load functions
$\mathcal{B}_s$	–	shrinkage function
$\mathcal{B}_d, \mathcal{B}_{fb}, \mathcal{B}_{fd}$	–	creep functions
$\mathcal{B}_r$	–	relaxation function
b_t	–	tension stiffening coefficient
$\boldsymbol{C}_T$	–	tangent constitutive tensor of 4th order
$\boldsymbol{C}_t, \boldsymbol{C}$	–	tangent constitutive matrix in the (x, y, z)-system (various superscripts)
$\boldsymbol{C}_m$	–	tangent constitutive matrix in the (x, m)-system (various additional sub- and superscripts)
$\boldsymbol{C}_c$	–	concrete tangent constitutive matrix in the principal $(1, 2)$-system

C_n, C_o, C_{on} . .	–	deformed, and undeformed initial and corotated configurations
C_{tol}	–	convergence tolerance parameter
C_r	–	specific relaxation coefficient of prestressing steel
$\boldsymbol{d}$	–	displacement conversion matrix
$\boldsymbol{E}$	–	Green strain tensor (Chap. 2)
${}^o\boldsymbol{E}, {}^n\boldsymbol{E}$	–	nodal eccentricity matrices for configurations C_o and C_n
${}^o\boldsymbol{E}_l, {}^n\boldsymbol{E}_l$	–	load eccentricity matrices for configurations C_o and C_n
$\boldsymbol{e}$	–	Green strain vector (Chap. 2)
${}^o\boldsymbol{e}, {}^n\boldsymbol{e}$	–	nodal eccentricity vectors for configurations C_o and C_n
${}^o\boldsymbol{e}_l, {}^n\boldsymbol{e}_l$	–	load eccentricity vectors for configurations C_o and C_n
E	–	elastic modulus
E_c, E_{c28}	–	current and 28 day elastic moduli of concrete
E_o, E_h	–	secant moduli of concrete corresponding to ϵ_o and ϵ_h
$E_u^{(c)}, E_{u28}^{(c)}$	–	current and 28 day unloading/reloading moduli of concrete in compression
$E_u^{(t)}, E_{u28}^{(t)}$	–	current and 28 day unloading/reloading moduli of concrete in tension
E_d	–	'smeared' elastic modulus of equivalent reinforcement
E_{dc}	–	'smeared' elastic modulus of critical reinforcement
E_b	–	slope corresponding to ϵ_b
E_s, E_p, E_b	–	elastic moduli of rebars, tendons and pbars
$E_y, E_{0.2}$	–	plastic hardening moduli of reinforcing and prestressing steels
e	–	normalized strain (various subscripts)
e_{ijk}	–	permutation symbol
$\boldsymbol{F}$	–	deformation gradient tensor (Chap. 2)
$\boldsymbol{F}$	–	discrete nodal force vector (various sub- and superscripts)
$\boldsymbol{f}$	–	body force vector (various sub- and superscripts)
F_x, F_y, F_z	–	force components
f_{cc}, f_{cc28}	–	current and 28 day compressive strengths of concrete (negative)
f_{ct}, f_{ct28}	–	current and 28 day tensile strengths of concrete
f_{cm}, f_{cm28}	–	current and 28 day mean compressive strengths of concrete (negative)
f_y	–	yield stress of reinforcing steel
f_d	–	'smeared' yield stress of equivalent reinforcement
$f_{0.2}, f_{0.1}$	–	stresses at 0.2 % and 0.1 % strain offset of prestressing steel
$\boldsymbol{G}$	–	subvector of generalized forces (various subscripts)
$\boldsymbol{g}$	–	subvector of generalized forces per unit axial length (various subscripts)
G	–	shear modulus
$\tilde{g}_{ey}, \tilde{g}_{ez}$	–	strain DOFs (strain gradients)
g_{Tx}, g_{Ty}, g_{Tz} . .	–	reference temperature gradients
H	–	pbar panel height

h	–	notional member size
h_l, h_d, h_T	–	scaling factors for load, displacement and temperature deviation
$\boldsymbol{I}_i$	–	global base vector triad
$\boldsymbol{i}_i$	–	base vector triad (various accents, sub- and superscripts)
${}^n\boldsymbol{i}_i$	–	nodal base vector triad for configuration C_n
${}_o\boldsymbol{i}_i, {}_{on}\boldsymbol{i}_i$	–	element base vector triads for configurations C_o and C_{on}
I_y	–	moment of inertia
$\boldsymbol{J}$	–	vector of tendon (X, Y, Z)-Jacobians
J_X, J_Y, J_Z	–	components of $\boldsymbol{J}$
J_S	–	tendon curve-Jacobian
$\boldsymbol{K}$	–	system stiffness matrix
$\boldsymbol{k}$	–	resulting element stiffness matrix (i.e. $\boldsymbol{k}_m + \boldsymbol{k}_g - \boldsymbol{k}_{lc}^{(CL)} - \boldsymbol{k}_{lu}^{(CL)}$)
$\boldsymbol{k}_g$	–	geometric element stiffness matrix
$\boldsymbol{k}_{lc}^{(CL)}$	–	element (or nodal) load stiffness matrix due to corotational loading, CL-formulation
$\boldsymbol{k}_{lu}^{(CL)}$	–	element (or nodal) load stiffness matrix due to unidirectional loading, CL-formulation
$\boldsymbol{k}_{lc}, \boldsymbol{k}_{lu}$	–	element (or nodal) load stiffness matrices with reference fixed
$\boldsymbol{k}_m$	–	material element stiffness matrix
$\boldsymbol{k}_m, \tilde{\boldsymbol{k}}_m$	–	material element stiffness matrices, conventional and hierarchical (Chap. 3)
$\boldsymbol{k}_b, \boldsymbol{k}_s$	–	bending and shear energy parts of $\boldsymbol{k}_m$ (Chap. 3)
k	–	wobble friction coefficient
L_o	–	element length in undeformed configuration
L_n	–	element secant length in deformed configuration C_n
$\boldsymbol{M}$	–	discrete nodal moment vector
M_x, M_y, M_z	–	moment components
m_x, m_y, m_z	–	moment components per unit axial length
mix	–	cement type parameter
$\boldsymbol{N}, \boldsymbol{n}$	–	outward unit normal vectors to a plane, undeformed and deformed configurations (Chap. 2)
$\boldsymbol{n}$	–	tendon unit principal normal vector (Chap. 6)
$\boldsymbol{N}, \boldsymbol{N}_a$	–	shape function matrices for interpolation of $\boldsymbol{u}$ and $\boldsymbol{u}_a$
$\boldsymbol{N}_f$	–	shape function vector for interpolation of field quantity f
$N_f^{(d)}$	–	shape function polynomial for interpolation of field quantity f from DOF d
$\boldsymbol{P}$	–	applied system node-force vector
$\boldsymbol{p}$	–	applied element (or nodal load) node-force vector (various subscripts)

$\boldsymbol{p}, \tilde{\boldsymbol{p}}$	–	applied element node-force vectors, conventional and hierarchical (Chap. 3)
P_z	–	tip load (Chap. 3)
P	–	tendon force
P_1, P_2	–	tendon forces applied from the jack at endpoints 1 and 2
p_o, p	–	pbar forces, applied from the jack and after anchorage loss, per unit length normal to the bar axis
$\boldsymbol{q}$	–	vector of forces per unit axial length (various sub- and superscripts)
$\boldsymbol{q}_s$	–	vector of distributed tendon forces per unit arclength
q_x, q_y, q_z	–	force components per unit axial length
$\boldsymbol{R}$	–	internal system node-force vector
$\boldsymbol{r}$	–	internal element node-force vector
R, R_o	–	relaxation coefficients, time dependent and 'notional'
RH	–	relative humidity of the ambient atmosphere
$\boldsymbol{S}$	–	2nd Piola-Kirchhoff stress tensor
$\boldsymbol{s}$	–	2nd Piola-Kirchhoff stress vector
S_o	–	cross section perimeter in undeformed configuration
S_i	–	system number
S	–	length along tendon curve from endpoint 1
S_t	–	total tendon length
S_{s1}, S_{s2}	–	tendon 'slip'-locations measured from endpoint 1
S_r	–	tendon 'reverse'-location measured from endpoint 1
S_b	–	characteristic pbar length
s_i	–	relative concrete stress during Δt_i
s_{ai}	–	concrete stress relative to strength at t_{Ta} during Δt_i
$\boldsymbol{T}$	–	transformation matrix (various accents, sub- and superscripts)
${}^n\boldsymbol{T}$	–	nodal rotation matrix for configuration C_n
${}_o\boldsymbol{T}, {}_{on}\boldsymbol{T}$	–	element transformation matrices for configurations C_o and C_{on}
$\boldsymbol{T}_e$	–	DOFs transformation matrix for element with eccentricities
$\boldsymbol{t}, \check{\boldsymbol{t}}$	–	(prescribed surface) traction vector (various sub- and superscripts)
$\boldsymbol{t}$	–	tendon unit tangent vector (Chap. 6)
T, T_n, T_i, T_o . .	–	absolute temperatures; current, current, generic and reference
$\overline{T}$	–	average temperature (various subscripts)
$\overline{T}_s$	–	mean seasonal temperature
$\overline{T}_{max}, \overline{T}_{min}$ . .	–	mean values of extreme seasonal temperatures
ΔT	–	deviation from mean seasonal temperature
ΔT_1	–	reference temperature deviation at element node 1
$t, t_n, t_i, t_o, t_a, t_e$	–	times; current, current, generic, at beginning of shrinkage, at first load application and at tensioning state
$\Delta t_n, \Delta t_i$	–	current and generic time steps

t_{fi} . . . . . – time to failure due to s_i

$t_T, t_{Ti}, t_{To}, t_{Ta}$ – temperature adjusted ages; current, generic, initial and at first load application

$\hat{t}_n, \hat{t}_i, \hat{t}_a$ . . . . . – ages corresponding to t_n, t_i and t_a, adjusted for temperature and type of cement

t . . . . . – line unit thickness (various subscripts)

$\boldsymbol{u}, \check{\boldsymbol{u}}, \boldsymbol{u}_a$ . . . . . – ordinary, prescribed and augmented displacement vector fields

u, v, w . . . . . – displacement (x, y, z)-components

u_o, v_o, w_o . . . . . – displacement (x, y, z)-components at the centroid

u_s . . . . . – anchorage slip

$\boldsymbol{V}$ . . . . . – system nodal displacement vector (various subvectors with accent, sub- and superscripts)

$\boldsymbol{v}$ . . . . . – vector of DOFs (various accents, sub- and superscripts)

V_o . . . . . – volume in undeformed configuration

∂V_o . . . . . – boundary surface in undeformed configuration

v_r, w_r . . . . . – relative transverse displacements

v_{xi}, v_{yi}, v_{zi} . . . – translational DOFs pertaining to node i (= 1 or 2)

$\tilde{v}_{x3}$ . . . . . – translational hierarchical DOF of internal node 3

$\boldsymbol{X}$ . . . . . – position vector in undeformed configuration (Chap. 2)

$\boldsymbol{X}$ . . . . . – position vector in global system (various sub- and superscripts)

$\boldsymbol{x}$ . . . . . – position vector in deformed configuration (Chap. 2)

$\boldsymbol{x}$ . . . . . – position vector in local element system

X, Y, Z . . . . . – Cartesian coordinates in global system (various sub- and superscripts)

x, y, z . . . . . – Cartesian coordinates in local element system (various subscripts)

α . . . . . – angle between y-axis and m-axis (transverse in-plane panel axis)

α_c, α_s . . . . . – coefficients of thermal expansion for concrete and steel

β_{c1} . . . . . – angle between x-axis and principal 1-direction

β_s, β_b . . . . . – angles between x-axis and bar directions of rebars and pbars

$\Delta\beta_i$ . . . . . – angle between β_{c1} and a bar direction

$\gamma_{xy}, \gamma_{xz}, \gamma_{yz}$ . . – shear strain components of $\boldsymbol{\epsilon}$

γ_{xm} . . . . . – shear strain component of $\boldsymbol{\epsilon}_m$

γ_c, γ_t . . . . . – internal concrete parameters (Chap. 8)

γ_c, γ_s . . . . . – specific weights of concrete and steel

γ_i . . . . . – rate of loss of relative strength due to s_i

$\Delta \cdot\cdot$ . . . . . – incremental quantity

$\delta \cdot\cdot$ . . . . . – virtual quantity; variation of the quantity

δ_{ij} . . . . . – Kronecker delta

$\boldsymbol{\epsilon}$ . . . . . – infinitesimal strain vector in the (x, y, z)-system

$\boldsymbol{\epsilon}_m$ . . . . . – strain vector in the (x, m)-system

$\boldsymbol{\epsilon}_c$ . . . . . – total strain vector in the principal $(1, 2)$-system

$\epsilon_x, \epsilon_y, \epsilon_z$	–	normal strain components of $\boldsymbol{\epsilon}$
ϵ_x, ϵ_m	–	normal strain components of $\boldsymbol{\epsilon}_m$
ϵ_1, ϵ_2	–	components of $\boldsymbol{\epsilon}_c$
ϵ_t	–	normal strain in the bar or tangential tendon direction
$\tilde{\epsilon}_{yo}, \tilde{\epsilon}_{zo}$	–	strain DOFs (normal strains)
$\epsilon, \epsilon^{(m)}, \epsilon^{(n)}$ . . .	–	total, mechanical and nonmechanical strains
$\epsilon_{cT}, \epsilon_{sT}$	–	thermal strains of concrete and steel (nonmechanical)
$\epsilon_{cs}, \epsilon_{cc}, \epsilon_{ca}$	–	concrete strains due to shrinkage, creep and aging (nonmechanical)
ϵ_{cso}	–	notional shrinkage strain
$\epsilon_{cc}^{(d)}, \epsilon_{cc}^{(fb)}, \epsilon_{cc}^{(fd)}$	–	creep strain components due to delayed elasticity, basic flow and drying flow
$\epsilon_{c\sigma}$	–	resulting stress dependent concrete strain
$\epsilon_{c1}, \epsilon_{c2}$	–	principal mechanical concrete strains
$\epsilon_s, \epsilon_p, \epsilon_b$	–	mechanical rebar, tendon and pbar strains
$\epsilon_p^{(o)}, \epsilon_b^{(o)}$	–	tendon and pbar strains at the final tensioning state
$\Delta\epsilon_p^{(o)}, \Delta\epsilon_b^{(o)}$ . .	–	additional tendon and pbar strains (in relation to concrete strain) at the final tensioning state
ϵ_{eo}	–	tensioning strain prior to anchorage loss
$\epsilon_o, \epsilon_{o28}$	–	current and 28 day strains at peak concrete stress in uniaxial compression
$\epsilon_h, \epsilon_{h28}$	–	current and 28 day strains at 50 % of peak concrete stress on the descending branch in uniaxial compression
ϵ_{cr}	–	strain at peak concrete stress in uniaxial tension
ϵ_b	–	strain at the internal connection point in the tension stiffening formulation
$\hat{\epsilon}_c^{(c)}, \hat{\epsilon}_c^{(t)}$	–	extreme concrete strains in compression and tension
ϵ_y	–	yield strain of reinforcing steel or equivalent reinforcement
$\hat{\epsilon}_y$	–	modified yield strain of equivalent reinforcement
ϵ_r	–	recorded strain offset for reinforcing steel
ϵ_ω	–	strain at the elasticity-limit of prestressing steel
$\epsilon_{0.2}$	–	prestressing steel strain corresponding to $f_{0.2}$
ϵ_e	–	maximum recorded strain for prestressing steel
η	–	lower bound of $\mathcal{B}_{sus}$ (Chap. 9)
η	–	natural line unit or quad unit coordinate (Chap. 10)
$\eta_{c1}, \eta_{c2}, \eta_t$	–	internal concrete parameters
$\theta_x, \theta_y, \theta_z$	–	cross sectional rotations
$\theta_{xi}, \theta_{yi}, \theta_{zi}$ . . .	–	rotational DOFs pertaining to node i (= 1 or 2)
$\tilde{\theta}_{y3}, \tilde{\theta}_{z3}$	–	rotational hierarchical DOFs of internal node 3
$\boldsymbol{\kappa}$	–	tendon curvature vector
κ	–	resulting tendon curvature
$\bar{\kappa}$	–	mean tendon curvature

λ	–	'neutral time' parameter
μ	–	curvature friction coefficient
μ	–	principal strain ratio (Chap. 8)
μ	–	natural quad unit coordinate (Chap. 10)
ξ	–	natural beam coordinate
ρ	–	natural tendon coordinate (Chap. 6)
ρ	–	steel to concrete area ratio
$\boldsymbol{\sigma}$	–	Cauchy stress tensor (Chap. 2)
$\boldsymbol{\sigma}$	–	Cauchy stress vector in the (x, y, z)-system (corresponding to $\boldsymbol{\epsilon}$)
$\boldsymbol{\sigma}_m$	–	stress vector in the (x, m)-system (various additional sub- and superscripts)
$\boldsymbol{\sigma}_c$	–	concrete stress vector in the principal $(1, 2)$-system
$\sigma_x, \sigma_y, \sigma_z$	–	normal stress components of $\boldsymbol{\sigma}$
σ_x, σ_m	–	normal stress components of $\boldsymbol{\sigma}_m$
$\sigma^{(e)}, \sigma^{(i)}$	–	envelope and interior stresses (various subscripts)
σ_{c1}, σ_{c2}	–	components of $\boldsymbol{\sigma}_c$
$\hat{\sigma}_c^{(c)}, \hat{\sigma}_c^{(t)}$	–	concrete stresses corresponding to $\hat{\epsilon}_c^{(c)}$ and $\hat{\epsilon}_c^{(t)}$
$\sigma_c^{(p)}$	–	concrete stress at the previous equilibrium state
$\bar{\sigma}_{cn}, \bar{\sigma}_{ci}$	–	mean concrete stresses during Δt_n and Δt_i
$\breve{\sigma}_c$	–	estimated current concrete stress
$\sigma_s^{(s)}$	–	'smeared' rebar stress
$\sigma_p, \sigma_b^{(s)}$	–	tendon and 'smeared' pbar instantaneous stresses
$\sigma_r, \sigma_r^{(s)}$	–	tendon and 'smeared' pbar relaxation stresses (negative)
$\sigma_f, \sigma_f^{(s)}$	–	tendon and 'smeared' pbar total (final) stresses
$\sigma_{ir}, \sigma_{ir}^{(s)}$	–	tendon and 'smeared' pbar internal resistance-contributing stresses
$\sigma_p^{(o)}, \sigma_b^{(o)}$	–	tendon and pbar stresses at the final tensioning state
σ_{eo}	–	tensioning stress prior to anchorage loss
$\bar{\sigma}_{pi}$	–	mean instantaneous tendon stress during Δt_i
$\hat{\sigma}_{fi-1}$	–	modified total (final) tendon stress at t_{i-1}
$\hat{\sigma}_{pi}$	–	fictitious initial tendon stress
$\tau_{xy}, \tau_{xz}, \tau_{yz}$ . . .	–	shear stress components of $\boldsymbol{\sigma}$
τ_{xm}	–	shear stress component of $\boldsymbol{\sigma}_m$
$\phi_d, \phi_{fb}, \phi_{fd}$ . . .	–	creep coefficients due to delayed elasticity, basic flow and drying flow
ϕ_c	–	resulting creep coefficient
ϕ_a	–	aging coefficient
ϕ_{d0}, ϕ_{d1}	–	notional creep coefficients due to delayed elasticity
ϕ_{fb0}, ϕ_{fb1}	–	notional creep coefficients due to basic flow
$\phi_{fd0}, \phi_{fd1}, \phi_{fd2}$	–	notional creep coefficients due to drying flow

φ_i	–	shape function polynomials for tendon ($i = 1 - 3$), line unit ($i = 1 - 2$) and quad unit ($i = 1 - 4$)
ψ_c, ψ_t	–	quantities controlling biaxial effects in principal compression and tension
ω	–	elasticity-limit factor of prestressing steel

Chapter 1

Introduction

Reinforced concrete structures play a major role in today's construction industry. For design engineers the common practice has been to make elastic analyses of such structures followed by design checks with inelastic material properties appropriate for the limit state considered. This will probably also be common practice for several years to come, although the lack of consistence in material properties from analysis to design is highly unsatisfactory. Nonlinear (consistent) analysis of reinforced concrete has on the other hand become increasingly popular among researchers during the last 25 years. Such analyses are almost exclusively based on application of the finite element method (FEM). Often the intention has been to gain better insight into and understanding of the more fundamental aspects of concrete and reinforced concrete behavior. The necessity of such work is of course unquestionable. However, at the same time there is also a need for draining the present knowledge in this field back to the design office.

This work will deal with nonlinear FEM-analysis of reinforced concrete structures using beam elements. Such analyses have been carried out by several investigators previously, like Aas-Jakobsen [20], Åldstedt [21], Kang [22], Mari [23], Carol and Murcia [13, 14], Kasti [26] and Kanstad [27]. All those referred to have included the effects of cracking, crushing and creep in concrete and yielding in reinforcing steel. To a varying extent, also geometric nonlinearities, effects of prestress, temperature and segmental construction, in addition to time effects in concrete from shrinkage, aging and sustained loading, or interaction effect with reinforcement due to bond slip/tension stiffening have been accounted for. Only Mari and Kasti have studied three dimensional (3D) frames. However, none of the investigators have included transverse shear in their element formulation, and thus, only problems where the axial-bending modes are critical can reliably be analyzed. This of course limits the applicability of the analysis-tool for practical use. To this author's knowledge, nonlinear FEM-analysis of shear related problems in reinforced concrete beams has on the other hand only been carried out using membrane or solid elements. Then application to large scale structures soon becomes impractical because of the growing

number of degrees of freedom (DOFs) involved. Thus, there seems to be a need for a beam element that can model the behavior of reinforced concrete in each one and combinations of the axial, bending, shear and torsion modes.

The aim of this work is to make an analysis-model that allows for large displacements and material nonlinearities, applicable to large scale 3D beam structures of reinforced and prestressed concrete. In this author's opinion, it is then necessary to develop a beam element that reliably can handle all the deformation/failure modes mentioned previously. That task is considered to be the main challenge of the work. Naturally, this implies also that stress and strain expressions become on multiaxial form (compared to uniaxial for the ordinary 'bending' beam element). Furthermore, the analysis-model should include all time and history effects the design engineer needs or may want to account for through the various stages of the life of a structure; such as creep, shrinkage and aging in concrete and relaxation in prestressing steel, to mention some. Effects of temperature and construction sequences are others. Thus, the vision is to have the analysis-model as realistic as possible, but still with the least amount of DOFs. Also important is that the input-data required should be limited to such that are known to the engineer at the design stage.

This thesis is subdivided into thirteen chapters. The next one to follow contains a summary of concepts and equations in solid mechanics that form the basis for the nonlinear finite element formulations. Chapter 3 deals with 2D beam element formulations with transverse shear based on linear elastic material properties. First a review of existing formulations is given. Then an element formulation with five DOFs is introduced, both on conventional and hierarchical form. The performance of the element is demonstrated through a few examples. In Chapter 4 the 2D hierarchical five DOFs element is extended to a nonlinear 3D version. Then the element consists of fifteen displacement DOFs and four strain DOFs; the latter being introduced to allow for lateral expansion of the cross section. Chapter 5 ends the finite element part of the work. Here various subjects related to nonlinear analysis of beam structures are treated. In Chapter 6 the prestressing tendon modeling is presented. This consists mainly of the geometric description, the force distribution at the tensioning state and the corresponding loading and strain analysis at the element level. Chapter 7 deals with the same topics for prestressing bars. The material modeling part of the work starts with Chapter 8. Here constitutive models (stress-strain relationships) for concrete, reinforcing and prestressing steels are presented. These models reflect the short-time behavior of the materials. For concrete a so-called 2D rotating 'smeared' crack model is adopted. Then Chapter 9 carries on with models for time and temperature dependent effects. Among the time dependent phenomena considered are creep, shrinkage, aging and strength reduction due to high sustained loading for concrete, while stress relaxation is included for prestressing steel. Chapter 10 deals with the cross section analysis, which is the part that connects the material models to the 3D shear-beam element formulation. Here an approach is employed based on subdividing the total cross section into generic units or 'building blocks'. A computer program DARC has been developed as a part of this study. This is briefly reviewed in Chap-

ter 11. Then next follows the application examples in Chapter 12. The thesis closes with summary, conclusions and recommendations for future research in Chapter 13.

Chapter 2

Some Fundamentals of Solid Mechanics

2.1 Introductory Remarks

The purpose of this chapter is to give a brief summary of concepts and equations that form the basis for the large displacement analysis adopted in this work. Furthermore, the presentation will also serve as a convenient reference when starting to specialize the basic equations in succeeding chapters. Thorough treatment of fundamental solid mechanics theory may be found in textbooks like [1, 2].

In this chapter the indicial notation is employed in expressions involving the Cartesian components. Thus, a single or free index is understood to take values in the range one to three, whereas a repeated or dummy index in an expression implies summation over the same range (Einstein's summation convention).

2.2 Lagrangian Description of Motion

2.2.1 General

The motion of a body in space is usually described by the *Lagrangian* description of motion, also referred to as the *material* description. In this context a body consists of an infinite set of material particles occupying a region in space. The simultaneous position of this particle set at a given time is called a *configuration* of the body. A sequence of such configurations defines the motion of the body.

Different optional Lagrangian formulations are available depending on the reference configuration used for the kinematic and static variables involved. The most

common forms are [3]:

- **Total Lagrangian** (TL) description based on the initial configuration C_o as reference.
- **Updated Lagrangian**[1] (UL) description based on the current deformed configuration C_n as reference.
- **Corotated Lagrangian** (CL) description based on a moving undeformed configuration C_{on} (positioned 'close' to C_n) as reference. C_{on} is often termed the 'ghost' reference configuration.

CL-description is in fact a modification of TL in the sense that both are referring to an undeformed state. However, for large displacement analysis it is easier to introduce simplifications in the CL-formulation since rigid body motions there are extracted before computing strains and stresses. The CL-concept has thus been successfully adopted in several works in the recent years, e.g. by Nygård [4] and Mathisen [5], and it also serves as basis for the large displacement formulation in the general purpose finite element program FENRIS [6].

The selected formulation for this work will be the CL-description of motion. At this general level however, it is no need to distinguish clearly between the CL- and TL-formulations. Thus, the expressions presented in the sequel are equally applicable to both formulations as long as the correct reference configuration is employed. The UL-formulation on the other hand, will not be covered further.

2.2.2 Displacements and Strains

The *displacement* vector field $\boldsymbol{u}$ of a deformed body is given by

$$\boldsymbol{u} = \boldsymbol{x} - \boldsymbol{X} \tag{2.1}$$

where $\boldsymbol{x}$ is the deformed position of a material particle and $\boldsymbol{X}$ is the corresponding position of the particle in the reference configuration. The *deformation gradient* tensor $\boldsymbol{F}$ of the body is defined as

$$d\boldsymbol{x} = \boldsymbol{F} \cdot d\boldsymbol{X} \tag{2.2}$$

Using Eq.(2.1), its Cartesian components become

$$F_{ij} = \frac{\partial x_i}{\partial X_j} = \delta_{ij} + \frac{\partial u_i}{\partial X_j} \tag{2.3}$$

where δ_{ij} is the Kronecker delta [1].

[1] In some literature also termed Eulerian description.

The strains are measured in terms of the *Green strain* tensor $\boldsymbol{E}$ which is defined through

$$ds^2 \; - \; dS^2 \; = \; 2\, d\boldsymbol{X} \cdot \boldsymbol{E} \cdot d\boldsymbol{X} \tag{2.4}$$

where dS and ds are the lengths of the infinitesimal material vectors $d\boldsymbol{X}$ and $d\boldsymbol{x}$, respectively. $\boldsymbol{E}$ can be expressed in terms $\boldsymbol{F}$ by

$$\boldsymbol{E} \; = \; \frac{1}{2}\,(\boldsymbol{F}^T \cdot \boldsymbol{F} \; - \; \mathbf{1}) \tag{2.5}$$

where $\mathbf{1}$ is the unit tensor whose components are given by δ_{ij}. In terms of displacements, $\boldsymbol{E}$ reads on indicial form

$$E_{ij} \; = \; \frac{1}{2}\,(\frac{\partial u_i}{\partial X_j} \; + \; \frac{\partial u_j}{\partial X_i} \; + \; \frac{\partial u_k}{\partial X_i}\,\frac{\partial u_k}{\partial X_j}) \tag{2.6}$$

From the last expression it is seen that $\boldsymbol{E}$ is a symmetric tensor, i.e.

$$E_{ij} \; = \; E_{ji} \tag{2.7}$$

Thus, the number of independent components in the tensor reduces from nine to six. The Green strain tensor has further the properties that it vanishes for rigid body motions and reduces to infinitesimal strains (the linear terms in Eq.(2.6)) when both displacements and rotations are 'small'.

The strain increments when going from a deformed configuration C_n to C_{n+1}, are given as the difference between Green strains in the two configurations

$$\Delta\boldsymbol{E} \; = \; {}^{n+1}\boldsymbol{E} \; - \; {}^{n}\boldsymbol{E} \tag{2.8}$$

Note that the strains in this expression are all referring to the same reference configuration. Using Eq.(2.6), the Cartesian components become

$$\Delta E_{ij} \; = \; \frac{1}{2}\,(\frac{\partial \Delta u_i}{\partial X_j} \; + \; \frac{\partial \Delta u_j}{\partial X_i} \; + \; \frac{\partial u_k}{\partial X_i}\,\frac{\partial \Delta u_k}{\partial X_j} \; + \; \frac{\partial \Delta u_k}{\partial X_i}\,\frac{\partial u_k}{\partial X_j}) \tag{2.9}$$

where quadratic incremental terms have been left out.

It may also be proved [4] that Green strain components referring to configuration C_o and configuration C_{on} (with corotated base vectors) become identical. In a CL-formulation this implies that the strain components for a deformed state can be carried over from one reference configuration to the next without transformation.

In succeeding chapters strains will be referred to a column vector of the six independent strain components rather than using a full tensor representation. The off-diagonal terms in $\boldsymbol{E}$ are first added to retain a full shear strain characteristic. Using Eq.(2.7) gives

$$G_{ij} \; = \; E_{ij} \; + \; E_{ji} \; = \; 2\,E_{ij} \qquad ; \quad i \; > \; j \tag{2.10}$$

The column vector of independent strain components may then be symbolized by

$$\boldsymbol{e} \; = \; \left\{ \begin{array}{c} E_{ii} \\ G_{ij} \end{array} \right\} \tag{2.11}$$

2.2.3 Stresses and Equilibrium

The *traction* or stress vector $\boldsymbol{t}$ at a point referred to the deformed configuration of a body is defined by

$$\boldsymbol{t} \;=\; \frac{d\boldsymbol{f}}{dA} \tag{2.12}$$

where $d\boldsymbol{f}$ is the infinitesimal force vector that acts on the infinitesimal area dA at the surface or section. Note that $\boldsymbol{t}$ is not a vector field since it depends not only on the position, but also on the direction of the outward unit normal vector $\boldsymbol{n}$ to the area dA.

Equilibrium at the point of an infinitesimal tetrahedron whose faces are normal to the Cartesian base vectors and to $\boldsymbol{n}$, leads to the following expression involving the *Cauchy stress* tensor $\boldsymbol{\sigma}$

$$\boldsymbol{t} \;=\; \boldsymbol{n}\cdot\boldsymbol{\sigma} \tag{2.13}$$

or on component form

$$t_i \;=\; n_j\,\sigma_{ji} \tag{2.14}$$

Force equilibrium in the deformed configuration gives the static version of Cauchy's equation of motion

$$\frac{\partial \sigma_{ji}}{\partial x_j} \;+\; f_i \;=\; 0 \tag{2.15}$$

where f_i is the *body force* per unit deformed volume. Furthermore, moment equilibrium reveals the symmetry of the Cauchy stress tensor, i.e.

$$\sigma_{ij} \;=\; \sigma_{ji} \tag{2.16}$$

Thus, the number of independent components in the tensor reduces from nine to six.

Since the Cauchy stress tensor refers to the deformed configuration, it will not be energy-conjugate to the Green strain tensor. Thus, there is a need for an alternative stress measure that has the undeformed configuration as reference. Such a stress measure can be derived in the following way:

Instead of the real force $d\boldsymbol{f}$ acting on dA in the deformed configuration, a 'pseudo'-force $d\boldsymbol{f}^*$ acting on dA_o in the undeformed configuration is constructed through the relation

$$d\boldsymbol{f}^* \;=\; \boldsymbol{F}^{-1}\cdot d\boldsymbol{f} \tag{2.17}$$

Thus, $d\boldsymbol{f}^*$ relates to $d\boldsymbol{f}$ in the same way as $d\boldsymbol{X}$ relates to $d\boldsymbol{x}$ according to the inverse of Eq.(2.2). Analogous to Eqs.(2.12-2.14), a 'pseudo'-traction $\boldsymbol{t}^*$ is defined

$$\boldsymbol{t}^* \;=\; \frac{d\boldsymbol{f}^*}{dA_o} \tag{2.18}$$

together with a 'pseudo'-stress tensor $\boldsymbol{S}$

$$\boldsymbol{t}^* \;=\; \boldsymbol{N}\cdot\boldsymbol{S} \tag{2.19}$$

or on component form

$$t_i^* \;=\; N_j\, S_{ji} \tag{2.20}$$

Here $\boldsymbol{N}$ is the outward unit normal vector to the area dA_o, and $\boldsymbol{S}$ is commonly referred to as the *2nd Piola-Kirchhoff stress* tensor. The latter can be related to the Cauchy stress tensor by use of Nanson's formula [1], which gives

$$\boldsymbol{S} \;=\; \frac{\rho_o}{\rho}\,\boldsymbol{F}^{-1}\cdot\boldsymbol{\sigma}\cdot\left(\boldsymbol{F}^{-1}\right)^T \tag{2.21}$$

with Cartesian components

$$S_{ij} \;=\; \frac{\rho_o}{\rho}\,\frac{\partial X_i}{\partial x_k}\,\sigma_{kl}\,\frac{\partial X_j}{\partial x_l} \;=\; \frac{\rho_o}{\rho}\left(\delta_{ik}-\frac{\partial u_i}{\partial x_k}\right)\sigma_{kl}\left(\delta_{jl}-\frac{\partial u_j}{\partial x_l}\right) \tag{2.22}$$

where ρ and ρ_o are the mass densities in deformed and undeformed configurations, respectively[2]. The above stress relationship represents a symmetric transformation, and since the Cauchy stress tensor in itself is symmetric, so becomes also the 2nd Piola-Kirchhoff stress tensor, i.e.

$$S_{ij} \;=\; S_{ji} \tag{2.23}$$

Thus, the number of independent components in $\boldsymbol{S}$ reduces from nine to six. When both displacements and rotations are 'small', the 2nd Piola-Kirchhoff stress approaches the Cauchy stress. As for the Green strain components, it may also be proved that the components of $\boldsymbol{S}$ referring to configuration C_o and configuration C_{on} (with corotated base vectors) become identical. Consequently, the stress components for a deformed state using a CL-formulation can be carried over from one reference configuration to the next without transformation.

By inserting the inverse relationship of Eq.(2.22(first part)) into Eq.(2.15), the static equilibrium in deformed configuration expressed in terms of the 2nd Piola-Kirchhoff stress, takes the form

$$\frac{\partial}{\partial X_j}\left(S_{jk}\,\frac{\partial x_i}{\partial X_k}\right) \;+\; f_{oi} \;=\; 0 \tag{2.24}$$

where

$$f_{oi} \;=\; \frac{\rho_o}{\rho}\,f_i \tag{2.25}$$

which is the body force intensity in deformed configuration scaled to a unit volume of the undeformed state ($dV/dV_o = \rho_o/\rho$).

Like strains, stresses will in succeeding chapters also be referred to a column vector of the six independent components rather than using a full tensor representation. Denoting the off-diagonal terms of the symmetric $\boldsymbol{S}$-tensor by

$$T_{ij} \;=\; S_{ij} \qquad ;\quad i > j \tag{2.26}$$

[2]Usually the ratio of mass densities will be close to unity.

the column vector of independent stress components may then be symbolized

$$\boldsymbol{s} \;=\; \left\{ \begin{array}{c} S_{ii} \\ T_{ij} \end{array} \right\} \tag{2.27}$$

2.2.4 Constitutive Relations

To give an expression in its most general form for computing total current stresses $\boldsymbol{S}$ is a difficult task. However, a functional relationship that fits within the frame of this work, may read

$$\boldsymbol{S} \;=\; \boldsymbol{S}(\boldsymbol{E}, \Delta T, m_i, \kappa_i) \tag{2.28}$$

where $\boldsymbol{E}$ represents the current strains[3] and ΔT is the current change in temperature from the reference state. Furthermore, m_i signifies material properties that in return may depend on previous histories of time, temperature, humidity, stresses and strains. Finally, κ_i symbolizes effects related to internal state variables which again may depend on previous histories of stresses and strains.

In nonlinear analysis a need typically arises for an incremental material law. Differentiation of Eq.(2.28) with respect to $\boldsymbol{E}$ yields

$$\Delta\boldsymbol{S} \;=\; \boldsymbol{C_T} : \Delta\boldsymbol{E} \tag{2.29}$$

where $\Delta\boldsymbol{S}$ and $\Delta\boldsymbol{E}$ denote small but finite increments of stresses and strains, and $\boldsymbol{C_T}$ is the incremental or *tangential constitutive tensor* of 4th order. The Cartesian components become

$$\Delta S_{ij} \;=\; C_{Tijkl}\, \Delta E_{kl} \tag{2.30}$$

In principle, $\boldsymbol{C_T}$ may be expressed by a similar functional relationship as $\boldsymbol{S}$, thus

$$\boldsymbol{C_T} \;=\; \boldsymbol{C_T}(\boldsymbol{E}, \Delta T, m_i, \kappa_i) \tag{2.31}$$

With the column vector representation of the six independent components of stresses and strains, i.e. $\boldsymbol{s}$ and $\boldsymbol{e}$, the incremental material law takes the form

$$\Delta\boldsymbol{s} \;=\; \boldsymbol{C_t}\, \Delta\boldsymbol{e} \tag{2.32}$$

where now $\boldsymbol{C_t}$ is termed the incremental or *tangential constitutive matrix*. This is the adopted form of the incremental material law for succeeding chapters of this work. Indeed, the components of $\boldsymbol{C_t}$ are obtained by direct differentiation of the stress-strain relationships, i.e.

$$\boldsymbol{C_t} \;=\; \frac{\partial \boldsymbol{s}}{\partial \boldsymbol{e}} \tag{2.33}$$

Since $\boldsymbol{C_t}$ in general not becomes symmetric, it will consist of 36 independent components for the 3D case.

[3] Effect of ('high') current strain rates is left out since this work deals with static conditions.

2.2.5 Boundary Conditions

Boundary conditions are divided into two kinds. The *displacement boundary conditions* are given by

$$\boldsymbol{u} \;=\; \check{\boldsymbol{u}} \qquad \text{on} \quad \partial V_{ou} \tag{2.34}$$

or on component form

$$u_i \;=\; \check{u}_i \qquad \text{on} \quad \partial V_{ou} \tag{2.35}$$

where $\check{\boldsymbol{u}}$ is the prescribed displacement vector on the boundary surface ∂V_{ou}.

The stress or *traction boundary conditions* are specified on the complementary boundary surface ∂V_{ot}. From Eqs.(2.19, 2.20) the compact and component forms become

$$\boldsymbol{N} \cdot \boldsymbol{S} \;=\; \check{\boldsymbol{t}}^* \qquad \text{on} \quad \partial V_{ot} \tag{2.36}$$

$$N_j \, S_{ji} \;=\; \check{t}_i^* \qquad \text{on} \quad \partial V_{ot} \tag{2.37}$$

where $\check{\boldsymbol{t}}^*$ is the prescribed surface 'pseudo'-traction vector that acts in the undeformed configuration. The correspondence to the actual prescribed surface traction $\check{\boldsymbol{t}}$ in the deformed configuration can be obtained by combining Eqs.(2.12,2.17,2.18). Thus

$$\check{\boldsymbol{t}}^* \;=\; \frac{d(\partial V)}{d(\partial V_o)} \, \boldsymbol{F}^{-1} \cdot \check{\boldsymbol{t}} \;=\; \boldsymbol{F}^{-1} \cdot \check{\boldsymbol{t}}_{\boldsymbol{o}} \tag{2.38}$$

or in terms of Cartesian components

$$\check{t}_i^* \;=\; \frac{d(\partial V)}{d(\partial V_o)} \, \frac{\partial X_i}{\partial x_j} \, \check{t}_j \;=\; \frac{\partial X_i}{\partial x_j} \, \check{t}_{oj} \tag{2.39}$$

where $\check{\boldsymbol{t}}_{\boldsymbol{o}}$ is the prescribed surface traction in deformed configuration scaled to a unit surface of the undeformed state, i.e.

$$\check{\boldsymbol{t}}_{\boldsymbol{o}} \;=\; \frac{d(\partial V)}{d(\partial V_o)} \, \check{\boldsymbol{t}} \tag{2.40}$$

2.3 Variational Formulations

2.3.1 General

The preceding section presented the connecting or *governing equations* that are linking the various unknown fields ($\boldsymbol{u}$,$\boldsymbol{E}$,$\boldsymbol{S}$) and known fields ($\boldsymbol{f_o}$,$\check{\boldsymbol{t}}_{\boldsymbol{o}}$,$\check{\boldsymbol{u}}$). In solid mechanics several principles exist for constructing *variational forms* of the governing equations. Two classes of principles of fundamental importance in this context are the *variational* or *stationary energy principles* and the *virtual work principles*.[4] Such

[4]Several authors use *variational principles* as a common term for both classes.

principles are stated on integral form that emanates from relaxing some of the governing equations to *weak* or mean connections rather than keeping the original *strong* or point-by-point enforcements. When subjecting the primary unknown field(s) to some kind of discretization, the integral form in turn converts to algebraic equations yielding approximate solution(s) of the problem. Often the various principles may lead to identical solutions when subjected to the same approximating field expansion.

2.3.2 Principle of Virtual Displacements

A suitable starting point for finite element discretization based on displacements as the primary unknown field, is to apply the *principle of virtual displacements* that pertains to the virtual work-class of principles. This principle can be derived by taking the volume equilibrium equations (Eq.(2.24)) and traction boundary conditions (Eq.(2.37)) as weak connections, combined with an arbitrary virtual displacement that satisfies the strain-displacement equations (Eq.(2.6)) and displacement boundary conditions (Eq.(2.35)[5]) strongly. Note that no requirements are placed on the material properties. The final result becomes

$$\int_{V_o} \delta \boldsymbol{E} : \boldsymbol{S}\, dV_o \;=\; \int_{V_o} \delta \boldsymbol{u} \cdot \boldsymbol{f_o}\, dV_o \;+\; \int_{\partial V_o} \delta \boldsymbol{u} \cdot \check{\boldsymbol{t}}_{\boldsymbol{o}}\, d(\partial V_o) \tag{2.41}$$

or on component form

$$\int_{V_o} \delta E_{ij}\, S_{ij}\, dV_o \;=\; \int_{V_o} \delta u_i\, f_{oi}\, dV_o \;+\; \int_{\partial V_o} \delta u_i\, \check{t}_{oi}\, d(\partial V_o) \tag{2.42}$$

Here $\delta \boldsymbol{u}$ is the virtual displacement vector, and $\delta \boldsymbol{E}$ is the virtual strain tensor whose components in terms of displacements result from Eq.(2.6)

$$\delta E_{ij} \;=\; \frac{1}{2}\left(\frac{\partial \delta u_i}{\partial X_j} \;+\; \frac{\partial \delta u_j}{\partial X_i} \;+\; \frac{\partial u_k}{\partial X_i}\frac{\partial \delta u_k}{\partial X_j} \;+\; \frac{\partial \delta u_k}{\partial X_i}\frac{\partial u_k}{\partial X_j}\right) \tag{2.43}$$

which is on a form similar to the incremental strain components in Eq.(2.9). Furthermore, $\boldsymbol{f_o}$ and $\check{\boldsymbol{t}}_{\boldsymbol{o}}$ are the body force intensity and prescribed surface traction as given by Eqs.(2.25,2.40), respectively.

With the column vector representation of the six independent components of stresses and strains, i.e. $\boldsymbol{s}$ and $\boldsymbol{e}$, the mathematical statement of the principle of virtual displacements takes the form

$$\int_{V_o} \delta \boldsymbol{e}^{\boldsymbol{T}} \boldsymbol{s}\, dV_o \;=\; \int_{V_o} \delta \boldsymbol{u}^{\boldsymbol{T}} \boldsymbol{f_o}\, dV_o \;+\; \int_{\partial V_o} \delta \boldsymbol{u}^{\boldsymbol{T}} \check{\boldsymbol{t}}_{\boldsymbol{o}}\, d(\partial V_o) \tag{2.44}$$

where now also $\boldsymbol{u}$, $\boldsymbol{f_o}$ and $\check{\boldsymbol{t}}_{\boldsymbol{o}}$ are treated as column vectors. When subjecting the displacement field to discretization in a finite element method, the left hand side of Eq.(2.44) gives rise to the *internal node-force vector*, while the *applied* or *consistent node-force vector* arises from the right hand side.

[5]The right hand side of Eq.(2.35) is always zero for a virtual displacement since it becomes in excess of the actual prescribed value $\check{u}_i$.

2.3.3 Incremental Form of Principle of Virtual Displacements

By taking the difference in virtual work, according to Eq.(2.41), between two neighboring equilibrium configurations C_{n+1} and C_n, the following expression for the *principle of virtual displacements on incremental form* results

$$\int_{V_o} (\delta\Delta\boldsymbol{E} : \boldsymbol{S} \, + \, \delta\boldsymbol{E} : \Delta\boldsymbol{S}) \, dV_o \, = \, \int_{V_o} \delta\boldsymbol{u} \cdot \Delta\boldsymbol{f_o} \, dV_o \, + \, \int_{\partial V_o} \delta\boldsymbol{u} \cdot \Delta\check{\boldsymbol{t}}_{\boldsymbol{o}} \, d(\partial V_o) \quad (2.45)$$

or with Cartesian components

$$\int_{V_o} (\delta\Delta E_{ij} \, S_{ij} \, + \, \delta E_{ij} \, \Delta S_{ij}) \, dV_o \, = \, \int_{V_o} \delta u_i \, \Delta f_{oi} \, dV_o \, + \, \int_{\partial V_o} \delta u_i \, \Delta\check{t}_{oi} \, d(\partial V_o) \quad (2.46)$$

where quadratic incremental terms on the left hand side are left out. Here the arbitrary virtual displacement $\delta\boldsymbol{u}$ is taken to be the same for the two configurations, and thus

$$\delta\Delta\boldsymbol{u} \, = \, 0 \quad (2.47)$$

which gives, in combination with the variation of Eq.(2.9), the following expression for $\delta\Delta\boldsymbol{E}$ on component form

$$\delta\Delta E_{ij} \, = \, \frac{1}{2} \, (\frac{\partial\delta u_k}{\partial X_i} \frac{\partial\Delta u_k}{\partial X_j} \, + \, \frac{\partial\Delta u_k}{\partial X_i} \frac{\partial\delta u_k}{\partial X_j}) \quad (2.48)$$

Introducing the incremental material law from Eqs.(2.29,2.30), the stress increments in Eqs.(2.45,2.46) can be eliminated, i.e.

$$\int_{V_o} (\delta\Delta\boldsymbol{E} : \boldsymbol{S} + \delta\boldsymbol{E} : \boldsymbol{C_T} : \Delta\boldsymbol{E}) \, dV_o \, = \, \int_{V_o} \delta\boldsymbol{u} \cdot \Delta\boldsymbol{f_o} \, dV_o + \int_{\partial V_o} \delta\boldsymbol{u} \cdot \Delta\check{\boldsymbol{t}}_{\boldsymbol{o}} \, d(\partial V_o) \quad (2.49)$$

$$\int_{V_o} (\delta\Delta E_{ij} \, S_{ij} + \delta E_{ij} \, C_{Tijkl} \, \Delta E_{kl}) \, dV_o \, = \, \int_{V_o} \delta u_i \, \Delta f_{oi} \, dV_o + \int_{\partial V_o} \delta u_i \, \Delta\check{t}_{oi} \, d(\partial V_o) \quad (2.50)$$

where the components of $\Delta\boldsymbol{E}$ are given by Eq.(2.9).

With the column vector representation of the six independent components of stresses and strains, i.e. $\boldsymbol{s}$ and $\boldsymbol{e}$, Eq.(2.49) will take the alternative form

$$\int_{V_o} (\delta\Delta\boldsymbol{e}^{\boldsymbol{T}}\boldsymbol{s} \, + \, \delta\boldsymbol{e}^{\boldsymbol{T}}\boldsymbol{C_t}\Delta\boldsymbol{e}) \, dV_o \, = \, \int_{V_o} \delta\boldsymbol{u}^{\boldsymbol{T}}\Delta\boldsymbol{f_o} \, dV_o \, + \, \int_{\partial V_o} \delta\boldsymbol{u}^{\boldsymbol{T}}\Delta\check{\boldsymbol{t}}_{\boldsymbol{o}} \, d(\partial V_o) \quad (2.51)$$

where now again $\boldsymbol{u}$, $\boldsymbol{f_o}$ and $\check{\boldsymbol{t}}_{\boldsymbol{o}}$ are treated as column vectors. The tangent constitutive matrix $\boldsymbol{C_t}$ is defined through Eq.(2.33).

The incremental virtual work contributions from body force and surface traction in Eq.(2.51) can further be expressed by

$$\int_{V_o} \delta\boldsymbol{u}^{\boldsymbol{T}}\Delta\boldsymbol{f_o} \, dV_o \, = \, \int_{V_o} \left(\delta\boldsymbol{u}^{\boldsymbol{T}}\Delta\boldsymbol{f_o}(\Delta h_i(\lambda)) \, + \, \delta\boldsymbol{u}_{\boldsymbol{a}}^{\boldsymbol{T}}\Delta\boldsymbol{f_{oa}}(\Delta\boldsymbol{u}_a)\right) dV_o \quad (2.52)$$

$$\int_{\partial V_o} \delta\boldsymbol{u}^{\boldsymbol{T}}\Delta\check{\boldsymbol{t}}_{\boldsymbol{o}} \, d(\partial V_o) \, = \, \int_{\partial V_o} \left(\delta\boldsymbol{u}^{\boldsymbol{T}}\Delta\check{\boldsymbol{t}}_{\boldsymbol{o}}(\Delta h_i(\lambda)) \, + \, \delta\boldsymbol{u}_{\boldsymbol{a}}^{\boldsymbol{T}}\Delta\check{\boldsymbol{t}}_{\boldsymbol{oa}}(\Delta\boldsymbol{u}_a)\right) d(\partial V_o) \quad (2.53)$$

Here the first terms on the right hand side come from a change in load level caused by some externally prescribed scaling factors $\Delta h_i(\lambda)$, while the second terms arise from the change in position and direction of the loading as the body undergoes incremental displacements $\Delta \boldsymbol{u}_a$ between the two configurations. The subscript 'a' on the latter terms signifies that the displacement and loading vectors now are augmented with rotations and moment intensities, respectively.

When subjecting the displacement field to discretization in a finite element method, the first term on the left hand side of Eq.(2.51) gives rise to the *geometric stiffness matrix*, while the *material stiffness matrix* arises from the second term. Furthermore, the *load correction stiffness matrix* originates from the second terms on the right hand side of Eqs.(2.52,2.53); all matrices being on incremental form. Note that the final expression for the last mentioned matrix will depend on whether the loading is *unidirectional* or *corotational*.

Chapter 3

2D Elastic Shear-Beam Element Formulations

3.1 Review of Existing Formulations

Beam elements that account for shear deformation in addition to bending, are in the literature often classified as *Timoshenko beam elements* because of the relationship to the Timoshenko beam theory[1]. In this work, however, the more descriptive and general *shear-beam elements* will be the preferred term.

The review of shear-beam elements in this section will restrict to lower order elements that (for the linear elastic case) can model up to linear variation of bending moment at the interior. Although all elements considered employ linear elasticity (since this is the common form in literature), each formulation will be evaluated in light of its potential for extension into nonlinear materials, in particular reinforced concrete.

Several authors have derived the stiffness matrix for a two node four DOFs (degrees of freedom) beam element from a displacement assumption using the internal moment equilibrium equation as an additional constraint (i.e. shear force equals first moment derivative). E.g. Archer [8] and Narayanaswami and Adelman [9] obtained correct result according to Timoshenko beam theory. For a slender beam the stiffness matrix then simplifies to that of the *Bernoulli-Euler beam element* based on the classical beam theory for bending deformation only. As nodal DOFs were used displacement and bending rotation (i.e. cross section rotation). This selection of rotational DOF is crucial, since other authors have employed the displacement slope instead and obtained erroneous result. An important consequence of the internal moment equilibrium constraint for the linear elastic case is that the mean shear strain of the cross section becomes equal to the constant ratio of bending- to shear cross section stiffnesses, times the third displacement derivative. However, for nonlinear material properties such a simple relationship between shear strain and displacement derivative can not in general be established, which prevents this class of formulation

[1] For Timoshenko beam theory see e.g. [7].

from being suitable for application to nonlinear materials.

A more general approach for deriving displacement based shear-beam elements is to interpolate displacements (w) and bending rotations (θ) independently. Such formulations are not in general restricted to linear elastic materials. Best known in this category is the two node four DOFs beam element with linear interpolation assumption for both w and θ, in [10] referred to as the *Mindlin beam element*. For the linear elastic case this gives constant bending moment only within an element. In addition, the element becomes overly stiff in the slender beam regime, i.e. the element 'locks'. This can be overcomed, at least for the linear elastic case, by underintegrating the part of the stiffness matrix arising from the shear strain energy, which is often termed *selective reduced integration*. However, for nonlinear materials in general the constitutive relations will contain coupling terms between normal and shear strains, which implies that the total strain energy no more can be split into a simple sum of bending- and shear strain energies only. In particular reinforced concrete exhibits such a performance, and thus the remedy of selective reduced integration becomes doubtful.

The correct stiffness matrix according to Thimoshenko beam theory can also be derived from an equilibrium stress hybrid formulation, as given by Severn [11] and recently by Oral [12]. Such a formulation is in principle applicable to nonlinear materials, which has been demonstrated lately by Carol and Murcia [13, 14] for a 2D beam element formulation based on Bernoulli-Euler theory and with 1D stress-strain behavior. However, a further extension into a general nonlinear 3D shear-beam element formulation does not seem to be so straightforward as for a displacement formulation. Thus, the stress hybrid formulation is not considered to be the natural starting point for the finite element approximation in this work.

Based on the existing formulations reviewed so far, a need seems to be present for developing a lower order shear-beam element that can model linear variation of bending moment and constant transverse shear for the linear elastic case, and which is easily extendable to nonlinear materials. The derivation of such an element is presented in the next two sections. Although a complete nonlinear 3D shear-beam element formulation is the final goal, the succeeding presentation is made for linear elasticity on a 2D element in order to concentrate on essentials in the formulation and to demonstrate the performance of the element compared to analytical solutions. In Chapter 4 a complete extension to the nonlinear 3D version will be undertaken.

After the theoretical part of this work was ended, the author has been aware of a publication by Tessler and Dong [15] which presents a procedure for deriving a family of displacement based *virgin* elements from successively higher order interpolation of w and θ. For each element the order of w is always one degree higher than θ, which is referred to as *interdependent interpolation*. By again imposing successively reduced order of mean shear strain variations as constraints on each virgin element, a new family of *constrained* or condensed elements is then created. This condensation procedure is performed at the interpolation level by deriving a constrained interdependent interpolation field with fewer DOFs compared to the original virgin element.

In [15] it is stated that the constrained element denoted T1CC4 has stiffness matrix identical to the Mindlin beam element with selective reduced integration (linear elasticity). Furthermore, the constrained element denoted T2CC5 appears to be the same as the five DOFs element on conventional form as presented in the next section. However, no explicit expressions for final element quantities are given in [15]. This, in addition to the indirect and somewhat complex derivation procedure, may explain the surprisingly low attention this work has gained in the literature.

As will become evident, the five DOFs element on conventional form presented in the next section is derived by a direct and different approach compared to the T2CC5 element by Tessler and Dong. The hierarchical form of the element, as presented in the section thereafter, is believed to be new. Indeed, the latter is the version that forms basis for the extension into the 3D shear-beam element.

3.2 Element with Five DOFs

Consider a 2D beam lying in the (x, z)-plane of a right handed Cartesian coordinate system with the x-axis coinciding the longitudinal centroidal axis of the beam. To account for transverse shear deformation in addition to bending, plane sections that initially were normal to the longitudinal axis, are assumed to remain plane during deformation but not necessarily normal anymore. This assumption complies with the Timoshenko beam theory and deviates from the classical bending theory of Bernoulli-Euler by leaving out the normality constraint for the sections. The assumed deformational behavior is depicted in Fig. 3.1 where θ_y is the rotation of the cross section (bending rotation) and subscript 'o' on displacements refers to values at the centroid. Thus, the longitudinal displacement can be expressed

$$u(x,z) \;\approx\; u_o(x) \;+\; z\,\theta_y(x) \tag{3.1}$$

While the transverse displacement is taken to be same over the depth of the beam, i.e.

$$w(x,z) \;\approx\; w_o(x) \tag{3.2}$$

The derivations in the following will consider linear effects only. By neglecting the quadratic terms of the Green strain components in Eq.(2.6), the infinitesimal normal strain ϵ_x becomes

$$\epsilon_x \;=\; \frac{\partial u}{\partial x} \;=\; \frac{du_o}{dx} \;+\; z\,\frac{d\theta_y}{dx} \tag{3.3}$$

When also applying Eq.(2.10), the corresponding expression for the infinitesimal shear strain γ_{xz} takes the form

$$\gamma_{xz} \;=\; \frac{\partial u}{\partial z} \;+\; \frac{\partial w}{\partial x} \;=\; \theta_y \;+\; \frac{dw_o}{dx} \tag{3.4}$$

Thus, the bending rotation is connected to the infinitesimal shear strain and the slope of the transverse displacement through

$$\theta_y \;=\; \gamma_{xz} \;-\; \frac{dw_o}{dx} \tag{3.5}$$

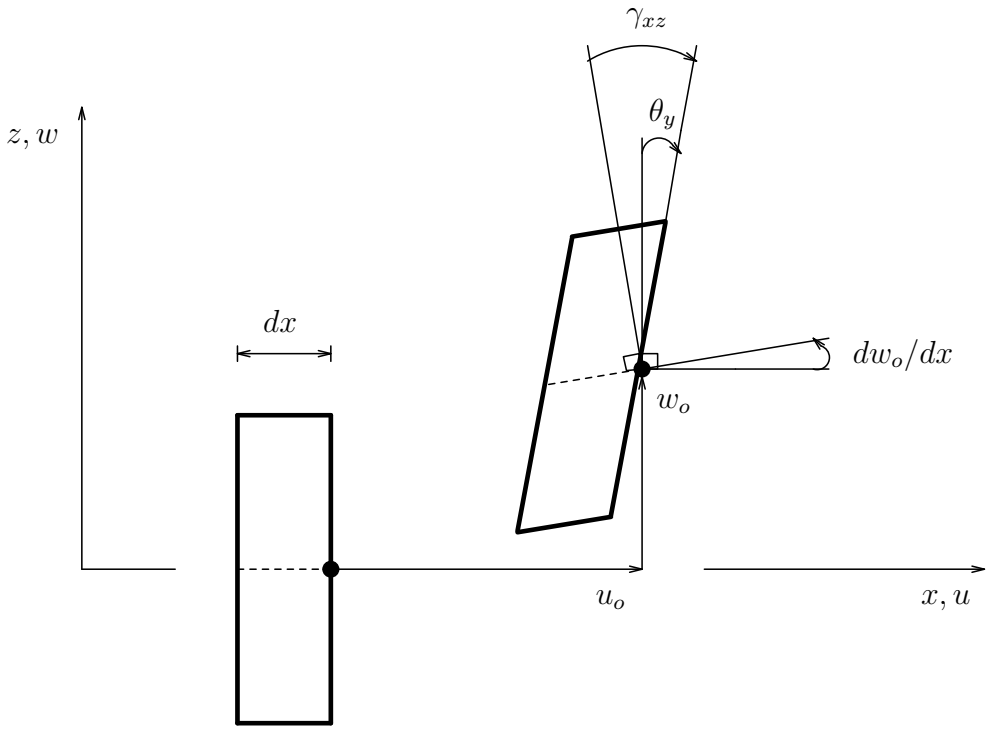

Figure 3.1: Deformations of a Beam 'Slice'

As already stated in the preceding section, the attempt now is to develop a lower order shear-beam element that can model linear variation of bending moment and constant transverse shear for the linear elastic case. Consequently, the natural choice should then be to subject the transverse displacement and the shear strain to trial expansions, respectively a cubic polynomial and a constant. Furthermore, the longitudinal centroidal displacement can be left out in this pure bending-shear problem. Thus

$$u_o \approx 0 \tag{3.6}$$

$$w_o \approx a_0 + a_1 x + a_2 x^2 + a_3 x^3 \tag{3.7}$$

$$\gamma_{xz} \approx b_0 \tag{3.8}$$

Then the expression for the normal strain in Eq.(3.3) simplifies to

$$\epsilon_x = -z \frac{d^2 w_o}{dx^2} \tag{3.9}$$

The problem of solving the displacement and strain fields of the beam element has now five unknowns, i.e. a_0 through a_3 and b_0. To seek a configuration of corresponding five physical DOFs, transverse displacement and bending rotation will be selected at locations that can give rise to states of constant shear and linear bending inside the element. The displacement and rotation at each endpoint of the element are obvious candidates. As opposed to the displacement at the midpoint, the rotation there is

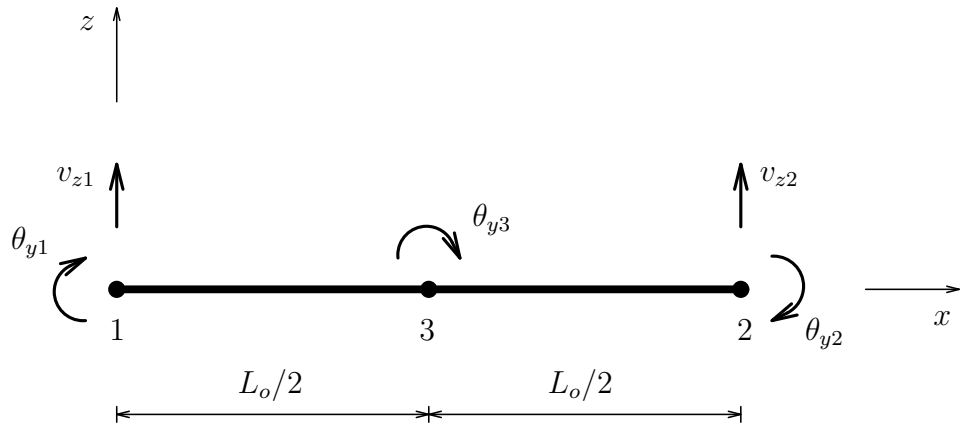

Figure 3.2: 2D Shear-Beam Element with Five DOFs

also creating constant shear, and thus the latter will be the selected fifth DOF. The finite element configuration then becomes as shown in Fig. 3.2.

The *shape functions* pertaining to each DOF can be found by imposing one DOF at a time equal to unity and the others equal to zero, and then solve for the five unknowns $(a_0 - a_3, b_0)$ in turn. Note that rotations are bending rotations as given by Eq.(3.5). The results can be written on the form

$$w_o \;=\; \boldsymbol{N}_{w_o}\,\boldsymbol{v} \tag{3.10}$$

$$\gamma_{xz} \;=\; \boldsymbol{N}_{\gamma_{xz}}\,\boldsymbol{v} \tag{3.11}$$

where

$$\boldsymbol{v}^T \;=\; \left[\begin{array}{ccccc} v_{z1} & \theta_{y1} & v_{z2} & \theta_{y2} & \theta_{y3} \end{array}\right] \tag{3.12}$$

$$\boldsymbol{N}_{w_o} \;=\; \left[\begin{array}{ccccc} N_{w_o}^{(v_1)} & N_{w_o}^{(\theta_1)} & N_{w_o}^{(v_2)} & N_{w_o}^{(\theta_2)} & N_{w_o}^{(\theta_3)} \end{array}\right] \tag{3.13}$$

$$\boldsymbol{N}_{\gamma_{xz}} \;=\; \left[\begin{array}{ccccc} N_{\gamma_{xz}}^{(v_1)} & N_{\gamma_{xz}}^{(\theta_1)} & N_{\gamma_{xz}}^{(v_2)} & N_{\gamma_{xz}}^{(\theta_2)} & N_{\gamma_{xz}}^{(\theta_3)} \end{array}\right] \tag{3.14}$$

with shape functions pertaining to transverse displacement given by

$$N_{w_o}^{(v_1)} \;=\; \frac{1}{2}\,(1 - \xi) \tag{3.15}$$

$$N_{w_o}^{(\theta_1)} \;=\; -\,\frac{L_o}{24}\,(3 - 2\xi)\,(1 - \xi^2) \tag{3.16}$$

$$N_{w_o}^{(v_2)} \;=\; \frac{1}{2}\,(1 + \xi) \tag{3.17}$$

$$N_{w_o}^{(\theta_2)} \;=\; \frac{L_o}{24}\,(3 + 2\xi)\,(1 - \xi^2) \tag{3.18}$$

$$N_{w_o}^{(\theta_3)} \;=\; -\,\frac{L_o}{6}\,\xi\,(1 - \xi^2) \tag{3.19}$$

and shape functions pertaining to shear strain

$$N_{\gamma_{xz}}^{(v_1)} = -\frac{1}{L_o} \tag{3.20}$$

$$N_{\gamma_{xz}}^{(\theta_1)} = \frac{1}{6} \tag{3.21}$$

$$N_{\gamma_{xz}}^{(v_2)} = \frac{1}{L_o} \tag{3.22}$$

$$N_{\gamma_{xz}}^{(\theta_2)} = \frac{1}{6} \tag{3.23}$$

$$N_{\gamma_{xz}}^{(\theta_3)} = \frac{2}{3} \tag{3.24}$$

Furthermore, ξ is the natural beam coordinate that takes the values -1, 1 and 0 at node 1, 2 and 3, respectively. Thus

$$\xi = \frac{2x}{L_o} - 1 \tag{3.25}$$

The shape functions are depicted in Fig. 3.3.

Having established the shape functions for the element, the next is to relate the strain field to the nodal DOFs through the *strain-displacement matrix* $\boldsymbol{B}$. For shear strain the relation needed is given by Eq.(3.11) directly, while for normal strain Eq.(3.10) has to be differentiated twice before inserted into Eq.(3.9). Thus

$$\boldsymbol{\epsilon} = \boldsymbol{B}\,\boldsymbol{v} \tag{3.26}$$

where

$$\boldsymbol{\epsilon} = \begin{Bmatrix} \epsilon_x \\ \gamma_{xz} \end{Bmatrix} \tag{3.27}$$

$$\boldsymbol{B} = \begin{bmatrix} \boldsymbol{b}_b \\ \boldsymbol{b}_s \end{bmatrix} \tag{3.28}$$

with the subvectors pertaining to bending (i.e. normal) strain $\boldsymbol{b}_b$ and shear strain $\boldsymbol{b}_s$ given by

$$\boldsymbol{b}_b = -z\frac{d^2\boldsymbol{N}_{w_o}}{dx^2} = \frac{z}{L_o}\begin{bmatrix} 0 & -(1-2\xi) & 0 & (1+2\xi) & -4\xi \end{bmatrix} \tag{3.29}$$

$$\boldsymbol{b}_s = \boldsymbol{N}_{\gamma_{xz}} = \begin{bmatrix} -\frac{1}{L_o} & \frac{1}{6} & \frac{1}{L_o} & \frac{1}{6} & \frac{2}{3} \end{bmatrix} \tag{3.30}$$

Since linear effects are the only considered here, the material law can now sufficiently be formulated on total form (as opposed to the incremental form in Eq.(2.32)). Thus

$$\boldsymbol{\sigma} = \boldsymbol{C}\,\boldsymbol{\epsilon} \tag{3.31}$$

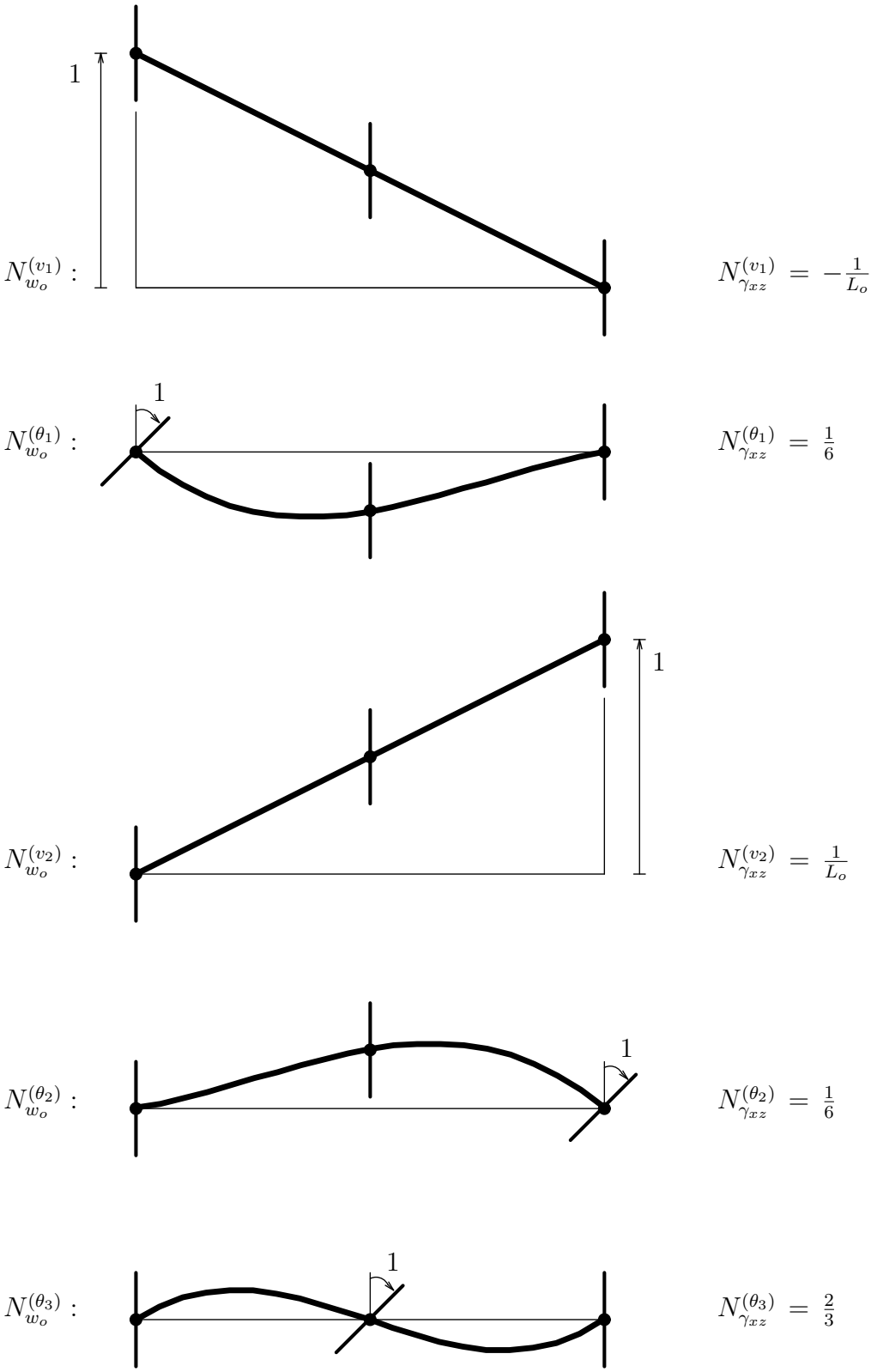

Figure 3.3: Shape Functions of the 2D Shear-Beam Element

where $\boldsymbol{\sigma}$ is the Cauchy stress vector corresponding to the infinitesimal strains, i.e.

$$\boldsymbol{\sigma} \;=\; \left\{ \begin{array}{c} \sigma_x \\ \tau_{xz} \end{array} \right\} \tag{3.32}$$

and $\boldsymbol{C}$ is the constitutive matrix, which for the 2D linear elastic material is given by

$$\boldsymbol{C} \;=\; \left[\begin{array}{cc} E & 0 \\ 0 & G \end{array} \right] \tag{3.33}$$

Here E is the elastic modulus and G is the shear modulus.

Finally, the applied load on the element will be specified in terms of transverse load per unit axial length of the beam q_z.

Now everything needed is defined for applying the principle of virtual displacements to carry out the expressions for the final element quantities. Again, since linear effects are the only considered here, the principle on total form becomes sufficient. Thus, from Eq.(2.44)

$$\int_{V_o} \delta\boldsymbol{\epsilon}^T \boldsymbol{\sigma}\, dV_o \;=\; \int_{L_o} \delta w_o^T\, q_z\, dL_o \tag{3.34}$$

Insertion of Eqs.(3.10,3.26,3.31) yields the discretized form

$$\delta\boldsymbol{v}^T \left(\int_{V_o} \boldsymbol{B}^T \boldsymbol{C}\, \boldsymbol{B}\, dV_o \right) \boldsymbol{v} \;=\; \delta\boldsymbol{v}^T \int_{L_o} \boldsymbol{N}_{w_o}^T\, q_z\, dL_o \tag{3.35}$$

which must be valid for an arbitrary $\delta\boldsymbol{v}$. Thus

$$\boldsymbol{k}_m\, \boldsymbol{v} \;=\; \boldsymbol{p} \tag{3.36}$$

where

$$\boldsymbol{k}_m \;=\; \int_{V_o} \boldsymbol{B}^T \boldsymbol{C}\, \boldsymbol{B}\, dV_o \tag{3.37}$$

$$\boldsymbol{p} \;=\; \int_{L_o} \boldsymbol{N}_{w_o}^T\, q_z\, dL_o \tag{3.38}$$

are the material stiffness matrix and the consistent node-force vector of the element, respectively.

The integral of $\boldsymbol{k}_m$ can most conveniently be solved by splitting the expression into two parts; one that arises from the bending energy $\boldsymbol{k}_b$, and one from the shear energy $\boldsymbol{k}_s$

$$\boldsymbol{k}_m \;=\; \boldsymbol{k}_b \;+\; \boldsymbol{k}_s \tag{3.39}$$

By applying Eqs.(3.25,3.28-3.30,3.33) these two contributions become

$$\boldsymbol{k}_b \;=\; E \int_{V_o} \boldsymbol{b}_b^T\, \boldsymbol{b}_b\, dV_o \;=\; \frac{EI_y}{2L_o} \int_{-1}^{1} \hat{\boldsymbol{b}}_b^T\, \hat{\boldsymbol{b}}_b\, d\xi \tag{3.40}$$

$$\boldsymbol{k}_s \;=\; G \int_{V_o} \boldsymbol{b}_s^T\, \boldsymbol{b}_s\, dV_o \;=\; G\, A_s\, L_o\, \boldsymbol{b}_s^T\, \boldsymbol{b}_s \tag{3.41}$$

where I_y is the moment of inertia of the cross section with respect to the y-axis, i.e.

$$I_y \;=\; \int_{A_o} z^2 \, dA_o \tag{3.42}$$

and $\hat{\boldsymbol{b}}_b$ is the part of $\boldsymbol{b}_b$ that is contained in the brackets of Eq.(3.29). Note that the effective shear area A_s is used in Eq.(3.41) instead of A_o to compensate for the approximation lying in Eq.(3.1) that leads to a uniform shear strain (stress) distribution over the cross section rather than the correct parabolic form for the linear elastic case. By carrying out the matrix product in Eq.(3.40) and integrating over the length of the beam, the final expression for the contribution from bending energy to the material stiffness matrix takes the form

$$\boldsymbol{k}_b \;=\; \frac{EI_y}{3L_o} \begin{bmatrix} 0 & 0 & 0 & 0 & 0 \\ 0 & 7 & 0 & 1 & -8 \\ 0 & 0 & 0 & 0 & 0 \\ 0 & 1 & 0 & 7 & -8 \\ 0 & -8 & 0 & -8 & 16 \end{bmatrix} \tag{3.43}$$

While the final form of the contribution from shear energy becomes by carrying out the matrix product of Eq.(3.41)

$$\boldsymbol{k}_s \;=\; \frac{GA_s}{L_o} \begin{bmatrix} 1 & -\frac{L_o}{6} & -1 & -\frac{L_o}{6} & -\frac{2L_o}{3} \\ -\frac{L_o}{6} & \frac{L_o^2}{36} & \frac{L_o}{6} & \frac{L_o^2}{36} & \frac{L_o^2}{9} \\ -1 & \frac{L_o}{6} & 1 & \frac{L_o}{6} & \frac{2L_o}{3} \\ -\frac{L_o}{6} & \frac{L_o^2}{36} & \frac{L_o}{6} & \frac{L_o^2}{36} & \frac{L_o^2}{9} \\ -\frac{2L_o}{3} & \frac{L_o^2}{9} & \frac{2L_o}{3} & \frac{L_o^2}{9} & \frac{4L_o^2}{9} \end{bmatrix} \tag{3.44}$$

The integral expression for the consistent node-force vector will be solved for two loading conditions; a uniformly distributed and a triangularly distributed transverse load as depicted in Fig. 3.4, i.e.

$$q_z \;=\; q_{z0} \tag{3.45}$$

$$q_z \;=\; \frac{1}{2}\,(1 \,+\, \xi)\, q_{z1} \tag{3.46}$$

By applying Eqs.(3.15-3.19,3.25), $\boldsymbol{p}$ takes the form for the two loading conditions

$$\boldsymbol{p}_0 \;=\; q_{z0}\,\frac{L_o}{2}\int_{-1}^{1} \boldsymbol{N}_{w_o}^T \, d\xi \;=\; q_{z0}\,\frac{L_o}{2} \begin{bmatrix} 1 & -\frac{L_o}{6} & 1 & \frac{L_o}{6} & 0 \end{bmatrix}^T \tag{3.47}$$

$$\boldsymbol{p}_1 \;=\; q_{z1}\,\frac{L_o}{4}\int_{-1}^{1} \boldsymbol{N}_{w_o}^T \,(1 \,+\, \xi)\, d\xi \;=\; q_{z1}\,\frac{L_o}{12} \begin{bmatrix} 2 & -\frac{13L_o}{30} & 4 & \frac{17L_o}{30} & -\frac{4L_o}{30} \end{bmatrix}^T \tag{3.48}$$

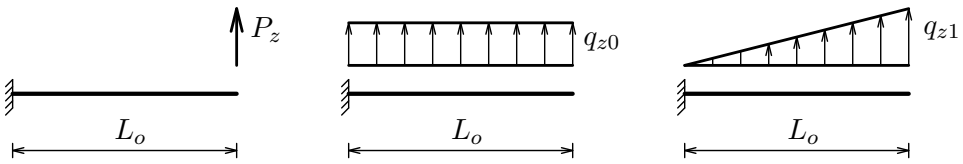

Figure 3.4: Loading Conditions of Cantilevered Beam

Note that for uniformly distributed transverse load, the consistent node-forces coalesce with those of the ordinary Bernoulli-Euler beam element.

When the stiffness equations are solved for the unknown DOFs, the internal bending moment M_y and shear force F_z can be recovered at the element level. Application of the strain expressions Eqs.(3.9-3.11) and the material law Eq.(3.31), and then integration of stresses over the cross section to force resultants, yield

$$M_y \;=\; -\,E\,I_y\,\frac{d^2 w_o}{dx^2} \;=\; -\,E\,I_y\,\frac{d^2 \boldsymbol{N}_{w_o}}{dx^2}\,\boldsymbol{v} \tag{3.49}$$

$$F_z \;=\; G\,A_s\,\gamma_{xz} \;=\; G\,A_s\,\boldsymbol{N}_{\gamma_{xz}}\,\boldsymbol{v} \tag{3.50}$$

where shape function expressions can be found from Eqs.(3.29,3.30).

Examples:
The performance of the element will now be investigated by considering a cantilevered beam, modeled with one single element, under the three different loading conditions in Fig. 3.4; concentrated *tip load*, *uniform load* and *triangular load*. Since the element handles only linear variation of moment and constant shear internally, it can possibly give exact results for the tip load case only. However, it is also of importance to clarify how good approximations can be obtained under higher order load variations.

Enforcing the boundary conditions $v_{z1} = 0$ and $\theta_{y1} = 0$, the constrained stiffness equations become

$$\left(\frac{EI_y}{3L_o} \begin{bmatrix} 0 & 0 & 0 \\ 0 & 7 & -8 \\ 0 & -8 & 16 \end{bmatrix} + \frac{GA_s}{L_o} \begin{bmatrix} 1 & \frac{L_o}{6} & \frac{2L_o}{3} \\ \frac{L_o}{6} & \frac{L_o^2}{36} & \frac{L_o^2}{9} \\ \frac{2L_o}{3} & \frac{L_o^2}{9} & \frac{4L_o^2}{9} \end{bmatrix} \right) \begin{Bmatrix} v_{z2} \\ \theta_{y2} \\ \theta_{y3} \end{Bmatrix} = \begin{Bmatrix} F_{z2} \\ M_{y2} \\ M_{y3} \end{Bmatrix} \tag{3.51}$$

where the load vector on the right hand side in turn will be substituted by

$$\begin{Bmatrix} P_z \\ 0 \\ 0 \end{Bmatrix} \quad ; \quad q_{z0}\,\frac{L_o}{2} \begin{Bmatrix} 1 \\ \frac{L_o}{6} \\ 0 \end{Bmatrix} \quad ; \quad q_{z1}\,\frac{L_o}{12} \begin{Bmatrix} 4 \\ \frac{17L_o}{30} \\ -\frac{4L_o}{30} \end{Bmatrix} \tag{3.52}$$

for tip load, uniform load and triangular load, respectively. Inversion of Eq.(3.51) yields

$$\begin{Bmatrix} v_{z2} \\ \theta_{y2} \\ \theta_{y3} \end{Bmatrix} = \frac{1}{|\boldsymbol{k}|} \begin{bmatrix} a_{11} & a_{12} & a_{13} \\ a_{21} & a_{22} & a_{23} \\ a_{31} & a_{32} & a_{33} \end{bmatrix} \begin{Bmatrix} F_{z2} \\ M_{y2} \\ M_{y3} \end{Bmatrix} \tag{3.53}$$

with the determinant of the constrained stiffness matrix given by

$$|\boldsymbol{k}| = \frac{16}{3} \left(\frac{EI_y}{L_o} \right)^2 \frac{GA_s}{L_o} \tag{3.54}$$

and the adjoints of the entries of $\boldsymbol{k}$

$$\begin{aligned} a_{11} &= \frac{16}{3} \frac{EI_y}{L_o} \left(\frac{EI_y}{L_o} + \frac{1}{3} GA_s L_o \right) \\ a_{12} &= a_{21} = -\frac{8}{3} \frac{EI_y}{L_o} GA_s \\ a_{13} &= a_{31} = -2 \frac{EI_y}{L_o} GA_s \\ a_{22} &= \frac{16}{3} \frac{EI_y}{L_o} \frac{GA_s}{L_o} \\ a_{23} &= a_{32} = \frac{8}{3} \frac{EI_y}{L_o} \frac{GA_s}{L_o} \\ a_{33} &= \frac{7}{3} \frac{EI_y}{L_o} \frac{GA_s}{L_o} \end{aligned} \tag{3.55}$$

Then the internal bending moment and shear force can be recovered from

$$M_y = \frac{EI_y}{L_o} \left([1 + 2\xi] \, \theta_{y2} - 4\xi \, \theta_{y3} \right) \tag{3.56}$$

$$F_z = \frac{GA_s}{L_o} \left(v_{z2} + \frac{L_o}{6} \theta_{y2} + \frac{2L_o}{3} \theta_{y3} \right) \tag{3.57}$$

The one element solutions for the three different loading conditions are summarized in Tab. 3.1, and the corresponding exact results according to Timoshenko beam theory are presented in Tab. 3.2. As can be seen; the nodal displacements $(v_{z2}, \theta_{y2}, \theta_{y3})$ are practically exact for all load cases. The only slight deviation ($\approx 0.5\%$) occurs at the midpoint rotation for triangular load. The internal forces (M_y, F_z) are exact as expected for the tip load case only. However, the linear approximations for bending moments are fairly close to the the exact solutions also for the two other load conditions, while the computed shear forces represent averages of the exact values. These results are best illustrated in Figs. 3.5 and 3.6 that depict the internal force variations for uniform and triangular loads, respectively. Here all values are scaled with respect to the corresponding exact values at the built-in support. Note that increasing number of elements will lead to closer fit to exact solutions for internal forces.

	Tip Load	*Uniform Load*	*Triangular Load*
v_{z2}	$\frac{1}{3}\frac{P_z L_o^3}{EI_y} + \frac{P_z L_o}{GA_s}$	$\frac{1}{8}\frac{q_{z0} L_o^4}{EI_y} + \frac{1}{2}\frac{q_{z0} L_o^2}{GA_s}$	$\frac{11}{120}\frac{q_{z1} L_o^4}{EI_y} + \frac{1}{3}\frac{q_{z1} L_o^2}{GA_s}$
θ_{y2}	$-\frac{1}{2}\frac{P_z L_o^2}{EI_y}$	$-\frac{1}{6}\frac{q_{z0} L_o^3}{EI_y}$	$-\frac{1}{8}\frac{q_{z1} L_o^3}{EI_y}$
θ_{y3}	$-\frac{3}{8}\frac{P_z L_o^2}{EI_y}$	$-\frac{7}{48}\frac{q_{z0} L_o^3}{EI_y}$	$-\frac{17}{160}\frac{q_{z1} L_o^3}{EI_y}$
M_y	$-\frac{1}{2}(1-\xi)P_z L_o$	$-\frac{1}{6}(1-\frac{3}{2}\xi)q_{z0} L_o^2$	$-\frac{1}{8}(1-\frac{7}{5}\xi)q_{z1} L_o^2$
F_z	P_z	$\frac{1}{2}q_{z0} L_o$	$\frac{1}{3}q_{z1} L_o$

Table 3.1: Results with One Element for Cantilevered Beam

	Tip Load	*Uniform Load*	*Triangular Load*
v_{z2}	$\frac{1}{3}\frac{P_z L_o^3}{EI_y} + \frac{P_z L_o}{GA_s}$	$\frac{1}{8}\frac{q_{z0} L_o^4}{EI_y} + \frac{1}{2}\frac{q_{z0} L_o^2}{GA_s}$	$\frac{11}{120}\frac{q_{z1} L_o^4}{EI_y} + \frac{1}{3}\frac{q_{z1} L_o^2}{GA_s}$
θ_{y2}	$-\frac{1}{2}\frac{P_z L_o^2}{EI_y}$	$-\frac{1}{6}\frac{q_{z0} L_o^3}{EI_y}$	$-\frac{1}{8}\frac{q_{z1} L_o^3}{EI_y}$
θ_{y3}	$-\frac{3}{8}\frac{P_z L_o^2}{EI_y}$	$-\frac{7}{48}\frac{q_{z0} L_o^3}{EI_y}$	$-\frac{41}{384}\frac{q_{z1} L_o^3}{EI_y}$
M_y	$-\frac{1}{2}(1-\xi)P_z L_o$	$-\frac{1}{8}(1-\xi)^2 q_{z0} L_o^2$	$-\frac{1}{48}(1-\xi)^2(5+\xi)q_{z1} L_o^2$
F_z	P_z	$\frac{1}{2}(1-\xi)q_{z0} L_o$	$\frac{1}{8}(1-\xi)(3+\xi)q_{z1} L_o$

Table 3.2: Exact Results for Cantilevered Beam

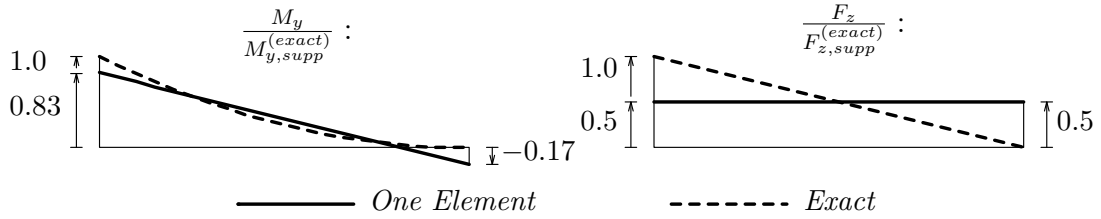

Figure 3.5: Moment and Shear Force Variations for Cantilevered Beam with *Uniform Load*

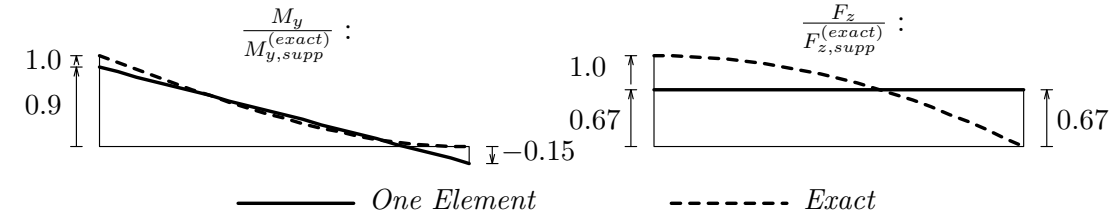

Figure 3.6: Moment and Shear Force Variations for Cantilevered Beam with *Triangular Load*

3.3 Hierarchical Form of the Five DOFs Element

The preceding section dealt with the conventional form of the five DOFs shear-beam element. The key step in going to the hierarchical form of this element is to express the internal DOF at the midpoint, now denoted $\tilde{\theta}_{y3}$, as the *deviation* in bending rotation from the value interpolated from the external DOFs at the endpoints. The external DOFs themselves stay the same. Thus, the hierarchical finite element configuration becomes as shown in Fig. 3.7.

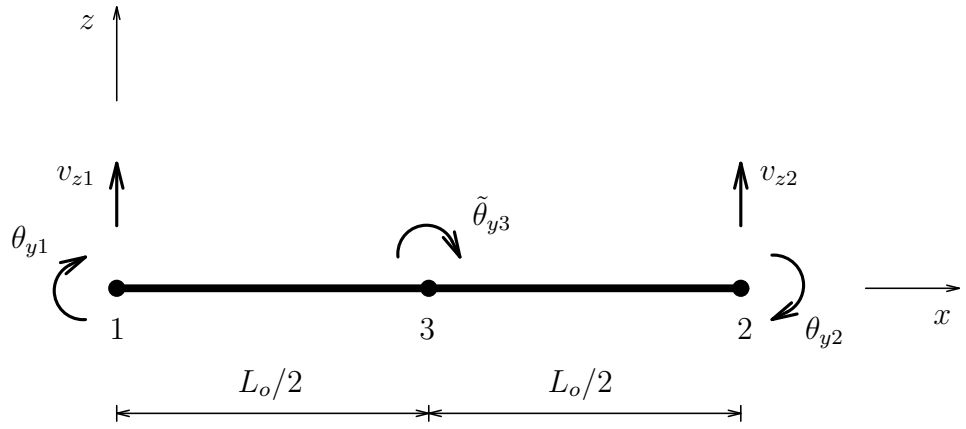

Figure 3.7: Hierarchical Version of the Five DOFs Shear-Beam Element

The reasons for converting to the hierarchical form are twofold: In large displacement analysis internal rotational DOFs should be 'small' quantities, which is better justified by having them on hierarchical form. Secondly; it is now possible to isolate the effect of shear deformation to the internal DOF only so that setting $\tilde{\theta}_{y3} = 0$ as an internal constraint, will lead to recovery of the ordinary Bernoulli-Euler beam element. Thus, the effect of shear on a particular problem can be evaluated by making comparative runs without and with this internal constraint.

The derivation of the hierarchical form may now start by expressing the interpolation of w_o and γ_{xz} in terms of the two different sets of DOFs

$$w_o \;=\; \boldsymbol{N}_{w_o}\,\boldsymbol{v} \;=\; \tilde{\boldsymbol{N}}_{w_o}\,\tilde{\boldsymbol{v}} \tag{3.58}$$

$$\gamma_{xz} \;=\; \boldsymbol{N}_{\gamma_{xz}}\,\boldsymbol{v} \;=\; \tilde{\boldsymbol{N}}_{\gamma_{xz}}\,\tilde{\boldsymbol{v}} \tag{3.59}$$

where the conventional DOFs and shape functions are ordered as in Eqs.(3.12-3.14), and the corresponding hierarchical siblings are

$$\tilde{\boldsymbol{v}}^T \;=\; \left[\begin{array}{ccccc} v_{z1} & \theta_{y1} & v_{z2} & \theta_{y2} & \tilde{\theta}_{y3} \end{array}\right] \tag{3.60}$$

$$\tilde{\boldsymbol{N}}_{w_o} \;=\; \left[\begin{array}{ccccc} \tilde{N}_{w_o}^{(v_1)} & \tilde{N}_{w_o}^{(\theta_1)} & \tilde{N}_{w_o}^{(v_2)} & \tilde{N}_{w_o}^{(\theta_2)} & \tilde{N}_{w_o}^{(\theta_3)} \end{array}\right] \tag{3.61}$$

$$\tilde{\boldsymbol{N}}_{\gamma_{xz}} \;=\; \left[\begin{array}{ccccc} \tilde{N}_{\gamma_{xz}}^{(v_1)} & \tilde{N}_{\gamma_{xz}}^{(\theta_1)} & \tilde{N}_{\gamma_{xz}}^{(v_2)} & \tilde{N}_{\gamma_{xz}}^{(\theta_2)} & \tilde{N}_{\gamma_{xz}}^{(\theta_3)} \end{array}\right] \tag{3.62}$$

Furthermore, the following transformation can be established that relates the conventional DOFs to the hierarchical

$$\boldsymbol{v} \;=\; \tilde{\boldsymbol{T}}\,\tilde{\boldsymbol{v}} \tag{3.63}$$

with the transformation matrix given by

$$\tilde{\boldsymbol{T}} \;=\; \begin{bmatrix} 1 & 0 & 0 & 0 & 0 \\ 0 & 1 & 0 & 0 & 0 \\ 0 & 0 & 1 & 0 & 0 \\ 0 & 0 & 0 & 1 & 0 \\ t_{51} & t_{52} & t_{53} & t_{54} & 1 \end{bmatrix} \tag{3.64}$$

Here the unknown entries t_{51} through t_{54} will be determined from the succeeding shear strain constraints. Insertion of Eq.(3.63) into Eq.(3.59) gives the following relationship between the two sets of shear strain shape functions

$$\tilde{\boldsymbol{N}}_{\gamma_{xz}} \;=\; \boldsymbol{N}_{\gamma_{xz}}\,\tilde{\boldsymbol{T}} \tag{3.65}$$

where the entries of $\boldsymbol{N}_{\gamma_{xz}}$ are given by Eqs.(3.20-3.24). By requiring zero shear strain contribution from each of the four external DOFs of the hierarchical element, the foregoing relationship yields

$$\tilde{N}^{(v_1)}_{\gamma_{xz}} \;=\; N^{(v_1)}_{\gamma_{xz}} \;+\; t_{51}\,N^{(\theta_3)}_{\gamma_{xz}} \;=\; 0 \quad\rightarrow\quad t_{51} \;=\; \frac{3}{2L_o} \tag{3.66}$$

$$\tilde{N}^{(\theta_1)}_{\gamma_{xz}} \;=\; N^{(\theta_1)}_{\gamma_{xz}} \;+\; t_{52}\,N^{(\theta_3)}_{\gamma_{xz}} \;=\; 0 \quad\rightarrow\quad t_{52} \;=\; -\,\frac{1}{4} \tag{3.67}$$

$$\tilde{N}^{(v_2)}_{\gamma_{xz}} \;=\; N^{(v_2)}_{\gamma_{xz}} \;+\; t_{53}\,N^{(\theta_3)}_{\gamma_{xz}} \;=\; 0 \quad\rightarrow\quad t_{53} \;=\; -\,\frac{3}{2L_o} \tag{3.68}$$

$$\tilde{N}^{(\theta_2)}_{\gamma_{xz}} \;=\; N^{(\theta_2)}_{\gamma_{xz}} \;+\; t_{54}\,N^{(\theta_3)}_{\gamma_{xz}} \;=\; 0 \quad\rightarrow\quad t_{54} \;=\; -\,\frac{1}{4} \tag{3.69}$$

and with the fifth equation yielding the only nonzero shear strain shape function of the hierarchical element

$$\tilde{N}^{(\theta_3)}_{\gamma_{xz}} \;=\; N^{(\theta_3)}_{\gamma_{xz}} \;=\; \frac{2}{3} \tag{3.70}$$

Then the transformation matrix is in final form

$$\tilde{\boldsymbol{T}} \;=\; \begin{bmatrix} 1 & 0 & 0 & 0 & 0 \\ 0 & 1 & 0 & 0 & 0 \\ 0 & 0 & 1 & 0 & 0 \\ 0 & 0 & 0 & 1 & 0 \\ \frac{3}{2L_o} & -\frac{1}{4} & -\frac{3}{2L_o} & -\frac{1}{4} & 1 \end{bmatrix} \tag{3.71}$$

Now the shape functions of the hierarchical element pertaining to transverse displacement can be found. By inserting Eq.(3.63) into Eq.(3.58), the relationship between the two sets of displacement shape functions becomes

$$\tilde{\boldsymbol{N}}_{w_o} \;=\; \boldsymbol{N}_{w_o}\,\tilde{\boldsymbol{T}} \tag{3.72}$$

where the entries of $\boldsymbol{N}_{w_o}$ are given by Eqs.(3.15-3.19). Carrying out the matrix product yields

$$\tilde{N}_{w_o}^{(v_1)} \;=\; N_{w_o}^{(v_1)} + \frac{3}{2L_o}\,N_{w_o}^{(\theta_3)} \;=\; \frac{1}{4}\,(2+\xi)\,(1-\xi)^2 \tag{3.73}$$

$$\tilde{N}_{w_o}^{(\theta_1)} \;=\; N_{w_o}^{(\theta_1)} - \frac{1}{4}\,N_{w_o}^{(\theta_3)} \;=\; -\frac{L_o}{8}\,(1+\xi)\,(1-\xi)^2 \tag{3.74}$$

$$\tilde{N}_{w_o}^{(v_2)} \;=\; N_{w_o}^{(v_2)} - \frac{3}{2L_o}\,N_{w_o}^{(\theta_3)} \;=\; \frac{1}{4}\,(2-\xi)\,(1+\xi)^2 \tag{3.75}$$

$$\tilde{N}_{w_o}^{(\theta_2)} \;=\; N_{w_o}^{(\theta_2)} - \frac{1}{4}\,N_{w_o}^{(\theta_3)} \;=\; \frac{L_o}{8}\,(1-\xi)\,(1+\xi)^2 \tag{3.76}$$

$$\tilde{N}_{w_o}^{(\theta_3)} \;=\; N_{w_o}^{(\theta_3)} \;=\; -\frac{L_o}{6}\,\xi\,(1-\xi)\,(1+\xi) \tag{3.77}$$

As indeed was the expected result; the displacement shape functions pertaining to the four external DOFs of the hierarchical element have now become the *Hermitian* cubic shape functions of the ordinary Bernoulli-Euler beam element. The shape function pertaining to the hierarchical internal DOF stays the same as for the conventional shear-beam element. Fig. 3.8 shows a summary of the hierarchical shape functions.

The remaining steps to form the material stiffness matrix $\tilde{\boldsymbol{k}}_m$ and the consistent node-force vector $\tilde{\boldsymbol{p}}$ of the hierarchical element may now follow two optional lines: Since the final expressions for the conventional element already exist, the hierarchical counterparts may be found from the transformations

$$\tilde{\boldsymbol{k}}_m \;=\; \tilde{\boldsymbol{T}}^T\,\boldsymbol{k}_m\,\tilde{\boldsymbol{T}} \tag{3.78}$$

$$\tilde{\boldsymbol{p}} \;=\; \tilde{\boldsymbol{T}}^T\,\boldsymbol{p} \tag{3.79}$$

The alternative way is to form $\tilde{\boldsymbol{k}}_m$ and $\tilde{\boldsymbol{p}}$ directly based on the hierarchical shape functions by proceeding as outlined in the previous section for the conventional element. The latter will be the main option here in order to be consistent with the presentation given in Chapter 4 when going to the nonlinear 3D formulation (where only the hierarchical version will be treated). Thus, the strain-displacement relationship now becomes

$$\boldsymbol{\epsilon} \;=\; \tilde{\boldsymbol{B}}\,\tilde{\boldsymbol{v}} \tag{3.80}$$

where $\boldsymbol{\epsilon}$ is from Eq.(3.27) and with the new strain-displacement matrix given by

$$\tilde{\boldsymbol{B}} = \begin{bmatrix} -z\frac{d^2\tilde{\boldsymbol{N}}_{w_o}}{dx^2} \\ \tilde{\boldsymbol{N}}_{\gamma_{xz}} \end{bmatrix} = \begin{bmatrix} -\frac{6}{L_o^2}z\xi & \frac{1}{L_o}z(3\xi-1) & \frac{6}{L_o^2}z\xi & \frac{1}{L_o}z(3\xi+1) & -\frac{4}{L_o}z\xi \\ 0 & 0 & 0 & 0 & \frac{2}{3} \end{bmatrix} \tag{3.81}$$

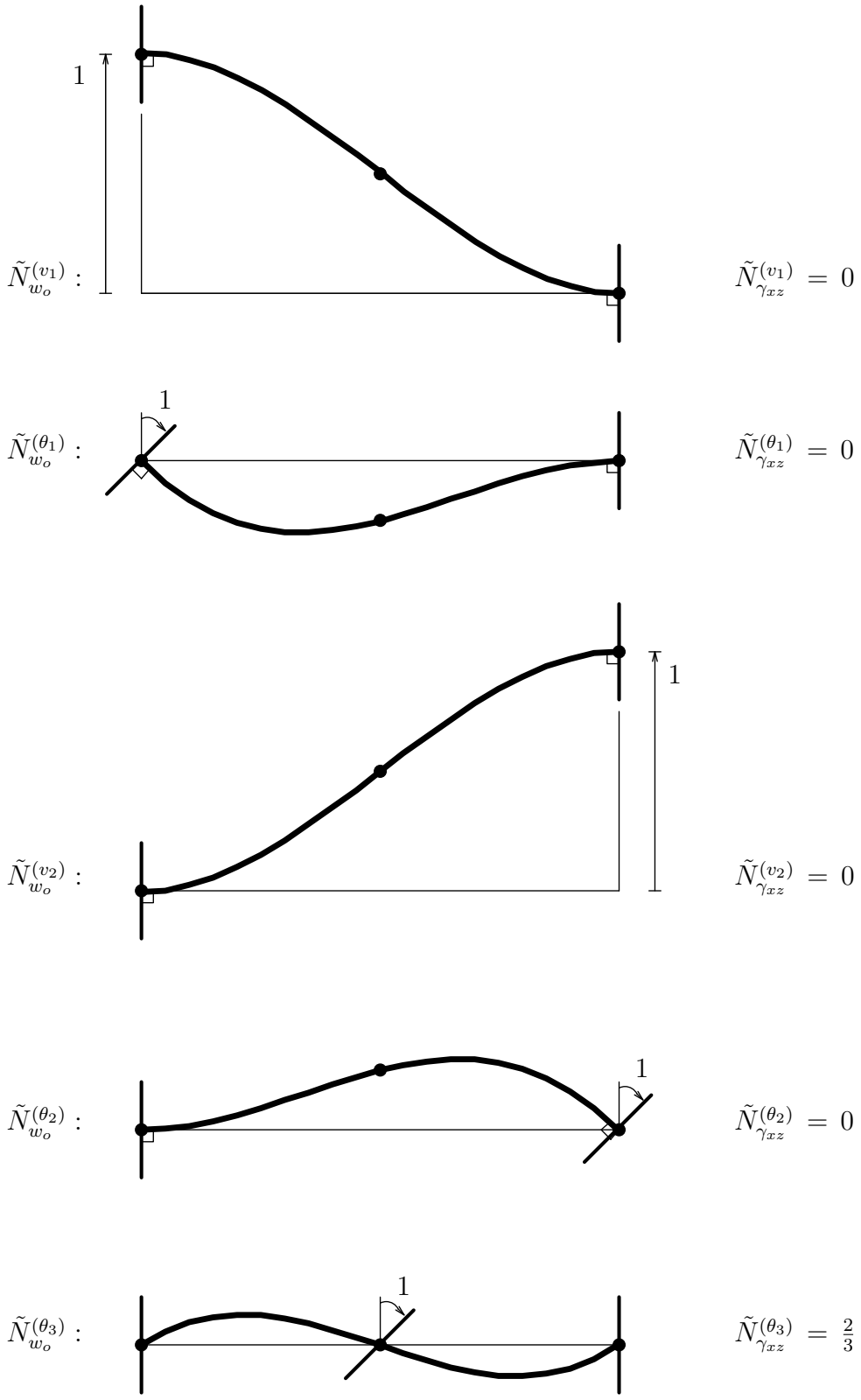

Figure 3.8: Shape Functions of the Hierarchical 2D Shear-Beam Element

Application of the principle of virtual displacements as stated in Eq.(3.34), inserting Eqs.(3.31,3.58(last part),3.80), yields the stiffness equations of the hierarchical element

$$\tilde{\boldsymbol{k}}_m \, \tilde{\boldsymbol{v}} \; = \; \tilde{\boldsymbol{p}} \tag{3.82}$$

where

$$\tilde{\boldsymbol{k}}_m \; = \; \int_{V_o} \tilde{\boldsymbol{B}}^T \boldsymbol{C} \, \tilde{\boldsymbol{B}} \, dV_o \tag{3.83}$$

$$\tilde{\boldsymbol{p}} \; = \; \int_{L_o} \tilde{\boldsymbol{N}}_{w_o}^T \, q_z \, dL_o \tag{3.84}$$

Because of the favorable hierarchical form, the shear energy will contribute to one entry of the material stiffness matrix only. Hence, the final expressions for $\tilde{\boldsymbol{k}}_m$ may now conveniently be given as a single matrix (rather than making a split as in Eq.(3.39) for the conventional element). By introducing Eqs.(3.25,3.33,3.81), Eq.(3.83) converts to

$$\tilde{\boldsymbol{k}}_m \; = \; \frac{E I_y L_o}{2} \int_{-1}^{1} \left(\frac{d^2 \tilde{\boldsymbol{N}}_{w_o}}{dx^2} \right)^T \left(\frac{d^2 \tilde{\boldsymbol{N}}_{w_o}}{dx^2} \right) d\xi \; + \; G \, A_s \, L_o \, \tilde{\boldsymbol{N}}_{\gamma_{xz}}^T \, \tilde{\boldsymbol{N}}_{\gamma_{xz}} \tag{3.85}$$

Then by carrying out the matrix products and integrating the first part over the length of the beam, the material stiffness matrix of the hierarchical element finally becomes

$$\tilde{\boldsymbol{k}}_m \; = \; \frac{E I_y}{L_o} \begin{bmatrix} \frac{12}{L_o^2} & -\frac{6}{L_o} & -\frac{12}{L_o^2} & -\frac{6}{L_o} & \frac{8}{L_o} \\ -\frac{6}{L_o} & 4 & \frac{6}{L_o} & 2 & -4 \\ -\frac{12}{L_o^2} & \frac{6}{L_o} & \frac{12}{L_o^2} & \frac{6}{L_o} & -\frac{8}{L_o} \\ -\frac{6}{L_o} & 2 & \frac{6}{L_o} & 4 & -4 \\ \frac{8}{L_o} & -4 & -\frac{8}{L_o} & -4 & \frac{16}{3}+\alpha \end{bmatrix} \tag{3.86}$$

where

$$\alpha \; = \; \frac{4}{9} \frac{G A_s L_o^2}{E I_y} \tag{3.87}$$

As also previously indicated; the submatrix of $\tilde{\boldsymbol{k}}_m$ pertaining to the four external DOFs (i.e. first four rows and columns) can be recognized as the stiffness matrix of the ordinary Bernoulli-Euler beam element.

The consistent node-force vector of the hierarchical element will then be developed for the same loading conditions as the conventional element, i.e. for the uniformly and triangularly distributed transverse loads given by Eqs.(3.45,3.46), respectively. By applying Eqs.(3.25,3.73-3.77), Eq.(3.84) takes the form for the two loading conditions

$$\tilde{\boldsymbol{p}}_0 \; = \; q_{z0} \frac{L_o}{2} \int_{-1}^{1} \tilde{\boldsymbol{N}}_{w_o}^T \, d\xi \; = \; q_{z0} \frac{L_o}{2} \begin{bmatrix} 1 & -\frac{L_o}{6} & 1 & \frac{L_o}{6} & 0 \end{bmatrix}^T \tag{3.88}$$

$$\tilde{\boldsymbol{p}}_1 = q_{z1} \frac{L_o}{4} \int_{-1}^{1} \tilde{\boldsymbol{N}}_{w_o}^T (1+\xi) d\xi = q_{z1} \frac{L_o}{20} \begin{bmatrix} 3 & -\frac{2L_o}{3} & 7 & L_o & -\frac{2L_o}{9} \end{bmatrix}^T \tag{3.89}$$

Similarly to the stiffness matrix; here the subvectors pertaining to the four external DOFs are the same as the consistent node-force vectors of the Bernoulli-Euler element. Furthermore, $\tilde{\boldsymbol{p}}_0$ and $\boldsymbol{p}_0$ become identical.

Finally, the expressions for the internal bending moment M_y and shear force F_z will be given. Correspondingly to Eqs.(3.49,3.50), these now become

$$M_y \;=\; -\,E\,I_y\,\frac{d^2 w_o}{dx^2} \;=\; -\,E\,I_y\,\frac{d^2 \tilde{\boldsymbol{N}}_{w_o}}{dx^2}\,\tilde{\boldsymbol{v}} \tag{3.90}$$

$$F_z \;=\; G\,A_s\,\gamma_{xz} \;=\; G\,A_s\,\tilde{\boldsymbol{N}}_{\gamma_{xz}}\,\tilde{\boldsymbol{v}} \;=\; \frac{2}{3}\,G\,A_s\,\tilde{\theta}_{y3} \tag{3.91}$$

where the shape function derivatives may be taken from Eq.(3.81).

Examples:
The cantilever beam examples from the preceding section will now be revisited in order to demonstrate that the hierarchical and conventional versions of the five DOFs shear-beam element indeed yield identical results. Enforcing the boundary conditions $v_{z1} = 0$ and $\theta_{y1} = 0$, the constrained stiffness equations of the hierarchical element become

$$\frac{EI_y}{L_o}\begin{bmatrix} \frac{12}{L_o^2} & \frac{6}{L_o} & -\frac{8}{L_o} \\ \frac{6}{L_o} & 4 & -4 \\ -\frac{8}{L_o} & -4 & \frac{16}{3}+\alpha \end{bmatrix}\begin{Bmatrix} v_{z2} \\ \theta_{y2} \\ \tilde{\theta}_{y3} \end{Bmatrix} = \begin{Bmatrix} F_{z2} \\ M_{y2} \\ \tilde{M}_{y3} \end{Bmatrix} \tag{3.92}$$

where α is from Eq.(3.87), and the load vector on the right hand side in turn will be substituted by

$$\begin{Bmatrix} P_z \\ 0 \\ 0 \end{Bmatrix} \quad ; \quad q_{z0}\,\frac{L_o}{2}\begin{Bmatrix} 1 \\ \frac{L_o}{6} \\ 0 \end{Bmatrix} \quad ; \quad q_{z1}\,\frac{L_o}{20}\begin{Bmatrix} 7 \\ L_o \\ -\frac{2L_o}{9} \end{Bmatrix} \tag{3.93}$$

for tip load, uniform load and triangular load, respectively. Inversion of Eq.(3.92) yields

$$\begin{Bmatrix} v_{z2} \\ \theta_{y2} \\ \tilde{\theta}_{y3} \end{Bmatrix} = \frac{1}{|\tilde{\boldsymbol{k}}|}\begin{bmatrix} \tilde{a}_{11} & \tilde{a}_{12} & \tilde{a}_{13} \\ \tilde{a}_{21} & \tilde{a}_{22} & \tilde{a}_{23} \\ \tilde{a}_{31} & \tilde{a}_{32} & \tilde{a}_{33} \end{bmatrix}\begin{Bmatrix} F_{z2} \\ M_{y2} \\ \tilde{M}_{y3} \end{Bmatrix} \tag{3.94}$$

with the determinant of the constrained stiffness matrix given by

$$|\tilde{\boldsymbol{k}}| \;=\; \frac{16}{3}\left(\frac{EI_y}{L_o}\right)^2\frac{GA_s}{L_o} \tag{3.95}$$

and the adjoints of the entries of $\tilde{\boldsymbol{k}}$

$$\begin{aligned}
\tilde{a}_{11} &= \frac{16}{3}\frac{EI_y}{L_o}\left(\frac{EI_y}{L_o} + \frac{1}{3}GA_sL_o\right)\\
\tilde{a}_{12} &= \tilde{a}_{21} = -\frac{8}{3}\frac{EI_y}{L_o}GA_s\\
\tilde{a}_{13} &= \tilde{a}_{31} = 8\frac{(EI_y)^2}{L_o^3}\\
\tilde{a}_{22} &= \frac{16}{3}\frac{EI_y}{L_o}\frac{GA_s}{L_o}\\
\tilde{a}_{23} &= \tilde{a}_{32} = 0\\
\tilde{a}_{33} &= 12\frac{(EI_y)^2}{L_o^4}
\end{aligned} \tag{3.96}$$

Compared with the corresponding expressions in Eqs.(3.54,3.55) for the conventional element, only terms pertaining to the internal DOF have changed. Furthermore, the internal bending moment can be recovered from

$$M_y = \frac{EI_y}{L_o}\left(\frac{6}{L_o}\xi\, v_{z2} + [3\xi + 1]\,\theta_{y2} - 4\xi\,\tilde{\theta}_{y3}\right) \tag{3.97}$$

while the shear force expression is given by the last part of Eq.(3.91). Finally, for the sake of making a complete comparison with the conventional element solutions, the total bending rotation at the midpoint of the hierarchical element can be recovered from the last transformation in Eq.(3.63). Thus

$$\theta_{y3} = -\frac{3}{2L_o}v_{z2} - \frac{1}{4}\theta_{y2} + \tilde{\theta}_{y3} \tag{3.98}$$

	Tip Load	*Uniform Load*	*Triangular Load*
v_{z2}	$\frac{1}{3}\frac{P_zL_o^3}{EI_y} + \frac{P_zL_o}{GA_s}$	$\frac{1}{8}\frac{q_{z0}L_o^4}{EI_y} + \frac{1}{2}\frac{q_{z0}L_o^2}{GA_s}$	$\frac{11}{120}\frac{q_{z1}L_o^4}{EI_y} + \frac{1}{3}\frac{q_{z1}L_o^2}{GA_s}$
θ_{y2}	$-\frac{1}{2}\frac{P_zL_o^2}{EI_y}$	$-\frac{1}{6}\frac{q_{z0}L_o^3}{EI_y}$	$-\frac{1}{8}\frac{q_{z1}L_o^3}{EI_y}$
$\tilde{\theta}_{y3}$	$\frac{3}{2}\frac{P_z}{GA_s}$	$\frac{3}{4}\frac{q_{z0}L_o}{GA_s}$	$\frac{1}{2}\frac{q_{z1}L_o}{GA_s}$
θ_{y3}	$-\frac{3}{8}\frac{P_zL_o^2}{EI_y}$	$-\frac{7}{48}\frac{q_{z0}L_o^3}{EI_y}$	$-\frac{17}{160}\frac{q_{z1}L_o^3}{EI_y}$
M_y	$-\frac{1}{2}(1-\xi)P_zL_o$	$-\frac{1}{6}(1-\frac{3}{2}\xi)q_{z0}L_o^2$	$-\frac{1}{8}(1-\frac{7}{5}\xi)q_{z1}L_o^2$
F_z	P_z	$\frac{1}{2}q_{z0}L_o$	$\frac{1}{3}q_{z1}L_o$

Table 3.3: Results with One Hierarchical Element for Cantilevered Beam

The results with one hierarchical element for the cantilevered beam are summarized in Tab. 3.3. A comparison with the one conventional element solutions as presented in Tab. 3.1, confirms that the results are identical in every respect.

Chapter 4

3D Nonlinear Shear-Beam Element

4.1 Beam Kinematics

Consider a 3D beam element in a local right handed Cartesian coordinate system (x, y, z) with x-axis as the longitudinal reference axis. The deformational behavior at the element level can be based on rotations of small or moderate size, since the large displacement analysis will adopt the Corotated Lagrangian (CL-) formulation (Section 5.1). In the axial-bending-shear modes, the beam is assumed to comply with the Timoshenko theory (i.e. plane sections initially normal to the longitudinal axis remain plane, but not necessarily normal to the deformed axis). In the torsion mode, warping will be neglected (i.e. zero longitudinal displacement), and thus, sections normal to the longitudinal axis rotate like rigid disks in their own plane. In addition, the section is allowed to expand (or contract) laterally by introducing transverse displacement components relative to the values at the reference axis (*relative transverse displacements*). The main motivation for including these additional modes is to account for (in a simplified manner) the internal redistribution of strains (stresses) that takes place in a reinforced concrete section subjected to shear and torsion, when the tensile strength of concrete is exceeded and the stirrups get into action. Thus, denoting the three components of displacement and cross sectional rotation by (u, v, w) and $(\theta_x, \theta_y, \theta_z)$, respectively, the deformational behavior of the beam can be expressed by

$$u(x,y,z) \approx u_o(x) - y\,\theta_z(x) + z\,\theta_y(x) \tag{4.1}$$

$$v(x,y,z) \approx v_o(x) - z\,\theta_x(x) + v_r(x,y,z) \tag{4.2}$$

$$w(x,y,z) \approx w_o(x) + y\,\theta_x(x) + w_r(x,y,z) \tag{4.3}$$

where subscript 'o' on displacement components refers to values at the reference axis. For the relative transverse displacement components v_r and w_r, the more specific expressions are assumed

$$v_r(x,y,z) \approx y\,a_0(x) + y\,z\,a_1(x) \tag{4.4}$$

$$w_r(x,y,z) \approx z\,b_0(x) + y\,z\,b_1(x) \tag{4.5}$$

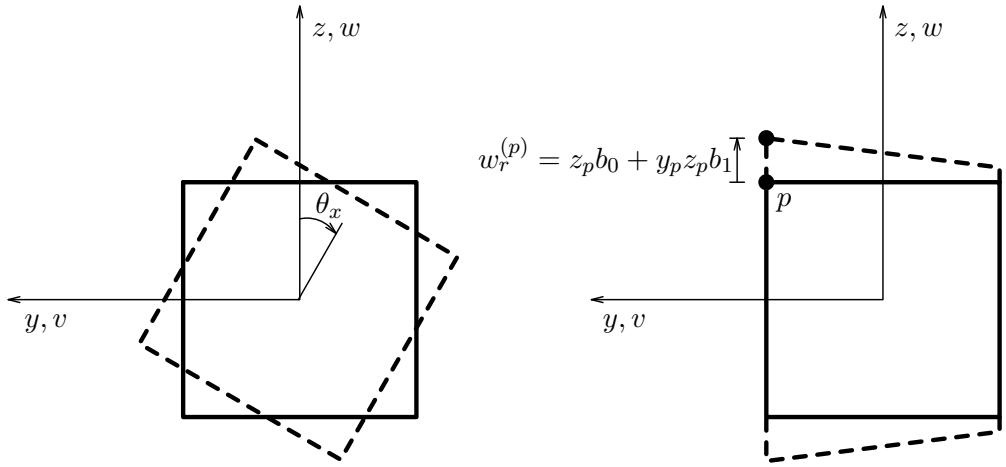

Figure 4.1: Torsion and Relative w-Displacement Modes of a Beam Section

Here the first term of each expression is expected to reflect the postcracking behavior in pure shear or torsion with reasonable accuracy, while the second term is also considered necessary when dealing with combined action of these two modes. Due to the simplified form of these relative displacements, the longitudinal reference axis should be placed at the centroid of the beam cross section.

The deformation modes of torsion and relative w-displacement are shown for a section in Fig. 4.1, while the axial-bending-shear modes in the (x,z)-plane are depicted in Fig. 3.1, Section 3.2.

4.2 Finite Element Configuration

Using the CL-formulation for the large displacement analysis, an acceptable simplification at the element level is to retain only the linear terms of the Green strain components when forming the internal node-force vector and the incremental material stiffness matrix [3]. Thus, neglecting the quadratic terms in Eq.(2.6) and also applying Eq.(2.10) for the shear strains, the linear or infinitesimal strain expressions for the assumed deformational behavior of the beam become

$$\epsilon_x = \frac{\partial u}{\partial x} = \frac{du_o}{dx} - y\frac{d\theta_z}{dx} + z\frac{d\theta_y}{dx} \tag{4.6}$$

$$\gamma_{xy} = \frac{\partial u}{\partial y} + \frac{\partial v}{\partial x} = -\theta_z + \frac{dv_o}{dx} - z\frac{d\theta_x}{dx} + y\frac{da_0}{dx} + y\,z\frac{da_1}{dx} \tag{4.7}$$

$$\gamma_{xz} = \frac{\partial u}{\partial z} + \frac{\partial w}{\partial x} = \theta_y + \frac{dw_o}{dx} + y\frac{d\theta_x}{dx} + z\frac{db_0}{dx} + y\,z\frac{db_1}{dx} \tag{4.8}$$

$$\epsilon_y = \frac{\partial v}{\partial y} = a_0 + z\,a_1 \tag{4.9}$$

$$\epsilon_z = \frac{\partial w}{\partial z} = b_0 + y\,b_1 \tag{4.10}$$

$$\gamma_{yz} \;=\; \frac{\partial v}{\partial z} \,+\, \frac{\partial w}{\partial y} \;=\; y\,a_1 \,+\, z\,b_1 \tag{4.11}$$

Thus, from Eqs.(4.7,4.8) it follows that the bending rotations (θ_z, θ_y) are connected to the corresponding slopes of transverse displacements (v_o, w_o) and shear strains coming from transverse shear $(\gamma_{xy}^{(s)}, \gamma_{xz}^{(s)})$, through

$$\theta_z \;=\; \frac{dv_o}{dx} \,-\, \gamma_{xy}^{(s)} \tag{4.12}$$

$$\theta_y \;=\; -\,\frac{dw_o}{dx} \,+\, \gamma_{xz}^{(s)} \tag{4.13}$$

In a manner similar to the 2D case, (v_o, w_o) and $(\gamma_{xy}^{(s)}, \gamma_{xz}^{(s)})$ will be subjected to trial expansions, respectively in terms of cubic polynomials and constants. The hierarchical approach from Section 3.3 will be the adopted form. Given that $(\gamma_{xy}^{(s)}, \gamma_{xz}^{(s)})$ now are constants, the normal x-strain then reduces to the well known form

$$\epsilon_x \;=\; \frac{du_o}{dx} \,-\, y\,\frac{d^2v_o}{dx^2} \,-\, z\,\frac{d^2w_o}{dx^2} \tag{4.14}$$

To avoid *artificial self straining* in the solution, the ϵ_x-contributions from the three displacement components should possess the same order of variation in the longitudinal direction. Consequently, the axial displacement u_o must have a quadratic expansion. Then three DOFs are necessary, and again, the hierarchical approach will be adopted. Of the same reason; shear strains coming from different modes should also possess the same order of variation. Then the twisting rotation θ_x must have a linear expansion in order to produce a shear strain state that are constant in the longitudinal direction, and thus, two DOFs become sufficient. Furthermore, since the relative transverse displacements are included basically to account for the postcracking behavior of reinforced concrete in shear and torsion, the x-dependency in Eqs.(4.4,4.5) will be neglected. Then a consistency with the corresponding shear strain variations (i.e. the main 'sources') is achieved. However, this is again a simplification, since the cracking limit itself is influenced by the bending and axial modes, as well. The remaining revised strain expressions then become

$$\gamma_{xy} \;=\; \gamma_{xy}^{(s)} \,-\, z\,\frac{d\theta_x}{dx} \tag{4.15}$$

$$\gamma_{xz} \;=\; \gamma_{xz}^{(s)} \,+\, y\,\frac{d\theta_x}{dx} \tag{4.16}$$

$$\epsilon_y \;=\; \tilde{\epsilon}_{yo} \,+\, z\,\tilde{g}_{ey} \tag{4.17}$$

$$\epsilon_z \;=\; \tilde{\epsilon}_{zo} \,+\, y\,\tilde{g}_{ez} \tag{4.18}$$

$$\gamma_{yz} \;=\; y\,\tilde{g}_{ey} \,+\, z\,\tilde{g}_{ez} \tag{4.19}$$

Now the coefficients (a_0, b_0) have been substituted by $(\tilde{\epsilon}_{yo}, \tilde{\epsilon}_{zo})$, which are the normal strains in the (y, z)-directions at the reference axis, while (a_1, b_1) have been substituted by the strain gradients $(\tilde{g}_{ey}, \tilde{g}_{ez})$. These strains and strain gradients will be

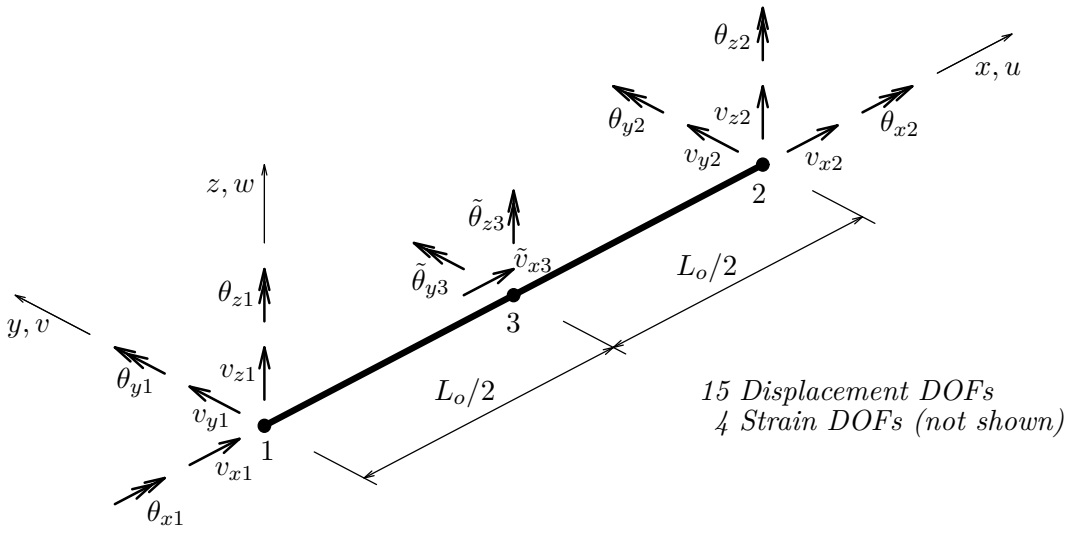

Figure 4.2: 3D Hierarchical Shear-Beam Element with 19 DOFs

referred to as the *strain DOFs* of the element. The accent '˜' is used to signify that the strain DOFs work like hierarchical DOFs, since the *basic* element contains no such values (i.e. deviations from zero).

Based on the preceding considerations, a 3D nonlinear shear-beam element with 19 DOFs has been constructed. The configuration of displacement DOFs is depicted in Fig. 4.2, and the interpolations are given by

$$u_o = \boldsymbol{N}_{u_o}\,\boldsymbol{v}_{u_o} \quad ; \text{where} \quad \boldsymbol{v}_{u_o}^T = \begin{bmatrix} v_{x1} & v_{x2} & \tilde{v}_{x3} \end{bmatrix} \tag{4.20}$$
$$\boldsymbol{N}_{u_o} = \begin{bmatrix} N_{u_o}^{(v_1)} & N_{u_o}^{(v_2)} & N_{u_o}^{(\tilde{v}_3)} \end{bmatrix}$$

$$v_o = \boldsymbol{N}_{v_o}\,\boldsymbol{v}_{v_o} \quad ; \text{where} \quad \boldsymbol{v}_{v_o}^T = \begin{bmatrix} v_{y1} & \theta_{z1} & v_{y2} & \theta_{z2} & \tilde{\theta}_{z3} \end{bmatrix} \tag{4.21}$$
$$\boldsymbol{N}_{v_o} = \begin{bmatrix} N_{v_o}^{(v_1)} & N_{v_o}^{(\theta_1)} & N_{v_o}^{(v_2)} & N_{v_o}^{(\theta_2)} & N_{v_o}^{(\tilde{\theta}_3)} \end{bmatrix}$$

$$\gamma_{xy}^{(s)} = \boldsymbol{N}_{\gamma_{xy}}\,\boldsymbol{v}_{v_o} \quad ; \text{where} \quad \boldsymbol{N}_{\gamma_{xy}} = \begin{bmatrix} 0 & 0 & 0 & 0 & N_{\gamma_{xy}}^{(\tilde{\theta}_3)} \end{bmatrix} \tag{4.22}$$

$$w_o = \boldsymbol{N}_{w_o}\,\boldsymbol{v}_{w_o} \quad ; \text{where} \quad \boldsymbol{v}_{w_o}^T = \begin{bmatrix} v_{z1} & \theta_{y1} & v_{z2} & \theta_{y2} & \tilde{\theta}_{y3} \end{bmatrix} \tag{4.23}$$
$$\boldsymbol{N}_{w_o} = \begin{bmatrix} N_{w_o}^{(v_1)} & N_{w_o}^{(\theta_1)} & N_{w_o}^{(v_2)} & N_{w_o}^{(\theta_2)} & N_{w_o}^{(\tilde{\theta}_3)} \end{bmatrix}$$

$$\gamma_{xz}^{(s)} = \boldsymbol{N}_{\gamma_{xz}}\,\boldsymbol{v}_{w_o} \quad ; \text{where} \quad \boldsymbol{N}_{\gamma_{xz}} = \begin{bmatrix} 0 & 0 & 0 & 0 & N_{\gamma_{xz}}^{(\tilde{\theta}_3)} \end{bmatrix} \tag{4.24}$$

$$\theta_x = \boldsymbol{N}_{\theta_x}\,\boldsymbol{v}_{\theta_x} \quad ; \text{where} \quad \boldsymbol{v}_{\theta_x}^T = \begin{bmatrix} \theta_{x1} & \theta_{x2} \end{bmatrix} \tag{4.25}$$
$$\boldsymbol{N}_{\theta_x} = \begin{bmatrix} N_{\theta_x}^{(\theta_1)} & N_{\theta_x}^{(\theta_2)} \end{bmatrix}$$

$$v_r \;=\; \boldsymbol{N}_{v_r}\,\boldsymbol{v}_{v_r} \quad ;\text{ where } \quad \boldsymbol{v}_{v_r}^T \;=\; \left[\begin{array}{cc} \tilde{\epsilon}_{yo} & \tilde{g}_{ey} \end{array}\right] \tag{4.26}$$

$$\boldsymbol{N}_{v_r} \;=\; \left[\begin{array}{cc} N_{v_r}^{(\tilde{\epsilon})} & N_{v_r}^{(\tilde{g})} \end{array}\right]$$

$$w_r \;=\; \boldsymbol{N}_{w_r}\,\boldsymbol{v}_{w_r} \quad ;\text{ where } \quad \boldsymbol{v}_{w_r}^T \;=\; \left[\begin{array}{cc} \tilde{\epsilon}_{zo} & \tilde{g}_{ez} \end{array}\right] \tag{4.27}$$

$$\boldsymbol{N}_{w_r} \;=\; \left[\begin{array}{cc} N_{w_r}^{(\tilde{\epsilon})} & N_{w_r}^{(\tilde{g})} \end{array}\right]$$

The shape functions pertaining to the bending-shear modes in the (x,z)-plane are already given by Eqs.(3.70,3.73-3.77). However, they will be repeated here along with the others in order to make the presentation complete. Thus

$$N_{u_o}^{(v_1)} \;=\; N_{\theta_x}^{(\theta_1)} \;=\; \frac{1}{2}\,(1\,-\,\xi) \tag{4.28}$$

$$N_{u_o}^{(v_2)} \;=\; N_{\theta_x}^{(\theta_2)} \;=\; \frac{1}{2}\,(1\,+\,\xi) \tag{4.29}$$

$$N_{u_o}^{(\tilde{v}_3)} \;=\; (1\,-\,\xi)\,(1\,+\,\xi) \tag{4.30}$$

$$N_{v_o}^{(v_1)} \;=\; N_{w_o}^{(v_1)} \;=\; \frac{1}{4}\,(2\,+\,\xi)\,(1\,-\,\xi)^2 \tag{4.31}$$

$$N_{v_o}^{(\theta_1)} \;=\; -\,N_{w_o}^{(\theta_1)} \;=\; \frac{L_o}{8}\,(1\,+\,\xi)\,(1\,-\,\xi)^2 \tag{4.32}$$

$$N_{v_o}^{(v_2)} \;=\; N_{w_o}^{(v_2)} \;=\; \frac{1}{4}\,(2\,-\,\xi)\,(1\,+\,\xi)^2 \tag{4.33}$$

$$N_{v_o}^{(\theta_2)} \;=\; -\,N_{w_o}^{(\theta_2)} \;=\; -\,\frac{L_o}{8}\,(1\,-\,\xi)\,(1\,+\,\xi)^2 \tag{4.34}$$

$$N_{v_o}^{(\tilde{\theta}_3)} \;=\; -\,N_{w_o}^{(\tilde{\theta}_3)} \;=\; \frac{L_o}{6}\,\xi\,(1\,-\,\xi)\,(1\,+\,\xi) \tag{4.35}$$

$$N_{\gamma_{xy}}^{(\tilde{\theta}_3)} \;=\; -\,N_{\gamma_{xz}}^{(\tilde{\theta}_3)} \;=\; -\,\frac{2}{3} \tag{4.36}$$

$$N_{v_r}^{(\tilde{\epsilon})} \;=\; y \tag{4.37}$$

$$N_{v_r}^{(\tilde{g})} \;=\; N_{w_r}^{(\tilde{g})} \;=\; y\,z \tag{4.38}$$

$$N_{w_r}^{(\tilde{\epsilon})} \;=\; z \tag{4.39}$$

where again the natural beam coordinate is given by

$$\xi \;=\; \frac{2x}{L_o}\;-\;1 \tag{4.40}$$

Finally, the complete displacement field $\boldsymbol{u}$ of the element can be expressed in terms of the preceding interpolation of components. Insertion into Eqs.(4.1-4.5,4.12,4.13) yields

$$\boldsymbol{u} \;=\; \boldsymbol{N}\,\boldsymbol{v} \tag{4.41}$$

where

$$\boldsymbol{u}^T \;=\; \left[\begin{array}{ccc} u & v & w \end{array}\right] \tag{4.42}$$

$$\boldsymbol{v}^T \;=\; \left[\begin{array}{cccccc} \boldsymbol{v}_{u_o}^T & \boldsymbol{v}_{v_o}^T & \boldsymbol{v}_{w_o}^T & \boldsymbol{v}_{\theta_x}^T & \boldsymbol{v}_{v_r}^T & \boldsymbol{v}_{w_r}^T \end{array}\right] \tag{4.43}$$

$$\boldsymbol{N} \;=\; \left[\begin{array}{cccccc} \boldsymbol{N}_{u_o} & -y\boldsymbol{N}_{\theta_z} & z\boldsymbol{N}_{\theta_y} & \boldsymbol{0} & \boldsymbol{0} & \boldsymbol{0} \\ \boldsymbol{0} & \boldsymbol{N}_{v_o} & \boldsymbol{0} & -z\boldsymbol{N}_{\theta_x} & \boldsymbol{N}_{v_r} & \boldsymbol{0} \\ \boldsymbol{0} & \boldsymbol{0} & \boldsymbol{N}_{w_o} & y\boldsymbol{N}_{\theta_x} & \boldsymbol{0} & \boldsymbol{N}_{w_r} \end{array}\right] \tag{4.44}$$

Here for brevity the shape function vectors $(\boldsymbol{N}_{\theta_z}, \boldsymbol{N}_{\theta_y})$ pertaining to bending rotations are introduced, i.e.

$$\theta_z \;=\; \boldsymbol{N}_{\theta_z}\,\boldsymbol{v}_{v_o} \quad ;\text{where}\quad \boldsymbol{N}_{\theta_z} \;=\; \left[\begin{array}{ccccc} N_{\theta_z}^{(v_1)} & N_{\theta_z}^{(\theta_1)} & N_{\theta_z}^{(v_2)} & N_{\theta_z}^{(\theta_2)} & N_{\theta_z}^{(\tilde{\theta}_3)} \end{array}\right] \tag{4.45}$$

$$= \left[\begin{array}{cccccc} \frac{dN_{v_o}^{(v_1)}}{dx} & \frac{dN_{v_o}^{(\theta_1)}}{dx} & \frac{dN_{v_o}^{(v_2)}}{dx} & \frac{dN_{v_o}^{(\theta_2)}}{dx} & (\frac{dN_{v_o}^{(\tilde{\theta}_3)}}{dx} - N_{\gamma_{xy}}^{(\tilde{\theta}_3)}) \end{array}\right]$$

$$\theta_y \;=\; \boldsymbol{N}_{\theta_y}\,\boldsymbol{v}_{w_o} \quad ;\text{where}\quad \boldsymbol{N}_{\theta_y} \;=\; \left[\begin{array}{ccccc} N_{\theta_y}^{(v_1)} & N_{\theta_y}^{(\theta_1)} & N_{\theta_y}^{(v_2)} & N_{\theta_y}^{(\theta_2)} & N_{\theta_y}^{(\tilde{\theta}_3)} \end{array}\right] \tag{4.46}$$

$$= -\left[\begin{array}{cccccc} \frac{dN_{w_o}^{(v_1)}}{dx} & \frac{dN_{w_o}^{(\theta_1)}}{dx} & \frac{dN_{w_o}^{(v_2)}}{dx} & \frac{dN_{w_o}^{(\theta_2)}}{dx} & (\frac{dN_{w_o}^{(\tilde{\theta}_3)}}{dx} - N_{\gamma_{xz}}^{(\tilde{\theta}_3)}) \end{array}\right]$$

By carrying out the differentiations, the components of $(\boldsymbol{N}_{\theta_z}, \boldsymbol{N}_{\theta_y})$ become

$$N_{\theta_z}^{(v_1)} \;=\; -\,N_{\theta_y}^{(v_1)} \;=\; -\,\frac{3}{2L_o}\,(1-\xi)\,(1+\xi) \tag{4.47}$$

$$N_{\theta_z}^{(\theta_1)} \;=\; N_{\theta_y}^{(\theta_1)} \;=\; -\,\frac{1}{4}\,(1-\xi)\,(1+3\xi) \tag{4.48}$$

$$N_{\theta_z}^{(v_2)} \;=\; -\,N_{\theta_y}^{(v_2)} \;=\; \frac{3}{2L_o}\,(1-\xi)\,(1+\xi) \tag{4.49}$$

$$N_{\theta_z}^{(\theta_2)} \;=\; N_{\theta_y}^{(\theta_2)} \;=\; -\,\frac{1}{4}\,(1+\xi)\,(1-3\xi) \tag{4.50}$$

$$N_{\theta_z}^{(\tilde{\theta}_3)} \;=\; N_{\theta_y}^{(\tilde{\theta}_3)} \;=\; (1-\xi)\,(1+\xi) \tag{4.51}$$

4.3 Internal Node-Force Vector

Now the interpolations Eqs.(4.20-4.27) can be combined with the strain expressions Eqs.(4.14-4.19) to form the strain-displacement relationship of the element. Thus

$$\boldsymbol{\epsilon} \;=\; \boldsymbol{B}\,\boldsymbol{v} \tag{4.52}$$

where $\boldsymbol{v}$ is given by Eq.(4.43) and with the strain field $\boldsymbol{\epsilon}$ ordered

$$\boldsymbol{\epsilon}^T \;=\; \left[\begin{array}{cccccc} \epsilon_x & \gamma_{xy} & \gamma_{xz} & \epsilon_y & \epsilon_z & \gamma_{yz} \end{array}\right] \tag{4.53}$$

yielding the strain-displacement matrix $\boldsymbol{B}$ on the form

$$\boldsymbol{B} = \begin{bmatrix} \frac{d}{dx}\boldsymbol{N}_{u_o} & -y\frac{d^2}{dx^2}\boldsymbol{N}_{v_o} & -z\frac{d^2}{dx^2}\boldsymbol{N}_{w_o} & \mathbf{0} & \mathbf{0} & \mathbf{0} \\ \mathbf{0} & \boldsymbol{N}_{\gamma_{xy}} & \mathbf{0} & -z\frac{d}{dx}\boldsymbol{N}_{\theta_x} & \mathbf{0} & \mathbf{0} \\ \mathbf{0} & \mathbf{0} & \boldsymbol{N}_{\gamma_{xz}} & y\frac{d}{dx}\boldsymbol{N}_{\theta_x} & \mathbf{0} & \mathbf{0} \\ \mathbf{0} & \mathbf{0} & \mathbf{0} & \mathbf{0} & \frac{d}{dy}\boldsymbol{N}_{v_r} & \mathbf{0} \\ \mathbf{0} & \mathbf{0} & \mathbf{0} & \mathbf{0} & \mathbf{0} & \frac{d}{dz}\boldsymbol{N}_{w_r} \\ \mathbf{0} & \mathbf{0} & \mathbf{0} & \mathbf{0} & \frac{d}{dz}\boldsymbol{N}_{v_r} & \frac{d}{dy}\boldsymbol{N}_{w_r} \end{bmatrix} \tag{4.54}$$

The expressions for the shape function derivatives that take part in the nonzero subvectors of $\boldsymbol{B}$, follow from Eqs.(4.28-4.39). Thus

$$\frac{dN_{u_o}^{(v_1)}}{dx} = \frac{dN_{\theta_x}^{(\theta_1)}}{dx} = -\frac{1}{L_o} \tag{4.55}$$

$$\frac{dN_{u_o}^{(v_2)}}{dx} = \frac{dN_{\theta_x}^{(\theta_2)}}{dx} = \frac{1}{L_o} \tag{4.56}$$

$$\frac{dN_{u_o}^{(\tilde{v}_3)}}{dx} = -\frac{4}{L_o}\xi \tag{4.57}$$

$$\frac{d^2N_{v_o}^{(v_1)}}{dx^2} = \frac{d^2N_{w_o}^{(v_1)}}{dx^2} = \frac{6}{L_o^2}\xi \tag{4.58}$$

$$\frac{d^2N_{v_o}^{(\theta_1)}}{dx^2} = -\frac{d^2N_{w_o}^{(\theta_1)}}{dx^2} = -\frac{1}{L_o}(1-3\xi) \tag{4.59}$$

$$\frac{d^2N_{v_o}^{(v_2)}}{dx^2} = \frac{d^2N_{w_o}^{(v_2)}}{dx^2} = -\frac{6}{L_o^2}\xi \tag{4.60}$$

$$\frac{d^2N_{v_o}^{(\theta_2)}}{dx^2} = -\frac{d^2N_{w_o}^{(\theta_2)}}{dx^2} = \frac{1}{L_o}(1+3\xi) \tag{4.61}$$

$$\frac{d^2N_{v_o}^{(\tilde{\theta}_3)}}{dx^2} = -\frac{d^2N_{w_o}^{(\tilde{\theta}_3)}}{dx^2} = -\frac{4}{L_o}\xi \tag{4.62}$$

$$\frac{dN_{v_r}^{(\tilde{\epsilon})}}{dy} = \frac{dN_{w_r}^{(\tilde{\epsilon})}}{dz} = 1 \tag{4.63}$$

$$\frac{dN_{v_r}^{(\tilde{g})}}{dy} = \frac{dN_{w_r}^{(\tilde{g})}}{dy} = z \tag{4.64}$$

$$\frac{dN_{v_r}^{(\tilde{\epsilon})}}{dz} = \frac{dN_{w_r}^{(\tilde{\epsilon})}}{dy} = 0 \tag{4.65}$$

$$\frac{dN_{v_r}^{(\tilde{g})}}{dz} = \frac{dN_{w_r}^{(\tilde{g})}}{dz} = y \tag{4.66}$$

Retaining only the linear terms of the Green strain components implies that the 2nd Piola-Kirchhoff stresses now convert to Cauchy stresses $\boldsymbol{\sigma}$, which with the same

ordering of components as for $\boldsymbol{\epsilon}$, read

$$\boldsymbol{\sigma}^T \;=\; \left[\begin{array}{cccccc} \sigma_x & \tau_{xy} & \tau_{xz} & \sigma_y & \sigma_z & \tau_{yz} \end{array}\right] \tag{4.67}$$

Furthermore, the expressions for total and virtual strains in Eqs.(2.6,2.43), respectively, reduce to similar forms when only linear terms are retained. Consequently, Eq.(4.52) holds also for the virtual quantities, i.e.

$$\delta\boldsymbol{\epsilon} \;=\; \boldsymbol{B}\,\delta\boldsymbol{v} \tag{4.68}$$

Then the left hand side of Eq.(2.44), that states the principle of virtual displacements, now becomes

$$\int_{V_o} \delta\boldsymbol{\epsilon}^T\boldsymbol{\sigma}\,dV_o \;=\; \delta\boldsymbol{v}^T\int_{V_o}\boldsymbol{B}^T\boldsymbol{\sigma}\,dV_o \;=\; \delta\boldsymbol{v}^T\boldsymbol{r} \tag{4.69}$$

i.e.

$$\boldsymbol{r} \;=\; \int_{V_o}\boldsymbol{B}^T\boldsymbol{\sigma}\,dV_o \tag{4.70}$$

which is the internal node-force vector of the element. Carrying out the product $\boldsymbol{B}^T\boldsymbol{\sigma}$ by using Eqs.(4.54,4.67), $\boldsymbol{r}$ gets into final form

$$\boldsymbol{r} \;=\; \left\{\begin{array}{c} \boldsymbol{r}_{u_o} \\ \boldsymbol{r}_{v_o} \\ \boldsymbol{r}_{w_o} \\ \boldsymbol{r}_{\theta_x} \\ \boldsymbol{r}_{v_r} \\ \boldsymbol{r}_{w_r} \end{array}\right\} \;=\; \int_{L_o}\left\{\begin{array}{c} F_x\frac{d}{dx}\boldsymbol{N}^T_{u_o} \\ M_z\frac{d^2}{dx^2}\boldsymbol{N}^T_{v_o} \;+\; F_y\boldsymbol{N}^T_{\gamma_{xy}} \\ -M_y\frac{d^2}{dx^2}\boldsymbol{N}^T_{w_o} \;+\; F_z\boldsymbol{N}^T_{\gamma_{xz}} \\ M_x\frac{d}{dx}\boldsymbol{N}^T_{\theta_x} \\ \boldsymbol{G}_{yy} \;+\; \boldsymbol{G}_{yz} \\ \boldsymbol{G}_{zz} \;+\; \boldsymbol{G}_{zy} \end{array}\right\} dL_o \tag{4.71}$$

where the member forces have been introduced

$$F_x \;=\; \int_{A_o}\sigma_x\,dA_o \tag{4.72}$$

$$F_y \;=\; \int_{A_o}\tau_{xy}\,dA_o \tag{4.73}$$

$$F_z \;=\; \int_{A_o}\tau_{xz}\,dA_o \tag{4.74}$$

$$M_x \;=\; \int_{A_o}(y\tau_{xz} \;-\; z\tau_{xy})\,dA_o \tag{4.75}$$

$$M_y \;=\; \int_{A_o}z\sigma_x\,dA_o \tag{4.76}$$

$$M_z \;=\; -\int_{A_o}y\sigma_x\,dA_o \tag{4.77}$$

and the generalized member force vectors pertaining to the strain DOFs

$$\boldsymbol{G}_{yy} = \int_{A_o} \sigma_y \frac{d\boldsymbol{N}_{v_r}^T}{dy}\, dA_o \tag{4.78}$$

$$\boldsymbol{G}_{yz} = \int_{A_o} \tau_{yz} \frac{d\boldsymbol{N}_{v_r}^T}{dz}\, dA_o \tag{4.79}$$

$$\boldsymbol{G}_{zz} = \int_{A_o} \sigma_z \frac{d\boldsymbol{N}_{w_r}^T}{dz}\, dA_o \tag{4.80}$$

$$\boldsymbol{G}_{zy} = \int_{A_o} \tau_{yz} \frac{d\boldsymbol{N}_{w_r}^T}{dy}\, dA_o \tag{4.81}$$

The integrals may be solved numerically, e.g. by Gauss quadrature. Chapter 10 deals with the cross section analysis, where expressions for the stress vector $\boldsymbol{\sigma}$ and the geometric quantities (y, z, dA_o) are given for each class of elementary units ('building blocks') that a reinforced concrete section may consist of.

4.4 Material Stiffness Matrix

When retaining only the linear terms of the Green strain components, the expression for the incremental strains in Eq.(2.9) also reduces to a similar form as the total strains, and thus, Eq.(4.52) holds for incremental quantities as well

$$\Delta\boldsymbol{\epsilon} = \boldsymbol{B}\, \Delta\boldsymbol{v} \tag{4.82}$$

With this relationship and the similar for virtual strains in Eq.(4.68), the second term on the left hand side of Eq.(2.51), that states the principle of virtual displacements on incremental form, now becomes

$$\int_{V_o} \delta\boldsymbol{\epsilon}^T \boldsymbol{C}_t\, \Delta\boldsymbol{\epsilon}\, dV_o = \delta\boldsymbol{v}^T \left(\int_{V_o} \boldsymbol{B}^T \boldsymbol{C}_t\, \boldsymbol{B}\, dV_o \right) \Delta\boldsymbol{v} = \delta\boldsymbol{v}^T \boldsymbol{k}_m\, \Delta\boldsymbol{v} \tag{4.83}$$

i.e.

$$\boldsymbol{k}_m = \int_{V_o} \boldsymbol{B}^T \boldsymbol{C}_t\, \boldsymbol{B}\, dV_o \tag{4.84}$$

which is the incremental material stiffness matrix of the element. Here the tangent constitutive matrix in general will be a full, nonsymmetric matrix. Thus from Eq.(2.33)

$$\boldsymbol{C}_t = \frac{\partial\boldsymbol{\sigma}}{\partial\boldsymbol{\epsilon}} = \begin{bmatrix} c_{11} & c_{12} & c_{13} & c_{14} & c_{15} & c_{16} \\ c_{21} & c_{22} & c_{23} & c_{24} & c_{25} & c_{26} \\ c_{31} & c_{32} & c_{33} & c_{34} & c_{35} & c_{36} \\ c_{41} & c_{42} & c_{43} & c_{44} & c_{45} & c_{46} \\ c_{51} & c_{52} & c_{53} & c_{54} & c_{55} & c_{56} \\ c_{61} & c_{62} & c_{63} & c_{64} & c_{65} & c_{66} \end{bmatrix} \tag{4.85}$$

By carrying out the product $\boldsymbol{B}^T \boldsymbol{C}_t \boldsymbol{B}$, where $\boldsymbol{B}$ is taken from Eq.(4.54), the expression for $\boldsymbol{k}_m$ becomes

$$\boldsymbol{k}_m = \begin{bmatrix} \boldsymbol{k}^{(m)}_{u_o u_o} & \boldsymbol{k}^{(m)}_{u_o v_o} & \boldsymbol{k}^{(m)}_{u_o w_o} & \boldsymbol{k}^{(m)}_{u_o \theta_x} & \boldsymbol{k}^{(m)}_{u_o v_r} & \boldsymbol{k}^{(m)}_{u_o w_r} \\ \boldsymbol{k}^{(m)}_{v_o u_o} & \boldsymbol{k}^{(m)}_{v_o v_o} & \boldsymbol{k}^{(m)}_{v_o w_o} & \boldsymbol{k}^{(m)}_{v_o \theta_x} & \boldsymbol{k}^{(m)}_{v_o v_r} & \boldsymbol{k}^{(m)}_{v_o w_r} \\ \boldsymbol{k}^{(m)}_{w_o u_o} & \boldsymbol{k}^{(m)}_{w_o v_o} & \boldsymbol{k}^{(m)}_{w_o w_o} & \boldsymbol{k}^{(m)}_{w_o \theta_x} & \boldsymbol{k}^{(m)}_{w_o v_r} & \boldsymbol{k}^{(m)}_{w_o w_r} \\ \boldsymbol{k}^{(m)}_{\theta_x u_o} & \boldsymbol{k}^{(m)}_{\theta_x v_o} & \boldsymbol{k}^{(m)}_{\theta_x w_o} & \boldsymbol{k}^{(m)}_{\theta_x \theta_x} & \boldsymbol{k}^{(m)}_{\theta_x v_r} & \boldsymbol{k}^{(m)}_{\theta_x w_r} \\ \boldsymbol{k}^{(m)}_{v_r u_o} & \boldsymbol{k}^{(m)}_{v_r v_o} & \boldsymbol{k}^{(m)}_{v_r w_o} & \boldsymbol{k}^{(m)}_{v_r \theta_x} & \boldsymbol{k}^{(m)}_{v_r v_r} & \boldsymbol{k}^{(m)}_{v_r w_r} \\ \boldsymbol{k}^{(m)}_{w_r u_o} & \boldsymbol{k}^{(m)}_{w_r v_o} & \boldsymbol{k}^{(m)}_{w_r w_o} & \boldsymbol{k}^{(m)}_{w_r \theta_x} & \boldsymbol{k}^{(m)}_{w_r v_r} & \boldsymbol{k}^{(m)}_{w_r w_r} \end{bmatrix} \tag{4.86}$$

where

$$\boldsymbol{k}^{(m)}_{u_o u_o} = \int_{L_o} \left(\int_{A_o} c_{11}\, dA_o \right) \frac{d\boldsymbol{N}^T_{u_o}}{dx} \frac{d\boldsymbol{N}_{u_o}}{dx}\, dL_o \tag{4.87}$$

$$\boldsymbol{k}^{(m)}_{u_o v_o} = \int_{L_o} \left\{ \left(\int_{A_o} -y c_{11}\, dA_o \right) \frac{d\boldsymbol{N}^T_{u_o}}{dx} \frac{d^2\boldsymbol{N}_{v_o}}{dx^2} + \left(\int_{A_o} c_{12}\, dA_o \right) \frac{d\boldsymbol{N}^T_{u_o}}{dx} \boldsymbol{N}_{\gamma_{xy}} \right\} dL_o \tag{4.88}$$

$$\boldsymbol{k}^{(m)}_{u_o w_o} = \int_{L_o} \left\{ \left(\int_{A_o} -z c_{11}\, dA_o \right) \frac{d\boldsymbol{N}^T_{u_o}}{dx} \frac{d^2\boldsymbol{N}_{w_o}}{dx^2} + \left(\int_{A_o} c_{13}\, dA_o \right) \frac{d\boldsymbol{N}^T_{u_o}}{dx} \boldsymbol{N}_{\gamma_{xz}} \right\} dL_o \tag{4.89}$$

$$\boldsymbol{k}^{(m)}_{u_o \theta_x} = \int_{L_o} \left(\int_{A_o} [-z c_{12} + y c_{13}]\, dA_o \right) \frac{d\boldsymbol{N}^T_{u_o}}{dx} \frac{d\boldsymbol{N}_{\theta_x}}{dx}\, dL_o \tag{4.90}$$

$$\boldsymbol{k}^{(m)}_{u_o v_r} = \int_{L_o} \frac{d\boldsymbol{N}^T_{u_o}}{dx} \left(\int_{A_o} [c_{14} \frac{d\boldsymbol{N}_{v_r}}{dy} + c_{16} \frac{d\boldsymbol{N}_{v_r}}{dz}]\, dA_o \right) dL_o \tag{4.91}$$

$$\boldsymbol{k}^{(m)}_{u_o w_r} = \int_{L_o} \frac{d\boldsymbol{N}^T_{u_o}}{dx} \left(\int_{A_o} [c_{15} \frac{d\boldsymbol{N}_{w_r}}{dz} + c_{16} \frac{d\boldsymbol{N}_{w_r}}{dy}]\, dA_o \right) dL_o \tag{4.92}$$

$$\boldsymbol{k}^{(m)}_{v_o u_o} = \int_{L_o} \left\{ \left(\int_{A_o} -y c_{11}\, dA_o \right) \frac{d^2\boldsymbol{N}^T_{v_o}}{dx^2} \frac{d\boldsymbol{N}_{u_o}}{dx} + \left(\int_{A_o} c_{21}\, dA_o \right) \boldsymbol{N}^T_{\gamma_{xy}} \frac{d\boldsymbol{N}_{u_o}}{dx} \right\} dL_o \tag{4.93}$$

$$\boldsymbol{k}^{(m)}_{v_o v_o} = \int_{L_o} \left\{ \left(\int_{A_o} y^2 c_{11}\, dA_o \right) \frac{d^2\boldsymbol{N}^T_{v_o}}{dx^2} \frac{d^2\boldsymbol{N}_{v_o}}{dx^2} - \left(\int_{A_o} y c_{21}\, dA_o \right) \boldsymbol{N}^T_{\gamma_{xy}} \frac{d^2\boldsymbol{N}_{v_o}}{dx^2} - \left(\int_{A_o} y c_{12}\, dA_o \right) \frac{d^2\boldsymbol{N}^T_{v_o}}{dx^2} \boldsymbol{N}_{\gamma_{xy}} \right.$$

$$+ \left(\int_{A_o} c_{22}\, dA_o\right) \boldsymbol{N}_{\gamma_{xy}}^T\, \boldsymbol{N}_{\gamma_{xy}} \Big\}\, dL_o \tag{4.94}$$

$$\begin{aligned}
\boldsymbol{k}_{v_o w_o}^{(m)} &= \int_{L_o} \Bigg\{ \left(\int_{A_o} yzc_{11}\, dA_o\right) \frac{d^2 \boldsymbol{N}_{v_o}^T}{dx^2}\, \frac{d^2 \boldsymbol{N}_{w_o}}{dx^2} \\
&\quad - \left(\int_{A_o} zc_{21}\, dA_o\right) \boldsymbol{N}_{\gamma_{xy}}^T\, \frac{d^2 \boldsymbol{N}_{w_o}}{dx^2} \\
&\quad - \left(\int_{A_o} yc_{13}\, dA_o\right) \frac{d^2 \boldsymbol{N}_{v_o}^T}{dx^2}\, \boldsymbol{N}_{\gamma_{xz}} \\
&\quad + \left(\int_{A_o} c_{23}\, dA_o\right) \boldsymbol{N}_{\gamma_{xy}}^T\, \boldsymbol{N}_{\gamma_{xz}} \Bigg\}\, dL_o
\end{aligned} \tag{4.95}$$

$$\begin{aligned}
\boldsymbol{k}_{v_o \theta_x}^{(m)} &= \int_{L_o} \Bigg\{ \left(\int_{A_o} [yzc_{12} - y^2 c_{13}]\, dA_o\right) \frac{d^2 \boldsymbol{N}_{v_o}^T}{dx^2}\, \frac{d\boldsymbol{N}_{\theta_x}}{dx} \\
&\quad + \left(\int_{A_o} [-zc_{22} + yc_{23}]\, dA_o\right) \boldsymbol{N}_{\gamma_{xy}}^T\, \frac{d\boldsymbol{N}_{\theta_x}}{dx} \Bigg\}\, dL_o
\end{aligned} \tag{4.96}$$

$$\begin{aligned}
\boldsymbol{k}_{v_o v_r}^{(m)} &= \int_{L_o} \Bigg\{ -\frac{d^2 \boldsymbol{N}_{v_o}^T}{dx^2} \left(\int_{A_o} [yc_{14} \frac{d\boldsymbol{N}_{v_r}}{dy} + yc_{16} \frac{d\boldsymbol{N}_{v_r}}{dz}]\, dA_o\right) \\
&\quad + \boldsymbol{N}_{\gamma_{xy}}^T \left(\int_{A_o} [c_{24} \frac{d\boldsymbol{N}_{v_r}}{dy} + c_{26} \frac{d\boldsymbol{N}_{v_r}}{dz}]\, dA_o\right) \Bigg\}\, dL_o
\end{aligned} \tag{4.97}$$

$$\begin{aligned}
\boldsymbol{k}_{v_o w_r}^{(m)} &= \int_{L_o} \Bigg\{ -\frac{d^2 \boldsymbol{N}_{v_o}^T}{dx^2} \left(\int_{A_o} [yc_{15} \frac{d\boldsymbol{N}_{w_r}}{dz} + yc_{16} \frac{d\boldsymbol{N}_{w_r}}{dy}]\, dA_o\right) \\
&\quad + \boldsymbol{N}_{\gamma_{xy}}^T \left(\int_{A_o} [c_{25} \frac{d\boldsymbol{N}_{w_r}}{dz} + c_{26} \frac{d\boldsymbol{N}_{w_r}}{dy}]\, dA_o\right) \Bigg\}\, dL_o
\end{aligned} \tag{4.98}$$

$$\begin{aligned}
\boldsymbol{k}_{w_o u_o}^{(m)} &= \int_{L_o} \Bigg\{ \left(\int_{A_o} -zc_{11}\, dA_o\right) \frac{d^2 \boldsymbol{N}_{w_o}^T}{dx^2}\, \frac{d\boldsymbol{N}_{u_o}}{dx} \\
&\quad + \left(\int_{A_o} c_{31}\, dA_o\right) \boldsymbol{N}_{\gamma_{xz}}^T\, \frac{d\boldsymbol{N}_{u_o}}{dx} \Bigg\}\, dL_o
\end{aligned} \tag{4.99}$$

$$\begin{aligned}
\boldsymbol{k}_{w_o v_o}^{(m)} &= \int_{L_o} \Bigg\{ \left(\int_{A_o} yzc_{11}\, dA_o\right) \frac{d^2 \boldsymbol{N}_{w_o}^T}{dx^2}\, \frac{d^2 \boldsymbol{N}_{v_o}}{dx^2} \\
&\quad - \left(\int_{A_o} yc_{31}\, dA_o\right) \boldsymbol{N}_{\gamma_{xz}}^T\, \frac{d^2 \boldsymbol{N}_{v_o}}{dx^2} \\
&\quad - \left(\int_{A_o} zc_{12}\, dA_o\right) \frac{d^2 \boldsymbol{N}_{w_o}^T}{dx^2}\, \boldsymbol{N}_{\gamma_{xy}} \\
&\quad + \left(\int_{A_o} c_{32}\, dA_o\right) \boldsymbol{N}_{\gamma_{xz}}^T\, \boldsymbol{N}_{\gamma_{xy}} \Bigg\}\, dL_o
\end{aligned} \tag{4.100}$$

$$\begin{aligned}
\boldsymbol{k}_{w_o w_o}^{(m)} &= \int_{L_o} \Bigg\{ \left(\int_{A_o} z^2 c_{11}\, dA_o\right) \frac{d^2 \boldsymbol{N}_{w_o}^T}{dx^2}\, \frac{d^2 \boldsymbol{N}_{w_o}}{dx^2} \\
&\quad - \left(\int_{A_o} zc_{31}\, dA_o\right) \boldsymbol{N}_{\gamma_{xz}}^T\, \frac{d^2 \boldsymbol{N}_{w_o}}{dx^2}
\end{aligned}$$

$$
\begin{aligned}
&- \left(\int_{A_o} z c_{13}\, dA_o\right) \frac{d^2 \boldsymbol{N}_{w_o}^T}{dx^2}\, \boldsymbol{N}_{\gamma_{xz}} \\
&+ \left(\int_{A_o} c_{33}\, dA_o\right) \boldsymbol{N}_{\gamma_{xz}}^T\, \boldsymbol{N}_{\gamma_{xz}} \Big\}\, dL_o \qquad (4.101)
\end{aligned}
$$

$$
\begin{aligned}
\boldsymbol{k}_{w_o\theta_x}^{(m)} &= \int_{L_o} \left\{ \left(\int_{A_o} [z^2 c_{12} - yz c_{13}]\, dA_o\right) \frac{d^2 \boldsymbol{N}_{w_o}^T}{dx^2}\, \frac{d\boldsymbol{N}_{\theta_x}}{dx} \right. \\
&\quad \left. + \left(\int_{A_o} [-z c_{32} + y c_{33}]\, dA_o\right) \boldsymbol{N}_{\gamma_{xz}}^T\, \frac{d\boldsymbol{N}_{\theta_x}}{dx} \right\} dL_o \qquad (4.102)
\end{aligned}
$$

$$
\begin{aligned}
\boldsymbol{k}_{w_o v_r}^{(m)} &= \int_{L_o} \left\{ -\frac{d^2 \boldsymbol{N}_{w_o}^T}{dx^2} \left(\int_{A_o} [z c_{14} \frac{d\boldsymbol{N}_{v_r}}{dy} + z c_{16} \frac{d\boldsymbol{N}_{v_r}}{dz}]\, dA_o\right) \right. \\
&\quad \left. + \boldsymbol{N}_{\gamma_{xz}}^T \left(\int_{A_o} [c_{34} \frac{d\boldsymbol{N}_{v_r}}{dy} + c_{36} \frac{d\boldsymbol{N}_{v_r}}{dz}]\, dA_o\right) \right\} dL_o \qquad (4.103)
\end{aligned}
$$

$$
\begin{aligned}
\boldsymbol{k}_{w_o w_r}^{(m)} &= \int_{L_o} \left\{ -\frac{d^2 \boldsymbol{N}_{w_o}^T}{dx^2} \left(\int_{A_o} [z c_{15} \frac{d\boldsymbol{N}_{w_r}}{dz} + z c_{16} \frac{d\boldsymbol{N}_{w_r}}{dy}]\, dA_o\right) \right. \\
&\quad \left. + \boldsymbol{N}_{\gamma_{xz}}^T \left(\int_{A_o} [c_{35} \frac{d\boldsymbol{N}_{w_r}}{dz} + c_{36} \frac{d\boldsymbol{N}_{w_r}}{dy}]\, dA_o\right) \right\} dL_o \qquad (4.104)
\end{aligned}
$$

$$
\boldsymbol{k}_{\theta_x u_o}^{(m)} = \int_{L_o} \left(\int_{A_o} [-z c_{21} + y c_{31}]\, dA_o\right) \frac{d\boldsymbol{N}_{\theta_x}^T}{dx}\, \frac{d\boldsymbol{N}_{u_o}}{dx}\, dL_o \qquad (4.105)
$$

$$
\begin{aligned}
\boldsymbol{k}_{\theta_x v_o}^{(m)} &= \int_{L_o} \left\{ \left(\int_{A_o} [yz c_{21} - y^2 c_{31}]\, dA_o\right) \frac{d\boldsymbol{N}_{\theta_x}^T}{dx}\, \frac{d^2 \boldsymbol{N}_{v_o}}{dx^2} \right. \\
&\quad \left. + \left(\int_{A_o} [-z c_{22} + y c_{32}]\, dA_o\right) \frac{d\boldsymbol{N}_{\theta_x}^T}{dx}\, \boldsymbol{N}_{\gamma_{xy}} \right\} dL_o \qquad (4.106)
\end{aligned}
$$

$$
\begin{aligned}
\boldsymbol{k}_{\theta_x w_o}^{(m)} &= \int_{L_o} \left\{ \left(\int_{A_o} [z^2 c_{21} - yz c_{31}]\, dA_o\right) \frac{d\boldsymbol{N}_{\theta_x}^T}{dx}\, \frac{d^2 \boldsymbol{N}_{w_o}}{dx^2} \right. \\
&\quad \left. + \left(\int_{A_o} [-z c_{23} + y c_{33}]\, dA_o\right) \frac{d\boldsymbol{N}_{\theta_x}^T}{dx}\, \boldsymbol{N}_{\gamma_{xz}} \right\} dL_o \qquad (4.107)
\end{aligned}
$$

$$
\begin{aligned}
\boldsymbol{k}_{\theta_x \theta_x}^{(m)} &= \int_{L_o} \left(\int_{A_o} [z^2 c_{22} - yz c_{32} - yz c_{23} + y^2 c_{33}]\, dA_o\right) \\
&\quad \frac{d\boldsymbol{N}_{\theta_x}^T}{dx}\, \frac{d\boldsymbol{N}_{\theta_x}}{dx}\, dL_o \qquad (4.108)
\end{aligned}
$$

$$
\begin{aligned}
\boldsymbol{k}_{\theta_x v_r}^{(m)} &= \int_{L_o} \left\{ \frac{d\boldsymbol{N}_{\theta_x}^T}{dx} \left(\int_{A_o} [-z c_{24} + y c_{34}]\, \frac{d\boldsymbol{N}_{v_r}}{dy}\, dA_o\right) \right. \\
&\quad \left. + \frac{d\boldsymbol{N}_{\theta_x}^T}{dx} \left(\int_{A_o} [-z c_{26} + y c_{36}]\, \frac{d\boldsymbol{N}_{v_r}}{dz}\, dA_o\right) \right\} dL_o \qquad (4.109)
\end{aligned}
$$

$$
\begin{aligned}
\boldsymbol{k}_{\theta_x w_r}^{(m)} &= \int_{L_o} \left\{ \frac{d\boldsymbol{N}_{\theta_x}^T}{dx} \left(\int_{A_o} [-z c_{25} + y c_{35}]\, \frac{d\boldsymbol{N}_{w_r}}{dz}\, dA_o\right) \right. \\
&\quad \left. + \frac{d\boldsymbol{N}_{\theta_x}^T}{dx} \left(\int_{A_o} [-z c_{26} + y c_{36}]\, \frac{d\boldsymbol{N}_{w_r}}{dy}\, dA_o\right) \right\} dL_o \qquad (4.110)
\end{aligned}
$$

$$\boldsymbol{k}^{(m)}_{v_r u_o} = \int_{L_o} \left(\int_{A_o} [c_{41} \frac{d\boldsymbol{N}^T_{v_r}}{dy} + c_{61} \frac{d\boldsymbol{N}^T_{v_r}}{dz}] \, dA_o \right) \frac{d\boldsymbol{N}_{u_o}}{dx} \, dL_o \tag{4.111}$$

$$\boldsymbol{k}^{(m)}_{v_r v_o} = \int_{L_o} \left\{ - \left(\int_{A_o} [y c_{41} \frac{d\boldsymbol{N}^T_{v_r}}{dy} + y c_{61} \frac{d\boldsymbol{N}^T_{v_r}}{dz}] \, dA_o \right) \frac{d^2\boldsymbol{N}_{v_o}}{dx^2} + \left(\int_{A_o} [c_{42} \frac{d\boldsymbol{N}^T_{v_r}}{dy} + c_{62} \frac{d\boldsymbol{N}^T_{v_r}}{dz}] \, dA_o \right) \boldsymbol{N}_{\gamma_{xy}} \right\} dL_o \tag{4.112}$$

$$\boldsymbol{k}^{(m)}_{v_r w_o} = \int_{L_o} \left\{ - \left(\int_{A_o} [z c_{41} \frac{d\boldsymbol{N}^T_{v_r}}{dy} + z c_{61} \frac{d\boldsymbol{N}^T_{v_r}}{dz}] \, dA_o \right) \frac{d^2\boldsymbol{N}_{w_o}}{dx^2} + \left(\int_{A_o} [c_{43} \frac{d\boldsymbol{N}^T_{v_r}}{dy} + c_{63} \frac{d\boldsymbol{N}^T_{v_r}}{dz}] \, dA_o \right) \boldsymbol{N}_{\gamma_{xz}} \right\} dL_o \tag{4.113}$$

$$\boldsymbol{k}^{(m)}_{v_r \theta_x} = \int_{L_o} \left\{ \left(\int_{A_o} [-z c_{42} + y c_{43}] \, \frac{d\boldsymbol{N}^T_{v_r}}{dy} \, dA_o \right) \frac{d\boldsymbol{N}_{\theta_x}}{dx} + \left(\int_{A_o} [-z c_{62} + y c_{63}] \, \frac{d\boldsymbol{N}^T_{v_r}}{dz} \, dA_o \right) \frac{d\boldsymbol{N}_{\theta_x}}{dx} \right\} dL_o \tag{4.114}$$

$$\boldsymbol{k}^{(m)}_{v_r v_r} = \int_{L_o} \left\{ \left(\int_{A_o} \frac{d\boldsymbol{N}^T_{v_r}}{dy} [c_{44} \frac{d\boldsymbol{N}_{v_r}}{dy} + c_{46} \frac{d\boldsymbol{N}_{v_r}}{dz}] \, dA_o \right) + \left(\int_{A_o} \frac{d\boldsymbol{N}^T_{v_r}}{dz} [c_{64} \frac{d\boldsymbol{N}_{v_r}}{dy} + c_{66} \frac{d\boldsymbol{N}_{v_r}}{dz}] \, dA_o \right) \right\} dL_o \tag{4.115}$$

$$\boldsymbol{k}^{(m)}_{v_r w_r} = \int_{L_o} \left\{ \left(\int_{A_o} \frac{d\boldsymbol{N}^T_{v_r}}{dy} [c_{45} \frac{d\boldsymbol{N}_{w_r}}{dz} + c_{46} \frac{d\boldsymbol{N}_{w_r}}{dy}] \, dA_o \right) + \left(\int_{A_o} \frac{d\boldsymbol{N}^T_{v_r}}{dz} [c_{65} \frac{d\boldsymbol{N}_{w_r}}{dz} + c_{66} \frac{d\boldsymbol{N}_{w_r}}{dy}] \, dA_o \right) \right\} dL_o \tag{4.116}$$

$$\boldsymbol{k}^{(m)}_{w_r u_o} = \int_{L_o} \left(\int_{A_o} [c_{51} \frac{d\boldsymbol{N}^T_{w_r}}{dz} + c_{61} \frac{d\boldsymbol{N}^T_{w_r}}{dy}] \, dA_o \right) \frac{d\boldsymbol{N}_{u_o}}{dx} \, dL_o \tag{4.117}$$

$$\boldsymbol{k}^{(m)}_{w_r v_o} = \int_{L_o} \left\{ - \left(\int_{A_o} [y c_{51} \frac{d\boldsymbol{N}^T_{w_r}}{dz} + y c_{61} \frac{d\boldsymbol{N}^T_{w_r}}{dy}] \, dA_o \right) \frac{d^2\boldsymbol{N}_{v_o}}{dx^2} + \left(\int_{A_o} [c_{52} \frac{d\boldsymbol{N}^T_{w_r}}{dz} + c_{62} \frac{d\boldsymbol{N}^T_{w_r}}{dy}] \, dA_o \right) \boldsymbol{N}_{\gamma_{xy}} \right\} dL_o \tag{4.118}$$

$$\boldsymbol{k}^{(m)}_{w_r w_o} = \int_{L_o} \left\{ - \left(\int_{A_o} [z c_{51} \frac{d\boldsymbol{N}^T_{w_r}}{dz} + z c_{61} \frac{d\boldsymbol{N}^T_{w_r}}{dy}] \, dA_o \right) \frac{d^2\boldsymbol{N}_{w_o}}{dx^2} + \left(\int_{A_o} [c_{53} \frac{d\boldsymbol{N}^T_{w_r}}{dz} + c_{63} \frac{d\boldsymbol{N}^T_{w_r}}{dy}] \, dA_o \right) \boldsymbol{N}_{\gamma_{xz}} \right\} dL_o \tag{4.119}$$

$$\boldsymbol{k}^{(m)}_{w_r \theta_x} = \int_{L_o} \left\{ \left(\int_{A_o} [-z c_{52} + y c_{53}] \, \frac{d\boldsymbol{N}^T_{w_r}}{dz} \, dA_o \right) \frac{d\boldsymbol{N}_{\theta_x}}{dx} + \left(\int_{A_o} [-z c_{62} + y c_{63}] \, \frac{d\boldsymbol{N}^T_{w_r}}{dy} \, dA_o \right) \frac{d\boldsymbol{N}_{\theta_x}}{dx} \right\} dL_o \tag{4.120}$$

$$\boldsymbol{k}^{(m)}_{w_r v_r} = \int_{L_o} \left\{ \left(\int_{A_o} [c_{54} \frac{d\boldsymbol{N}^T_{w_r}}{dz} + c_{64} \frac{d\boldsymbol{N}^T_{w_r}}{dy}] \, dA_o \right) \frac{d\boldsymbol{N}_{v_r}}{dy} + \left(\int_{A_o} [c_{56} \frac{d\boldsymbol{N}^T_{w_r}}{dz} + c_{66} \frac{d\boldsymbol{N}^T_{w_r}}{dy}] \, dA_o \right) \frac{d\boldsymbol{N}_{v_r}}{dz} \right\} dL_o \tag{4.121}$$

$$\boldsymbol{k}^{(m)}_{w_r w_r} = \int_{L_o} \left\{ \left(\int_{A_o} \frac{d\boldsymbol{N}^T_{w_r}}{dz} [c_{55} \frac{d\boldsymbol{N}_{w_r}}{dz} + c_{56} \frac{d\boldsymbol{N}_{w_r}}{dy}] \, dA_o \right) + \left(\int_{A_o} \frac{d\boldsymbol{N}^T_{w_r}}{dy} [c_{65} \frac{d\boldsymbol{N}_{w_r}}{dz} + c_{66} \frac{d\boldsymbol{N}_{w_r}}{dy}] \, dA_o \right) \right\} dL_o \tag{4.122}$$

Again the integrals may be solved numerically, e.g. by Gauss quadrature. Chapter 10 deals with the cross section analysis, where the tangent constitutive matrix $\boldsymbol{C}_t$ and the geometric quantities (y, z, dA_o) are expressed for each class of elementary section units. Finally, note that since $\boldsymbol{C}_t$ is nonsymmetric, so becomes also the material stiffness matrix $\boldsymbol{k}_m$.

4.5 Geometric Stiffness Matrix

So far, only infinitesimal strain expressions have been considered when deriving the internal node-force vector and the incremental material stiffness matrix of the element. This simplification has been justified by the adoption of the CL-formulation for the large displacement analysis. To account for the geometric nonlinear effects at the element level, however, it is necessary to include higher order strain expressions. The most important strain component in this respect for a beam is apparently the normal x-strain. Thus, higher order terms will now be added to this strain component, while retaining the remaining five other components linear. As a further simplification; only the two quadratic rotational terms of the normal x-strain will be included since these generally are larger than the quadratic axial term for a beam. Then from Eq.(2.6) the normal x-strain now becomes

$$E_x = \frac{\partial u}{\partial x} + \frac{1}{2} \left(\frac{\partial v}{\partial x} \right)^2 + \frac{1}{2} \left(\frac{\partial w}{\partial x} \right)^2 \tag{4.123}$$

and from Eq.(2.48) the variation of the strain increment

$$\delta \Delta E_x = \frac{\partial \delta v}{\partial x} \frac{\partial \Delta v}{\partial x} + \frac{\partial \delta w}{\partial x} \frac{\partial \Delta w}{\partial x} \tag{4.124}$$

Note that the variation of a linear strain increment becomes zero because of the assumption made in Eq.(2.47). Using the beam displacement expressions in Eqs.(4.2,4.3) and remembering that the relative displacement components are assumed independent of x, Eq.(4.124) converts to

$$\delta \Delta E_x = \left(\frac{d\delta v_o}{dx} - z \frac{d\delta \theta_x}{dx} \right) \left(\frac{d\Delta v_o}{dx} - z \frac{d\Delta \theta_x}{dx} \right) + \left(\frac{d\delta w_o}{dx} + y \frac{d\delta \theta_x}{dx} \right) \left(\frac{d\Delta w_o}{dx} + y \frac{d\Delta \theta_x}{dx} \right) \tag{4.125}$$

By introducing the interpolations of (v_o, w_o, θ_x) from Eqs.(4.21,4.23,4.25), respectively, $\delta\Delta E_x$ further takes the form

$$\begin{aligned}\delta\Delta E_x \;=\; & \left(\delta\boldsymbol{v}_{v_o}^T\frac{d\boldsymbol{N}_{v_o}^T}{dx} \;-\; z\,\delta\boldsymbol{v}_{\theta_x}^T\frac{d\boldsymbol{N}_{\theta_x}^T}{dx}\right)\left(\frac{d\boldsymbol{N}_{v_o}}{dx}\,\Delta\boldsymbol{v}_{v_o} \;-\; z\,\frac{d\boldsymbol{N}_{\theta_x}}{dx}\,\Delta\boldsymbol{v}_{\theta_x}\right) \\ & +\left(\delta\boldsymbol{v}_{w_o}^T\frac{d\boldsymbol{N}_{w_o}^T}{dx} \;+\; y\,\delta\boldsymbol{v}_{\theta_x}^T\frac{d\boldsymbol{N}_{\theta_x}^T}{dx}\right)\left(\frac{d\boldsymbol{N}_{w_o}}{dx}\,\Delta\boldsymbol{v}_{w_o} \;+\; y\,\frac{d\boldsymbol{N}_{\theta_x}}{dx}\,\Delta\boldsymbol{v}_{\theta_x}\right)\end{aligned} \tag{4.126}$$

Here the components of $\frac{d}{dx}\boldsymbol{N}_{\theta_x}$ are given by Eqs.(4.55,4.56), while the components of $(\frac{d}{dx}\boldsymbol{N}_{v_o}, \frac{d}{dx}\boldsymbol{N}_{w_o})$ can be found from Eqs.(4.45-4.51). However, the explicit expressions for the latters will also be given in order to make the presentation complete

$$\frac{N_{v_o}^{(v_1)}}{dx} \;=\; \frac{N_{w_o}^{(v_1)}}{dx} \;=\; -\,\frac{3}{2L_o}\,(1\,-\,\xi)\,(1\,+\,\xi) \tag{4.127}$$

$$\frac{N_{v_o}^{(\theta_1)}}{dx} \;=\; -\,\frac{N_{w_o}^{(\theta_1)}}{dx} \;=\; -\,\frac{1}{4}\,(1\,-\,\xi)\,(1\,+\,3\xi) \tag{4.128}$$

$$\frac{N_{v_o}^{(v_2)}}{dx} \;=\; \frac{N_{w_o}^{(v_2)}}{dx} \;=\; \frac{3}{2L_o}\,(1\,-\,\xi)\,(1\,+\,\xi) \tag{4.129}$$

$$\frac{N_{v_o}^{(\theta_2)}}{dx} \;=\; -\,\frac{N_{w_o}^{(\theta_2)}}{dx} \;=\; -\,\frac{1}{4}\,(1\,+\,\xi)\,(1\,-\,3\xi) \tag{4.130}$$

$$\frac{N_{v_o}^{(\tilde{\theta}_3)}}{dx} \;=\; -\,\frac{N_{w_o}^{(\tilde{\theta}_3)}}{dx} \;=\; (1\,-\,\xi)\,(1\,+\,\xi)\;-\;\frac{2}{3} \tag{4.131}$$

The stress, energy-conjugate to E_x, will be the 2nd Piola-Kirchhoff stress component S_x, which relates to the Cauchy stresses through Eq.(2.22). From the last part of this equation it is clear that the gradients contributing to S_x come from the u-displacement only, and thus they are all of infinitesimal size. Hence

$$S_x \;\approx\; \sigma_x \tag{4.132}$$

Now, insertion of Eqs.(4.126,4.132) into the first term on the left hand side of Eq.(2.51), i.e. the incremental version of the principle of virtual displacements, yields the discretized form

$$\int_{V_o}\delta\Delta\boldsymbol{e}^T\boldsymbol{s}\,dV_o \;=\; \int_{V_o}\delta\Delta E_x\,\sigma_x\,dV_o \;=\; \delta\boldsymbol{v}^T\boldsymbol{k}_g\,\Delta\boldsymbol{v} \tag{4.133}$$

where $\boldsymbol{v}$ is ordered according to Eq.(4.43) and the incremental geometric stiffness

matrix $\boldsymbol{k}_g$ of the element given by

$$\boldsymbol{k}_g \;=\; \begin{bmatrix} \mathbf{0} & \mathbf{0} & \mathbf{0} & \mathbf{0} & \mathbf{0} & \mathbf{0} \\ \mathbf{0} & \boldsymbol{k}^{(g)}_{v_o v_o} & \mathbf{0} & \boldsymbol{k}^{(g)}_{v_o \theta_x} & \mathbf{0} & \mathbf{0} \\ \mathbf{0} & \mathbf{0} & \boldsymbol{k}^{(g)}_{w_o w_o} & \boldsymbol{k}^{(g)}_{w_o \theta_x} & \mathbf{0} & \mathbf{0} \\ \mathbf{0} & \boldsymbol{k}^{(g)}_{\theta_x v_o} & \boldsymbol{k}^{(g)}_{\theta_x w_o} & \boldsymbol{k}^{(g)}_{\theta_x \theta_x} & \mathbf{0} & \mathbf{0} \\ \mathbf{0} & \mathbf{0} & \mathbf{0} & \mathbf{0} & \mathbf{0} & \mathbf{0} \\ \mathbf{0} & \mathbf{0} & \mathbf{0} & \mathbf{0} & \mathbf{0} & \mathbf{0} \end{bmatrix} \tag{4.134}$$

with the nonzero submatrices

$$\boldsymbol{k}^{(g)}_{v_o v_o} \;=\; \int_{L_o} F_x \, \frac{d\boldsymbol{N}^T_{v_o}}{dx} \, \frac{d\boldsymbol{N}_{v_o}}{dx} \, dL_o \tag{4.135}$$

$$\boldsymbol{k}^{(g)}_{v_o \theta_x} \;=\; \boldsymbol{k}^{(g)\,T}_{\theta_x v_o} \;=\; -\int_{L_o} M_y \, \frac{d\boldsymbol{N}^T_{v_o}}{dx} \, \frac{d\boldsymbol{N}_{\theta_x}}{dx} \, dL_o \tag{4.136}$$

$$\boldsymbol{k}^{(g)}_{w_o w_o} \;=\; \int_{L_o} F_x \, \frac{d\boldsymbol{N}^T_{w_o}}{dx} \, \frac{d\boldsymbol{N}_{w_o}}{dx} \, dL_o \tag{4.137}$$

$$\boldsymbol{k}^{(g)}_{w_o \theta_x} \;=\; \boldsymbol{k}^{(g)\,T}_{\theta_x w_o} \;=\; -\int_{L_o} M_z \, \frac{d\boldsymbol{N}^T_{w_o}}{dx} \, \frac{d\boldsymbol{N}_{\theta_x}}{dx} \, dL_o \tag{4.138}$$

$$\boldsymbol{k}^{(g)}_{\theta_x \theta_x} \;=\; \int_{L_o} B \, \frac{d\boldsymbol{N}^T_{\theta_x}}{dx} \, \frac{d\boldsymbol{N}_{\theta_x}}{dx} \, dL_o \tag{4.139}$$

Here the member forces (F_x, M_y, M_z) are given by Eqs.(4.72,4.76,4.77), respectively, while the new quantity B has been introduced in the expression for $\boldsymbol{k}^{(g)}_{\theta_x \theta_x}$

$$B \;=\; \int_{A_o} \left(y^2 \,+\, z^2\right) \sigma_x \, dA_o \tag{4.140}$$

Note that $\boldsymbol{k}_g$ becomes a symmetric matrix. Finally, the integrals may be solved numerically, e.g. by Gauss quadrature.

4.6 Applied Node-Force Vector

From Eq.(4.41) the variation of the displacement field $\boldsymbol{u}$ can be expressed by the interpolation formula

$$\delta \boldsymbol{u} \;=\; \boldsymbol{N} \, \delta \boldsymbol{v} \tag{4.141}$$

where the quantities involved are defined by Eqs.(4.42-4.44). With the above expression the right hand side of Eq.(2.44), that states the principle of virtual displacements, now becomes

$$\int_{V_o} \delta \boldsymbol{u}^T \boldsymbol{f}_o \, dV_o \;+\; \int_{\partial V_o} \delta \boldsymbol{u}^T \boldsymbol{t}_o \, d(\partial V_o) \;=$$

$$\delta \boldsymbol{v}^T \left(\int_{V_o} \boldsymbol{N}^T \boldsymbol{f}_o \, dV_o \, + \, \int_{\partial V_o} \boldsymbol{N}^T \boldsymbol{t}_o \, d(\partial V_o) \right) \, = \, \delta \boldsymbol{v}^T \left(\boldsymbol{p}_f \, + \, \boldsymbol{p}_t \right) \tag{4.142}$$

i.e.

$$\boldsymbol{p}_f \, = \, \int_{V_o} \boldsymbol{N}^T \boldsymbol{f}_o \, dV_o \tag{4.143}$$

$$\boldsymbol{p}_t \, = \, \int_{\partial V_o} \boldsymbol{N}^T \boldsymbol{t}_o \, d(\partial V_o) \tag{4.144}$$

which are the applied node-force vectors of the element due to body force intensity $\boldsymbol{f}_o$ and prescribed surface traction $\boldsymbol{t}_o$, respectively. Carrying out the integrand products of these expressions by using Eq.(4.44), the two kinds of applied node-forces take the unified form

$$\boldsymbol{p} \, = \, \left\{ \begin{array}{c} \boldsymbol{p}_{u_o} \\ \boldsymbol{p}_{v_o} \\ \boldsymbol{p}_{w_o} \\ \boldsymbol{p}_{\theta_x} \\ \boldsymbol{p}_{v_r} \\ \boldsymbol{p}_{w_r} \end{array} \right\} \, = \, \int_{L_o} \left\{ \begin{array}{c} q_x \, \boldsymbol{N}_{u_o}^T \\ m_z \, \boldsymbol{N}_{\theta_z}^T \, + \, q_y \, \boldsymbol{N}_{v_o}^T \\ m_y \, \boldsymbol{N}_{\theta_y}^T \, + \, q_z \, \boldsymbol{N}_{w_o}^T \\ m_x \, \boldsymbol{N}_{\theta_x}^T \\ \boldsymbol{g}_{yy} \\ \boldsymbol{g}_{zz} \end{array} \right\} dL_o \tag{4.145}$$

where $(q_x, q_y, q_z, m_x, m_y, m_z)$ are the force resultants per unit axial length of the beam, while the vectors $(\boldsymbol{g}_{yy}, \boldsymbol{g}_{zz})$ are the generalized counterparts that pertain to the strain DOFs. For the body force field these quantities read

$$\begin{aligned} q_x^{(f)} \, &= \, \int_{A_o} f_x \, dA_o \qquad ; \quad m_y^{(f)} \, = \, \int_{A_o} z f_x \, dA_o \\ q_y^{(f)} \, &= \, \int_{A_o} f_y \, dA_o \qquad ; \quad m_z^{(f)} \, = \, -\int_{A_o} y f_x \, dA_o \\ q_z^{(f)} \, &= \, \int_{A_o} f_z \, dA_o \qquad ; \quad \boldsymbol{g}_{yy}^{(f)} \, = \, \int_{A_o} f_y \boldsymbol{N}_{v_r}^T \, dA_o \\ m_x^{(f)} \, &= \, \int_{A_o} (y f_z \, - \, z f_y) \, dA_o \quad ; \quad \boldsymbol{g}_{zz}^{(f)} \, = \, \int_{A_o} f_z \boldsymbol{N}_{w_r}^T \, dA_o \end{aligned} \tag{4.146}$$

Here (f_x, f_y, f_z) are the components $\boldsymbol{f}_o$. Note that when x coincides with the centroidal axis and (y, z) follow the principal axes, all terms $(m_x^{(f)}, m_y^{(f)}, m_z^{(f)}, \boldsymbol{g}_{yy}^{(f)}, \boldsymbol{g}_{zz}^{(f)})$ vanish for a uniform body force field. The vanishing of $(\boldsymbol{g}_{yy}^{(f)}, \boldsymbol{g}_{zz}^{(f)})$ become clear by keeping in mind that the components of $(\boldsymbol{N}_{v_r}, \boldsymbol{N}_{w_r})$ consist only of linear (y, z) terms, ref. Eqs.(4.37-4.39). For the prescribed surface traction the corresponding quantities become

$$\begin{aligned} q_x^{(t)} \, &= \, \int_{S_o} t_x \, dS_o \qquad ; \quad m_y^{(t)} \, = \, \int_{S_o} z \, t_x \, dS_o \\ q_y^{(t)} \, &= \, \int_{S_o} t_y \, dS_o \qquad ; \quad m_z^{(t)} \, = \, -\int_{S_o} y \, t_x \, dS_o \\ q_z^{(t)} \, &= \, \int_{S_o} t_z \, dS_o \qquad ; \quad \boldsymbol{g}_{yy}^{(t)} \, = \, \int_{S_o} t_y \boldsymbol{N}_{v_r}^T \, dS_o \\ m_x^{(t)} \, &= \, \int_{S_o} (y \, t_z \, - \, z \, t_y) \, dS_o \quad ; \quad \boldsymbol{g}_{zz}^{(t)} \, = \, \int_{S_o} t_z \boldsymbol{N}_{w_r}^T \, dS_o \end{aligned} \tag{4.147}$$

where (t_x, t_y, t_z) are the components of $\boldsymbol{t}_o$, and (y, z) are now the corresponding coordinates at the perimeter S_o of the section.

When the applied load is specified in terms of force per unit axial length of the beam $\boldsymbol{q}_o$, the derived section force quantities are simply given by

$$\begin{aligned} m_x^{(q)} &= y_q q_z - z_q q_y \quad ; \quad \boldsymbol{g}_{yy}^{(q)} = q_y \boldsymbol{N}_{v_r}^T \\ m_y^{(q)} &= z_q q_x \quad ; \quad \boldsymbol{g}_{zz}^{(q)} = q_z \boldsymbol{N}_{w_r}^T \\ m_z^{(q)} &= -y_q q_x \end{aligned} \tag{4.148}$$

Here (q_x, q_y, q_z) are the components of $\boldsymbol{q}_o$ and (y_q, z_q) are the coordinates at the loading point. Note that these coordinates are also intervening in $(\boldsymbol{N}_{v_r}, \boldsymbol{N}_{w_r})$.

In general the integrals may be solved numerically, e.g. by Gauss quadrature. However, for the simple case of a uniform load per unit axial length (q_x^*, q_y^*, q_z^*) with uniform position along the beam (y_q^*, z_q^*), the integrals of Eq.(4.145) have been solved analytically. Introduction of the shape function expressions from Eqs.(4.28-4.39) and Eqs.(4.47-4.51) yields the final results for the subvectors of the node-force vector $\boldsymbol{p}_{q^*}$

$$\boldsymbol{p}_{u_o}^{(q^*)} = q_x^* L_o \begin{Bmatrix} \frac{1}{2} \\ \frac{1}{2} \\ \frac{2}{3} \end{Bmatrix} \quad ; \quad \boldsymbol{p}_{\theta_x}^{(q^*)} = m_x^* L_o \begin{Bmatrix} \frac{1}{2} \\ \frac{1}{2} \end{Bmatrix}$$

$$\boldsymbol{p}_{v_o}^{(q^*)} = \begin{Bmatrix} \frac{1}{2} q_y^* L_o - m_z^* \\ \frac{1}{12} q_y^* L_o^2 \\ \frac{1}{2} q_y^* L_o + m_z^* \\ -\frac{1}{12} q_y^* L_o^2 \\ \frac{2}{3} m_z^* L_o \end{Bmatrix} \quad ; \quad \boldsymbol{p}_{w_o}^{(q^*)} = \begin{Bmatrix} \frac{1}{2} q_z^* L_o + m_y^* \\ -\frac{1}{12} q_z^* L_o^2 \\ \frac{1}{2} q_z^* L_o - m_y^* \\ \frac{1}{12} q_z^* L_o^2 \\ \frac{2}{3} m_y^* L_o \end{Bmatrix} \tag{4.149}$$

$$\boldsymbol{p}_{v_r}^{(q^*)} = q_y^* L_o \begin{Bmatrix} y_q^* \\ y_q^* z_q^* \end{Bmatrix} \quad ; \quad \boldsymbol{p}_{w_r}^{(q^*)} = q_z^* L_o \begin{Bmatrix} z_q^* \\ y_q^* z_q^* \end{Bmatrix}$$

where the components of the uniform moment per unit axial length (m_x^*, m_y^*, m_z^*) are found from Eq.(4.148). The force terms of the various subvectors correspond to the ordering of DOFs given in Eqs.(4.20-4.27).

4.7 Load Correction Stiffness Matrices

4.7.1 Load Characterization

In this context two types of applied loading will be considered; unidirectional and corotational loading. For both categories, the loads are assumed attached to the body and thus will follow its deformed position. In addition, corotational loading will also change direction in accordance with the rotation of the body. Fig. 4.3 demonstrates the two categories of loading for a body going from deformed configuration C_n to C_{n+1}.

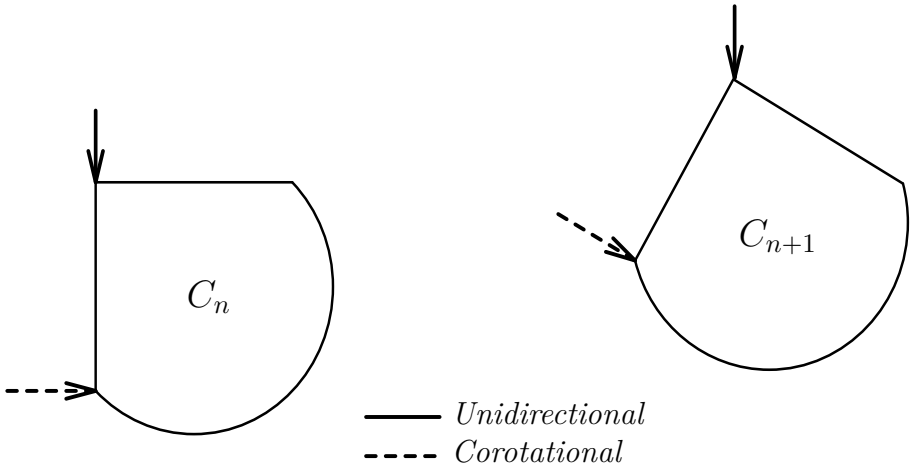

Figure 4.3: Unidirectional versus Corotational Loading

Note that both types of load are assumed to be so-called *body attached*, i.e. their magnitude is independent of the current position in space (as opposed to *space attached*) [5].

4.7.2 Corotational Load Stiffness Matrix

Eqs.(4.41-4.44) define the interpolation of the displacement field $\boldsymbol{u}$ of the element. A similar interpolation can be established for the augmented displacement field $\boldsymbol{u}_a$ where also rotations are included. Thus

$$\boldsymbol{u}_a \;=\; \boldsymbol{N}_a\, \boldsymbol{v} \tag{4.150}$$

where the new quantities are

$$\boldsymbol{u}_a^T \;=\; \left[\begin{array}{cccccc} u & v & w & \theta_x & \theta_y & \theta_z \end{array}\right] \tag{4.151}$$

$$\boldsymbol{N}_a \;=\; \left[\begin{array}{cccccc} \boldsymbol{N}_{u_o} & -y\boldsymbol{N}_{\theta_z} & z\boldsymbol{N}_{\theta_y} & \boldsymbol{0} & \boldsymbol{0} & \boldsymbol{0} \\ \boldsymbol{0} & \boldsymbol{N}_{v_o} & \boldsymbol{0} & -z\boldsymbol{N}_{\theta_x} & \boldsymbol{N}_{v_r} & \boldsymbol{0} \\ \boldsymbol{0} & \boldsymbol{0} & \boldsymbol{N}_{w_o} & y\boldsymbol{N}_{\theta_x} & \boldsymbol{0} & \boldsymbol{N}_{w_r} \\ \boldsymbol{0} & \boldsymbol{0} & \boldsymbol{0} & \boldsymbol{N}_{\theta_x} & \boldsymbol{0} & \boldsymbol{0} \\ \boldsymbol{0} & \boldsymbol{0} & \boldsymbol{N}_{\theta_y} & \boldsymbol{0} & \boldsymbol{0} & \boldsymbol{0} \\ \boldsymbol{0} & \boldsymbol{N}_{\theta_z} & \boldsymbol{0} & \boldsymbol{0} & \boldsymbol{0} & \boldsymbol{0} \end{array}\right] \tag{4.152}$$

and $\boldsymbol{v}$ remains as in Eq.(4.43). Then the increment and variation of the augmented displacement field, respectively, become

$$\Delta\boldsymbol{u}_a \;=\; \boldsymbol{N}_a\,\Delta\boldsymbol{v} \tag{4.153}$$

$$\delta\boldsymbol{u}_a \;=\; \boldsymbol{N}_a\,\delta\boldsymbol{v} \tag{4.154}$$

The augmented body force intensity vector reads

$$\boldsymbol{f}_{oa}^T \;=\; \left[\begin{array}{cccccc} f_x & f_y & f_z & \nu_x & \nu_y & \nu_z \end{array}\right] \tag{4.155}$$

where (ν_x, ν_y, ν_z) are the local body force moment intensities that are zero prior to the incremental action. The similar expression for the augmented prescribed surface traction vector is

$$\boldsymbol{t}_{oa}^T \;=\; \left[\begin{array}{cccccc} t_x & t_y & t_z & \mu_x & \mu_y & \mu_z \end{array}\right] \tag{4.156}$$

where (μ_x, μ_y, μ_z) are the local traction moment intensities that also are zero prior to the incremental action.

Assuming corotational loading and small rotations, the increments of augmented body forces and surface tractions can be connected to the increments of augmented displacements through the relations

$$\Delta\boldsymbol{f}_{oa}^{(c)} \;\approx\; \left\{\begin{array}{c} f_z\,\Delta\theta_y \;-\; f_y\,\Delta\theta_z \\ -f_z\,\Delta\theta_x \;+\; f_x\,\Delta\theta_z \\ f_y\,\Delta\theta_x \;-\; f_x\,\Delta\theta_y \\ f_z\,\Delta v \;-\; f_y\,\Delta w \\ -f_z\,\Delta u \;+\; f_x\,\Delta w \\ f_y\,\Delta u \;-\; f_x\,\Delta v \end{array}\right\} \;=\; \boldsymbol{F}_c\,\Delta\boldsymbol{u}_a \tag{4.157}$$

$$\Delta \boldsymbol{t}_{oa}^{(c)} \approx \left\{ \begin{array}{c} t_z\,\Delta\theta_y - t_y\,\Delta\theta_z \\ -t_z\,\Delta\theta_x + t_x\,\Delta\theta_z \\ t_y\,\Delta\theta_x - t_x\,\Delta\theta_y \\ t_z\,\Delta v - t_y\,\Delta w \\ -t_z\,\Delta u + t_x\,\Delta w \\ t_y\,\Delta u - t_x\,\Delta v \end{array} \right\} = \boldsymbol{T}_c\,\Delta \boldsymbol{u}_a \tag{4.158}$$

thus

$$\boldsymbol{F}_c = \begin{bmatrix} 0 & 0 & 0 & 0 & f_z & -f_y \\ 0 & 0 & 0 & -f_z & 0 & f_x \\ 0 & 0 & 0 & f_y & -f_x & 0 \\ 0 & f_z & -f_y & 0 & 0 & 0 \\ -f_z & 0 & f_x & 0 & 0 & 0 \\ f_y & -f_x & 0 & 0 & 0 & 0 \end{bmatrix} \tag{4.159}$$

$$\boldsymbol{T}_c = \begin{bmatrix} 0 & 0 & 0 & 0 & t_z & -t_y \\ 0 & 0 & 0 & -t_z & 0 & t_x \\ 0 & 0 & 0 & t_y & -t_x & 0 \\ 0 & t_z & -t_y & 0 & 0 & 0 \\ -t_z & 0 & t_x & 0 & 0 & 0 \\ t_y & -t_x & 0 & 0 & 0 & 0 \end{bmatrix} \tag{4.160}$$

Now, insertion of Eqs.(4.153,4.154,4.157,4.158) into the second terms on the right hand side of Eqs.(2.52,2.53), that constitute the incremental virtual work contributions from body force and surface traction, yields

$$\int_{V_o} \delta \boldsymbol{u}_a^T \Delta \boldsymbol{f}_{oa}^{(c)}\, dV_o + \int_{\partial V_o} \delta \boldsymbol{u}_a^T \Delta \boldsymbol{t}_{oa}^{(c)}\, d(\partial V_o) =$$

$$\delta \boldsymbol{v}^T \left(\int_{V_o} \boldsymbol{N}_a^T \boldsymbol{F}_c\, \boldsymbol{N}_a\, dV_o + \int_{\partial V_o} \boldsymbol{N}_a^T \boldsymbol{T}_c\, \boldsymbol{N}_a\, d(\partial V_o) \right) \Delta \boldsymbol{v} =$$

$$\delta \boldsymbol{v}^T \left(\boldsymbol{k}_{lc}^{(f)} + \boldsymbol{k}_{lc}^{(t)} \right) \Delta \boldsymbol{v} \tag{4.161}$$

i.e.

$$\boldsymbol{k}_{lc}^{(f)} = \int_{V_o} \boldsymbol{N}_a^T \boldsymbol{F}_c\, \boldsymbol{N}_a\, dV_o \tag{4.162}$$

$$\boldsymbol{k}_{lc}^{(t)} = \int_{\partial V_o} \boldsymbol{N}_a^T \boldsymbol{T}_c\, \boldsymbol{N}_a\, d(\partial V_o) \tag{4.163}$$

which are the incremental load stiffness matrices of the element due to corotational body force and surface traction, respectively. Carrying out the integrand products of these expressions by using Eqs.(4.152,4.159,4.160), the two kinds of corotational load stiffnesses take the unified form

$$\boldsymbol{k}_{lc} = \begin{bmatrix} \mathbf{0} & \boldsymbol{k}^{(lc)}_{u_o v_o} & \boldsymbol{k}^{(lc)}_{u_o w_o} & \mathbf{0} & \mathbf{0} & \mathbf{0} \\ \boldsymbol{k}^{(lc)}_{v_o u_o} & \boldsymbol{k}^{(lc)}_{v_o v_o} & \boldsymbol{k}^{(lc)}_{v_o w_o} & \boldsymbol{k}^{(lc)}_{v_o \theta_x} & \boldsymbol{k}^{(lc)}_{v_o v_r} & \mathbf{0} \\ \boldsymbol{k}^{(lc)}_{w_o u_o} & \boldsymbol{k}^{(lc)}_{w_o v_o} & \boldsymbol{k}^{(lc)}_{w_o w_o} & \boldsymbol{k}^{(lc)}_{w_o \theta_x} & \mathbf{0} & \boldsymbol{k}^{(lc)}_{w_o w_r} \\ \mathbf{0} & \boldsymbol{k}^{(lc)}_{\theta_x v_o} & \boldsymbol{k}^{(lc)}_{\theta_x w_o} & \mathbf{0} & \boldsymbol{k}^{(lc)}_{\theta_x v_r} & \boldsymbol{k}^{(lc)}_{\theta_x w_r} \\ \mathbf{0} & \boldsymbol{k}^{(lc)}_{v_r v_o} & \mathbf{0} & \boldsymbol{k}^{(lc)}_{v_r \theta_x} & \mathbf{0} & \mathbf{0} \\ \mathbf{0} & \mathbf{0} & \boldsymbol{k}^{(lc)}_{w_r w_o} & \boldsymbol{k}^{(lc)}_{w_r \theta_x} & \mathbf{0} & \mathbf{0} \end{bmatrix} \tag{4.164}$$

with the nonzero submatrices

$$\boldsymbol{k}^{(lc)}_{u_o v_o} = -\boldsymbol{k}^{(lc)\,T}_{v_o u_o} = -\int_{L_o} q_y \, \boldsymbol{N}^T_{u_o} \, \boldsymbol{N}_{\theta_z} \, dL_o \tag{4.165}$$

$$\boldsymbol{k}^{(lc)}_{u_o w_o} = -\boldsymbol{k}^{(lc)\,T}_{w_o u_o} = \int_{L_o} q_z \, \boldsymbol{N}^T_{u_o} \, \boldsymbol{N}_{\theta_y} \, dL_o \tag{4.166}$$

$$\boldsymbol{k}^{(lc)}_{v_o v_o} = \int_{L_o} q_x \left(\boldsymbol{N}^T_{v_o} \, \boldsymbol{N}_{\theta_z} - \boldsymbol{N}^T_{\theta_z} \, \boldsymbol{N}_{v_o} \right) dL_o \tag{4.167}$$

$$\boldsymbol{k}^{(lc)}_{v_o w_o} = -\boldsymbol{k}^{(lc)\,T}_{w_o v_o} = -\int_{L_o} m_x \, \boldsymbol{N}^T_{\theta_z} \, \boldsymbol{N}_{\theta_y} \, dL_o \tag{4.168}$$

$$\boldsymbol{k}^{(lc)}_{v_o \theta_x} = -\boldsymbol{k}^{(lc)\,T}_{\theta_x v_o} = \int_{L_o} \left(m_y \, \boldsymbol{N}^T_{\theta_z} \, \boldsymbol{N}_{\theta_x} - q_z \, \boldsymbol{N}^T_{v_o} \, \boldsymbol{N}_{\theta_x} \right) dL_o \tag{4.169}$$

$$\boldsymbol{k}^{(lc)}_{v_o v_r} = -\boldsymbol{k}^{(lc)\,T}_{v_r v_o} = -\int_{L_o} \boldsymbol{N}^T_{\theta_z} \, \boldsymbol{g}^T_{xy} \, dL_o \tag{4.170}$$

$$\boldsymbol{k}^{(lc)}_{w_o w_o} = -\int_{L_o} q_x \left(\boldsymbol{N}^T_{w_o} \, \boldsymbol{N}_{\theta_y} - \boldsymbol{N}^T_{\theta_y} \, \boldsymbol{N}_{w_o} \right) dL_o \tag{4.171}$$

$$\boldsymbol{k}^{(lc)}_{w_o \theta_x} = -\boldsymbol{k}^{(lc)\,T}_{\theta_x w_o} = -\int_{L_o} \left(m_z \, \boldsymbol{N}^T_{\theta_y} \, \boldsymbol{N}_{\theta_x} - q_y \, \boldsymbol{N}^T_{w_o} \, \boldsymbol{N}_{\theta_x} \right) dL_o \tag{4.172}$$

$$\boldsymbol{k}^{(lc)}_{w_o w_r} = -\boldsymbol{k}^{(lc)\,T}_{w_r w_o} = \int_{L_o} \boldsymbol{N}^T_{\theta_y} \, \boldsymbol{g}^T_{xz} \, dL_o \tag{4.173}$$

$$\boldsymbol{k}^{(lc)}_{\theta_x v_r} = -\boldsymbol{k}^{(lc)\,T}_{v_r \theta_x} = \int_{L_o} \boldsymbol{N}^T_{\theta_x} \, \boldsymbol{g}^T_{zy} \, dL_o \tag{4.174}$$

$$\boldsymbol{k}^{(lc)}_{\theta_x w_r} = -\boldsymbol{k}^{(lc)\,T}_{w_r \theta_x} = -\int_{L_o} \boldsymbol{N}^T_{\theta_x} \, \boldsymbol{g}^T_{yz} \, dL_o \tag{4.175}$$

Here the force resultants per unit axial length of the beam $(q_x, q_y, q_z, m_x, m_y, m_z)$ are given by Eqs.(4.146,4.147) for body force and surface traction, respectively. When the applied load is specified in terms of (q_x, q_y, q_z), Eq.(4.148) yields the corresponding moments. The column vectors of generalized force quantities $(\boldsymbol{g}_{xy}, \boldsymbol{g}_{xz}, \boldsymbol{g}_{yz}, \boldsymbol{g}_{zy})$ that pertain to the strain DOFs, are on the other hand new. For the body force field these

are given by

$$\begin{aligned} \boldsymbol{g}_{xy}^{(f)} &= \int_{A_o} f_x \boldsymbol{N}_{v_r}^T \, dA_o \quad ; \quad \boldsymbol{g}_{yz}^{(f)} = \int_{A_o} f_y \boldsymbol{N}_{w_r}^T \, dA_o \\ \boldsymbol{g}_{xz}^{(f)} &= \int_{A_o} f_x \boldsymbol{N}_{w_r}^T \, dA_o \quad ; \quad \boldsymbol{g}_{zy}^{(f)} = \int_{A_o} f_z \boldsymbol{N}_{v_r}^T \, dA_o \end{aligned} \tag{4.176}$$

while for the surface traction they read

$$\begin{aligned} \boldsymbol{g}_{xy}^{(t)} &= \int_{S_o} t_x \boldsymbol{N}_{v_r}^T \, dS_o \quad ; \quad \boldsymbol{g}_{yz}^{(t)} = \int_{S_o} t_y \boldsymbol{N}_{w_r}^T \, dS_o \\ \boldsymbol{g}_{xz}^{(t)} &= \int_{S_o} t_x \boldsymbol{N}_{w_r}^T \, dS_o \quad ; \quad \boldsymbol{g}_{zy}^{(t)} = \int_{S_o} t_z \boldsymbol{N}_{v_r}^T \, dS_o \end{aligned} \tag{4.177}$$

and in terms of specified force per unit axial length

$$\begin{aligned} \boldsymbol{g}_{xy}^{(q)} &= q_x \boldsymbol{N}_{v_r}^T \quad ; \quad \boldsymbol{g}_{yz}^{(q)} = q_y \boldsymbol{N}_{w_r}^T \\ \boldsymbol{g}_{xz}^{(q)} &= q_x \boldsymbol{N}_{w_r}^T \quad ; \quad \boldsymbol{g}_{zy}^{(q)} = q_z \boldsymbol{N}_{v_r}^T \end{aligned} \tag{4.178}$$

As becomes evident from Eqs.(4.164-4.175), the corotational load stiffness matrix $\boldsymbol{k}_{lc}$ takes a completely skewsymmetric form.

So far, the expressions derived in this subsection are based on a fixed reference frame for the incremental action. In the Corotated Lagrangian (CL) description of motion, however, the local reference system is attached to node 1 and moves along with the element (Subsection 5.1.3). This implies that rigid body translations will be eliminated, while rigid body rotations are taken care of through the transformation of element quantities to the global reference system (Subsection 5.2.1). Consequently, to comply with the CL-formulation, load corrections due to incremental rigid body translations $\Delta \boldsymbol{v}_{rt}$ must be extracted from the stiffness equations, i.e.

$$\Delta \boldsymbol{p}_c^{(CL)} = \boldsymbol{k}_{lc} \left(\Delta \boldsymbol{v} - \Delta \boldsymbol{v}_{rt} \right) \tag{4.179}$$

Here the only nonzero entries of $\Delta \boldsymbol{v}_{rt}$ are the equal incremental translations at the two endnodes where the values of node 1 are transferred to node 2. The incremental nodal displacements in excess of the rigid body translations may then again be related to the original nodal increments that refer to the fixed reference frame, through the relation

$$\Delta \boldsymbol{v} - \Delta \boldsymbol{v}_{rt} = \boldsymbol{d} \, \Delta \boldsymbol{v} \tag{4.180}$$

With ordering of DOFs according to Eq.(4.43), the new displacement conversion matrix $\boldsymbol{d}$ takes the form

$$\boldsymbol{d} = \begin{bmatrix} \boldsymbol{d}_{u_o} & \boldsymbol{0} & \boldsymbol{0} & \boldsymbol{0} & \boldsymbol{0} & \boldsymbol{0} \\ \boldsymbol{0} & \boldsymbol{d}_{v_o} & \boldsymbol{0} & \boldsymbol{0} & \boldsymbol{0} & \boldsymbol{0} \\ \boldsymbol{0} & \boldsymbol{0} & \boldsymbol{d}_{w_o} & \boldsymbol{0} & \boldsymbol{0} & \boldsymbol{0} \\ \boldsymbol{0} & \boldsymbol{0} & \boldsymbol{0} & \boldsymbol{d}_{\theta_x} & \boldsymbol{0} & \boldsymbol{0} \\ \boldsymbol{0} & \boldsymbol{0} & \boldsymbol{0} & \boldsymbol{0} & \boldsymbol{d}_{v_r} & \boldsymbol{0} \\ \boldsymbol{0} & \boldsymbol{0} & \boldsymbol{0} & \boldsymbol{0} & \boldsymbol{0} & \boldsymbol{d}_{w_r} \end{bmatrix} \tag{4.181}$$

where

$$\boldsymbol{d}_{u_o} = \begin{bmatrix} 0 & 0 & 0 \\ -1 & 1 & 0 \\ 0 & 0 & 1 \end{bmatrix} \tag{4.182}$$

$$\boldsymbol{d}_{v_o} = \boldsymbol{d}_{w_o} = \begin{bmatrix} 0 & 0 & 0 & 0 & 0 \\ 0 & 1 & 0 & 0 & 0 \\ -1 & 0 & 1 & 0 & 0 \\ 0 & 0 & 0 & 1 & 0 \\ 0 & 0 & 0 & 0 & 1 \end{bmatrix} \tag{4.183}$$

$$\boldsymbol{d}_{\theta_x} = \boldsymbol{d}_{v_r} = \boldsymbol{d}_{w_r} = \begin{bmatrix} 1 & 0 \\ 0 & 1 \end{bmatrix} \tag{4.184}$$

By combining Eqs.(4.179,4.180) the corrections of corotational node-forces in a CL-formulation due to incremental nodal displacements now become

$$\Delta \boldsymbol{p}_c^{(CL)} = \boldsymbol{k}_{lc}^{(CL)} \, \Delta \boldsymbol{v} \tag{4.185}$$

with the corotational load stiffness matrix expressed through the product

$$\boldsymbol{k}_{lc}^{(CL)} = \boldsymbol{k}_{lc} \, \boldsymbol{d} \tag{4.186}$$

Here $(\boldsymbol{k}_{lc}, \boldsymbol{d})$ are given by Eqs.(4.164,4.181), respectively. Then by carrying out the matrix product, $\boldsymbol{k}_{lc}^{(CL)}$ takes the final form

$$\boldsymbol{k}_{lc}^{(CL)} = \begin{bmatrix} \mathbf{0} & \boldsymbol{k}_{u_o v_o}^{(lc)} \boldsymbol{d}_{v_o} & \boldsymbol{k}_{u_o w_o}^{(lc)} \boldsymbol{d}_{w_o} & \mathbf{0} & \mathbf{0} & \mathbf{0} \\ \boldsymbol{k}_{v_o u_o}^{(lc)} \boldsymbol{d}_{u_o} & \boldsymbol{k}_{v_o v_o}^{(lc)} \boldsymbol{d}_{v_o} & \boldsymbol{k}_{v_o w_o}^{(lc)} \boldsymbol{d}_{w_o} & \boldsymbol{k}_{v_o \theta_x}^{(lc)} & \boldsymbol{k}_{v_o v_r}^{(lc)} & \mathbf{0} \\ \boldsymbol{k}_{w_o u_o}^{(lc)} \boldsymbol{d}_{u_o} & \boldsymbol{k}_{w_o v_o}^{(lc)} \boldsymbol{d}_{v_o} & \boldsymbol{k}_{w_o w_o}^{(lc)} \boldsymbol{d}_{w_o} & \boldsymbol{k}_{w_o \theta_x}^{(lc)} & \mathbf{0} & \boldsymbol{k}_{w_o w_r}^{(lc)} \\ \mathbf{0} & \boldsymbol{k}_{\theta_x v_o}^{(lc)} \boldsymbol{d}_{v_o} & \boldsymbol{k}_{\theta_x w_o}^{(lc)} \boldsymbol{d}_{w_o} & \mathbf{0} & \boldsymbol{k}_{\theta_x v_r}^{(lc)} & \boldsymbol{k}_{\theta_x w_r}^{(lc)} \\ \mathbf{0} & \boldsymbol{k}_{v_r v_o}^{(lc)} \boldsymbol{d}_{v_o} & \mathbf{0} & \boldsymbol{k}_{v_r \theta_x}^{(lc)} & \mathbf{0} & \mathbf{0} \\ \mathbf{0} & \mathbf{0} & \boldsymbol{k}_{w_r w_o}^{(lc)} \boldsymbol{d}_{w_o} & \boldsymbol{k}_{w_r \theta_x}^{(lc)} & \mathbf{0} & \mathbf{0} \end{bmatrix} \tag{4.187}$$

where the individual submatrices are expressed by Eqs.(4.165-4.175,4.182,4.183). In other words, $\boldsymbol{k}_{lc}^{(CL)}$ is obtained from $\boldsymbol{k}_{lc}$ by replacing the columns pertaining to incremental translations of node 1 with the corresponding columns of node 2, but with opposite sign. Consequently, the completely skewsymmetric form of $\boldsymbol{k}_{lc}$ will be lost when converting to $\boldsymbol{k}_{lc}^{(CL)}$. Finally note that since $\boldsymbol{k}_{lc}^{(CL)}$ arises from the right hand side of the incremental virtual work principle in Eq.(2.51), it will contribute to the

resulting stiffness matrix of the element with negative sign compared to the preceding expressions. Again, the integrals may be solved numerically, e.g. by Gauss quadrature.

4.7.3 Unidirectional Load Stiffness Matrix

The derivation of the load correction stiffness matrix for unidirectional loading may follow exactly the same steps as for corotational loading. The expressions differ in the way increments of augmented body forces and surface tractions are connected to increments of augmented displacements. Compared to the expressions for corotational loading in Eqs.(4.157,4.158), the first three relations of each equation now vanish since the loading does not change in direction. The last three relations, however, that originate from the change in load position, survive. Thus, for unidirectional loading

$$\Delta \boldsymbol{f}_{oa}^{(u)} \;=\; \boldsymbol{F}_u \, \Delta \boldsymbol{u}_a \tag{4.188}$$

$$\Delta \boldsymbol{t}_{oa}^{(u)} \;=\; \boldsymbol{T}_u \, \Delta \boldsymbol{u}_a \tag{4.189}$$

where

$$\boldsymbol{F}_u \;=\; \begin{bmatrix} 0 & 0 & 0 & 0 & 0 & 0 \\ 0 & 0 & 0 & 0 & 0 & 0 \\ 0 & 0 & 0 & 0 & 0 & 0 \\ 0 & f_z & -f_y & 0 & 0 & 0 \\ -f_z & 0 & f_x & 0 & 0 & 0 \\ f_y & -f_x & 0 & 0 & 0 & 0 \end{bmatrix} \tag{4.190}$$

$$\boldsymbol{T}_u \;=\; \begin{bmatrix} 0 & 0 & 0 & 0 & 0 & 0 \\ 0 & 0 & 0 & 0 & 0 & 0 \\ 0 & 0 & 0 & 0 & 0 & 0 \\ 0 & t_z & -t_y & 0 & 0 & 0 \\ -t_z & 0 & t_x & 0 & 0 & 0 \\ t_y & -t_x & 0 & 0 & 0 & 0 \end{bmatrix} \tag{4.191}$$

Then the new expressions for incremental load stiffness matrices of the element, similar to Eqs.(4.162,4.163), now become

$$\boldsymbol{k}_{lu}^{(f)} \;=\; \int_{V_o} \boldsymbol{N}_a^T \boldsymbol{F}_u \, \boldsymbol{N}_a \, dV_o \tag{4.192}$$

$$\boldsymbol{k}_{lu}^{(t)} \;=\; \int_{\partial V_o} \boldsymbol{N}_a^T \boldsymbol{T}_u \, \boldsymbol{N}_a \, d(\partial V_o) \tag{4.193}$$

which are due to unidirectional body force and surface traction, respectively. Carrying out the integrand products of these expressions by using Eqs.(4.152,4.190,4.191), the two kinds of unidirectional load stiffnesses take the unified form

$$\boldsymbol{k}_{lu} = \begin{bmatrix} \mathbf{0} & \mathbf{0} & \mathbf{0} & \mathbf{0} & \mathbf{0} & \mathbf{0} \\ \boldsymbol{k}^{(lu)}_{v_o u_o} & \boldsymbol{k}^{(lu)}_{v_o v_o} & \boldsymbol{k}^{(lu)}_{v_o w_o} & \boldsymbol{k}^{(lu)}_{v_o \theta_x} & \boldsymbol{k}^{(lu)}_{v_o v_r} & \mathbf{0} \\ \boldsymbol{k}^{(lu)}_{w_o u_o} & \boldsymbol{k}^{(lu)}_{w_o v_o} & \boldsymbol{k}^{(lu)}_{w_o w_o} & \boldsymbol{k}^{(lu)}_{w_o \theta_x} & \mathbf{0} & \boldsymbol{k}^{(lu)}_{w_o w_r} \\ \mathbf{0} & \boldsymbol{k}^{(lu)}_{\theta_x v_o} & \boldsymbol{k}^{(lu)}_{\theta_x w_o} & \boldsymbol{k}^{(lu)}_{\theta_x \theta_x} & \boldsymbol{k}^{(lu)}_{\theta_x v_r} & \boldsymbol{k}^{(lu)}_{\theta_x w_r} \\ \mathbf{0} & \mathbf{0} & \mathbf{0} & \mathbf{0} & \mathbf{0} & \mathbf{0} \\ \mathbf{0} & \mathbf{0} & \mathbf{0} & \mathbf{0} & \mathbf{0} & \mathbf{0} \end{bmatrix} \tag{4.194}$$

with the nonzero submatrices

$$\boldsymbol{k}^{(lu)}_{v_o u_o} = \int_{L_o} q_y \, \boldsymbol{N}^T_{\theta_z} \, \boldsymbol{N}_{u_o} \, dL_o \tag{4.195}$$

$$\boldsymbol{k}^{(lu)}_{v_o v_o} = -\int_{L_o} \left(g_{yy} \, \boldsymbol{N}^T_{\theta_z} \, \boldsymbol{N}_{\theta_z} + q_x \, \boldsymbol{N}^T_{\theta_z} \, \boldsymbol{N}_{v_o} \right) dL_o \tag{4.196}$$

$$\boldsymbol{k}^{(lu)}_{v_o w_o} = -\int_{L_o} m_{x2} \, \boldsymbol{N}^T_{\theta_z} \, \boldsymbol{N}_{\theta_y} \, dL_o \tag{4.197}$$

$$\boldsymbol{k}^{(lu)}_{v_o \theta_x} = \int_{L_o} m_y \, \boldsymbol{N}^T_{\theta_z} \, \boldsymbol{N}_{\theta_x} \, dL_o \tag{4.198}$$

$$\boldsymbol{k}^{(lu)}_{v_o v_r} = -\int_{L_o} \boldsymbol{N}^T_{\theta_z} \, \boldsymbol{g}^T_{xy} \, dL_o \tag{4.199}$$

$$\boldsymbol{k}^{(lu)}_{w_o u_o} = -\int_{L_o} q_z \, \boldsymbol{N}^T_{\theta_y} \, \boldsymbol{N}_{u_o} \, dL_o \tag{4.200}$$

$$\boldsymbol{k}^{(lu)}_{w_o v_o} = \int_{L_o} m_{x1} \, \boldsymbol{N}^T_{\theta_y} \, \boldsymbol{N}_{\theta_z} \, dL_o \tag{4.201}$$

$$\boldsymbol{k}^{(lu)}_{w_o w_o} = -\int_{L_o} \left(g_{zz} \, \boldsymbol{N}^T_{\theta_y} \, \boldsymbol{N}_{\theta_y} - q_x \, \boldsymbol{N}^T_{\theta_y} \, \boldsymbol{N}_{w_o} \right) dL_o \tag{4.202}$$

$$\boldsymbol{k}^{(lu)}_{w_o \theta_x} = -\int_{L_o} m_z \, \boldsymbol{N}^T_{\theta_y} \, \boldsymbol{N}_{\theta_x} \, dL_o \tag{4.203}$$

$$\boldsymbol{k}^{(lu)}_{w_o w_r} = \int_{L_o} \boldsymbol{N}^T_{\theta_y} \, \boldsymbol{g}^T_{xz} \, dL_o \tag{4.204}$$

$$\boldsymbol{k}^{(lu)}_{\theta_x v_o} = \int_{L_o} q_z \, \boldsymbol{N}^T_{\theta_x} \, \boldsymbol{N}_{v_o} \, dL_o \tag{4.205}$$

$$\boldsymbol{k}^{(lu)}_{\theta_x w_o} = -\int_{L_o} q_y \, \boldsymbol{N}^T_{\theta_x} \, \boldsymbol{N}_{w_o} \, dL_o \tag{4.206}$$

$$\boldsymbol{k}^{(lu)}_{\theta_x \theta_x} = -\int_{L_o} (g_{yy} + g_{zz}) \, \boldsymbol{N}^T_{\theta_x} \, \boldsymbol{N}_{\theta_x} \, dL_o \tag{4.207}$$

$$\boldsymbol{k}^{(lu)}_{\theta_x v_r} = \int_{L_o} \boldsymbol{N}^T_{\theta_x} \, \boldsymbol{g}^T_{zy} \, dL_o \tag{4.208}$$

$$\boldsymbol{k}^{(lu)}_{\theta_x w_r} = -\int_{L_o} \boldsymbol{N}^T_{\theta_x} \, \boldsymbol{g}^T_{yz} \, dL_o \tag{4.209}$$

Here again the force resultants per unit axial length of the beam $(q_x, q_y, q_z, m_y, m_z)$ are given by Eqs.(4.146,4.147) for body force and surface traction, respectively. When the applied load is specified in terms of (q_x, q_y, q_z), Eq.(4.148) yields the corresponding moments (m_y, m_z). Furthermore, the column vectors of generalized force quantities $(\boldsymbol{g}_{xy}, \boldsymbol{g}_{xz}, \boldsymbol{g}_{yz}, \boldsymbol{g}_{zy})$ are given by Eqs.(4.176-4.178) for the three mentioned kinds of applied loading. Finally, the new quantities are $(m_{x1}, m_{x2}, g_{yy}, g_{zz})$. For the body force field these are defined by

$$\begin{aligned} m_{x1}^{(f)} &= \int_{A_o} y f_z \, dA_o \quad ; \quad g_{yy}^{(f)} = \int_{A_o} y f_y \, dA_o \\ m_{x2}^{(f)} &= -\int_{A_o} z f_y \, dA_o \quad ; \quad g_{zz}^{(f)} = \int_{A_o} z f_z \, dA_o \end{aligned} \tag{4.210}$$

while for the surface traction they read

$$\begin{aligned} m_{x1}^{(t)} &= \int_{S_o} y \, t_z \, dS_o \quad ; \quad g_{yy}^{(t)} = \int_{S_o} y \, t_y \, dS_o \\ m_{x2}^{(t)} &= -\int_{S_o} z \, t_y \, dS_o \quad ; \quad g_{zz}^{(t)} = \int_{S_o} z \, t_z \, dS_o \end{aligned} \tag{4.211}$$

and in terms of specified force per unit axial length

$$\begin{aligned} m_{x1}^{(q)} &= y_q q_z \quad ; \quad g_{yy}^{(q)} = y_q q_y \\ m_{x2}^{(q)} &= -z_q q_y \quad ; \quad g_{zz}^{(q)} = z_q q_z \end{aligned} \tag{4.212}$$

Thus, the resulting twisting moment m_x is now split into the two separate terms (m_{x1}, m_{x2}). Note also that (g_{yy}, g_{zz}) in fact are the first entries of $(\boldsymbol{g}_{yy}, \boldsymbol{g}_{zz})$, respectively, that appear in Eq.(4.145).

Like corotational loading, also corrections of unidirectional node-forces due to incremental rigid body translations must be eliminated to comply with the CL-description of motion. Thus, similar to Eq.(4.185), the adjusted relationship now becomes

$$\Delta \boldsymbol{p}_u^{(CL)} = \boldsymbol{k}_{lu}^{(CL)} \, \Delta \boldsymbol{v} \tag{4.213}$$

where

$$\boldsymbol{k}_{lu}^{(CL)} = \boldsymbol{k}_{lu} \, \boldsymbol{d} \tag{4.214}$$

Here $(\boldsymbol{k}_{lu}, \boldsymbol{d})$ are given by Eqs.(4.194,4.181), respectively. By carrying out the matrix product, $\boldsymbol{k}_{lu}^{(CL)}$ takes the final form

$$\boldsymbol{k}_{lu}^{(CL)} = \begin{bmatrix} \mathbf{0} & \mathbf{0} & \mathbf{0} & \mathbf{0} & \mathbf{0} & \mathbf{0} \\ \boldsymbol{k}_{v_o u_o}^{(lu)} \boldsymbol{d}_{u_o} & \boldsymbol{k}_{v_o v_o}^{(lu)} \boldsymbol{d}_{v_o} & \boldsymbol{k}_{v_o w_o}^{(lu)} \boldsymbol{d}_{w_o} & \boldsymbol{k}_{v_o \theta_x}^{(lu)} & \boldsymbol{k}_{v_o v_r}^{(lu)} & \mathbf{0} \\ \boldsymbol{k}_{w_o u_o}^{(lu)} \boldsymbol{d}_{u_o} & \boldsymbol{k}_{w_o v_o}^{(lu)} \boldsymbol{d}_{v_o} & \boldsymbol{k}_{w_o w_o}^{(lu)} \boldsymbol{d}_{w_o} & \boldsymbol{k}_{w_o \theta_x}^{(lu)} & \mathbf{0} & \boldsymbol{k}_{w_o w_r}^{(lu)} \\ \mathbf{0} & \boldsymbol{k}_{\theta_x v_o}^{(lu)} \boldsymbol{d}_{v_o} & \boldsymbol{k}_{\theta_x w_o}^{(lu)} \boldsymbol{d}_{w_o} & \boldsymbol{k}_{\theta_x \theta_x}^{(lu)} & \boldsymbol{k}_{\theta_x v_r}^{(lu)} & \boldsymbol{k}_{\theta_x w_r}^{(lu)} \\ \mathbf{0} & \mathbf{0} & \mathbf{0} & \mathbf{0} & \mathbf{0} & \mathbf{0} \\ \mathbf{0} & \mathbf{0} & \mathbf{0} & \mathbf{0} & \mathbf{0} & \mathbf{0} \end{bmatrix} \tag{4.215}$$

where the individual submatrices are expressed by Eqs.(4.195-4.209,4.182,4.183). Again in other words, $\boldsymbol{k}_{lu}^{(CL)}$ is obtained from $\boldsymbol{k}_{lu}$ by replacing the columns pertaining to incremental translations of node 1 with the corresponding columns of node 2, but with opposite sign. Evidently, the derived unidirectional load stiffness matrix takes a non-symmetric form. Like corotational loading, also $\boldsymbol{k}_{lu}^{(CL)}$ will contribute to the resulting stiffness matrix of the element with negative sign compared to the preceding expressions. Finally, the integrals may be solved numerically, e.g. by Gauss quadrature.

4.8 Elimination of Internal DOFs

So far in this chapter, the individual terms of Eqs.(2.44,2.51), that state the principle of virtual displacements on total and incremental forms, respectively, have been adopted to arrive at the final element quantities. Combination of these results yields the corresponding equilibrium equations of the element.

The total form of the equilibrium equations arises from Eq.(2.44) and reads

$$^{n}\boldsymbol{r} \;=\; ^{n}\boldsymbol{p} \tag{4.216}$$

where $(\boldsymbol{r}, \boldsymbol{p})$ are the vectors of internal and applied node-forces which are given by Eqs.(4.71,4.145), respectively. The superscript 'n' signifies forces in deformed configuration C_n.

The incremental form of the equilibrium equations when going from deformed configuration C_n to C_{n+1} (but still referring to the same reference configuration C_{on}), arises from Eq.(2.51) and is given by

$$^{n}\boldsymbol{k}\,\Delta\boldsymbol{v} \;=\; \Delta\boldsymbol{p}(\Delta h_i(\lambda)) \tag{4.217}$$

Here $\Delta\boldsymbol{p}$ is caused by a change in load level due to some externally prescribed scaling factors $h_i(\lambda)$, i.e.

$$\Delta\boldsymbol{p}(\Delta h_i(\lambda)) \;=\; ^{n+1}\boldsymbol{p}(h_i(\lambda)) \;-\; ^{n}\boldsymbol{r} \tag{4.218}$$

where also Eq.(4.216) has been introduced. The effects of change in position and direction of the loading as the element undergoes incremental displacements $\Delta\boldsymbol{v}$, are incorporated in $^{n}\boldsymbol{k}$ through the load correction stiffness matrices $(\boldsymbol{k}_{lc}^{(CL)}, \boldsymbol{k}_{lu}^{(CL)})$ given by Eq.(4.187) and Eq.(4.215), respectively. Thus, the resulting stiffness matrix consists of the contributions

$$^{n}\boldsymbol{k} \;=\; ^{n}(\boldsymbol{k}_m \,+\, \boldsymbol{k}_g \,-\, \boldsymbol{k}_{lc}^{(CL)} \,-\, \boldsymbol{k}_{lu}^{(CL)}) \tag{4.219}$$

where in addition $(\boldsymbol{k}_m, \boldsymbol{k}_g)$ are the material and geometric stiffness matrices as given by Eqs.(4.84,4.134), respectively.

Now, combining Eqs.(4.217,4.218) and suppressing superscripts and functional dependencies, the incremental equilibrium equations of the element take the form

$$\boldsymbol{k}\,\Delta\boldsymbol{v} \;=\; \boldsymbol{p} \;-\; \boldsymbol{r} \tag{4.220}$$

Then by rearranging the DOFs so that the external DOFs at node 1 and 2 (see Fig. 4.2) do come before the internal DOFs at node 3 and the strain DOFs, the above relationship can be expressed on the partitioned form

$$\begin{bmatrix} \boldsymbol{k}_{ee} & \boldsymbol{k}_{ei} \\ \boldsymbol{k}_{ie} & \boldsymbol{k}_{ii} \end{bmatrix} \begin{Bmatrix} \Delta \boldsymbol{v}_e \\ \Delta \boldsymbol{v}_i \end{Bmatrix} = \begin{Bmatrix} \boldsymbol{p}_e \\ \boldsymbol{p}_i \end{Bmatrix} - \begin{Bmatrix} \boldsymbol{r}_e \\ \boldsymbol{r}_i \end{Bmatrix} \tag{4.221}$$

where subscripts 'e' and 'i' signify quantities pertaining to external and internal DOFs, respectively. Since internal DOFs are uncoupled from DOFs of adjacent elements, the second matrix equation becomes unaffected by the assembly process and can instead be solved at the element level without approximations. Thus

$$\Delta \boldsymbol{v}_i \;=\; \boldsymbol{k}_{ii}^{-1} \left(\boldsymbol{p}_i \;-\; \boldsymbol{r}_i \;-\; \boldsymbol{k}_{ie}\, \Delta \boldsymbol{v}_e \right) \tag{4.222}$$

which inserted into the first matrix equation of Eq.(4.221), yields the *condensed* incremental equilibrium equations of the *basic* 12 DOFs element

$$\hat{\boldsymbol{k}}_{ee}\, \Delta \boldsymbol{v}_e \;=\; \hat{\boldsymbol{p}}_e \;-\; \hat{\boldsymbol{r}}_e \tag{4.223}$$

Here

$$\hat{\boldsymbol{k}}_{ee} \;=\; \boldsymbol{k}_{ee} \;-\; \boldsymbol{k}_{ei}\, \boldsymbol{k}_{ii}^{-1}\, \boldsymbol{k}_{ie} \tag{4.224}$$

$$\hat{\boldsymbol{p}}_e \;=\; \boldsymbol{p}_e \;-\; \boldsymbol{k}_{ei}\, \boldsymbol{k}_{ii}^{-1}\, \boldsymbol{p}_i \tag{4.225}$$

$$\hat{\boldsymbol{r}}_e \;=\; \boldsymbol{r}_e \;-\; \boldsymbol{k}_{ei}\, \boldsymbol{k}_{ii}^{-1}\, \boldsymbol{r}_i \tag{4.226}$$

are the condensed versions of the stiffness matrix, applied node-fore vector and internal node-force vector of the element, respectively; which are the quantities to be transformed to global coordinates and assembled into the system equations as described in Subsection 5.2.1. This elemination process of internal DOFs is usually termed *static condensation*.

Chapter 5

Nonlinear Finite Element Analysis of Beam Structures

5.1 Large Displacement Analysis

5.1.1 Introductory Remark

This section deals with the large displacement analysis of beam elements based on the Corotated Lagrangian description of motion. In lack of a suitable reference document for comprehensive treatment of all subjects of relevance, the presentation in the sequel is to a level of detailing that makes the formulation available for computer implementation. The computer program that is developed as a part of this work, is reviewed in Chapter 11.

5.1.2 Rotational Update in Space

From the preceding chapter it is known that the external nodal points of the 3D shear-beam element (i.e. nodes 1 and 2) possess three translational and three rotational DOFs. Through the incremental-iterative solution procedure that will be adopted for solving the equilibrium equations of the system, the resulting motion of each node has to be identified at every iteration cycle. For translational DOFs this update is simply performed by adding the current increments to the resulting values at the previous deformed configuration, i.e.

$$^{n+1}\boldsymbol{v}_t \;=\; ^{n}\boldsymbol{v}_t \;+\; \Delta\boldsymbol{v}_t \tag{5.1}$$

where superscripts 'n' and '$n+1$' signify deformed configurations C_n and C_{n+1}, respectively, while subscript 't' denotes translations.

Rotational DOFs, however, can not be updated correspondingly since these are not true vectorial quantities. Instead, they can implicitly be defined through the transformation of a Cartesian base vector triad $^{n}\boldsymbol{i}_i$, that rotates along with the node

and that initially was parallel to the fixed global base vector triad $\boldsymbol{I}_i$. For configuration C_n the transformation reads

$$ {}^{n}\boldsymbol{i}_i \;=\; {}^{n}T_{ij}\,\boldsymbol{I}_j \tag{5.2} $$

where ${}^{n}T_{ij}$ are the components of the transformation or rotation matrix ${}^{n}\boldsymbol{T}$ that possesses the properties of a second order orthonormal tensor. Thus the spatial motion of a node in C_n is uniquely defined by the three translational components of ${}^{n}\boldsymbol{v}_t$ and the nine rotational components of ${}^{n}\boldsymbol{T}$.

The problem now is how to update Eq.(5.2) when going to the next configuration, i.e.

$$ {}^{n+1}\boldsymbol{i}_i \;=\; {}^{n+1}T_{ij}\,\boldsymbol{I}_j \tag{5.3} $$

on basis of the rotation matrix for the previous state ${}^{n}\boldsymbol{T}$ and the incremental nodal rotations $\Delta\boldsymbol{v}_r$ that result from the equilibrium equations of the system. The sought relation between the rotation matrices can be expressed on the form

$$ {}^{n+1}\boldsymbol{T} \;=\; {}^{n}\boldsymbol{T}\,\Delta\boldsymbol{T} \tag{5.4} $$

where the incremental rotation matrix $\Delta\boldsymbol{T}$ may be obtained in different ways. Nygård [4] has presented an explicit and simple form for the components of $\Delta\boldsymbol{T}$ given by

$$ \Delta T_{ij} \;=\; \delta_{ij}\,\cos(\Delta\Theta) \;+\; \frac{\Delta\theta_i}{\Delta\Theta}\,\frac{\Delta\theta_j}{\Delta\Theta}\,(1 \;-\; \cos(\Delta\Theta)) \;+\; e_{ijk}\,\frac{\sin(\Delta\Theta)}{\Delta\Theta}\,\Delta\theta_k \tag{5.5} $$

where $\Delta\theta_i$ are the components of $\Delta\boldsymbol{v}_r$ and

$$ \Delta\Theta \;=\; \sqrt{\Delta\theta_1^2 \;+\; \Delta\theta_2^2 \;+\; \Delta\theta_3^2} \tag{5.6} $$

Furthermore, δ_{ij} is the Kronecker delta and e_{ijk} the permutation symbol, i.e.

$$ e_{ijk} \;=\; \begin{cases} \;\;0 \;\; ; & \textit{when indices are not distinct} \\ +1 \;\; ; & \textit{when indices form a positive cyclic permutation} \\ -1 \;\; ; & \textit{when indices form a negative cyclic permutation} \end{cases} \tag{5.7} $$

Note that the derived expression by Nygård is invariant with respect to the order in which the incremental rotational components are applied, and it retains an orthonormal form of ${}^{n+1}\boldsymbol{T}$. It is also seen that the first two terms of Eq.(5.5) are symmetric in i and j, while the last term is skewsymmetric.

5.1.3 Corotated Element Reference System

Fig. 5.1 shows the spatial motion of a beam element. The external nodes 1 and 2 of the element are eccentrically and rigidly attached to the system nodes a and b, respectively. The offset from one of the system nodes to its corresponding element

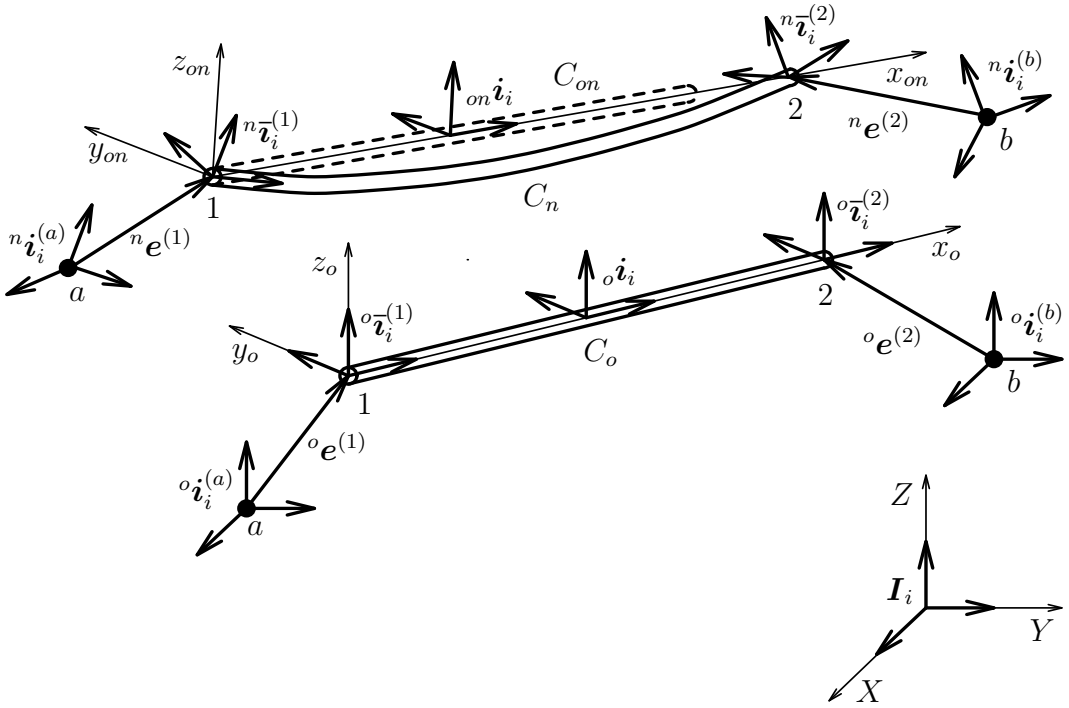

Figure 5.1: Spatial Motion of an Eccentrically Attached Beam Element

node is specified in terms of an eccentricity vector ${}^{n}\boldsymbol{e}$ for configuration C_n, while the initial offset is given by ${}^{o}\boldsymbol{e}$. Due to the rigid connection, ${}^{o}\boldsymbol{e}$ stays the same when referring to the base vector triad that rotates along with the system node. Thus, from Eq.(5.2)

$$ {}^{o}\boldsymbol{e} \;=\; {}^{n}\boldsymbol{T}\;{}^{n}\boldsymbol{e} \tag{5.8} $$

Then the updated eccentricity vector in the global system is given by the opposite relation, which, since ${}^{n}\boldsymbol{T}$ is orthonormal, becomes

$$ {}^{n}\boldsymbol{e} \;=\; {}^{n}\boldsymbol{T}^{T}\;{}^{o}\boldsymbol{e} \tag{5.9} $$

By introducing Eq.(5.4), the incremental eccentricity vector when going from configuration C_n to C_{n+1}, reads

$$ \Delta\boldsymbol{e} \;=\; {}^{n+1}\boldsymbol{e} \;-\; {}^{n}\boldsymbol{e} \;=\; \left(\Delta\boldsymbol{T}^{T} \;-\; \mathbf{1}\right)\;{}^{n}\boldsymbol{e} \tag{5.10} $$

where $\mathbf{1}$ is the diagonal unit matrix. Then the corresponding incremental global translations of the element node can be expressed

$$ \Delta\boldsymbol{v}_t^{(en)} \;=\; \Delta\boldsymbol{v}_t^{(sn)} \;+\; \Delta\boldsymbol{e} \tag{5.11} $$

where the new superscripts '(en)' and '(sn)' signify element node and system node, respectively. Finally, the resulting global translations of the element node for the new configuration C_{n+1} may be found from Eq.(5.1). Note that since this work will account for *segmental construction* (i.e. the static system is updated in accordance

with a construction sequence), ${}^{n}\boldsymbol{v}_t$ and ${}^{n}\boldsymbol{T}$ need to be recorded at the element node level in order to trace the motion of each element properly.

Two new base vector triads will now be defined; the first ${}_{on}\boldsymbol{i}_i$ is attached to the undeformed reference configuration of the element and relates to the global base vector triad through

$$ {}_{on}\boldsymbol{i}_i \;=\; {}_{on}T_{ij}\,\boldsymbol{I}_j \tag{5.12} $$

and for the initial state

$$ {}_{o}\boldsymbol{i}_i \;=\; {}_{o}T_{ij}\,\boldsymbol{I}_j \tag{5.13} $$

Here ${}_{o}T_{ij}$ and ${}_{on}T_{ij}$ are the components of the transformation matrices ${}_{o}\boldsymbol{T}$ and ${}_{on}\boldsymbol{T}$ corresponding to the reference configurations C_o and C_{on}, respectively. The second base vector triad ${}^{n}\bar{\boldsymbol{i}}_i$ is attached to each element node and is initially parallel to ${}_{o}\boldsymbol{i}_i$. Due to the rigid connections, the same rotations will take place in a system node and its corresponding element node. Thus, ${}^{n}\bar{\boldsymbol{i}}_i$ follows the base vector triad of its pertaining system node through the relation

$$ {}^{n}\bar{\boldsymbol{i}}_i \;=\; {}_{o}T_{ij}\,{}^{n}\boldsymbol{i}_j \tag{5.14} $$

Introduction of Eq.(5.2) gives the relation to the global base vectors

$$ {}^{n}\bar{\boldsymbol{i}}_i \;=\; {}_{o}T_{ik}\,{}^{n}T_{kj}\,\boldsymbol{I}_j \;=\; {}^{n}\bar{T}_{ij}\,\boldsymbol{I}_j \tag{5.15} $$

Now the problem of finding the components of ${}_{on}\boldsymbol{T}$ in Eq.(5.12) can be addressed. The undeformed reference configuration C_{on} should be positioned 'close' to C_n. As indicated in Fig. 5.1, the local axis system (x_{on}, y_{on}, z_{on}) in C_{on}, that is parallel to the base vector triad ${}_{on}\boldsymbol{i}_i$, has its origin located at the displaced position of node 1 of the element with the x_{on}-axis pointing in the direction of the displaced position of node 2. Thus, the first row of ${}_{on}\boldsymbol{T}$ is given by the direction cosines between the global axses $(X, Y, Z \equiv X_i)$ and the local x_{on}-axis

$$ {}_{on}T_{1i} \;=\; \frac{{}^{n}X_i^{(2)} \;-\; {}^{n}X_i^{(1)}}{L_n} \tag{5.16} $$

Here ${}^{n}X_i^{(en)}$ are the components of the global position vector ${}^{n}\boldsymbol{X}^{(en)}$ of an element node '(en)' in C_n, which is given by

$$ {}^{n}\boldsymbol{X}^{(en)} \;=\; {}^{o}\boldsymbol{X}^{(en)} \;+\; {}^{n}\boldsymbol{v}_t^{(en)} \tag{5.17} $$

where ${}^{o}\boldsymbol{X}^{(en)}$ is the initial position vector. Furthermore, L_n is the length of the deformed element along the local x_{on}-axis (i.e. the secant length). Thus

$$ L_n \;=\; \sqrt{\sum_{i=1}^{3}\left({}^{n}X_i^{(2)} \;-\; {}^{n}X_i^{(1)}\right)^2} \tag{5.18} $$

To establish the directions of the two remaining local axes (y_{on}, z_{on}), an auxiliary vector ${}_a\boldsymbol{i}$ is introduced that is taken to be in the average direction of ${}^n\bar{\boldsymbol{i}}_2$ at the two element nodes, i.e.

$$ {}_a\boldsymbol{i} \;=\; \frac{1}{2}\left({}^n\bar{\boldsymbol{i}}_2^{(1)} \;+\; {}^n\bar{\boldsymbol{i}}_2^{(2)}\right) \tag{5.19} $$

which from Eq.(5.15), gives the relation to the global base vectors

$$ {}_a\boldsymbol{i} \;=\; \frac{1}{2}\left({}^n\bar{T}_{2i}^{(1)} \;+\; {}^n\bar{T}_{2i}^{(2)}\right)\boldsymbol{I}_i \;=\; {}_aT_i\,\boldsymbol{I}_i \tag{5.20} $$

This auxiliary vector defines the local (x_{on}, y_{on})-plane of C_{on}. Thus, the z_{on}-direction is given through the vector product

$$ {}_{on}\boldsymbol{i}_3 \;=\; \frac{{}_{on}\boldsymbol{i}_1 \;\times\; {}_a\boldsymbol{i}}{|{}_{on}\boldsymbol{i}_1 \;\times\; {}_a\boldsymbol{i}|} \tag{5.21} $$

Formulas for computing vector products in terms of components may be found in standard textbooks of mathematics, e.g. [16]. Thus, by introducing the global components of ${}_{on}\boldsymbol{i}_1$ and ${}_a\boldsymbol{i}$ from Eqs.(5.16,5.20), respectively, the above expression yields the third row of ${}_{on}\boldsymbol{T}$

$$ {}_{on}T_{3i} \;=\; \frac{1}{|{}_{on}\boldsymbol{i}_1 \;\times\; {}_a\boldsymbol{i}|}\left({}_{on}T_{1j}\;{}_aT_k \;-\; {}_{on}T_{1k}\;{}_aT_j\right) \tag{5.22} $$

where the indices (j, k) here denote positive cyclic permutations of i; and

$$ |{}_{on}\boldsymbol{i}_1 \;\times\; {}_a\boldsymbol{i}| \;=\; \sqrt{\left({}_{on}T_{1i}\;{}_{on}T_{1i}\right)\left({}_aT_j\;{}_aT_j\right) - \left({}_{on}T_{1k}\;{}_aT_k\right)^2} \tag{5.23} $$

Note that ${}_{on}T_{1i}\;{}_{on}T_{1i} \;=\; 1$ in this general expression for the length of a vector product. Finally, the local y_{on}-direction is now given by

$$ {}_{on}\boldsymbol{i}_2 \;=\; {}_{on}\boldsymbol{i}_3 \;\times\; {}_{on}\boldsymbol{i}_1 \tag{5.24} $$

Thus, the components of the second row of ${}_{on}\boldsymbol{T}$, expressed in terms of the already found components of the third and first row, then become

$$ {}_{on}T_{2i} \;=\; {}_{on}T_{3j}\;{}_{on}T_{1k} \;-\; {}_{on}T_{3k}\;{}_{on}T_{1j} \tag{5.25} $$

where again, the indices (j, k) here denote positive cyclic permutations of i.

5.1.4 External DOFs at the Local Element Level

Having passed to a new deformed configuration C_{n+1} and the corresponding corotated element reference system $C_{o(n+1)}$ is established, the local nodal rotations of an external element node may then be extracted from the rotation matrix that relates the base vectors ${}^{n+1}\bar{\boldsymbol{i}}_i$ to ${}_{o(n+1)}\boldsymbol{i}_i$ (see Fig. 5.1); thus

$$ {}^{n+1}\bar{\boldsymbol{i}}_i \;=\; {}^{n+1}\hat{T}_{ij}\;{}_{o(n+1)}\boldsymbol{i}_j \tag{5.26} $$

Substituting the inverse of Eq.(5.12) into Eq.(5.15), the sought rotation matrix becomes

$$ {}^{n+1}\hat{\boldsymbol{T}} \;=\; {}_{o}\boldsymbol{T}\;{}^{n+1}\boldsymbol{T}\;{}_{o(n+1)}\boldsymbol{T}^{T} \tag{5.27} $$

Extracting the local nodal rotations from ${}^{n+1}\hat{\boldsymbol{T}}$ is in fact the reverse problem of collecting the terms of $\Delta\boldsymbol{T}$ in Eq.(5.5). Nygård [4] has presented the following expressions for this operation

$$ \Theta \;=\; \arccos\left[\frac{1}{2}\left({}^{n+1}\hat{T}_{ii} \;-\; 1\right)\right] \tag{5.28} $$

$$ \theta_1 \;=\; \frac{1}{2}\,\frac{\Theta}{\sin(\Theta)}\left({}^{n+1}\hat{T}_{23} \;-\; {}^{n+1}\hat{T}_{32}\right) \tag{5.29} $$

$$ \theta_2 \;=\; \frac{1}{2}\,\frac{\Theta}{\sin(\Theta)}\left(-{}^{n+1}\hat{T}_{13} \;+\; {}^{n+1}\hat{T}_{31}\right) \tag{5.30} $$

$$ \theta_3 \;=\; \frac{1}{2}\,\frac{\Theta}{\sin(\Theta)}\left({}^{n+1}\hat{T}_{12} \;-\; {}^{n+1}\hat{T}_{21}\right) \tag{5.31} $$

Note that these local nodal rotations are assumed to be of small or moderate size, since all large rotational effects are extracted from the element through the corotated reference concept.

Finally, the external nodal DOFs, ${}^{n+1}_{o(n+1)}\boldsymbol{v}_e$, of the beam element in configuration C_{n+1} with reference to $C_{o(n+1)}$ are now given by (see Fig. 4.2, Section 4.2 and Fig. 5.1)

$$ {}^{n+1}_{o(n+1)}\boldsymbol{v}_e \;=\; \left\{\begin{array}{c} v_{x1} \\ v_{y1} \\ v_{z1} \\ \theta_{x1} \\ \theta_{y1} \\ \theta_{z1} \\ v_{x2} \\ v_{y2} \\ v_{z2} \\ \theta_{x2} \\ \theta_{y2} \\ \theta_{z2} \end{array}\right\} \;=\; \left\{\begin{array}{c} 0 \\ 0 \\ 0 \\ \theta_1^{(1)} \\ \theta_2^{(1)} \\ \theta_3^{(1)} \\ L_{n+1} - L_o \\ 0 \\ 0 \\ \theta_1^{(2)} \\ \theta_2^{(2)} \\ \theta_3^{(2)} \end{array}\right\} \tag{5.32} $$

where L_{n+1} is the secant length of the deformed element in C_{n+1} (see Eq.(5.18)) and L_o is the initial (undeformed) length.

5.1.5 Internal DOFs Recovery

Section 4.8 dealt with elimination of the internal DOFs of the element. After the equilibrium equations of the system are solved for the incremental displacements, also internal DOFs need to be recovered for the next configuration before update of new element stiffnesses and node-forces can be performed.

The incremental translations of an external element node '(en)' when going from C_n to C_{n+1}, referring to C_{on}, are given by the transformation in Eq.(5.12). Thus

$$ {}_{on}\Delta\boldsymbol{v}_t^{(en)} \;=\; {}_{on}\boldsymbol{T}\;{}_g\Delta\boldsymbol{v}_t^{(en)} \tag{5.33} $$

where ${}_g\Delta\boldsymbol{v}_t^{(en)}$ are the global components from Eq.(5.11). The corresponding incremental nodal rotations, ${}_{on}\Delta\boldsymbol{v}_r^{(en)}$, may be retrieved from an incremental rotation matrix $\Delta\tilde{\boldsymbol{T}}$ that relates a new auxiliary base vector triad ${}^a\tilde{\boldsymbol{\imath}}_i$ to the base vectors ${}_{on}\boldsymbol{\imath}_i$ of C_{on}, thus

$$ {}^a\tilde{\boldsymbol{\imath}}_i \;=\; \Delta\tilde{T}_{ij}\;{}_{on}\boldsymbol{\imath}_j \tag{5.34} $$

where ${}^a\tilde{\boldsymbol{\imath}}_i$ is attached to the element node and parallel to ${}_{on}\boldsymbol{\imath}_i$ before the incremental rotations took place. Similarly, another auxiliary base vector triad ${}^a\tilde{\boldsymbol{I}}_i$, that is attached to the corresponding system node and parallel to $\boldsymbol{I}_i$ prior to the incremental rotations, is defined by

$$ {}^a\tilde{\boldsymbol{I}}_i \;=\; \Delta T_{ij}\,\boldsymbol{I}_j \tag{5.35} $$

where ΔT_{ij} are given by Eq.(5.5). Due to the rigid connection between element node and system node, ${}^a\tilde{\boldsymbol{\imath}}_i$ and ${}^a\tilde{\boldsymbol{I}}_i$ are related through

$$ {}^a\tilde{\boldsymbol{\imath}}_i \;=\; {}_{on}T_{ij}\;{}^a\tilde{\boldsymbol{I}}_j \tag{5.36} $$

By combining Eqs.(5.35,5.36) and the inverse of Eq.(5.12), $\Delta\tilde{\boldsymbol{T}}$ takes the form

$$ \Delta\tilde{\boldsymbol{T}} \;=\; {}_{on}\boldsymbol{T}\,\Delta\boldsymbol{T}\;{}_{on}\boldsymbol{T}^T \tag{5.37} $$

Now the components of ${}_{on}\Delta\boldsymbol{v}_r^{(en)}$ can be extracted from $\Delta\tilde{\boldsymbol{T}}$ using expressions similar to Eqs.(5.28-5.31). Thus

$$ \Delta\Theta \;=\; \arccos\left[\frac{1}{2}\left(\Delta\tilde{T}_{ii}\;-\;1\right)\right] \tag{5.38} $$

$$ \Delta\theta_1 \;=\; \frac{1}{2}\,\frac{\Delta\Theta}{\sin(\Delta\Theta)}\left(\Delta\tilde{T}_{23}\;-\;\Delta\tilde{T}_{32}\right) \tag{5.39} $$

$$ \Delta\theta_2 \;=\; \frac{1}{2}\,\frac{\Delta\Theta}{\sin(\Delta\Theta)}\left(-\Delta\tilde{T}_{13}\;+\;\Delta\tilde{T}_{31}\right) \tag{5.40} $$

$$ \Delta\theta_3 \;=\; \frac{1}{2}\,\frac{\Delta\Theta}{\sin(\Delta\Theta)}\left(\Delta\tilde{T}_{12}\;-\;\Delta\tilde{T}_{21}\right) \tag{5.41} $$

Then the incremental displacements of the external element nodes 1 and 2 when going

from C_n to C_{n+1} with reference to C_{on}, can be collected

$$ {}_{on}\Delta \boldsymbol{v}_e \;=\; \left\{ \begin{array}{c} {}_{on}\Delta \boldsymbol{v}_t^{(1)} \\ {}_{on}\Delta \boldsymbol{v}_r^{(1)} \\ {}_{on}\Delta \boldsymbol{v}_t^{(2)} \\ {}_{on}\Delta \boldsymbol{v}_r^{(2)} \end{array} \right\} \tag{5.42} $$

which inserted into Eq.(4.222), yields recovery of the corresponding incremental internal DOFs ${}_{on}\Delta \boldsymbol{v}_i$ of the element. As stated at several occasions previously; all rotations at the local element level are assumed to be of small or moderate size. Especially hierarchical rotations should match this assumption well, and thus the rotational DOFs at the internal node 3 may be treated vectorially (as well as the translational DOF). The strain DOFs are based on linear strain expressions and may easily also be superimposed. Consequently, the resulting values of the internal DOFs at C_{n+1} with reference to C_{on}, are obtained by adding the current increments to the previous values at C_n

$$ {}^{n+1}_{on}\boldsymbol{v}_i \;=\; {}^{n}_{on}\boldsymbol{v}_i \;+\; {}_{on}\Delta \boldsymbol{v}_i \tag{5.43} $$

Finally, these resulting values need to be carried over to the next undeformed configuration $C_{o(n+1)}$ as reference; an operation that is performed without any transformation. Thus

$$ {}^{n+1}_{o(n+1)}\boldsymbol{v}_i \;=\; {}^{n+1}_{on}\boldsymbol{v}_i \tag{5.44} $$

This simple formula may be justified by the following considerations: Since the two reference configurations deviate only by rigid body motions, the Green strain components become identical in the two systems [4]. By assuming linear approximations for all strains except for the normal x-strain, it follows automatically from the element formulation in Chapter 4 that the strain DOFs and the hierarchical rotational DOFs also must stay the same in the two systems since they are all exclusive contributors to various linear strain components at selected points in the element. Left is then the hierarchical translational DOF that contribute to the normal x-strain only. To justify the conservation of this DOF-value, a two-step reasoning may be undertaken. First consider the element with all except the mentioned DOF included. This reduced deformed state must give rise to identical strains in the two reference systems. Then apply the hierarchical translational DOF. In order to still attain identical resulting strains, the only additional strain, i.e. the normal x-strain, must also be the same in the two systems. By introducing the approximate nonlinear normal x-strain expression from Eq.(4.123) (i.e. the square term of the axial displacement gradient is neglected), this additional strain becomes linear in both systems, resulting in equal values for the hierarchical translational DOF. Thus, Eq.(5.44) does not involve further approximations than those already made in the strain expressions in Chapter 4.

5.1.6 Element Load Update

Section 4.6 and 4.7 dealt with expressions for element node-forces and load correction stiffnesses due to body force intensity $\boldsymbol{f}_o$ and surface traction $\boldsymbol{t}_o$. In addition, expressions were also given based on force per unit axial length $\boldsymbol{q}_o$, since this is a convenient way of specifying beam loads. For all three cases of applied loading, the intensities were given with direction as in deformed configuration and scaled to corresponding units of the undeformed reference configuration, i.e.

$$\begin{aligned} \boldsymbol{f}_o &= \boldsymbol{f}\,\frac{dV}{dV_o} \\ \boldsymbol{t}_o &= \boldsymbol{t}\,\frac{d(\partial V)}{d(\partial V_o)} \\ \boldsymbol{q}_o &= \boldsymbol{q}\,\frac{dL}{dL_o} \end{aligned} \tag{5.45}$$

Thus, through the incremental-iterative solution procedure there will be a need for updating these load intensities in each new deformed configuration C_n with reference to its corresponding C_{on}-configuration.

Since all loads considered in this work are of the body attached[1] kind, their intensities will always be known in the initial configuration. At configuration C_n the loads on a 'pseudo' element that still is kept in the C_o-position are thus, with reference to C_o, given by

$$\begin{aligned} {}^{no}_{o}\boldsymbol{f} &= h_l^{(f)}(\lambda_s)\,\boldsymbol{f}_{ref} \\ {}^{no}_{o}\boldsymbol{t} &= h_l^{(t)}(\lambda_s)\,\boldsymbol{t}_{ref} \\ {}^{no}_{o}\boldsymbol{q} &= h_l^{(q)}(\lambda_s)\,\boldsymbol{q}_{ref} \end{aligned} \tag{5.46}$$

i.e. the current load level is determined by scaling a given reference intensity with a load factor $h_l(\lambda_s)$ for the solution step. The treatment of load scaling factors is covered in Subsection 5.3.1. This implies that instead of using the general form in Eq.(5.45), the updated load intensities can be obtained by transferring the values in Eq.(5.46) to the current configuration. For unidirectional loading this may be done by first applying the inverse of Eq.(5.13) for transformation to the global system, and then transform back to the current element system using Eq.(5.12). Thus

$$\begin{aligned} \boldsymbol{f}_o^{(u)} &= {}^{n}_{on}\boldsymbol{f}^{(u)} = {}_{on}\boldsymbol{T}\;{}_{o}\boldsymbol{T}^T\;{}^{no}_{o}\boldsymbol{f}^{(u)} \\ \boldsymbol{t}_o^{(u)} &= {}^{n}_{on}\boldsymbol{t}^{(u)} = {}_{on}\boldsymbol{T}\;{}_{o}\boldsymbol{T}^T\;{}^{no}_{o}\boldsymbol{t}^{(u)} \\ \boldsymbol{q}_o^{(u)} &= {}^{n}_{on}\boldsymbol{q}^{(u)} = {}_{on}\boldsymbol{T}\;{}_{o}\boldsymbol{T}^T\;{}^{no}_{o}\boldsymbol{q}^{(u)} \end{aligned} \tag{5.47}$$

For corotational loading, the approximation will be made that the direction of loading can be based on the geometry of the rigid reference configuration C_{on} rather than

[1] The contrary is space attached loads that also are function of the current position in space.

on the actual deformed configuration C_n. Consequently, the updated load intensities and the values in Eq.(5.46) become equal, i.e.

$$\begin{aligned} \boldsymbol{f}_o^{(c)} &= {}_{on}^{n}\boldsymbol{f}^{(c)} \approx {}_{o}^{no}\boldsymbol{f}^{(c)} \\ \boldsymbol{t}_o^{(c)} &= {}_{on}^{n}\boldsymbol{t}^{(c)} \approx {}_{o}^{no}\boldsymbol{t}^{(c)} \\ \boldsymbol{q}_o^{(c)} &= {}_{on}^{n}\boldsymbol{q}^{(c)} \approx {}_{o}^{no}\boldsymbol{q}^{(c)} \end{aligned} \tag{5.48}$$

5.2 System Equations

5.2.1 Transformation and Assembly

In order to arrive at the final element expressions in Chapters 3 and 4, the principle of virtual displacements on total and incremental forms, as stated in Eqs.(2.44,2.51), was applied to an individual element only. By applying the principle to a structural system, and subdivide each integral as a sum over all elements that constitute this system, the incremental equilibrium equations of the structure may then be expressed on a form similar to Eq.(4.223) for an element. Thus

$$\boldsymbol{K}\,\Delta\boldsymbol{V} \;=\; \boldsymbol{P} \;-\; \boldsymbol{R} \tag{5.49}$$

where all quantities now are referred to global Cartesian coordinates and $\Delta\boldsymbol{V}$ is the incremental displacement vector of the collected system nodes. Furthermore, $(\boldsymbol{K}, \boldsymbol{P}, \boldsymbol{R})$ are the system versions of the incremental stiffness matrix, applied node-force vector and internal node-force vector, respectively, that relate to the corresponding element quantities through

$$\begin{aligned} \boldsymbol{K} &= \sum_{n_{el}} \boldsymbol{K}^{(e)} \\ \boldsymbol{P} &= \sum_{n_{el}} \boldsymbol{P}^{(e)} \\ \boldsymbol{R} &= \sum_{n_{el}} \boldsymbol{R}^{(e)} \end{aligned} \tag{5.50}$$

where n_{el} is the number of elements in the system in question. Here $(\boldsymbol{K}^{(e)}, \boldsymbol{P}^{(e)}, \boldsymbol{R}^{(e)})$ originate from the element quantities of the condensed 12 DOFs element as given by Eqs.(4.224,4.225,4.226) when related to the element nodes in local coordinates. Thus, the element quantities need to be transformed to global coordinates and related to the corresponding system nodes; an operation that will be described in the following.

By assuming small incremental nodal rotations, so that all DOFs can be treated vectorially, the transformation of incremental displacements of an element node '*en*' from global coordinates to local C_{on}-coordinates becomes from Eq.(5.12)

$$\begin{Bmatrix} \Delta\hat{\boldsymbol{v}}_t \\ \Delta\hat{\boldsymbol{v}}_r \end{Bmatrix}_{en} = \begin{bmatrix} {}_{on}\boldsymbol{T} & \boldsymbol{0} \\ \boldsymbol{0} & {}_{on}\boldsymbol{T} \end{bmatrix} \begin{Bmatrix} \Delta\boldsymbol{v}_t \\ \Delta\boldsymbol{v}_r \end{Bmatrix}_{en} \tag{5.51}$$

where local displacements now are identified with the accent ' ^ ', and subscripts 't' and 'r' again signify translations and rotations, respectively. Furthermore, the transformation of global incremental displacements from the system node 'sn' to the pertaining element node can be expressed by

$$\left\{ \begin{array}{c} \Delta \boldsymbol{v}_t \\ \Delta \boldsymbol{v}_r \end{array} \right\}_{en} = \left[\begin{array}{cc} \mathbf{1} & {}^{n}\boldsymbol{E} \\ \mathbf{0} & \mathbf{1} \end{array} \right] \left\{ \begin{array}{c} \Delta \boldsymbol{v}_t \\ \Delta \boldsymbol{v}_r \end{array} \right\}_{sn} \tag{5.52}$$

where $\mathbf{1}$ is the diagonal unit matrix and ${}^{n}\boldsymbol{E}$ is the eccentricity matrix, given by

$${}^{n}\boldsymbol{E} = \left[\begin{array}{ccc} 0 & e_z & -e_y \\ -e_z & 0 & e_x \\ e_y & -e_x & 0 \end{array} \right] \tag{5.53}$$

Here (e_x, e_y, e_z) are the components of ${}^{n}\boldsymbol{e}$ from Eq.(5.9). Combination of Eqs.(5.51,5.52) yields the final transformation of incremental displacements from a system node in global coordinates to an eccentrically attached element node in local C_{on}-coordinates

$$\left\{ \begin{array}{c} \Delta \hat{\boldsymbol{v}}_t \\ \Delta \hat{\boldsymbol{v}}_r \end{array} \right\}_{en} = \left[\begin{array}{cc} {}_{on}\boldsymbol{T} & {}_{on}\boldsymbol{T}\,{}^{n}\boldsymbol{E} \\ \mathbf{0} & {}_{on}\boldsymbol{T} \end{array} \right] \left\{ \begin{array}{c} \Delta \boldsymbol{v}_t \\ \Delta \boldsymbol{v}_r \end{array} \right\}_{sn} \tag{5.54}$$

Collection of this transformation for both endnodes into one matrix equation for the element reads

$$\Delta \hat{\boldsymbol{v}} = \boldsymbol{T}_e \, \Delta \boldsymbol{v} \tag{5.55}$$

where the DOFs-transformation matrix of the eccentrically attached element becomes

$$\boldsymbol{T}_e = \left[\begin{array}{cccc} {}_{on}\boldsymbol{T} & {}_{on}\boldsymbol{T}\,{}^{n}\boldsymbol{E}^{(1)} & \mathbf{0} & \mathbf{0} \\ \mathbf{0} & {}_{on}\boldsymbol{T} & \mathbf{0} & \mathbf{0} \\ \mathbf{0} & \mathbf{0} & {}_{on}\boldsymbol{T} & {}_{on}\boldsymbol{T}\,{}^{n}\boldsymbol{E}^{(2)} \\ \mathbf{0} & \mathbf{0} & \mathbf{0} & {}_{on}\boldsymbol{T} \end{array} \right] \tag{5.56}$$

Here $({}^{n}\boldsymbol{E}^{(1)}, {}^{n}\boldsymbol{E}^{(2)})$ are the eccentricity matrices pertaining to the external element nodes 1 and 2, respectively. Now, starting from the incremental equilibrium equations of an element in local coordinates (i.e. Eq.(4.223)) and in global coordinates when referred to the pertaining system nodes, and then equalizing the incremental work done, both internally and externally, in the two systems, and finally introducing Eq.(5.55), the sought transformations of element quantities from local to global coordinates become

$$\begin{aligned} \boldsymbol{k} &= \boldsymbol{T}_e^T \, \hat{\boldsymbol{k}} \, \boldsymbol{T}_e \\ \boldsymbol{p} &= \boldsymbol{T}_e^T \, \hat{\boldsymbol{p}} \\ \boldsymbol{r} &= \boldsymbol{T}_e^T \, \hat{\boldsymbol{r}} \end{aligned} \tag{5.57}$$

Here again local quantities are identified with the accent '$\hat{}$'. Now $(\boldsymbol{k}, \boldsymbol{p}, \boldsymbol{r})$ can be expanded to full 'system size' in $(\boldsymbol{K}^{(e)}, \boldsymbol{P}^{(e)}, \boldsymbol{R}^{(e)})$, and then assembled into $(\boldsymbol{K}, \boldsymbol{P}, \boldsymbol{R})$ through Eq.(5.50).

Note that this expand-and-add procedure is good for visualizing the assembly process. In practical computer implementation, however, the entries of $(\boldsymbol{k}, \boldsymbol{p}, \boldsymbol{r})$ are assembled directly into $(\boldsymbol{K}, \boldsymbol{P}, \boldsymbol{R})$ according to a 'pointer-indexing' scheme.

5.2.2 Discrete Nodal Load Contribution

The preceding subsection dealt with the assembly of element quantities into system quantities that did constitute the terms of the incremental equilibrium equations of a structure in Eq.(5.49). However, discrete loads applied at the system nodes were not accounted for. With these loads included, Eq.(5.49) retains its form, but the assembled system quantities now become

$$\begin{aligned} \boldsymbol{K} &= \sum_{n_{el}} \boldsymbol{K}^{(e)} - \sum_{n_{sn}} \boldsymbol{K}_l^{(n)} \\ \boldsymbol{P} &= \sum_{n_{el}} \boldsymbol{P}^{(e)} + \sum_{n_{sn}} \boldsymbol{P}^{(n)} \\ \boldsymbol{R} &= \sum_{n_{el}} \boldsymbol{R}^{(e)} \end{aligned} \tag{5.58}$$

Compared to Eq.(5.50); the new parameter n_{sn} is the number of system nodes in the structure, and the new contributions $(\boldsymbol{K}_l^{(n)}, \boldsymbol{P}^{(n)})$ are the 'expanded' versions of the load correction stiffness matrix and the applied node-force vector, respectively, due to discrete loading at a system node. The bases for these contributions are $(\boldsymbol{k}_l^{(CL)}, \boldsymbol{p})$ that refer to the 6 DOFs of the system node. In the following, expressions for the latter couple will be presented, both for unidirectional and corotational loading.

The elementary case of nodal loading is assumed to consist of a discrete force $\boldsymbol{F}$ that acts at an offset from the node given by the eccentricity vector $\boldsymbol{e}_l$. The components of the derived nodal moment $\boldsymbol{M}$ are thus given by

$$\begin{aligned} M_x &= e_y F_z - e_z F_y \\ M_y &= e_z F_x - e_x F_z \\ M_z &= e_x F_y - e_y F_x \end{aligned} \tag{5.59}$$

where (F_x, F_y, F_z) and (e_x, e_y, e_z) are the components of $\boldsymbol{F}$ and $\boldsymbol{e}_l$, respectively. Introduction of a load eccentricity matrix $\boldsymbol{E}_l$, similar to Eq.(5.53), yields the matrix form of Eq.(5.59)

$$\boldsymbol{M} = \boldsymbol{E}_l^T \boldsymbol{F} \tag{5.60}$$

As for the element, the discrete loading is also assumed to be rigidly attached to the system node. Thus, the load eccentricity vector in global system is updated for a new configuration according to Eq.(5.9). Furthermore, the nodal loading is known in

its initial configuration, like the distributed element loading in Subsection 5.1.6. At configuration C_n the known force in initial configuration reads

$$^{no}\boldsymbol{F} \;=\; h_l(\lambda_s)\,\boldsymbol{F}_{ref} \tag{5.61}$$

Thus, again the load level is determined by scaling a given reference value $\boldsymbol{F}_{ref}$ with a load factor $h_l(\lambda_s)$ for the solution step. For unidirectional nodal loading the corresponding node-force vector of a system node then takes the form

$$\boldsymbol{p}_u \;=\; \left\{ \begin{array}{c} {}^{n}\boldsymbol{F}^{(u)} \\ {}^{n}\boldsymbol{M}^{(u)} \end{array} \right\} \;=\; \left\{ \begin{array}{c} {}^{no}\boldsymbol{F} \\ {}^{n}\boldsymbol{E}_l^{T}\;{}^{n}\boldsymbol{F}^{(u)} \end{array} \right\} \tag{5.62}$$

while for corotational loading, the node-force vector becomes

$$\boldsymbol{p}_c \;=\; \left\{ \begin{array}{c} {}^{n}\boldsymbol{F}^{(c)} \\ {}^{n}\boldsymbol{M}^{(c)} \end{array} \right\} \;=\; \left\{ \begin{array}{c} {}^{n}\boldsymbol{T}^{T}\;{}^{no}\boldsymbol{F} \\ {}^{n}\boldsymbol{E}_l^{T}\;{}^{n}\boldsymbol{F}^{(c)} \end{array} \right\} \tag{5.63}$$

where ${}^{n}\boldsymbol{E}_l$ is the load eccentricity matrix for the C_n-configuration with components updated according to Eq.(5.9), and ${}^{n}\boldsymbol{T}$ is the nodal rotation matrix that is defined through Eq.(5.2).

The load correction stiffness matrix relates the increments of nodal loading to the increments of nodal displacements. Thus

$$\Delta\boldsymbol{p}^{(CL)} \;=\; \boldsymbol{k}_l^{(CL)}\,\Delta\boldsymbol{v} \tag{5.64}$$

Here the superscript '(CL)' implies that load corrections due to incremental translations are eliminated since in the Corotated Lagrangian description of motion the nodal reference frame moves along with the node. Thus, assuming small rotations, this relationship takes the form for corotational loading

$$\left\{ \begin{array}{c} \Delta F_x \\ \Delta F_y \\ \Delta F_z \\ \Delta M_x \\ \Delta M_y \\ \Delta M_z \end{array} \right\}_{c}^{(CL)} \;=\; \left[\begin{array}{cccccc} 0 & 0 & 0 & 0 & F_z & -F_y \\ 0 & 0 & 0 & -F_z & 0 & F_x \\ 0 & 0 & 0 & F_y & -F_x & 0 \\ 0 & 0 & 0 & 0 & M_z & -M_y \\ 0 & 0 & 0 & -M_z & 0 & M_x \\ 0 & 0 & 0 & M_y & -M_x & 0 \end{array} \right]_{lc}^{(CL)} \left\{ \begin{array}{c} \Delta v_x \\ \Delta v_y \\ \Delta v_z \\ \Delta \theta_x \\ \Delta \theta_y \\ \Delta \theta_z \end{array} \right\} \tag{5.65}$$

where (F_x, F_y, F_z) and (M_x, M_y, M_z) now are the components of ${}^{n}\boldsymbol{F}^{(c)}$ and ${}^{n}\boldsymbol{M}^{(c)}$,

respectively. For unidirectional loading the same relationship becomes

$$\left\{\begin{array}{c}\Delta F_x\\ \Delta F_y\\ \Delta F_z\\ \Delta M_x\\ \Delta M_y\\ \Delta M_z\end{array}\right\}_u^{(CL)} = \left[\begin{array}{cccccc}0&0&0&0&0&0\\0&0&0&0&0&0\\0&0&0&0&0&0\\0&0&0&k_{44}&k_{45}&k_{46}\\0&0&0&k_{54}&k_{55}&k_{56}\\0&0&0&k_{64}&k_{65}&k_{66}\end{array}\right]_{lu}^{(CL)} \left\{\begin{array}{c}\Delta v_x\\ \Delta v_y\\ \Delta v_z\\ \Delta\theta_x\\ \Delta\theta_y\\ \Delta\theta_z\end{array}\right\} \tag{5.66}$$

with

$$\begin{array}{lll} k_{44} = -(e_y F_y + e_z F_z) & ; \quad k_{45} = e_x F_y & ; \quad k_{46} = e_x F_z \\ k_{54} = e_y F_x & ; \quad k_{55} = -(e_z F_z + e_x F_x) & ; \quad k_{56} = e_y F_z \\ k_{64} = e_z F_x & ; \quad k_{65} = e_z F_y & ; \quad k_{66} = -(e_x F_x + e_y F_y) \end{array} \tag{5.67}$$

Here (F_x, F_y, F_z) and (e_x, e_y, e_z) are the components of ${}^n\boldsymbol{F}^{(u)}$ and ${}^n\boldsymbol{e}_l$, respectively. Note that these expressions for the load correction stiffness matrices are consistent with the corresponding element expressions as given by Eqs.(4.187,4.215).

5.2.3 Prescribed Displacements

In this work prescribed displacements or displacement boundary conditions will be applied directly in the global system. At configuration C_n a set of prescribed displacements that pertain to a system node, are given by

$$ {}^n\check{\boldsymbol{v}} \;=\; h_d(\lambda_s)\;\check{\boldsymbol{v}}_{ref} \tag{5.68}$$

Thus, the displacement level is determined by scaling a given reference value $\check{\boldsymbol{v}}_{ref}$ with a factor $h_d(\lambda_s)$ for the solution step. The treatment of displacement scaling factors is covered in Subsection 5.3.2. When going from solution step 's' to '$s+1$', the increments of prescribed nodal displacements become

$$ \Delta\check{\boldsymbol{v}} \;=\; [h_d(\lambda_{s+1}) \;-\; h_d(\lambda_s)]\;\check{\boldsymbol{v}}_{ref} \tag{5.69}$$

By collecting all increments of prescribed nodal displacements in the system into a common vector $\Delta\check{\boldsymbol{V}}_2$, the incremental equilibrium equations of a structure in Eq.(5.49) may be presented on the partitioned form

$$\left[\begin{array}{cc}\boldsymbol{K}_{11} & \boldsymbol{K}_{12}\\ \boldsymbol{K}_{21} & \boldsymbol{K}_{22}\end{array}\right]\left\{\begin{array}{c}\Delta\boldsymbol{V}_1\\ \Delta\check{\boldsymbol{V}}_2\end{array}\right\} = \left\{\begin{array}{c}\boldsymbol{P}_1 \;-\; \boldsymbol{R}_1\\ \boldsymbol{P}_2 \;-\; \boldsymbol{R}_2\end{array}\right\} \tag{5.70}$$

where subscripts '1' and '2' signify quantities pertaining to unknown and prescribed displacements, respectively. Thus, only the first of the two matrix equations needs to be solved for the unknown DOFs. However, by exchanging the second matrix equation with the trivial expression $\mathbf{1}\,\Delta\check{\boldsymbol{V}}_2 = \Delta\check{\boldsymbol{V}}_2$, a new set of equations with the same size as the original unconstrained system, that yields the correct solution for all DOFs, becomes

$$\begin{bmatrix} \boldsymbol{K}_{11} & \mathbf{0} \\ \mathbf{0} & \mathbf{1} \end{bmatrix} \begin{Bmatrix} \Delta\boldsymbol{V}_1 \\ \Delta\check{\boldsymbol{V}}_2 \end{Bmatrix} = \begin{Bmatrix} \boldsymbol{P}_1 - \boldsymbol{R}_1 - \boldsymbol{K}_{12}\,\Delta\check{\boldsymbol{V}}_2 \\ \Delta\check{\boldsymbol{V}}_2 \end{Bmatrix} \tag{5.71}$$

Note that the partitioned form as indicated in Eq.(5.70) is made here only to simplify the presentation. The boundary conditions are imposed according to Eq.(5.71) in the original rows and columns without any physical rearrangement of equations.

5.3 History Concepts

5.3.1 Load History

The current level of a loading is determined by the product of a reference value and a scaling factor $h_l(\lambda)$. For distributed element loading, the actual relationships are in terms of intensities according to Eq.(5.46), while for discrete nodal loading Eq.(5.61) applies. The load scaling factor, or load history, is given as a function of a parameter λ. The same load history may be assigned to several loadings. λ is a common parameter to all histories (not only those for loads), and it may be interpreted as a 'neutral time'-measure that works like a 'driving wheel' for the nonlinear solution process. Once a new value of λ is established, all quantities necessary for carrying out the next solution will then be defined. Section 5.4 sums up the solution strategy that is adopted in this work.

Several options for defining loading histories are covered in [6]. In the computer program that is developed as a part of this work (Chapter 11) however, only load histories described by discrete curve points in (λ, h_l)-coordinates are included. The rules for interpreting the C^0-continuous history function $h_l(\lambda)$ are there as follows:

- When a given λ falls between two curve points, the corresponding h_l is determined by linear interpolation.
- When λ falls either below or above the range of curve points, the corresponding h_l is taken equal to the value at the nearest curve point.

Some typical loading histories are depicted in Fig. 5.2.

5.3.2 Displacement History

The current level of a set of prescribed nodal displacements is determined according to Eq.(5.68), i.e. as the product of a reference value $\check{\boldsymbol{v}}_{ref}$ and a scaling factor $h_d(\lambda_s)$.

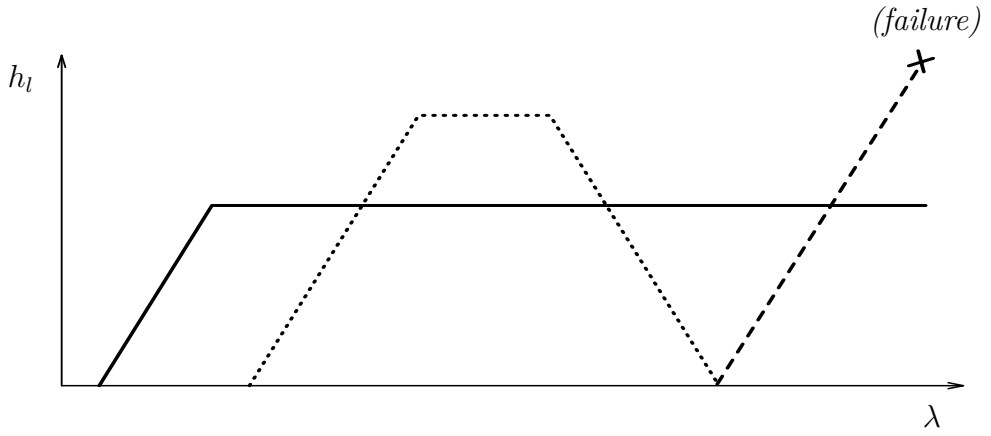

Figure 5.2: Load Histories

The same displacement scaling factor, or displacement history, may be assigned to several sets of prescribed displacements. Displacement histories are defined in exactly the same way as the histories of loading in the preceding subsection.

5.3.3 System History

In this context a system is understood to consist of an assembly of elements with corresponding boundary conditions (constrained DOFs). By identifying each system with a separate number S_i, i.e. the system number, the construction sequence, or system history, of the structural problem in question may then be characterized by a sequence of system numbers related to the parameter λ. In the computer program that is presented in Chapter 11, the system history data are given in terms of a sequence of discrete (λ, S)-values (points). The rules for defining the stepwise constant history function $S(\lambda)$ from these points are as follows:

- When a given λ falls between two points, the corresponding system number is the one that pertain to the larger λ-value.
- When λ falls either below or above the range of points, the corresponding system number is taken equal to the one at the nearest point.

The system history may be represented as in Fig. 5.3. Of convenience, the sequence of system numbers is here taken in consecutive order from 1 to n_{sy}; the latter being the number of systems in the structural problem in question.

5.3.4 Time History

The time history relates the actual time t to the parameter λ. In this work the function $t(\lambda)$ will be C^0-continuous in pertinent intervals of λ. However, backward shifts of time are allowed. This option may be of interest in conjunction with the start of a new construction sequence that is materialized in parallel with a previous one (e.g. a cantilevered bridge span that is built from both sides simultaneously). In

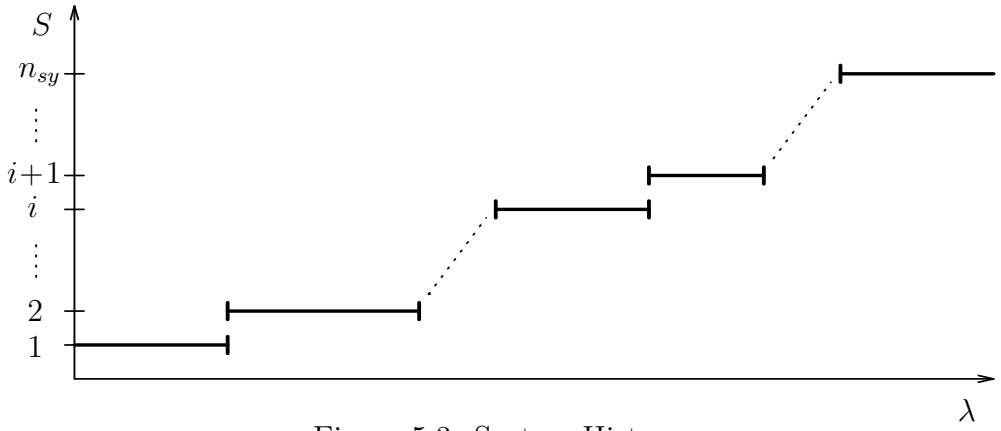

Figure 5.3: System History

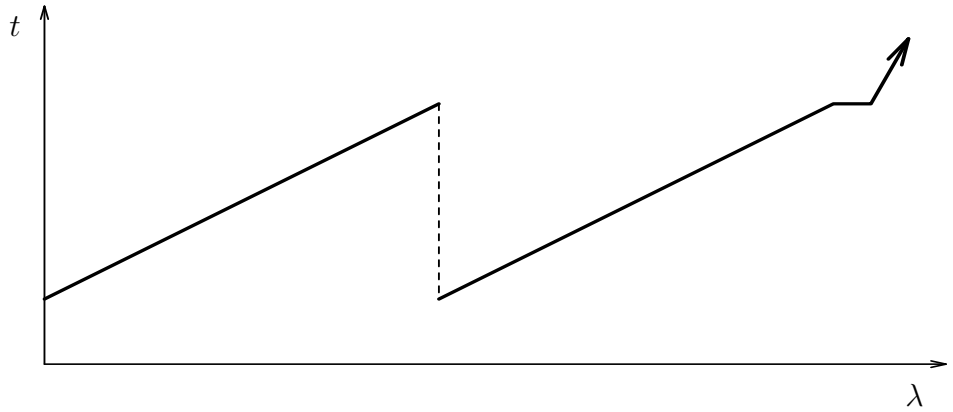

Figure 5.4: Time History

the computer program in Chapter 11, the time history data are given as a sequence of discrete curve points in (λ, t)-coordinates. The rules for defining the history function $t(\lambda)$ from these points are as follows:

- When a given λ falls between two curve points where the time is unchanged or increased, the corresponding actual time is determined by linear interpolation.

- When a given λ falls between two curve points with a decrease in time, the corresponding actual time is taken as the lower time.

- When λ falls either below or above the range of curve points, the corresponding time is taken equal to the value at the nearest curve point.

A time history (e.g. for the cantilevered bridge span) may look as depicted in Fig. 5.4.

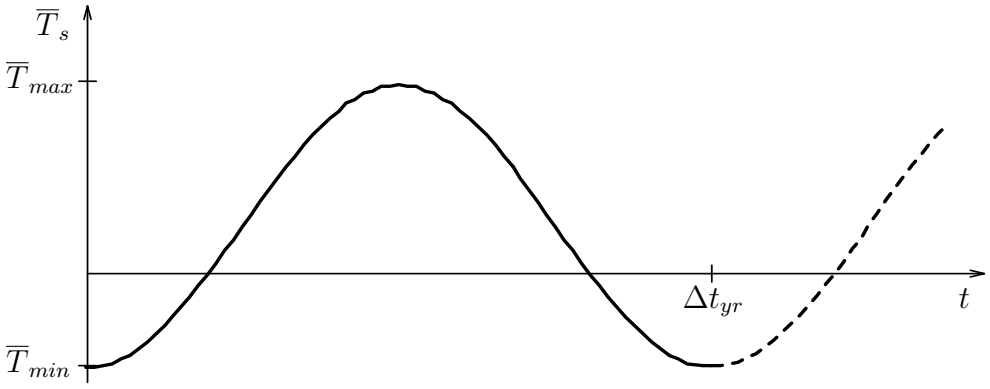

Figure 5.5: Mean Seasonal Temperature Variation

5.3.5 Mean Seasonal Temperature Variation

Similar to [17], the mean seasonal temperature $\overline{T}_s$ will be related to the actual time t through the simplified, periodic expression

$$\overline{T}_s(t) \;=\; \frac{\overline{T}_{max} \,+\, \overline{T}_{min}}{2} \;-\; \frac{\overline{T}_{max} \,-\, \overline{T}_{min}}{2} \,\cos\left(\frac{2\pi}{\Delta t_{yr}}\, t\right) \tag{5.72}$$

where $(\overline{T}_{max}, \overline{T}_{min})$ are the mean values of maximum and minimum seasonal temperature, respectively, and Δt_{yr} is the duration of a year. Normally, a day (24 hours) is used as the unit of time, as well as the averaging period for the temperature recordings that constitute the statistical basis for $(\overline{T}_{max}, \overline{T}_{min})$. The graphical representation of Eq.(5.72) is shown in Fig. 5.5. It is seen that $t = 0$ yields $\overline{T}_s = \overline{T}_{min}$. Thus, the time may be counted from January 1 in a certain year (northern hemisphere).

Since time dependent effects in concrete often also depend on the corresponding temperature level in a mean sense, an expression like Eq.(5.72) provides a simple and reasonably accurate basis for including such effects with a minimum of data-input. Time and temperature dependent effects are covered in Chapter 9. Note also that the mean seasonal temperature variation implicitly becomes a function of the parameter λ through the time history concept; thus $\overline{T}_s = \overline{T}_s\,(t(\lambda))$.

5.3.6 Temperature Deviation History

The current absolute temperature T may be obtained by superimposing the mean seasonal component $\overline{T}_s$ and a deviation from the mean ΔT, i.e.

$$T \;=\; \overline{T}_s \;+\; \Delta T \tag{5.73}$$

where $\overline{T}_s$ is covered in the preceding subsection. Analogous to the treatment of loads and prescribed displacements, ΔT will be determined by the product of a reference value ΔT_{ref} and a scaling factor $h_{\scriptscriptstyle T}(\lambda)$. Thus

$$\Delta T \;=\; h_{\scriptscriptstyle T}(\lambda)\, \Delta T_{ref} \tag{5.74}$$

The reference value is specified at the element level through

$$\Delta T_{ref} \;=\; \Delta T_1 \;+\; x\, g_{Tx} \;+\; y\, g_{Ty} \;+\; z\, g_{Tz} \tag{5.75}$$

where ΔT_1 is the value at node 1, and (g_{Tx}, g_{Ty}, g_{Tz}) are the constant temperature gradients in the local (x, y, z)-directions, respectively. The scaling factor, or temperature deviation history, is related to the parameter λ according to the same rules as described for the load history function in Subsection 5.3.1. The same temperature deviation history may be assigned to several reference values of temperature.

The split in temperature according to Eq.(5.73) allows for investigating extreme thermal effects at a certain instant of time by including the corresponding temperature deviations in the pertinent interval of λ, while long-time effects are continuously taken care of through the mean temperature component. Optionally, all thermal effects may be evaluated through the temperature deviation history concept by letting $\overline{T}_{max} = \overline{T}_{min} = 0$.

5.4 Solution Strategy

So far in this chapter, the ingredients for solving the nonlinear equilibrium problem based on an incremental-iterative procedure, have been presented. The simplest and probably most common method is to carry out consecutive solutions according to a prescribed sequence of the 'neutral time'-parameter λ; a method that is adopted in this work. Through the history concepts presented in the preceding section, it was seen that all problem-data were related to λ and thus are defined for the next solution step once the corresponding value of λ is given. The sequence of λ will here be chosen so that typical short-time phenomena (like load application) and long-time phenomena (like creep) are handled in separate solution steps. The advantage of this will become clear when dealing with the time dependent effects in Chapter 9. Then for each new λ the equilibrium state is determined to desired accuracy by repeatedly solving the incremental equilibrium equations on the linearized form in Eq.(5.49). The system quantities involved, i.e. $(\boldsymbol{K}, \boldsymbol{P}, \boldsymbol{R})$ from Eq.(5.58), are in general updated for the current configuration in each iteration cycle as described in Section 5.1 and 5.2. This corresponds to full or *true* Newton-Raphson iteration. However, necessary for convergence is only the update of the right hand side of Eq.(5.49) that expresses the current residual or out-of-balance forces. Using a *modified* Newton-Raphson iteration by retaining $\boldsymbol{K}$ unchanged for several iteration cycles, increases the number of iterations for convergence. On the other hand, computational effort is saved in each cycle by avoiding new formation and factorization of $\boldsymbol{K}$. The optimum choice depends to a great extent on the complexity of the constitutive model, since each iteration requires a new stress computation in order to form the current residual forces. For this reason, the computer program in Chapter 11 handles both true Newton-Raphson iteration and modified, based on reformation of $\boldsymbol{K}$ at the beginning of the first two iterations in each new solution step. Fig. 5.6 visualizes true and modified Newton-Raphson iteration as applied to the solution step λ_{s+1}.

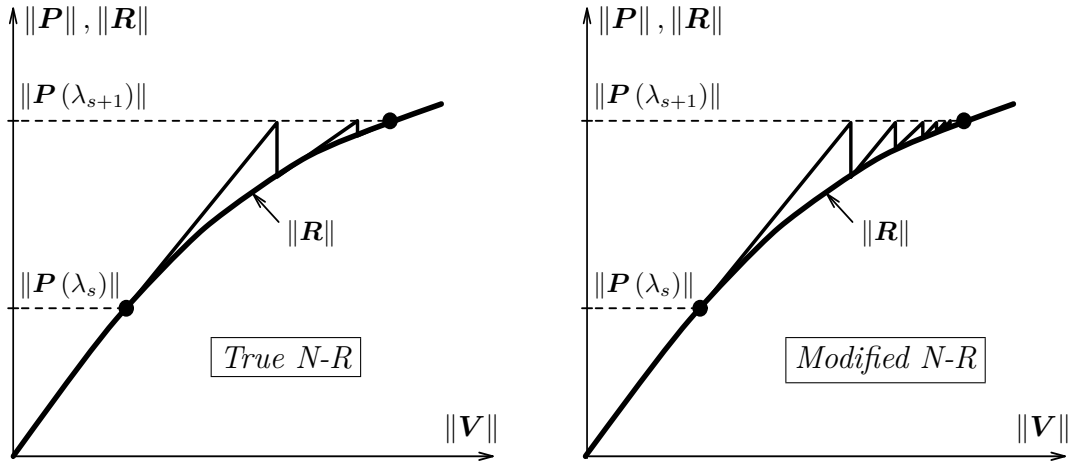

Figure 5.6: True versus Modified Newton-Raphson Iteration

To make a clearer distinction; $\boldsymbol{K}$ is here updated only at the beginning of the first iteration (i.e. at start of the solution step) for the modified case.

A convergence criterion for terminating the equilibrium iterations at desired accuracy is also needed. In the computer program in Chapter 11 termination is done either when the number of iteration cycles has reached a given maximum number i_{max}, or when the following criterion is satisfied

$$\left| \frac{{}^{i+1}\|\boldsymbol{V}_t\| - {}^{i}\|\boldsymbol{V}_t\|}{{}^{i+1}\|\boldsymbol{V}_t\|} \right| < C_{tol} \tag{5.76}$$

where superscripts 'i' and '$i+1$' refer to the previous and current iteration cycles, respectively, while subscript 't' implies nodal translations. C_{tol} is a prescribed convergence tolerance parameter that determines the accuracy of the solution. A typical value of C_{tol} may be 10^{-3}. Finally, the so-called modified Euclidean norm based on translational DOFs is expressed by

$$\|\boldsymbol{V}_t\| = \frac{1}{n_{td}} \sqrt{\sum_{j=1}^{n_{td}} v_{tj}^2} \tag{5.77}$$

where n_{td} is the number of translational DOFs in the system in question and v_{tj} is the j'th nodal translational component. Thus, rotational DOFs are not contributing to the termination criterion. This criterion was originally proposed by Mollestad [18] and is also implemented in [6].

Despite its popularity, the above solution procedure based on prescribed incrementation, has some shortcomings when dealing with complex nonlinearities (like handling bifurcation points). For such problems a number of so-called path-following algorithms have been developed where the loading is incremented automatically and is also allowed to vary during the iterations, see e.g. Bjærum [19]. However, for the nonlinearities investigated in this work, the selected solution procedure is found to

work satisfactorily in combination with a 'restart'-option (i.e. restart of execution from a saved equilibrium state (rather than redoing the whole analysis)). In [19] some termination criteria alternative to Eq.(5.76) are also presented.

Chapter 6

Prestressing Tendon Modeling

6.1 Introduction

Prestressed concrete structures may be classified into:

- Pretensioned structures.
- Posttensioned bonded structures.
- Posttensioned unbonded structures.

In this work, only posttensioned bonded structures will be considered. Here the prestressing force is applied gradually during the tensioning or jacking operation, and finally the tendon is anchored against the hardened concrete. Then bond between steel and concrete is established by grouting the duct that guides the tendon.

Several investigators [22]-[27] have included prestress in finite element analysis of concrete beam structures. A common geometry approximation is then to subdivide the curved tendon into a series of straight line segments, one segment for each element the tendon passes through. A further common approximation is to assume constant prestressing force within each element. In the present study, neither of these approximations will be retained. The geometric modeling and the force distribution at the tensioning state are instead based on assuming the tendon curve as a quadratic polynomial in space on parametrized form. After bond is established, the tendon is treated as an integral part of the cross section where strains in excess of those from the tensioning state are consistently derived from the assumed displacement field of the element formulation.

6.2 Tendon Geometry Description in Space

Each tendon, or part of a tendon (Subsection 6.3.4), is assumed described by the coordinates of three points along its path; namely the two endpoints, denoted '1'

and '2', and an intermediate point, denoted '3'. Between the three given points the coordinates of the tendon curve are interpolated through the parametric expression

$$\boldsymbol{X} = \left\{ \begin{array}{c} X \\ Y \\ Z \end{array} \right\} = \left[\begin{array}{ccc} X_1 & X_2 & X_3 \\ Y_1 & Y_2 & Y_3 \\ Z_1 & Z_2 & Z_3 \end{array} \right] \left\{ \begin{array}{c} \varphi_1 \\ \varphi_2 \\ \varphi_3 \end{array} \right\} \tag{6.1}$$

where subscript numbers refer to the corresponding tendon points. The shape functions become

$$\begin{aligned} \varphi_1 &= -\frac{1}{2}\rho\,(1-\rho) \\ \varphi_2 &= \frac{1}{2}\rho\,(1+\rho) \\ \varphi_3 &= (1-\rho)\,(1+\rho) \end{aligned} \tag{6.2}$$

Here ρ is the natural tendon coordinate or curve parameter that takes the values -1, 1 and 0 at the tendon points 1, 2 and 3, respectively. The parametrized tendon curve is depicted in Fig. 6.1. At this stage, the coordinates refer to the global system (symbolized with capital letters). When treating tendons at the element level, however, the corresponding local system applies (Section 6.4). A restriction on the finite element discretization is that there must be an external element node in every cross section that also contains a tendon endpoint. Thus, a tendon can not cover an element only partly. On the other hand, a tendon curve may span several elements.

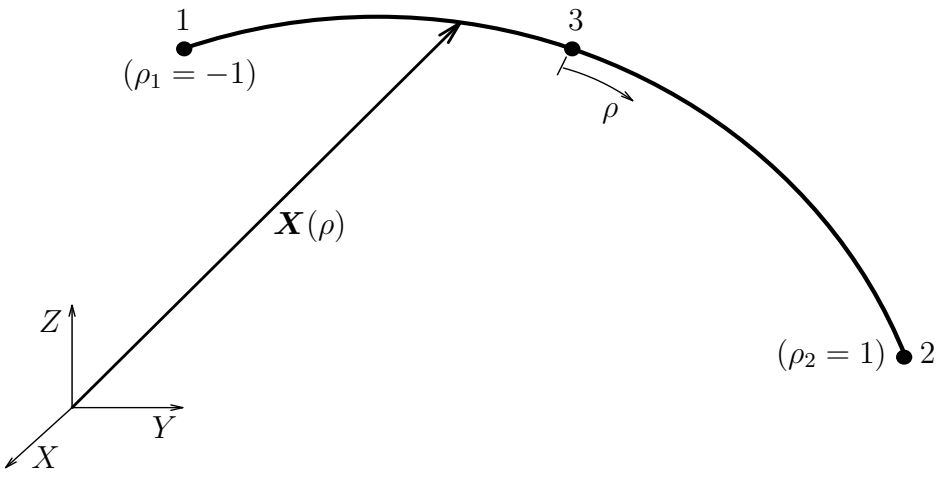

Figure 6.1: Parametric Tendon Representation

The (X, Y, Z)-Jacobians of the tendon curve are defined through

$$\boldsymbol{J} = \frac{d\boldsymbol{X}}{d\rho} \tag{6.3}$$

Thus, from Eq.(6.1)

$$\boldsymbol{J} = \left\{ \begin{array}{c} J_X \\ J_Y \\ J_Z \end{array} \right\} = \left[\begin{array}{ccc} X_1 & X_2 & X_3 \\ Y_1 & Y_2 & Y_3 \\ Z_1 & Z_2 & Z_3 \end{array} \right] \left\{ \begin{array}{c} \frac{d\varphi_1}{d\rho} \\ \frac{d\varphi_2}{d\rho} \\ \frac{d\varphi_3}{d\rho} \end{array} \right\} \tag{6.4}$$

with the shape function derivatives found from Eq.(6.2)

$$\begin{aligned} \frac{d\varphi_1}{d\rho} &= -\frac{1}{2}\,(1 - 2\rho) \\ \frac{d\varphi_2}{d\rho} &= \frac{1}{2}\,(1 + 2\rho) \\ \frac{d\varphi_3}{d\rho} &= -2\rho \end{aligned} \tag{6.5}$$

Note that this parametrized expression will work as intended only as long as the curve is monotonic in the 'axial' direction of the tendon. Assuming the 'axial' direction to be the X-direction, i.e.

$$|X_2 - X_1| > \max\left(|Y_2 - Y_1|, |Z_2 - Z_1|\right) \tag{6.6}$$

implies that J_X must be either entirely positive or negative in the interval $-1 \leq \rho \leq 1$. Since it follows from Eqs.(6.4,6.5) that J_X is a linear function of ρ, an equivalent requirement is that ρ_0, which is the solution of $J_X(\rho_0) = 0$, must fall outside the interval of interest. Thus $|\rho_0| > 1$; which leads to the following condition

$$\left| \frac{X_3 - \frac{1}{2}\,(X_1 + X_2)}{X_2 - X_1} \right| < \frac{1}{4} \tag{6.7}$$

Consequently, in order to make the parametric expression valid, the intermediate point 3 must be located within the 'quarter'-points in the 'axial' direction of the tendon curve.

The infinitesimal arclength element dS is defined by

$$dS = \sqrt{dX^2 + dY^2 + dZ^2} \tag{6.8}$$

Introduction of Eq.(6.3) yields

$$dS = J_S\, d\rho \tag{6.9}$$

where J_S is the curve-Jacobian

$$J_S = \sqrt{J_X^2 + J_Y^2 + J_Z^2} \tag{6.10}$$

Then the length of a tendon curve from endpoint 1 to the location ρ is given by

$$S(\rho) \;=\; \int_{-1}^{\rho} J_S \, d\tilde{\rho} \tag{6.11}$$

where the variable of integration now is termed $\tilde{\rho}$ to formally distinguish from the upper limit ρ. This integral may be solved numerically, e.g. by Gauss quadrature. In that case a simple linear coordinate transformation is necessary in order to obtain the standard integration interval $(-1, 1)$. Here instead, a closed form solution will be presented. By introducing Eqs.(6.4,6.5,6.10), Eq.(6.11) takes the form

$$S(\rho) \;=\; \int_{-1}^{\rho} \sqrt{A\,\tilde{\rho}^2 \;+\; B\,\tilde{\rho} \;+\; C}\; d\tilde{\rho} \tag{6.12}$$

Here (A, B, C) are constants, expressed in terms of the coordinates of the three given tendon points

$$\begin{aligned}
A \;&=\; (X_1 + X_2 - 2X_3)^2 \;+\; (Y_1 + Y_2 - 2Y_3)^2 \;+\; (Z_1 + Z_2 - 2Z_3)^2 \\
B \;&=\; (X_1 + X_2 - 2X_3)\,(X_2 - X_1) \;+\; (Y_1 + Y_2 - 2Y_3)\,(Y_2 - Y_1) \\
&\quad +\; (Z_1 + Z_2 - 2Z_3)\,(Z_2 - Z_1) \\
C \;&=\; \frac{1}{4}\,(X_2 - X_1)^2 \;+\; \frac{1}{4}\,(Y_2 - Y_1)^2 \;+\; \frac{1}{4}\,(Z_2 - Z_1)^2
\end{aligned} \tag{6.13}$$

By use of formulas in [28], the solution becomes

$$\begin{aligned}
S(\rho) \;=\; &\left(\frac{B}{4A} + \frac{\rho}{2}\right)\sqrt{A\rho^2 + B\rho + C} \;-\; \left(\frac{B}{4A} - \frac{1}{2}\right)\sqrt{A - B + C} \\
&+\; \frac{4AC - B^2}{8A\sqrt{A}}\left[\ln\left(\sqrt{A\rho^2 + B\rho + C} \;+\; \frac{B + 2A\rho}{2\sqrt{A}}\right)\right. \\
&\left. \qquad -\; \ln\left(\sqrt{A - B + C} \;+\; \frac{B - 2A}{2\sqrt{A}}\right)\right]
\end{aligned} \tag{6.14}$$

This expression does not work when $A = B = 0$. Then the tendon curve is reduced to a straight line with point 3 located at the midpoint. For this special case the solution simply becomes

$$S(\rho) \;=\; \sqrt{C}\;(1 \;+\; \rho) \tag{6.15}$$

The unit tangent vector is given by

$$\boldsymbol{t} \;=\; \frac{d\boldsymbol{X}}{dS} \;=\; \frac{\boldsymbol{J}}{J_S} \tag{6.16}$$

where the last term is obtained by introducing Eqs.(6.3,6.9). The components of $\boldsymbol{t}$ then read

$$\boldsymbol{t} \;=\; \left\{ \begin{array}{c} t_X \\ t_Y \\ t_Z \end{array} \right\} \;=\; \frac{1}{J_S} \left\{ \begin{array}{c} J_X \\ J_Y \\ J_Z \end{array} \right\} \tag{6.17}$$

Curvature is usually treated as a scalar and may be introduced through the 1st Frenet formula [16]

$$\frac{d\boldsymbol{t}}{dS} = \kappa\,\boldsymbol{n} \tag{6.18}$$

where $\boldsymbol{n}$ is the unit principal normal vector. In this work it is found appropriate to also define a corresponding curvature vector

$$\boldsymbol{\kappa} = \frac{d\boldsymbol{t}}{dS} \tag{6.19}$$

Application of the chain rule with respect to ρ and introduction of Eqs.(6.9,6.16(last term)), plus some elementary differentiations involving also Eq.(6.10), yield the following expression

$$\boldsymbol{\kappa} = \frac{1}{J_S^2}\left[\frac{d\boldsymbol{J}}{d\rho} - \frac{1}{J_S^2}\left(\boldsymbol{J}\cdot\frac{d\boldsymbol{J}}{d\rho}\right)\boldsymbol{J}\right] \tag{6.20}$$

Thus, the components of $\boldsymbol{\kappa}$ become

$$\boldsymbol{\kappa} = \left\{\begin{array}{c}\kappa_X\\ \kappa_Y\\ \kappa_Z\end{array}\right\} = \frac{1}{J_S^2}\left\{\begin{array}{l}\dfrac{dJ_X}{d\rho} - \dfrac{1}{J_S^2}\left(J_X\dfrac{dJ_X}{d\rho} + J_Y\dfrac{dJ_Y}{d\rho} + J_Z\dfrac{dJ_Z}{d\rho}\right)J_X\\ \dfrac{dJ_Y}{d\rho} - \dfrac{1}{J_S^2}\left(J_X\dfrac{dJ_X}{d\rho} + J_Y\dfrac{dJ_Y}{d\rho} + J_Z\dfrac{dJ_Z}{d\rho}\right)J_Y\\ \dfrac{dJ_Z}{d\rho} - \dfrac{1}{J_S^2}\left(J_X\dfrac{dJ_X}{d\rho} + J_Y\dfrac{dJ_Y}{d\rho} + J_Z\dfrac{dJ_Z}{d\rho}\right)J_Z\end{array}\right\} \tag{6.21}$$

where from Eqs.(6.4,6.5)

$$\frac{d\boldsymbol{J}}{d\rho} = \left\{\begin{array}{c}\dfrac{dJ_X}{d\rho}\\ \dfrac{dJ_Y}{d\rho}\\ \dfrac{dJ_Z}{d\rho}\end{array}\right\} = \left\{\begin{array}{c}X_1 + X_2 - 2X_3\\ Y_1 + Y_2 - 2Y_3\\ Z_1 + Z_2 - 2Z_3\end{array}\right\} \tag{6.22}$$

Then the resulting curvature follows from Eq.(6.20), also utilizing Eq.(6.10)

$$\kappa = |\boldsymbol{\kappa}| = \sqrt{\boldsymbol{\kappa}\cdot\boldsymbol{\kappa}} = \frac{1}{J_S^2}\sqrt{\frac{d\boldsymbol{J}}{d\rho}\cdot\frac{d\boldsymbol{J}}{d\rho} - \frac{1}{J_S^2}\left(\boldsymbol{J}\cdot\frac{d\boldsymbol{J}}{d\rho}\right)^2} \tag{6.23}$$

or

$$\kappa = \frac{1}{J_S^2}\sqrt{\left(\frac{dJ_X}{d\rho}\right)^2 + \left(\frac{dJ_Y}{d\rho}\right)^2 + \left(\frac{dJ_Z}{d\rho}\right)^2 - \frac{1}{J_S^2}\left(J_X\frac{dJ_X}{d\rho} + J_Y\frac{dJ_Y}{d\rho} + J_Z\frac{dJ_Z}{d\rho}\right)^2} \tag{6.24}$$

Finally, the mean curvature along the tendon curve may then be found by numerical integration of the following expression

$$\bar{\kappa} \;=\; \frac{1}{S_t} \int_{-1}^{1} \kappa \, J_S \, d\rho \tag{6.25}$$

where the total length of the tendon curve S_t follows from Eq.(6.14/6.15) by inserting $\rho = 1$.

6.3 Force Distribution at the Tensioning State

6.3.1 Loss Due to Friction

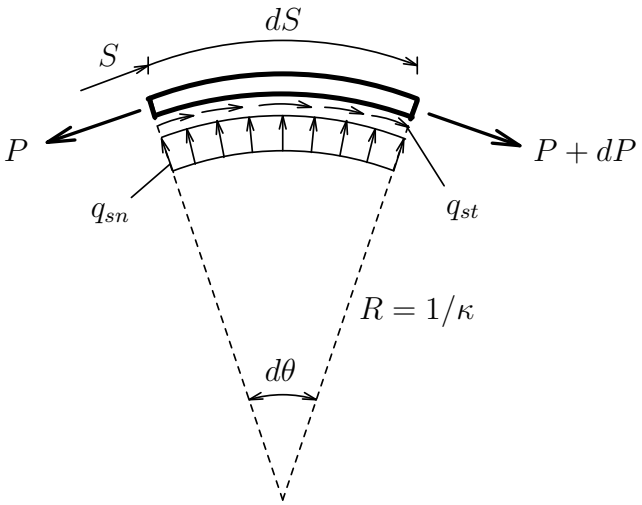

Figure 6.2: Forces on an Infinitesimal Tendon Element

Consider equilibrium of an infinitesimal tendon element, as depicted in Fig. 6.2. Equilibrium in the radial or normal direction leads to the following expression for the contact pressure-force per unit arclength

$$q_{sn} \;=\; P\,\kappa \tag{6.26}$$

while equilibrium in the circumferential or tangential direction yields the frictional force per unit arclength

$$q_{st} \;=\; -\,\frac{dP}{dS} \tag{6.27}$$

The following approximate friction law will be adopted

$$q_{st} \;=\; \mu\, q_{sn} \;+\; k\, P \tag{6.28}$$

where μ is the ordinary friction coefficient, for tendons usually termed *curvature friction coefficient*, while k is denoted the *wobble friction coefficient*. Combination of

the three equations yields the following differential equation for the prestressing force

$$\frac{dP}{dS} + (\mu\,\kappa + k)\,P = 0 \tag{6.29}$$

The solution may be expressed on the form

$$P = P_1\, e^{-\left(\mu \int_0^S \kappa\, d\tilde{S} + kS\right)} \tag{6.30}$$

where P_1 is the applied prestressing force at location $S = 0$, i.e. at tendon endpoint 1. The integral in the exponent may be solved numerically for each new tendon location as explained in conjunction with Eq.(6.11). However, a simplification is to substitute the varying curvature by its mean value along the tendon curve from Eq.(6.25). Then Eq.(6.30) takes the simplified form

$$P = P_1\, e^{-(\mu\bar{\kappa} + k)\,S} \tag{6.31}$$

Analogous, if a prestressing force P_2 is applied at tendon endpoint 2, the corresponding formula reads

$$P = P_2\, e^{-(\mu\bar{\kappa} + k)\,(S_t - S)} \tag{6.32}$$

where S_t is the total length of the tendon curve.

6.3.2 Loss Due to Anchorage Slip

When transferring the tensioning force from the jack to the anchor, a slip motion in the tendon may arise which results in a loss of prestressing. However, due to the frictional force, this loss again will vanish at a certain location, here termed the 'slip'-location S_s. Fig. 6.3 illustrates this situation for a tendon jacked from endpoint 1. Mari [23] developed a numerical search procedure for determining S_{s1} and the corresponding loss variation based on the assumptions that the force curves prior to and after the anchorage slip are symmetric about the horizontal dotted line in Fig. 6.3, and further that the area between the two curves is proportional to the amount of slip at the anchor. The same approach was later adopted in [24]-[27]. While the latter of these two assumptions is correct, the first one is not, since the slope of the force curve will always be proportional to the force itself at the same location (ref. Eq.(6.29)). However, a quite simple closed form solution of the problem may be found, which will be covered in the following.

Let the force at the intersection between the initial force curve from endpoint 1 and the curve including anchorage loss be denoted P_{s1}. By solving Eq.(6.29) for the latter branch, it follows that this force variation can be expressed by

$$P_{a1} = P_{s1}\, e^{-(\mu\bar{\kappa} + k)\,(S_{s1} - S)} \tag{6.33}$$

where subscript '$a1$' signifies that anchorage loss now is included. P_{s1} itself is given by Eq.(6.31)

$$P_{s1} = P_1\, e^{-(\mu\bar{\kappa} + k)\,S_{s1}} \tag{6.34}$$

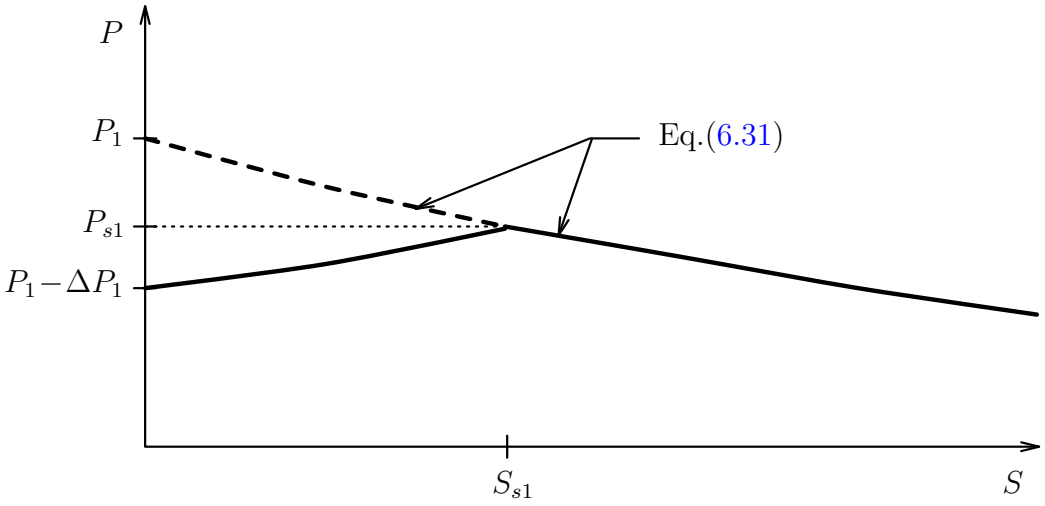

Figure 6.3: Loss at Tendon Endpoint 1

and thus

$$P_{a1} \;=\; P_1\, e^{-\,(\mu\bar{\kappa}\,+\,k)\,(2S_{s1}\,-\,S)} \tag{6.35}$$

The force variation P_{i1} along the initial branch is also expressed by Eq.(6.31). Then the prestressing loss due to anchorage slip becomes

$$\begin{aligned} \Delta P \;&=\; P_{i1} \;-\; P_{a1} \\ &=\; P_1 \left[e^{-\,(\mu\bar{\kappa}\,+\,k)\,S} \;-\; e^{-\,(\mu\bar{\kappa}\,+\,k)\,(2S_{s1}\,-\,S)} \right] \end{aligned} \tag{6.36}$$

Now, let the slip at the anchor be denoted u_s. This slip must be related to the change in strain due to prestressing loss as follows

$$u_s \;=\; \int_0^{S_{s1}} \Delta\epsilon_p \, dS \tag{6.37}$$

Since the anchorage loss is an unloading process, a linear stress-strain relationship can be assumed, i.e.

$$\Delta\epsilon_p \;=\; \frac{\Delta\sigma_p}{E_p} \;=\; \frac{\Delta P}{E_p\, A_p} \tag{6.38}$$

where E_p is the modulus of elasticity of prestressing steel, and A_p is the cross section area of the tendon. Combination of the last three equations yields the expression

$$u_s \;=\; \frac{P_1}{E_p\, A_p} \left[\int_0^{S_{s1}} e^{-\,(\mu\bar{\kappa}\,+\,k)\,S}\, dS \;-\; e^{-2\,(\mu\bar{\kappa}\,+\,k)\,S_{s1}} \int_0^{S_{s1}} e^{(\mu\bar{\kappa}\,+\,k)\,S}\, dS \right] \tag{6.39}$$

By solving the integrals, the result can be written on the form

$$e^{-2\,(\mu\bar{\kappa}\,+\,k)\,S_{s1}} \;-\; 2\, e^{-\,(\mu\bar{\kappa}\,+\,k)\,S_{s1}} \;+\; 1 \;-\; \frac{E_p\, A_p\, u_s\, (\mu\bar{\kappa}\,+\,k)}{P_1} \;=\; 0 \tag{6.40}$$

This is a quadratic equation in the term $\exp\{-(\mu\bar{\kappa}+k)S_{s1}\}$. The correct solution becomes

$$e^{-(\mu\bar{\kappa}+k)\,S_{s1}} \;=\; 1 \;-\; \sqrt{\frac{E_p\,A_p\,u_s\,(\mu\bar{\kappa}+k)}{P_1}} \tag{6.41}$$

Thus, the inverse relationship yields the solution for the slip-location S_{s1}

$$S_{s1} \;=\; -\,\frac{1}{\mu\bar{\kappa}+k}\,\ln\left[1-\sqrt{\frac{E_p\,A_p\,u_s\,(\mu\bar{\kappa}+k)}{P_1}}\right] \tag{6.42}$$

Analogous to Eqs.(6.35,6.42); when jacking the tendon from endpoint 2, the expressions for the force variation after anchorage loss P_{a2} and for the slip-location S_{s2} (measured from endpoint 1) become

$$P_{a2} \;=\; P_2\,e^{-(\mu\bar{\kappa}+k)\,(S_t-2S_{s2}+S)} \tag{6.43}$$

$$S_{s2} \;=\; S_t \;+\; \frac{1}{\mu\bar{\kappa}+k}\,\ln\left[1-\sqrt{\frac{E_p\,A_p\,u_s\,(\mu\bar{\kappa}+k)}{P_2}}\right] \tag{6.44}$$

Finally note that the loss due to anchorage slip is assumed to be a local effect near the anchor. If the amount of slip was sufficiently large (or the friction sufficiently small), so that the loss would affect the prestressing over the entire length of the tendon, the expressions derived in this subsection are not strictly valid. Then Eq.(6.42) (or Eq.(6.44)) would identify a fictitious slip-location behind the opposite end of the tendon, resulting in underestimated loss predictions. In such a case, the force after loss at the opposite end should be treated as the unknown rather than the slip-location.

6.3.3 Force Distribution for a 'Single-Curve' Tendon

In this subsection the final force distribution at the tensioning state will be found for a tendon consisting only of one parametrized curve, for short called a 'single-curve' tendon.

In general, tendons may be subjected to jacking from both ends, or from either one of the two ends only. When dealing with two-end jacking, the frictional force will change direction somewhere along the tendon. At this location, here termed the 'reverse'-location S_r, the prestressing forces arising from jacking from each end are equal. Thus, from Eqs.(6.31,6.32)

$$P_1\,e^{-(\mu\bar{\kappa}+k)\,S_r} \;=\; P_2\,e^{-(\mu\bar{\kappa}+k)\,(S_t-S_r)} \tag{6.45}$$

By taking the natural logarithm on both sides, the solution becomes

$$S_r \;=\; \frac{S_t}{2} \;+\; \frac{1}{2\,(\mu\bar{\kappa}+k)}\,\ln\frac{P_1}{P_2} \tag{6.46}$$

Now, by also including anchorage losses, the force distribution for a single-curve tendon subjected to two-end jacking, can be summarized as follows

$$P = \begin{cases} P_1\, e^{-(\mu\bar{\kappa}+k)\,(2S_{s1}-S)} & ; \quad 0 \le S \le S_{s1} \\ P_1\, e^{-(\mu\bar{\kappa}+k)\,S} & ; \quad S_{s1} < S \le S_r \\ P_2\, e^{-(\mu\bar{\kappa}+k)\,(S_t-S)} & ; \quad S_r < S \le S_{s2} \\ P_2\, e^{-(\mu\bar{\kappa}+k)\,(S_t-2S_{s2}+S)} & ; \quad S_{s2} < S \le S_t \end{cases} \tag{6.47}$$

where the individual force expressions are taken from Eqs.(6.35,6.31,6.32,6.43), in their order of appearance. Furthermore, the expressions for (S_{s1}, S_r, S_{s2}) are given by Eqs.(6.42,6.46,6.44), respectively, while S_t follows from Eq.(6.14/6.15) by inserting $\rho = 1$. The force distribution is depicted in Fig. 6.4.

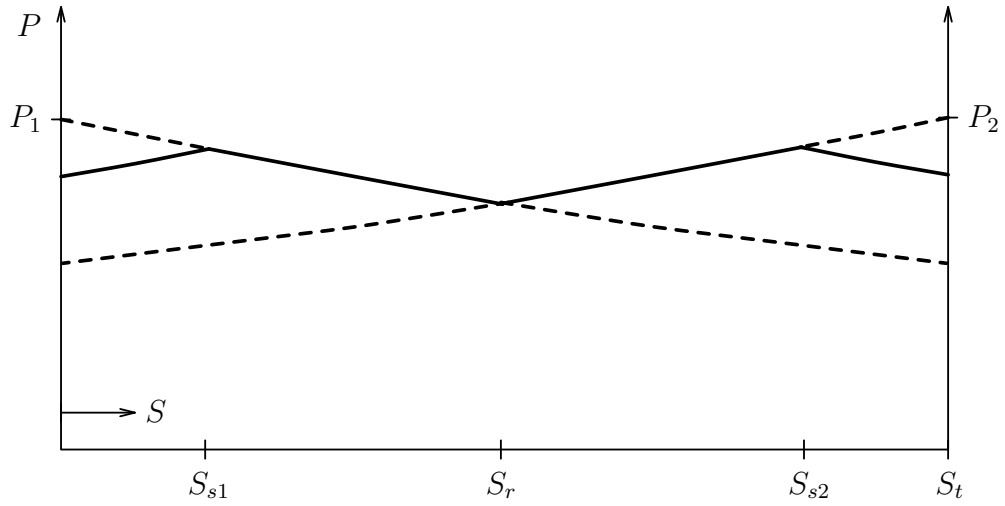

Figure 6.4: Force Profile for a 'Single-Curve' Tendon Jacked from Both Ends

The case of one-end jacking from endpoint 1 is covered by the first two formulas of Eq.(6.47), which is obtained by setting $S_r = S_{s2} = S_t$. Similarly, one-end jacking from endpoint 2 can be retrieved from Eq.(6.47) by setting $S_{s1} = S_r = 0$.

Although the anchorage loss is considered to be a local effect (ref. the closing remark in the preceding subsection), it is necessary in a computer program to foresee all possible situations. When, for two-end jacking, the condition $S_{s1} < S_r < S_{s2}$ is not satisfied, the final force distribution will be influenced by the actual tensioning procedure (i.e. which end is jacked first). Since this information is not included as input to the problem, the following interpretations are made for these (rare) situations in the computer program in Chapter 11:

- If $S_r < S_{s1}$ and $S_r < S_{s2}$, then the case is converted to one-end jacking from endpoint 2.
- If $S_r > S_{s1}$ and $S_r > S_{s2}$, then the case is converted to one-end jacking from endpoint 1.

- If $S_{s2} < S_r < S_{s1}$, then the force distribution is considered undefined (error message).

In addition, since the expressions for (S_{s1}, S_r, S_{s2}) do not work for zero friction, a separate handling of this simple case is also included. Then the loss due to anchorage slip is uniform along the tendon, given by

$$\Delta P = \frac{E_p\, A_p\, u_s}{S_t} \tag{6.48}$$

6.3.4 Force Distribution for a 'Multiple-Curve' Tendon

This subsection deals with the final force distribution at the tensioning state for a tendon composed of more than one parametrized curve, for short called a 'multiple-curve' tendon. In the computer program that is reviewed in Chapter 11, this type of tendon may consist of two or three parametrized curves. The procedure for establishing the final force distribution for a multiple-curve tendon is closely related to the concept for a single-curve tendon, but it becomes far more extensive. Nevertheless, the main features can be summarized in the four steps:

- First, treat all parametrized curves on an individual basis (i.e. either one-end or trivial 'zero-zero' jacking), and determine the quantities $(P_1, P_2, S_{s1}, S_r, S_{s2})$. If P_1 is the applied force at endpoint 1, P_2 is now the computed force at endpoint 2; and vice versa.

- Next, check the values of the endforces at the continuation points and determine whether the resulting tendon is two-end jacked, or if not; from which end it is one-end jacked.

- Then, correct the slip-locations in adjoining parts if initial values indicate crossing of continuation points. For two-end jacking, also determine the reverse-location.

- Finally, update the endforces of each part based on the new found information.

The result of this procedure is that each parametrized curve now has an updated set of quantities $(P_1, P_2, S_{s1}, S_r, S_{s2})$, from which the final force distribution may be retrieved using Eq.(6.47).

Note for two-end jacking, if the condition $S_{s1} < S_r < S_{s2}$ now is not satisfied for the resulting tendon, the similar interpretations are made as described for a single-curve tendon. Also the separate case for zero friction is included similarly. Finally, note that the simplification of substituting the varying curvature with its mean value (as basis for the frictional force), now is taken for each parametrized curve separately. This is a better approximation than applying the mean value for the resulting tendon as a whole. However, if slip-locations are crossing continuation points, the mean curvature is not adjusted accordingly (i.e. the mean curvature from the original end-curve is still retained).

6.4 Tendon Treated at the Element Level

6.4.1 Introduction

So far, tendons have been treated with reference to the global coordinate system. In that frame it was convenient to establish the set of quantities $(P_1, P_2, \bar{\kappa}, S_{s1}, S_r, S_{s2}, S_t)$ that define the final force distribution at the tensioning state for each parametrized curve. When treating tendons at the element level, each parametrized curve may now be considered decoupled from its origin as either a single-curve or a part of a multiple-curve tendon. Consequently, the presentation in the sequel will concentrate on an individual parametrized curve only.

6.4.2 Correspondence between Tendon and Element

The coordinate transformation from the global system to the initial local element system can be deduced from Eq.(5.13) and reads

$$\boldsymbol{x} = {}_o\boldsymbol{T}\left(\boldsymbol{X} - \boldsymbol{X}^{(1)}\right) \tag{6.49}$$

where $(\boldsymbol{X}, \boldsymbol{x})$ are, respectively, the global and local position vectors to a common point in space, while $\boldsymbol{X}^{(1)}$ is the global position vector to the origin of the local system, i.e. to element node 1. Furthermore, ${}_o\boldsymbol{T}$ is the transformation matrix corresponding to the initial reference configuration C_o. Since this configuration now is the only considered, indices on coordinates referring to the current configuration have been suppressed.

An inherent property of the parametric representation in Eqs.(6.1,6.2) of the tendon curve is its invariance of Cartesian coordinate system. The reason for this is that the sum of shape functions always equals unity. Thus, by applying Eq.(6.49) for the transformation of coordinates for each of the three tendon points in turn, the curve from Eq.(6.1) can now be exactly recovered in the local system through the similar expression

$$\boldsymbol{x} = \left\{ \begin{array}{c} x \\ y \\ z \end{array} \right\} = \left[\begin{array}{ccc} x_1 & x_2 & x_3 \\ y_1 & y_2 & y_3 \\ z_1 & z_2 & z_3 \end{array} \right] \left\{ \begin{array}{c} \varphi_1 \\ \varphi_2 \\ \varphi_3 \end{array} \right\} \tag{6.50}$$

where again subscript numbers refer to the corresponding tendon points, and shape functions are given by Eq.(6.2). Consequently, all results derived previously in the global system are equally valid in the local system.

Having reestablished the parametric expression for the tendon curve in the local element system, the correspondence between the natural tendon coordinate ρ and the natural beam coordinate ξ may now be found. The latter is given by

$$\xi = \frac{2x}{L_o} - 1 \tag{6.51}$$

where L_o is the initial (undeformed) element length. The inverse expression reads

$$x \;=\; \frac{L_o}{2}\,(1 \,+\, \xi) \tag{6.52}$$

The corresponding relation between x and ρ can be derived from the first equation of the above parametric representation, i.e.

$$x \;=\; x_1\varphi_1 \,+\, x_2\varphi_2 \,+\, x_3\varphi_3 \tag{6.53}$$

Insertion of the shape functions from Eq.(6.2) yields the expression

$$x \;=\; \frac{1}{2}\,(x_1 + x_2 - 2x_3)\,\rho^2 \;+\; \frac{1}{2}\,(x_2 - x_1)\,\rho \;+\; x_3 \tag{6.54}$$

Then the quadratic correspondence between ρ and ξ follows by equating Eqs.(6.52,6.54)

$$\frac{1}{2}\,(x_1 + x_2 - 2x_3)\,\rho^2 \;+\; \frac{1}{2}\,(x_2 - x_1)\,\rho \;+\; x_3 \;-\; \frac{L_o}{2}\,(1 \,+\, \xi) \;=\; 0 \tag{6.55}$$

and the correct solution for ρ becomes

$$\rho \;=\; \frac{x_1 - x_2}{2\,(x_1 + x_2 - 2x_3)}\left[1 \;-\; \sqrt{1 \;-\; \frac{8\,(x_1 + x_2 - 2x_3)\left(x_3 - \dfrac{L_o}{2}\,(1+\xi)\right)}{(x_1 - x_2)^2}}\right] \tag{6.56}$$

Evidently, this expression does not work when $2x_3 = x_1 + x_2$. From Eq.(6.55) it is seen that the relationship between ρ and ξ then becomes linear, given by

$$\rho \;=\; \frac{x_1 + x_2 - L_o\,(1+\xi)}{x_1 - x_2} \tag{6.57}$$

It may not seem obvious that the minus sign in front of the square-root expression in Eq.(6.56) always yields the correct solution for ρ. However, from Eq.(6.7) it follows that

$$\left|\frac{x_1 - x_2}{2\,(x_1 + x_2 - 2x_3)}\right| \;>\; 1 \tag{6.58}$$

Consequently, since $|\rho| < 1$, the minus sign must always apply. Also the roots have to be real since the tendon covers the whole element (ref. the restriction made in Section 6.2 on the finite element discretization).

6.4.3 Applied Tendon Node-Force Vector

The applied tendon node-force vector of an element may take contributions from:

- Concentrated endforces at the anchoring points.

- Distributed forces due to friction and curvature.

In the next, the latter contribution will be covered first.

The vector of distributed tendon forces per unit arclength $\boldsymbol{q}_s$, that act *on* the surrounding concrete, may be expressed by

$$\boldsymbol{q}_s \;=\; q_{sn}\,\boldsymbol{n} \;+\; q_{st}\,\boldsymbol{t} \tag{6.59}$$

where (q_{sn}, q_{st}) are, respectively, the corresponding forces due to contact pressure and friction, while $(\boldsymbol{n}, \boldsymbol{t})$ are the unit vectors in the normal and tangential directions of the curve, respectively. Introduction of the relationships from Eqs.(6.26,6.27) (but keeping in mind that forces now are acting on the concrete) yields

$$\boldsymbol{q}_s \;=\; P\,\kappa\,\boldsymbol{n} \;+\; \frac{dP}{dS}\,\boldsymbol{t} \;=\; P\,\boldsymbol{\kappa} \;+\; \frac{dP}{dS}\,\boldsymbol{t} \tag{6.60}$$

Here also the curvature vector $\boldsymbol{\kappa}$ has been introduced in the last part by combining Eqs.(6.18,6.19). Instead of using force per unit arclength, the preferred reference is to unit axial length of the beam. This force vector $\boldsymbol{q}$ (subscript 'x' suppressed) is given by

$$\boldsymbol{q} \;=\; \boldsymbol{q}_s\,\frac{dS}{dx} \;=\; \boldsymbol{q}_s\,\frac{1}{|t_x|} \tag{6.61}$$

where t_x is the x-component of $\boldsymbol{t}$, obtained by using Eq.(6.16). Now, combining the two preceding equations, and also introducing the prestressing force expressions from Eq.(6.47), the reference vector $\boldsymbol{q}_{ref}$ of distributed tendon forces per unit axial length takes the form

$$\boldsymbol{q}_{ref} \;=\; P\,[\boldsymbol{\kappa} \;+\; \alpha\,(\mu\bar{\kappa} + k)\,\boldsymbol{t}]\,\frac{1}{|t_x|} \tag{6.62}$$

where

$$\alpha \;=\; \begin{cases} 1 & ;\;\; 0 \le S \le S_{s1} \\ -1 & ;\;\; S_{s1} < S \le S_r \\ 1 & ;\;\; S_r < S \le S_{s2} \\ -1 & ;\;\; S_{s2} < S \le S_t \end{cases} \tag{6.63}$$

and $(P, \boldsymbol{\kappa}, \bar{\kappa}, \boldsymbol{t})$ are expressed by Eqs.(6.47,6.21,6.25,6.17), respectively. In conjunction with Eq.(6.47) are also given references to the expressions for $(S_{s1}, S_r, S_{s2}, S_t)$, while S is determined by Eq.(6.14/6.15) once ρ is known. Since applied loading from prestress is of the corotational kind, it follows from Subsection 5.1.6 (Eqs.(5.46,5.48)) that the updated load intensity vector $\boldsymbol{q}_o$ in configuration C_n with reference to C_{on}, may be approximated by

$$\boldsymbol{q}_o \;\approx\; h_l(\lambda_s)\,\boldsymbol{q}_{ref} \tag{6.64}$$

where $h_l(\lambda_s)$ is the load scaling factor for the solution step, that typically takes values in the range $0 \le h_l(\lambda_s) \le 1$ for prestressing. The corresponding (y, z)-location

of the loading in the cross section follows from the last two expressions of Eq.(6.50). Now the applied node-force vector of the element, as given by Eq.(4.145), can be addressed. In this case the integrals are solved numerically. Then ξ is given by the numerical integration scheme. Once ρ is determined from Eq.(6.56/6.57), all quantities necessary for determining $\boldsymbol{q}_o$ and the derived moments etc. in Eq.(4.148) are then available.

The part of the applied node-force vector that arises from concentrated tendon forces will in this work take contributions from forces at both ends of an element in general (rather than from the endforces at the anchoring points only). There are three reasons for making this generalization:

- Multiple-curve tendons are initially only C^o-continuous at the continuation points. Thus, this inaccuracy should be compensated for in any case by including the effect of concentrated forces at adjacent sides of a continuation point.

- Due to the simplification that the direction of corotational loading is based on the geometry of the rigid reference configuration C_{on} instead of the actual deformed configuration C_n, a similar lack of slope-continuity will also arise at each element boundary as the structure undergoes deformations.

- Inclusion of the concentrated forces at each element end yields a better representation of the load terms pertaining to the internal strain DOFs.

A reference prestressing force vector at an external element node '(en)' may thus take the form

$$\boldsymbol{F}_{ref}^{(en)} \;=\; \beta^{(en)}\, P^{(en)}\, \boldsymbol{t}^{(en)} \tag{6.65}$$

where $(P^{(en)}, \boldsymbol{t}^{(en)})$ again are expressed by Eqs.(6.47,6.17), now inserted (S, ρ)-values that correspond to $\xi = (-1, 1)$ for $en = (1, 2)$, respectively. The factor $\beta^{(en)}$, introduced to give the correct direction of the loading (i.e. *on* the concrete), reads for the two endnodes

$$\begin{aligned} \beta^{(1)} \;&=\; \begin{cases} 1 & ; \quad x_2 > x_1 \\ -1 & ; \quad x_2 < x_1 \end{cases} \\ \beta^{(2)} \;&=\; \begin{cases} -1 & ; \quad x_2 > x_1 \\ 1 & ; \quad x_2 < x_1 \end{cases} \end{aligned} \tag{6.66}$$

Here (x_1, x_2) are the x-coordinates of tendon endpoints 1 and 2, respectively; introduced to determine the orientation of the tendon curve in relation to the element. Similarly to Eq.(6.64), an updated force vector $\boldsymbol{F}_o^{(en)}$ at element endnode (en) in

configuration C_n and with reference to C_{on}, may now be approximated by

$$\boldsymbol{F}_o^{(en)} = \left\{ \begin{array}{c} F_x \\ F_y \\ F_z \end{array} \right\}^{(en)} \approx h_l(\lambda_s)\, \boldsymbol{F}_{ref}^{(en)} \tag{6.67}$$

The derived moment vector $\boldsymbol{M}^{(en)}$ becomes

$$\boldsymbol{M}^{(en)} = \left\{ \begin{array}{c} M_x \\ M_y \\ M_z \end{array} \right\}^{(en)} = \left\{ \begin{array}{c} yF_z - zF_y \\ zF_x \\ -yF_x \end{array} \right\}^{(en)} \tag{6.68}$$

Furthermore, the generalized load vectors $(\boldsymbol{p}_{v_r}, \boldsymbol{p}_{w_r})$ pertaining to the strain DOFs $(\boldsymbol{v}_{v_r}, \boldsymbol{v}_{w_r})$ take contributions from the forces at both element ends, i.e.

$$\boldsymbol{p}_{v_r} = \left\{ \begin{array}{c} yF_y \\ yzF_y \end{array} \right\}^{(1)} + \left\{ \begin{array}{c} yF_y \\ yzF_y \end{array} \right\}^{(2)} \tag{6.69}$$

$$\boldsymbol{p}_{w_r} = \left\{ \begin{array}{c} zF_z \\ yzF_z \end{array} \right\}^{(1)} + \left\{ \begin{array}{c} zF_z \\ yzF_z \end{array} \right\}^{(2)} \tag{6.70}$$

Again the (y, z)-location of the loading in the cross section follows from the last two expressions of Eq.(6.50), now inserting the ρ-value that corresponds to the element endnode in question.

Finally note that the procedure of applying the prestressing forces according to Eqs.(6.64,6.67), i.e. by scaling the force profile from the final tensioning state by a factor ranging from zero and up to one, is indeed a simplification of the real physical procedure. Intermediated states of possible concern, like e.g. the state after jacking but before anchorage loss (ref. the dashed lines in Fig. 6.4), are thus not taken into account.

6.4.4 Tendon Load Correction Stiffness Matrix

As for the node-force vector, the load correction stiffness matrix of an element due to prestress takes contributions from distributed as well as concentrated tendon forces. The distributed force contribution is given by Eq.(4.187). Again integrals are solved numerically. From the preceding subsection it was shown how the load intensity vector $\boldsymbol{q}_o$ and its corresponding (y, z)-location in the cross section were readily available once a new value of ξ was selected according to the numerical integration scheme. Thus, the distributed tendon force contribution to the load correction stiffness matrix does not need further comments.

For the concentrated tendon force contribution, no expressions have been given so far. The analogous problem at the system level is the discrete corotational nodal loading with load correction stiffness given by Eq.(5.65). Here in contrast however, a fixed reference frame for the incremental action will now initially be adopted. Then a completely skewsymmetric form of the stiffness matrix is attained. Thus, for the concentrated tendon forces at element endnode (en)

$$\left\{ \begin{array}{c} \Delta \boldsymbol{F}_o \\ \Delta \boldsymbol{M} \end{array} \right\}^{(en)} = \left[\begin{array}{cccccc} 0 & 0 & 0 & 0 & F_z & -F_y \\ 0 & 0 & 0 & -F_z & 0 & F_x \\ 0 & 0 & 0 & F_y & -F_x & 0 \\ 0 & F_z & -F_y & 0 & M_z & -M_y \\ -F_z & 0 & F_x & -M_z & 0 & M_x \\ F_y & -F_x & 0 & M_y & -M_x & 0 \end{array} \right]^{(en)} \left\{ \begin{array}{c} \Delta \boldsymbol{v}_t \\ \Delta \boldsymbol{v}_\theta \end{array} \right\}^{(en)} \tag{6.71}$$

where the components (F_x, F_y, F_z) and (M_x, M_y, M_z) are given by Eqs.(6.67,6.68), respectively. Furthermore, $(\boldsymbol{v}_t, \boldsymbol{v}_\theta)$ now symbolize the corresponding (x, y, z)-components of nodal translations and rotations, respectively. In addition, also terms due to coupling between strain DOFs and nodal rotations will arise. These terms are derived here by specializing the corresponding expressions for distributed loading in conjunction with Eq.(4.164). The results become

$$\Delta \boldsymbol{p}_{v_r} = \left[\begin{array}{ccc} -yF_z & 0 & yF_x \\ -yzF_z & 0 & yzF_x \end{array} \right]^{(en)} \Delta \boldsymbol{v}_\theta^{(en)} \tag{6.72}$$

$$\Delta \boldsymbol{M}^{(en)} = \left[\begin{array}{cc} yF_z & yzF_z \\ 0 & 0 \\ -yF_x & -yzF_x \end{array} \right]^{(en)} \Delta \boldsymbol{v}_{v_r} \tag{6.73}$$

$$\Delta \boldsymbol{p}_{w_r} = \left[\begin{array}{ccc} zF_y & -zF_x & 0 \\ yzF_y & -yzF_x & 0 \end{array} \right]^{(en)} \Delta \boldsymbol{v}_\theta^{(en)} \tag{6.74}$$

$$\Delta \boldsymbol{M}^{(en)} = \left[\begin{array}{cc} -zF_y & -yzF_y \\ zF_x & yzF_x \\ 0 & 0 \end{array} \right]^{(en)} \Delta \boldsymbol{v}_{w_r} \tag{6.75}$$

where again the (y, z)-location of the loading in the cross section is given by the last two expressions of Eq.(6.50), inserting the ρ-value that corresponds to the element endnode in question.

As mentioned, Eq.(6.71) is based on a fixed reference frame for the incremental action. Since in the Corotated Lagrangian (CL) description of motion the local reference system instead is attached to node 1 and moves along with the element, load corrections due to incremental rigid body translations must finally be eliminated. Here this is conveniently done by replacing the columns of the load stiffness pertaining to incremental translations of node 1 with the corresponding columns of node 2, but with opposite sign. Thus

$$\begin{aligned} k^{(CL)}_{i,v_{x1}} &= -k_{i,v_{x2}} \\ k^{(CL)}_{i,v_{y1}} &= -k_{i,v_{y2}} \\ k^{(CL)}_{i,v_{z1}} &= -k_{i,v_{z2}} \end{aligned} \tag{6.76}$$

6.4.5 Strain Analysis at the Tensioning State

During the tensioning operation there is no bond established yet between tendon and concrete. Consequently, the preceding expressions for the tendon node-force vector and the load correction stiffness matrix of an element are based on forces that act on the concrete structure, while at the same time the tendon is not included in the cross section analysis when forming the internal node-force vector and the material and geometric stiffness matrices of the element. At the final tensioning state the tendon force P at a certain location is given by one of the expressions in Eq.(6.47). The corresponding stress $\sigma_p^{(o)}$ reads

$$\sigma_p^{(o)} = \frac{P}{A_p} \tag{6.77}$$

where A_p is the cross section area of the tendon. The stress-strain relationship of prestressing steel will be treated separately in Section 8.3. Here this relationship will only be symbolized by

$$\sigma_p = f(\epsilon_p) \tag{6.78}$$

Then the inverse relation yields the prestressing steel strain $\epsilon_p^{(o)}$ at the final tensioning state

$$\epsilon_p^{(o)} = f^{-1}(\sigma_p^{(o)}) \tag{6.79}$$

After equilibrium is achieved, the strain in the concrete structure at the tendon location can be recovered using Eq.(4.52). Thus

$$\boldsymbol{\epsilon} = \boldsymbol{B}\,\boldsymbol{v} \tag{6.80}$$

where the nodal displacement vector $\boldsymbol{v}$ and the strain-displacement matrix $\boldsymbol{B}$ are given by Eqs.(4.43,4.54), respectively. Of convenience, the strain vector $\boldsymbol{\epsilon}$ will be repeated here

$$\boldsymbol{\epsilon}^T = \begin{bmatrix} \epsilon_x & \gamma_{xy} & \gamma_{xz} & \epsilon_y & \epsilon_z & \gamma_{yz} \end{bmatrix} \tag{6.81}$$

The normal strain ϵ_t in the tangential direction of the tendon may now be determined from the transformation

$$\epsilon_t = \boldsymbol{a}_t\,\boldsymbol{\epsilon} \tag{6.82}$$

where the transformation vector $\boldsymbol{a}_t$ is given by[1]

$$\boldsymbol{a}_t = \begin{bmatrix} t_x^2 & t_x t_y & t_x t_z & t_y^2 & t_z^2 & t_y t_z \end{bmatrix} \tag{6.83}$$

Here (t_x, t_y, t_z) are the components of the unit tangent vector $\boldsymbol{t}$ from Eq.(6.17). Thus, the additional strain in the tendon $\Delta\epsilon_p^{(o)}$ in relation to the surrounding concrete at the final tensioning state becomes

$$\Delta\epsilon_p^{(o)} = \epsilon_p^{(o)} - \epsilon_t \tag{6.84}$$

From now on bond between tendon and concrete will be established, which means that this strain difference will be retained throughout the remaining life of the structure.

6.4.6 Tendon Analysis after Bond

After bond is established, the prestressing forces from the final tensioning state are still retained as applied loading. However, the tendon is now also included in the beam cross section, and as such contributes to the internal resistance of the structure with its amount of stress in excess of the initial prestress. In brief; this implies that the additional strain in the tendon from the final tensioning state (i.e. $\Delta\epsilon_p^{(o)}$) first is added to the current 'concrete' strain (as derived from the nodal displacements) to form the total tendon strain. Then the stress-strain relationship of prestressing steel is applied to determine the total stress and the tangent modulus. Finally, the initial prestress is subtracted from the total stress before computing the internal node-force contribution from the tendon. The details of this procedure will be given in Section 10.5, where also stress relaxation and thermal strain are accounted for.

[1] For transformation of strains, see e.g. [10].

Chapter 7

Prestressing Bar (Pbar) Modeling

7.1 Introduction

The finite element formulation derived in Chapter 4 allows for introduction of lateral prestressing of the cross section. Although this is a rare solution compared to using ordinary shear reinforcement, considerable gain on the shear capacity may be the possible outcome. This optimistic prediction is based on the reflection that introducing prestress, brings the capacities of concrete and steel to act more in parallel. On the other hand, also a more brittle behavior is to be expected.

7.2 Geometry and Force Description

The structural unit used here to impose lateral prestressing is taken to be a prestressing bar, for short termed a 'pbar'. A group of pbars, smeared out in a rectangular plane that is both parallel to the longitudinal axis and spans the whole length of the corresponding element, is said to constitute a 'pbar panel'. In addition, the bars need to have uniform orientation, characterized by the angle β_b with the longitudinal element axis, and uniform intensities of cross section a_b and prestressing force p, both quantities measured per unit length normal to the bar axis. A pbar panel is depicted in Fig. 7.1. As will become clear in Section 10.2, pbar panels are incorporated into section units ('building blocks') of the 'line unit'-class when performing the cross section analysis. Thus, the endpoints of a pbar panel need to coincide with the extreme endpoints of the line units it is assigned to. In other words; a pbar panel may span several line units, but it needs to cover each one of them completely. Also; the beam cross section may contain several pbar panels.

Since pbars are straight and 'short', no loss of prestress due to friction will be considered. However, loss due to anchorage slip is accounted for. Similar to Eq.(6.48), this loss of prestress Δp is given by

$$\Delta p \;=\; \frac{E_b\, a_b\, u_s}{S_b} \tag{7.1}$$

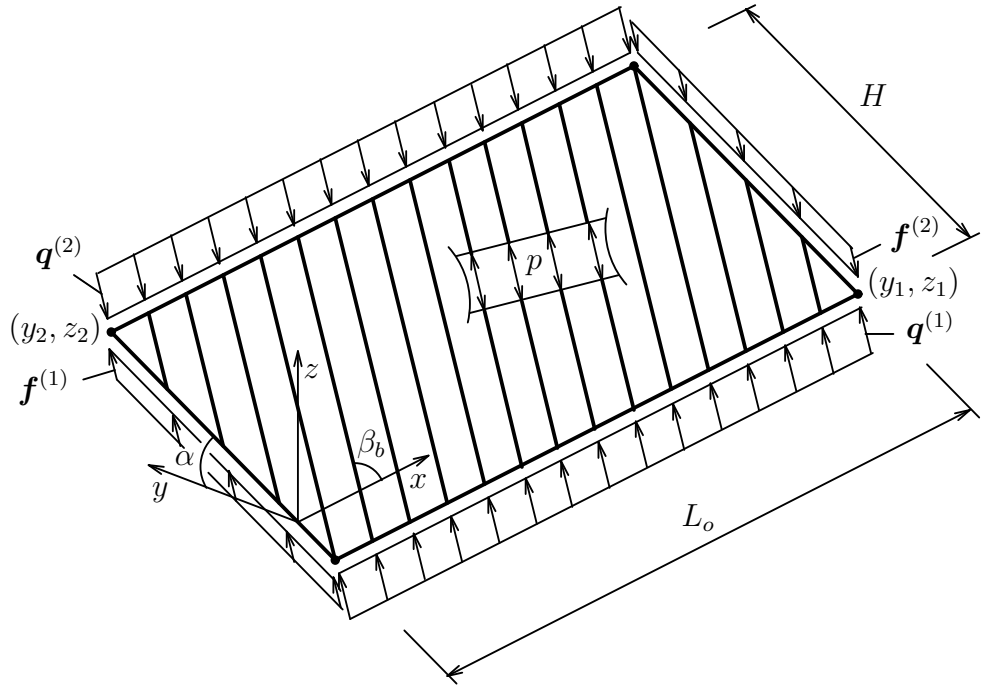

Figure 7.1: Pbar Panel

where E_b is the modulus of elasticity of pbar steel and u_s is the specific slip at the anchor. Furthermore, S_b is the characteristic pbar length taken as

$$S_b \;=\; \min\left(\frac{H}{|\sin\beta_b|}\,,\;\frac{L_o}{|\cos\beta_b|}\right) \tag{7.2}$$

Here L_o is the initial element length, and H is the pbar panel height expressed by

$$H \;=\; \sqrt{(y_2-y_1)^2 \;+\; (z_2-z_1)^2} \tag{7.3}$$

where the (y,z)-coordinates refer to the two longitudinal panel boundaries. Thus, the prestressing force intensity p at the final tensioning state becomes

$$p \;=\; p_o \;-\; \Delta p \tag{7.4}$$

where p_o is the value applied from the jack.

7.3 Applied Pbar Node-Force Vector

Before establishing the applied pbar node-force vector, the uniform prestressing force intensity p (i.e. force per unit length normal to the bar axis) has to be transformed to the (x,y,z)-system. By introducing the two reference vectors $(\boldsymbol{q}_{ref}, \boldsymbol{f}_{ref})$ of distributed forces per unit lengths, respectively in the longitudinal and transverse panel

directions, the corresponding transformations read

$$\boldsymbol{q}_{ref} \;=\; \left\{ \begin{array}{c} q_x \\ q_y \\ q_z \end{array} \right\}_{ref} \;=\; p \left\{ \begin{array}{c} \sin\beta_b \, \cos\beta_b \\ \sin^2\beta_b \, \cos\alpha \\ \sin^2\beta_b \, \sin\alpha \end{array} \right\} \tag{7.5}$$

$$\boldsymbol{f}_{ref} \;=\; \left\{ \begin{array}{c} f_x \\ f_y \\ f_z \end{array} \right\}_{ref} \;=\; p \left\{ \begin{array}{c} \cos^2\beta_b \\ \sin\beta_b \, \cos\beta_b \, \cos\alpha \\ \sin\beta_b \, \cos\beta_b \, \sin\alpha \end{array} \right\} \tag{7.6}$$

where α is the angle between the y-axis and the transverse panel direction. Note that the force intensities transform like stresses in the plane of the panel. The corresponding force resultant vector $\boldsymbol{F}_{ref}$ on a transverse section then becomes

$$\boldsymbol{F}_{ref} \;=\; \boldsymbol{f}_{ref} \, H \tag{7.7}$$

Since prestress loading in general is of the corotational kind, the pbar loads $(\boldsymbol{q}_o, \boldsymbol{F}_o)$ in configuration C_n with reference to C_{on} may be updated similarly to the tendon expressions in Eqs.(6.64,6.67). Thus

$$\boldsymbol{q}_o \;\approx\; h_l(\lambda_s) \, \boldsymbol{q}_{ref} \tag{7.8}$$

$$\boldsymbol{F}_o \;\approx\; h_l(\lambda_s) \, \boldsymbol{F}_{ref} \tag{7.9}$$

where again $h_l(\lambda_s)$ is the load scaling factor for the solution step, that typically takes values in the range $0 \le h_l(\lambda_s) \le 1$ for prestressing. Now the updated vector $\boldsymbol{q}_o^{(lb)}$ of distributed forces that act on the concrete along a longitudinal boundary '(lb)' of the panel, can be expressed by

$$\boldsymbol{q}_o^{(lb)} \;=\; \gamma^{(lb)} \, \boldsymbol{q}_o \tag{7.10}$$

while the corresponding vector $\boldsymbol{F}_o^{(en)}$ of section forces that act on the concrete at an external element node '(en)', takes the similar form

$$\boldsymbol{F}_o^{(en)} \;=\; \gamma^{(en)} \, \boldsymbol{F}_o \tag{7.11}$$

For both cases the factor γ, introduced to give the correct direction of the loading at the two boundaries and nodes, reads

$$\begin{aligned} \gamma^{(1)} &= \;\; 1 \\ \gamma^{(2)} &= -1 \end{aligned} \tag{7.12}$$

See also Fig. 7.1 for clarification.

The applied pbar node-force vector of the element can now be addressed. Like tendons, the pbar force vector takes contributions from the distributed forces per

unit axial length of the element, as well as the section forces at the external element nodes. The former contribution arises from uniform loading along each longitudinal boundary, and thus the expressions for $\boldsymbol{p}_{q^*}$ in Eq.(4.149) apply for each boundary load in turn. However, since the net distributed forces now are zero, i.e.

$$\boldsymbol{q}_o^* \;=\; \boldsymbol{q}_o^{(1)} \;+\; \boldsymbol{q}_o^{(2)} \;=\; \boldsymbol{0} \tag{7.13}$$

the resulting expressions for $\boldsymbol{p}_{q^*}$ simplify to

$$\begin{aligned}
&\boldsymbol{p}_{u_o}^{(q^*)} \;=\; \boldsymbol{0} && ;\;\; \boldsymbol{p}_{\theta_x}^{(q^*)} \;=\; \boldsymbol{0} \\
&\boldsymbol{p}_{v_o}^{(q^*)} \;=\; \begin{Bmatrix} -m_z^* \\ 0 \\ m_z^* \\ 0 \\ \frac{2}{3} m_z^* L_o \end{Bmatrix} && ;\;\; \boldsymbol{p}_{w_o}^{(q^*)} \;=\; \begin{Bmatrix} m_y^* \\ 0 \\ -m_y^* \\ 0 \\ \frac{2}{3} m_y^* L_o \end{Bmatrix} \\
&\boldsymbol{p}_{v_r}^{(q^*)} \;=\; -q_y L_o \begin{Bmatrix} y_2 - y_1 \\ y_2 z_2 - y_1 z_1 \end{Bmatrix} && ;\;\; \boldsymbol{p}_{w_r}^{(q^*)} \;=\; -q_z L_o \begin{Bmatrix} z_2 - z_1 \\ y_2 z_2 - y_1 z_1 \end{Bmatrix}
\end{aligned} \tag{7.14}$$

where the net distributed moment components are given by

$$\boldsymbol{m}^* \;=\; \begin{Bmatrix} m_x^* \\ m_y^* \\ m_z^* \end{Bmatrix} \;=\; \begin{Bmatrix} 0 \\ -\left(z_2 - z_1\right) q_x \\ \left(y_2 - y_1\right) q_x \end{Bmatrix} \tag{7.15}$$

and (q_x, q_y, q_z) are the components of $\boldsymbol{q}_o$ from Eq.(7.8). The force terms of the various subvectors correspond to the ordering of DOFs given in Eqs.(4.20-4.27).

The direct contribution $\boldsymbol{F}_o^{(en)}$ to the pbar node-force vector from force components at the external element node (en) is given already by Eq.(7.11). The derived moment components may be expressed on the form

$$\boldsymbol{M}^{(en)} \;=\; \begin{Bmatrix} M_x \\ M_y \\ M_z \end{Bmatrix}^{(en)} \;=\; \begin{Bmatrix} \bar{y} F_z \;-\; \bar{z} F_y \\ \bar{z} F_x \\ -\bar{y} F_x \end{Bmatrix}^{(en)} \tag{7.16}$$

where $(F_x, F_y, F_z)^{(en)}$ are the components of $\boldsymbol{F}_o^{(en)}$, and $(\bar{y}, \bar{z})$ are the centroidal coordinates of the panel section, i.e.

$$\begin{aligned} \bar{y} &= \tfrac{1}{2}(y_1 + y_2) \\ \bar{z} &= \tfrac{1}{2}(z_1 + z_2) \end{aligned} \tag{7.17}$$

Since the forces at the two ends cancel each other, i.e.

$$\boldsymbol{F}_o^{(1)} + \boldsymbol{F}_o^{(2)} = \boldsymbol{0} \tag{7.18}$$

no resulting contribution to the generalized load terms pertaining to the strain DOFs arises from the section forces at the external element nodes.

As for tendons, the simplifying procedure of applying the prestressing forces according to Eqs.(7.8,7.9) implies that the state of maximum prestress, i.e. after jacking but before anchorage loss, will not be properly accounted for. Also note that the preceding expressions work for any angle β_b of bar orientation, although, as stated introductorily, the main intention is to utilize pbars as shear reinforcement.

7.4 Pbar Load Correction Stiffness Matrix

Again the contributions arise from both distributed forces per unit axial length of the element and section forces at the external element nodes. The expressions involving the former contribution are referred to in conjunction with Eq.(4.187), now inserting $(\boldsymbol{q}_o^*, \boldsymbol{m}^*)$ from Eqs.(7.13,7.15) and the following relations for the generalized quantities pertaining to the strain DOFs

$$\begin{aligned} \boldsymbol{g}_{xy}^{(q^*)} &= -q_x \begin{Bmatrix} y_2 - y_1 \\ y_2 z_2 - y_1 z_1 \end{Bmatrix} \quad ; \quad \boldsymbol{g}_{yz}^{(q^*)} = -q_y \begin{Bmatrix} z_2 - z_1 \\ y_2 z_2 - y_1 z_1 \end{Bmatrix} \\ \boldsymbol{g}_{xz}^{(q^*)} &= -q_x \begin{Bmatrix} z_2 - z_1 \\ y_2 z_2 - y_1 z_1 \end{Bmatrix} \quad ; \quad \boldsymbol{g}_{zy}^{(q^*)} = -q_z \begin{Bmatrix} y_2 - y_1 \\ y_2 z_2 - y_1 z_1 \end{Bmatrix} \end{aligned} \tag{7.19}$$

where (q_x, q_y, q_z) are the components of $\boldsymbol{q}_o$ from Eq.(7.8). Since $(q_x^*, q_y^*, q_z^*, m_x^*)$ are all zero, several submatrices in Eq.(4.187) will vanish. Note that for this uniform loading the integrals for the remaining nonzero submatrices may easily be solved on explicit form. Of convenience, however, numerical integration is still retained.

The contribution to the load correction stiffness matrix from pbar panel loading acting at the external element node (en), takes a similar form as already given by Eqs.(6.71-6.75) for concentrated tendon forces. The components $(F_x, F_y, F_z)^{(en)}$ and $(M_x, M_y, M_z)^{(en)}$ are now given by Eqs.(7.11,7.16), respectively. In the submatrices that express the coupling to the strain DOFs, however, the (y, z)-location of the loading now has to be substituted by the force resultant location $(\bar{y}, \bar{z})$ from Eq.(7.17).

Furthermore, instead of the product (yz), also the combined mean value $(\overline{yz})$ intervenes, i.e.

$$\overline{yz} \;=\; \frac{1}{6}\,(y_1\,z_1 \;+\; 4\,\bar{y}\,\bar{z} \;+\; y_2\,z_2) \tag{7.20}$$

Finally note that the elimination of load corrections due to incremental rigid body translations, as explained in conjunction with Eq.(6.76) for concentrated tendon forces, also applies for the corresponding pbar forces.

7.5 Strain Analysis at the Tensioning State

The strain analysis at the tensioning state for pbars follows essentially the same procedure as described for tendons in Subsection 6.4.5. Thus, a brief revisit is sufficient.

The pbar steel strain $\epsilon_b^{(o)}$ at the final tensioning state may be expressed by

$$\epsilon_b^{(o)} \;=\; f^{-1}(\sigma_b^{(o)}) \;=\; f^{-1}(\frac{p}{a_b}) \tag{7.21}$$

Here the force intensity p is taken from Eq.(7.4), and a_b is the cross section area per unit length normal to the bar axis. Finally, $f^{-1}()$ symbolizes the inverse of the stress-strain relationship of pbar steel, as treated separately in Section 8.3. After equilibrium is achieved, the concrete strains

$$\boldsymbol{\epsilon}^T \;=\; \left[\begin{array}{cccccc} \epsilon_x & \gamma_{xy} & \gamma_{xz} & \epsilon_y & \epsilon_z & \gamma_{yz} \end{array}\right] \tag{7.22}$$

at the pbar location can be recovered using Eq.(4.52). Then the normal strain ϵ_t in the bar direction follows from the transformation

$$\epsilon_t \;=\; \boldsymbol{a}_t\,\boldsymbol{\epsilon} \tag{7.23}$$

where the transformation vector now takes the form

$$\begin{aligned} \boldsymbol{a}_t \;=\; \Big[\;& \cos^2\beta_b \quad \sin\beta_b\cos\beta_b\cos\alpha \quad \sin\beta_b\cos\beta_b\sin\alpha \\ & \sin^2\beta_b\cos^2\alpha \quad \sin^2\beta_b\sin^2\alpha \quad \sin^2\beta_b\sin\alpha\cos\alpha \;\Big] \end{aligned} \tag{7.24}$$

Thus, the additional pbar strain $\Delta\epsilon_b^{(o)}$ in relation to the surrounding concrete at the final tensioning state becomes

$$\Delta\epsilon_b^{(o)} \;=\; \epsilon_b^{(o)} \;-\; \epsilon_t \tag{7.25}$$

From now on bond between pbar and concrete will be established, which means that this strain difference will be retained throughout the remaining life of the structure.

7.6 Pbar Analysis after Bond

Again pbars are treated in accordance with the corresponding procedure for tendons as outlined in Subsection 6.4.6. Thus, the pbar forces from the final tensioning state are still retained as applied loading, while pbars are also contributing to the internal resistance of the structure with the amount of stress in excess of the initial prestress. As mentioned previously, pbar panels are added to 'building blocks' termed 'line units' when performing the cross section analysis. Details will be given in Section 10.2.

Chapter 8

Constitutive Modeling of Concrete and Steel

8.1 2D Rotating 'Smeared' Crack Model for Concrete

8.1.1 Introductory Considerations

Computer inspired modeling of concrete has grown to be an intensive area of research during the last two decades. Due to the material complexities, a wide variety of models has been proposed, ranging from simple orthotropic elasticity-based models down to microstructural modeling of the concrete constituents. While an approach of the latter kind may lead to better insight into fundamental plain concrete behavior, one still should look towards the other end of the scale when the purpose is to analyze large scale concrete structures. 'Complex' concrete models are naturally the more accurate at the constitutive level, but surely more consuming and often also less robust than 'simpler' ones. However, in a reinforced concrete setting the former models are not necessarily the more accurate any more (see e.g. [29]).

Cracking is a subject of major concern in concrete modeling. At the macro-level this is typically a localized phenomenon for plain concrete, while it converts to a more distributed process in presence of reinforcement. Thus, the concept of *'smeared'* cracks, which for plain concrete is merely an artifice, is more on line with the physical realities when it comes to reinforced concrete. Since concrete properties usually are derived from the plain concrete situation, it is often seen that concrete models applied to reinforced concrete problems possess the fracture energy-type of *softening* behavior, while the normally more important *tension stiffening* effect due to interaction with reinforcement is missing. Thus, in order to attain significant reinforced concrete behavior in a simplified manner, it may sometimes be fruitful to think in terms of reinforced concrete 'material properties'. Also the way cracks are treated after initiation is of importance. Due to redistribution of strains and stresses, cracks will in general change orientation. This is typically dominant when

the reinforcement yields in one direction. A *fixed* crack concept can not account for such variations properly, and may often lead to overstiff behavior (*stress-locking*) and overestimated collapse loads. The *rotating* crack concept provides a simple means to avoid stress-locking, and it has proved to agree reasonably well with observed behavior [30]. Here the current directions of principal strains and stresses are assumed to coincide, and thus stress build-up beyond the tensile strength can not occur.

One 2D rotating 'smeared' crack model that has gained special attention is the *modified compression field theory (MCFT)* by Vecchio and Collins [31]. It has been developed based on experimental results of 30 reinforced concrete panels tested under a variety of well-defined plane stress conditions. Here concrete is treated as an orthotropic nonlinear elastic material with unique stress-strain relationships in terms of average stresses and strains for the two principal directions. Unlike previous models, the compressive strength in MCFT degrades with the coexisting orthogonal tensile strain. Furthermore, the tension stiffening effect is included. Results obtained by finite element analyses using MCFT, with or without modifications, have been reported by several authors, e.g. [30],[32],[33]. Also this author has made an implementation of MCFT in a previous unpublished work. Here computed failure loads and deformation characteristics agreed well with experimental results, except for a test with nonproportional loading; a deficiency that seems to be a common problem for most models (ref. the predictions of panel D in [29]).

The constitutive model for concrete that will be presented in this work may be considered as an extension of MCFT. Although the shear-beam formulation allows for a 3D constitutive model, the derivation in the sequel will be restricted to 2D stress conditions. The reasons are twofold: The experimental basis for a full 3D formulation is still inadequate, and besides; since high-confinement dominated problems are not within the scope, a 2D version is considered sufficiently accurate to 'do the job'. Also for the latter reason, the Poisson effect is left out (as in MCFT). How the 2D constitutive model is combined with the 3D shear-beam formulation, will be treated in Chapter 10 in conjunction with the cross section analysis. Although this author considers the model in principle to be an extension of MCFT, it deviates substantially in several respects:

- The shape of the stress-strain relationship in compression is now described by a four-parameter expression (two in MCFT).

- The tension stiffening formulation is made dependent on the amount of reinforcement. In addition, the need for a separate stress control at cracks is eliminated.

- Introduction of increased compressive strength in biaxial compression and reduced tensile strength in tension/compression, both effects expressed in terms of the coexisting orthogonal strain.

- Unloading and reloading are accounted for.

- Various effects depending on time and temperature are included; like aging, strength under sustained loading, creep and shrinkage. These effects are treated separately in Chapter 9.

All expressions are held on explicit form, thus no iterational or integrational operations are needed at the constitutive level. Transitions are preferentially made 'smooth' (without concealing physical realities), and only a few state variables to account for history effects are introduced. These are circumstances that should improve the efficiency and robustness of the model, and reduce the need for computer-storage. In addition, the material input is limited to fairly standard parameters that are easily available.

8.1.2 Loading in Principal Compression

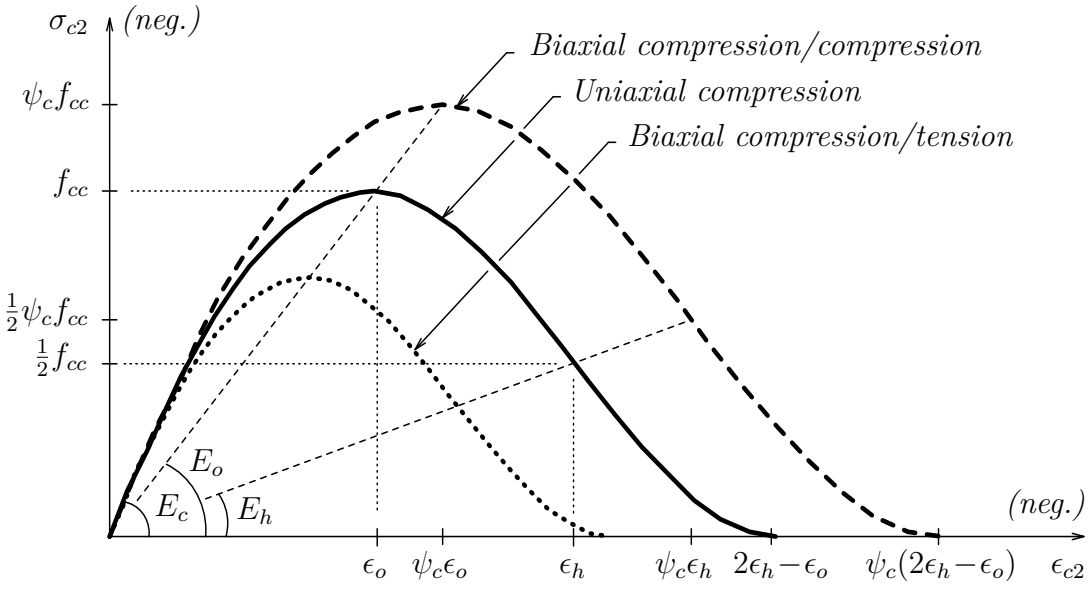

Figure 8.1: Compressive Stress-Strain Envelope for Concrete

The suggested stress-strain envelope for concrete in principal compression takes the form

$$\sigma_{c2}^{(e)} = \begin{cases} \psi_c E_c \epsilon_o e_{2\psi} \left[1 + \left(3\dfrac{f_{cc}}{E_c\epsilon_o} - 2 \right) e_{2\psi} + \left(1 - 2\dfrac{f_{cc}}{E_c\epsilon_o} \right) e_{2\psi}^2 \right] & ; 0 \le e_{2\psi} \le 1 \\ \dfrac{1}{4}\psi_c f_{cc} \left[4 - 3\left(\dfrac{e_{2\psi}-1}{e_h-1} \right)^2 + \left(\dfrac{e_{2\psi}-1}{e_h-1} \right)^3 \right] & ; 1 < e_{2\psi} \le 2e_h - 1 \\ 0 & ; 2e_h - 1 < e_{2\psi} \end{cases} \tag{8.1}$$

where the normalized strains are

$$e_{2\psi} = \frac{\epsilon_{c2}}{\psi_c \epsilon_o} \tag{8.2}$$

$$e_h = \frac{\epsilon_h}{\epsilon_o} \tag{8.3}$$

and with symbols defined in Fig. 8.1. Thus, the relationship is composed of two cubic polynomials, one for each of the ascending and descending branches. The resulting curve is C^1-continuous in its entire domain. Note that compressive strains and stresses, as well as the parameters $(f_{cc}, \epsilon_o, \epsilon_h)$, are all negative quantities. To account for biaxial effects, the curve is 'expanded' and 'contracted' as indicated on Fig. 8.1, based on the assumption that the moduli (E_c, E_o, E_h) can be regarded as constants. To keep E_c unchanged agrees with the results obtained by Kupfer et al. [34]. Also a constant E_o can be justified as 'reasonably accurate', based on the same reference. The corresponding assumption for E_h is primarily made here for simplicity. The confining effect of lateral reinforcement that leads to a substantial increase in ductility, may instead be accounted for directly in the input-value of ϵ_h. Some expressions for this parameter will be presented later in this subsection. The adjustments of the stress-strain relationship due to biaxial effects are controlled by the quantity ψ_c, that relates to the orthogonal principal strain ϵ_{c1}. The following expressions are suggested

$$\psi_c = \begin{cases} \dfrac{1}{0.8 - 0.34\, e_1} & ; e_1 \leq -1.03857 \\ 1 - 0.1231 e_1^2 & ; -1.03857 < e_1 \leq 0 \\ 1 + \gamma_c \left(\dfrac{e_1}{\eta_{c1}}\right)^2 \left(3 - 2\dfrac{e_1}{\eta_{c1}}\right) & ; 0 < e_1 \leq \eta_{c1} \\ 1 + \gamma_c \left[1 - 3\left(\dfrac{e_1 - \eta_{c1}}{\eta_{c2} - \eta_{c1}}\right)^2 + 2\left(\dfrac{e_1 - \eta_{c1}}{\eta_{c2} - \eta_{c1}}\right)^3\right] & ; \eta_{c1} < e_1 \leq \eta_{c2} \\ 1 & ; \eta_{c2} < e_1 \end{cases} \tag{8.4}$$

where the new normalized strain is

$$e_1 = \frac{\epsilon_{c1}}{\epsilon_o} \tag{8.5}$$

Here the first expression in Eq.(8.4) is taken from MCFT [31], while the second is a transition parabola proposed by Stevens et al. [32] in order to obtain C^1-continuity in the tensile strain region (i.e. e_1 negative). The two cubic expressions for the compressive strain region are new suggestions. Here, $(\gamma_c, \eta_{c1}, \eta_{c2})$ are internal parameters, whose values will be determined in Subsection 8.1.7 by a fit to the biaxial strength

results of Kupfer et al. [34]. These expressions render ψ_c C^1-continuous throughout the entire strain domain.

The tangent moduli are obtained by differentiation of Eq.(8.1). Thus for the 'direct' modulus

$$\frac{\partial \sigma_{c2}^{(e)}}{\partial \epsilon_{c2}} = \begin{cases} E_c \left[1 + 2\left(3\dfrac{f_{cc}}{E_c\epsilon_o} - 2\right) e_{2\psi} + 3\left(1 - 2\dfrac{f_{cc}}{E_c\epsilon_o}\right) e_{2\psi}^2\right] & ; 0 \le e_{2\psi} \le 1 \\ -\dfrac{3f_{cc}(e_{2\psi}-1)}{4\epsilon_o(e_h-1)^2}\left(2 - \dfrac{e_{2\psi}-1}{e_h-1}\right) & ; 1 < e_{2\psi} \le 2e_h - 1 \\ 0 & ; 2e_h - 1 < e_{2\psi} \end{cases} \tag{8.6}$$

The 'cross' modulus is conveniently derived using the chain rule

$$\frac{\partial \sigma_{c2}^{(e)}}{\partial \epsilon_{c1}} = \frac{\partial \sigma_{c2}^{(e)}}{\partial \psi_c} \frac{\partial \psi_c}{\partial \epsilon_{c1}} \tag{8.7}$$

where

$$\frac{\partial \sigma_{c2}^{(e)}}{\partial \psi_c} = \begin{cases} -E_c\epsilon_o e_{2\psi}^2 \left[3\dfrac{f_{cc}}{E_c\epsilon_o} - 2 + 2\left(1 - 2\dfrac{f_{cc}}{E_c\epsilon_o}\right) e_{2\psi}\right] & ; 0 \le e_{2\psi} \le 1 \\ \dfrac{1}{4} f_{cc}\left[4 + 3\dfrac{(e_{2\psi}-1)(e_{2\psi}+1)}{(e_h-1)^2} - \dfrac{(e_{2\psi}-1)^2(2e_{2\psi}+1)}{(e_h-1)^3}\right] & ; 1 < e_{2\psi} \le 2e_h - 1 \\ 0 & ; 2e_h - 1 < e_{2\psi} \end{cases} \tag{8.8}$$

$$\frac{\partial \psi_c}{\partial \epsilon_{c1}} = \begin{cases} \dfrac{0.34}{\epsilon_o(0.8 - 0.34\, e_1)^2} & ; e_1 \le -1.03857 \\ -\dfrac{0.2462\, e_1}{\epsilon_o} & ; -1.03857 < e_1 \le 0 \\ \dfrac{6\gamma_c e_1}{\epsilon_o \eta_{c1}^2}\left(1 - \dfrac{e_1}{\eta_{c1}}\right) & ; 0 < e_1 \le \eta_{c1} \\ -\dfrac{6\gamma_c(e_1 - \eta_{c1})}{\epsilon_o(\eta_{c2} - \eta_{c1})^2}\left(1 - \dfrac{e_1 - \eta_{c1}}{\eta_{c2} - \eta_{c1}}\right) & ; \eta_{c1} < e_1 \le \eta_{c2} \\ 0 & ; \eta_{c2} < e_1 \end{cases} \tag{8.9}$$

Here the last equation is obtained by differentiation of Eq.(8.4).

The suggested stress-strains relationship involves the four external material parameters $(f_{cc}, E_c, \epsilon_o, \epsilon_h)$, as defined in Fig. 8.1. While the first three are well known, ϵ_h

is more uncommon. However, in the final draft-version of Model Code 1990 (MC90) [35] an expression for the unconfined ϵ_h is given

$$\epsilon_{hu} = \left(\omega + \sqrt{\omega^2 - \frac{1}{2}}\right)\epsilon_o \tag{8.10}$$

where

$$\omega = \frac{1}{2}\left(\frac{1}{2}\frac{E_c\epsilon_o}{f_{cc}} + 1\right) \tag{8.11}$$

Of convenience, the relation is slightly rewritten here compared to MC90. Also Kent and Park have proposed expressions for ϵ_h, both unconfined as well as confined by rectangular hoops. The succeeding formulas are taken from [36], but modified here in order both to comply with the sign convention in this work and also to convert the strength-unit from psi to MPa. Thus, for the unconfined ϵ_h

$$\epsilon_{hu} = \frac{3 - 0.29f'_c}{145f'_c + 1000} \tag{8.12}$$

and the confined ϵ_h

$$\epsilon_{hc} = \epsilon_{hu} - \frac{3}{4}\rho_s\sqrt{\frac{b''}{s_h}} \tag{8.13}$$

Here f'_c is the concrete compressive cylinder strength (negative) in MPa, while ρ_s is the volume ratio of transverse reinforcement to concrete core measured to outside of hoops. Furthermore, b'' is the width of confined core measured to outside of hoops, and finally s_h is the spacing of hoops.

With a 3D constitutive model and the Poisson effect included, confinement-dominated problems may have been treated more consistently. However, as already stated, that is considered to be outside the scope of this work.

8.1.3 Tension Stiffening Model

Consider a reinforced concrete bar subjected to a gradually increasing tensile force. Initially, both concrete and reinforcement are in their linear elastic ranges. The first crack will open when the (randomly distributed) tensile strength of concrete is exceeded in the weakest section. Across the crack the tensile force is now carried by the reinforcement alone. However, due to bond between the two components, tensile stresses rebuild in the concrete and a corresponding stress reduction takes place in the reinforcement; until the original uniform strain state is recovered at a certain distance away from the crack. At slightly higher load levels additional cracks will form in the same manner. This crack formation process goes on until the spacing between cracks reaches a typical minimum value. Above this load level cracks are growing, but the crack pattern is almost stable. Finally, the load capacity of the bar is governed by yielding of the reinforcement. Since concrete after initial cracking still has an average tensile stress capability due to interaction with reinforcement,

the corresponding stiffness contribution may be interpreted as an additional stiffness of the tensile reinforcement. Thus, in the literature this effect is frequently termed *tension stiffening*.

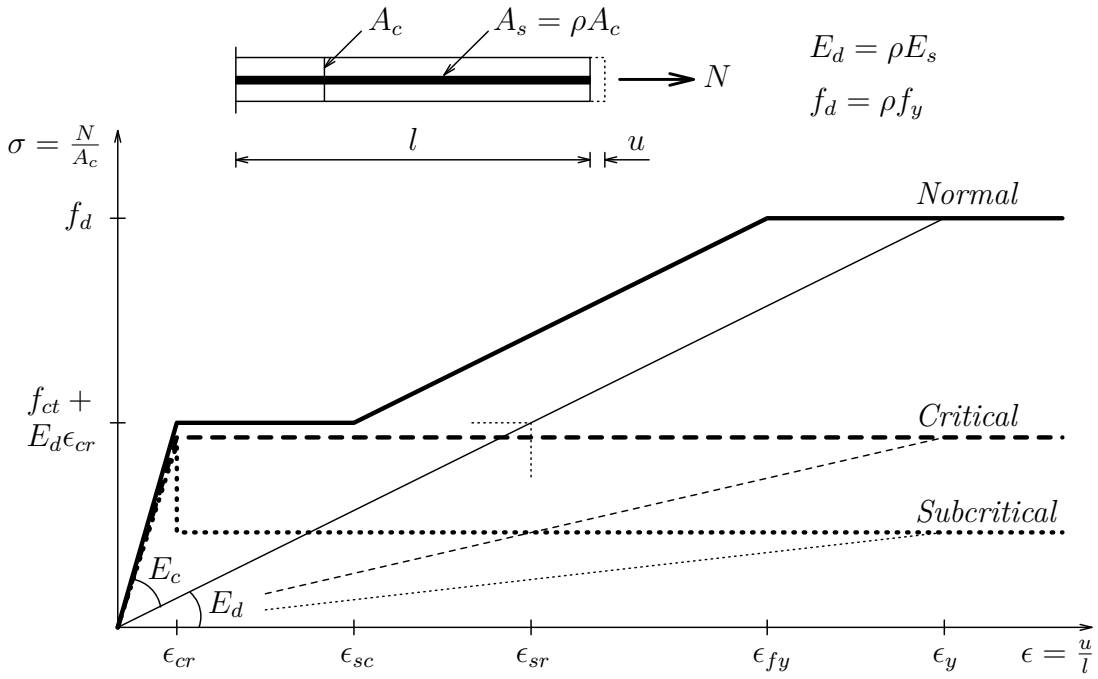

Figure 8.2: Response of Reinforced Concrete Tension Member

Noakowski and Krawinkler [37] have presented a deformation model for reinforced concrete in tension based on the simplifying assumptions that the two consecutive phases of crack formation and crack growth are taking place under constant force and constant tension stiffening, respectively. These assumptions make the model purely 'strain-driven', which is attractive in conjunction with displacement-based finite elements, since average strains then are known when the constitutive model is entered. The behavior of the model in terms of equivalent concrete stress versus average strain is depicted by the 'thick' solid line in Fig. 8.2. Here $(\epsilon_{cr}, \epsilon_{sc}, \epsilon_{fy})$ are the average strains at the incidents of first cracking, stabilized crack pattern and (first) yielding, respectively. The 'thin' solid line is for the response of reinforcement alone (or at cracks). Here $(\epsilon_{sr}, \epsilon_y)$ are the steel strains corresponding to initial cracking and yielding, respectively. Thus, the former strain is expressed by

$$\epsilon_{sr} \;=\; \epsilon_{cr} \;+\; \frac{f_{ct}}{E_d} \tag{8.14}$$

where f_{ct} is the tensile strength of concrete and E_d is the 'smeared' modulus of elasticity of reinforcing steel. In this work the tension stiffening coefficient b_t will be defined through

$$\epsilon_{sc} \;=\; \epsilon_{sr} \;-\; b_t \left(\epsilon_{sr} - \epsilon_{cr}\right) \tag{8.15}$$

This definition agrees with the adopted form in MC90 [35], but deviates slightly from the expression used in [37] where the ϵ_{cr}-term is omitted. The latter is believed to be a simplification, since the bond-slip arises from the strain difference $(\epsilon_{sr} - \epsilon_{cr})$ and not from ϵ_{sr} alone. In [37] a value of 0.42 for b_t is suggested, while MC90 recommends 0.40 for short-term loading and 0.25 for long-term or repeated loading; all values refer to deformed bars. Combination of Eqs.(8.14,8.15) gives for the average strain at the end of crack formation

$$\epsilon_{sc} = \epsilon_{cr} + (1 - b_t) \frac{f_{ct}}{E_d} \tag{8.16}$$

Since the tension stiffening effect is assumed constant throughout the crack growth phase, the average strain at start of yielding can be expressed

$$\epsilon_{fy} = \epsilon_y - b_t (\epsilon_{sr} - \epsilon_{cr}) \tag{8.17}$$

By using Eq.(8.14), the final form becomes

$$\epsilon_{fy} = \epsilon_y - b_t \frac{f_{ct}}{E_d} \tag{8.18}$$

The validity of the tension stiffening model limits to reinforcement ratios above the 'critical' level, as indicated in Fig. 8.2. In the 'subcritical' range the amount of reinforcement is insufficient to restrain the first crack that opens, and thus cracking converts to the localized phenomenon that characterizes the behavior of plain concrete. In a reinforced concrete beam section this situation may occur at locations (integration points) with light or no reinforcement in the vicinity. However, a properly designed beam will still exhibit an overall hardening response upon crack initiation. Thus, the situation with subcritical reinforcement will here only be covered by a simple softening model that approaches pure 'tension cut-off' for the bounding case of plain concrete. This behavior is depicted by the 'thick' dotted line in Fig. 8.2. The alternative to this vertical cut-off upon crack initiation would have been a softening formulation based on the fracture energy approach. However, that would involve the introduction of a maximum allowable element size in order to prevent 'snap-back' in the softening branch [38]. This requirement is related to the fracture energy of concrete, and it may limit the maximum element size to the order of 1 m. Such a restriction would be quite severe for a beam model, especially when the related phenomenon is believed to have minor influence on the overall behavior of reinforced concrete.

The presentation in this subsection has been focused on the combined response of concrete and reinforcement in tension. Of convenience, the two components will be modeled as separate materials in the sequel, but the important interaction effect of tension stiffening will be retained. This is simply done by modeling the reinforcement as 'steel alone' (indicated by 'thin' lines in Fig. 8.2), and assigning the remaining part of the combined response to the concrete. The modeling of reinforcing steel will be covered in more details in Section 8.2. Then hardening of the yield plateau is also included, although that has not been accounted for in the tension stiffening model. The modeling of concrete in principal tension follows in the next subsection.

Finally note that an inherent feature of the adopted tension stiffening model is that the sum of average forces in concrete and steel is always equal to the steel force at cracks. Thus, the need for a separate stress control at cracks is eliminated. This is in contrast to the tension stiffening formulation in MCFT.

8.1.4 Loading in Principal Tension

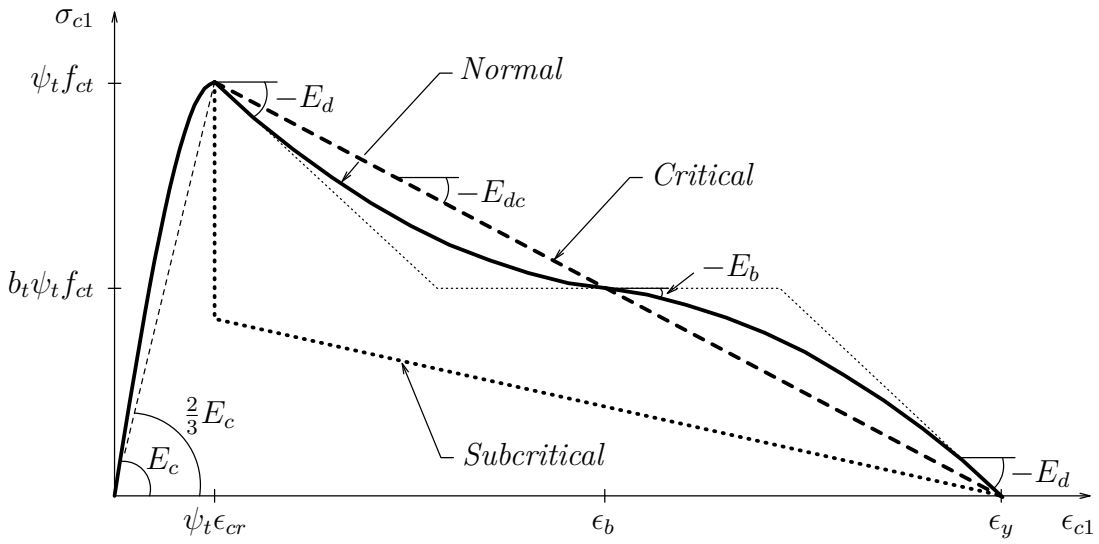

Figure 8.3: Tensile Stress-Strain Envelope for Concrete

The suggested the stress-strain envelope for concrete in principal tension is shown in Fig. 8.3. Compared to the response that can be derived directly from the tension stiffening model in the preceding subsection, some modifications of the shape are now made. These changes relate to the transitions between the various phases (i.e. pre-cracking, crack formation, crack growth and post-yielding). Although the response depicted in Fig. 8.2 is considered to be adequate, the abrupt transitions may cause numerical problems in a tangent stiffness formulation. Thus, the modifications are primarily introduced for the purpose of improving the numerical stability. However, since the actual physical behavior also tends to be more 'smooth' than shown in Fig. 8.2, some gain of accuracy may also be expected. To give the expressions for the proposed relationship, it is necessary to distinguish between reinforcement ratios above and below the critical level, i.e. for normal and subcritical reinforcement, respectively.

Normal, $E_d \geq E_{dc}$:

$$\sigma_{c1}^{(e)} = \begin{cases} \frac{3}{2} f_{ct} \frac{\epsilon_{c1}}{\epsilon_{cr}} \left[1 - \frac{1}{3} \left(\frac{\epsilon_{c1}}{\psi_t \epsilon_{cr}} \right)^2 \right] & ; 0 \leq \epsilon_{c1} \leq \psi_t \epsilon_{cr} \\ \psi_t f_{ct} - E_d(\epsilon_{c1} - \psi_t \epsilon_{cr}) + \frac{A_2(\epsilon_{c1} - \psi_t \epsilon_{cr})^2}{1 - b_t} + \frac{A_3(\epsilon_{c1} - \psi_t \epsilon_{cr})^3}{(1 - b_t)^2} & ; \psi_t \epsilon_{cr} < \epsilon_{c1} \leq \epsilon_b \\ E_d(\epsilon_y - \epsilon_{c1}) - \frac{A_2(\epsilon_y - \epsilon_{c1})^2}{b_t} - \frac{A_3(\epsilon_y - \epsilon_{c1})^3}{b_t^2} & ; \epsilon_b < \epsilon_{c1} \leq \epsilon_y \\ 0 & ; \epsilon_y < \epsilon_{c1} \end{cases} \tag{8.19}$$

Subcritical, $E_d < E_{dc}$:

$$\sigma_{c1}^{(e)} = \begin{cases} \frac{3}{2} f_{ct} \frac{\epsilon_{c1}}{\epsilon_{cr}} \left[1 - \frac{1}{3} \left(\frac{\epsilon_{c1}}{\psi_t \epsilon_{cr}} \right)^2 \right] & ; 0 \leq \epsilon_{c1} \leq \psi_t \epsilon_{cr} \\ E_d(\epsilon_y - \epsilon_{c1}) & ; \psi_t \epsilon_{cr} < \epsilon_{c1} \leq \epsilon_y \\ 0 & ; \epsilon_y < \epsilon_{c1} \end{cases} \tag{8.20}$$

where

$$\epsilon_{cr} = \frac{3}{2} \frac{f_{ct}}{E_c} \tag{8.21}$$

$$\epsilon_b = \psi_t \epsilon_{cr} + (1 - b_t)(\epsilon_y - \psi_t \epsilon_{cr}) \tag{8.22}$$

$$A_2 = \frac{2E_d + E_b - 3E_{dc}}{\epsilon_y - \psi_t \epsilon_{cr}} \tag{8.23}$$

$$A_3 = -\frac{E_d + E_b - 2E_{dc}}{(\epsilon_y - \psi_t \epsilon_{cr})^2} \tag{8.24}$$

$$E_{dc} = \frac{\psi_t f_{ct}}{\epsilon_y - \psi_t \epsilon_{cr}} \tag{8.25}$$

$$E_b = \begin{cases} 2E_{dc} - E_d & ; E_{dc} \leq E_d \leq 2E_{dc} \\ 0 & ; 2E_{dc} < E_d \end{cases} \tag{8.26}$$

Thus, instead of a linear relationship for the ascending branch, a cubic polynomial with a horizontal tangent at peak stress is introduced. In fact, the formula is a special case of the more generic expression for the ascending branch in compression, based on the constraint $E_o = \frac{2}{3} E_c$. For practical applications the suggested relationship corresponds fairly well with the bilinear form given in MC90 [35]. The descending

branch for the normal reinforcement case is composed of two cubic polynomials that constitute a C^1-continuous curve in the resulting domain. However, when the slope E_b at the internal connection point is nonzero, the variation reduces to quadratic form. In the limiting case of critical reinforcement (i.e. $E_d = E_{dc}$), the curve becomes linear. The tangents at the endpoints are always coinciding the lines of the C^0-continuous function derived directly from the tension stiffening model; indicated by the 'thin' dotted line in Fig. 8.3. The experimental results by Kupfer et al. [34] revealed a degrading tensile strength of concrete with an increasing orthogonal compressive stress. To account for this biaxial effect, the ascending branch is 'contracted' similarly as described for the compressive envelope, based on the assumption that the moduli ($E_c, E_o{=}\frac{2}{3}E_c$) can be regarded as constants. The adjustment is controlled by the quantity ψ_t, that is related to the orthogonal principal strain ϵ_{c2} through the suggested form

$$\psi_t \;=\; \begin{cases} 1 & ;e_2 \le 0 \\ f(e_2) & ;0 < e_2 \le 1 \\ 0 & ;1 < e_2 \end{cases} \tag{8.27}$$

where

$$e_2 \;=\; \frac{\epsilon_{c2}}{\epsilon_o} \tag{8.28}$$

$$\begin{aligned} f(e_2) \;=\; 1 + \frac{1}{\eta_t^2(1-\eta_t)^2} \Big\{ \Big[\gamma_t - 1 + \eta_t^3(4-3\eta_t)\Big]\, e_2^2 - 2\Big[\gamma_t - 1 + \eta_t^2(2-\eta_t^2)\Big]\, e_2^3 \\ + \Big[\gamma_t - 1 + \eta_t^2(3-2\eta_t)\Big]\, e_2^4 \Big\} \end{aligned} \tag{8.29}$$

Here (γ_t, η_t) are new internal parameters, linked through the relation $\gamma_t = f(\eta_t)$. Their values will be determined in Subsection 8.1.7 by a fit to the experimental results of Kupfer et al.. The suggested form renders ψ_t C^1-continuous throughout the entire strain domain. Since ϵ_o by definition is a negative quantity, the normalized strain e_2 becomes negative in tension.

In the preceding subsection the tension stiffening model was based on considering the behavior of a uniaxially loaded bar. There the reinforcing steel quantities (E_d, f_d, ϵ_y), i.e. 'smeared' modulus of elasticity, 'smeared' yield stress and yield strain, respectively, were as defined in Fig. 8.2. In the general case, however, with noncoinciding directions of reinforcement and principal tensile strain, a modified basis for these quantities is needed. Then the concept of *equivalent reinforcement*, that will be introduced in the following, provides a simple tool for this reinterpretation. At a certain location in the beam, consider a configuration of 'n' groups of reinforcement, all oriented in the same plane. Then the 'smeared' stress $\sigma_{si}^{(s)}$ in the reinforcement in direction 'i' is related to the in-plane principal strains $(\epsilon_{c1}, \epsilon_{c2})$ through

$$\sigma_{si}^{(s)} \;=\; \rho_i E_{si} \left(\epsilon_{c1} \cos^2\!\Delta\beta_i \;+\; \epsilon_{c2} \sin^2\!\Delta\beta_i\right) \tag{8.30}$$

where (ρ_i, E_{si}) are the area ratio and modulus of elasticity for the reinforcement, respectively, and $\Delta\beta_i$ is the angle between the principal tensile strain direction β_{c1} and the reinforcement direction β_{si}, i.e.

$$\Delta\beta_i \;=\; \beta_{si} \;-\; \beta_{c1} \tag{8.31}$$

The corresponding stress component in the principal tensile strain direction is given by

$$\sigma_{di} \;=\; \sigma_{si}^{(s)} \cos^2\Delta\beta_i \tag{8.32}$$

Insertion of Eq.(8.30) yields

$$\sigma_{di} \;=\; \rho_i E_{si} \cos^2\Delta\beta_i \left(\cos^2\Delta\beta_i \;+\; \mu\, \sin^2\Delta\beta_i\right) \epsilon_{c1} \tag{8.33}$$

where

$$\mu \;=\; \frac{\epsilon_{c2}}{\epsilon_{c1}} \tag{8.34}$$

Only reinforcement that is in tension will be accounted for in conjunction with the tension stiffening effect. Thus, the effective 'smeared' modulus in the principal tensile strain direction from reinforcement in the i-direction becomes

$$E_{di} \;=\; \begin{cases} \rho_i E_{si} \cos^2\Delta\beta_i \left(\cos^2\Delta\beta_i \;+\; \mu\, \sin^2\Delta\beta_i\right) & ;\mu \geq -\cot^2\Delta\beta_i \\ 0 & ;\mu < -\cot^2\Delta\beta_i \end{cases} \tag{8.35}$$

Summation of the contributions from the n individual groups of reinforcement yields the 'smeared' modulus of elasticity for the equivalent reinforcement in the principal tensile strain direction

$$E_d \;=\; \sum_{i=1}^{n} E_{di} \tag{8.36}$$

The effective 'smeared' yield stress in the principal tensile strain direction due to reinforcement in the i-direction may be obtained by a transformation similar to Eq.(8.32), i.e.

$$f_{di} \;=\; \begin{cases} \rho_i f_{yi} \cos^2\Delta\beta_i & ;\mu \geq -\cot^2\Delta\beta_i \\ 0 & ;\mu < -\cot^2\Delta\beta_i \end{cases} \tag{8.37}$$

where f_{yi} is the steel yield stress. Again, the reinforcement is included only if its current state is tension. Then the resulting 'smeared' yield stress for the equivalent reinforcement follows by summing the contributions from the individual groups. Thus

$$f_d \;=\; \sum_{i=1}^{n} f_{di} \tag{8.38}$$

Finally, the yield strain for the equivalent reinforcement becomes

$$\epsilon_y \;=\; \frac{f_d}{E_d} \tag{8.39}$$

For pbars, the 'yield' stress should be adjusted for the prestressing level. However, the deviation from perfectly elastic-plastic behavior will be disregarded here. Thus

$$\left.\begin{array}{rcl} E_{si} & \approx & E_b \\ f_{yi} & \approx & f_{0.2} - \sigma_b^{(o)} \end{array}\right\} Pbars \tag{8.40}$$

where E_b is the modulus of elasticity of pbar steel, while $(f_{0.2}, \sigma_b^{(o)})$ are the stress corresponding to 0.2% strain offset and the stress at the final tensioning state, respectively.

The tangent moduli are obtained by differentiation of Eq.(8.19/8.20) for reinforcement above and below the critical level, respectively. However, since the 'smeared' modulus of elasticity E_d now is a function of the principal strain ratio μ (ref. Eqs.(8.34-8.36), the expressions become quite involved. By applying the chain rule, the 'direct' modulus may take the form

$$\frac{\partial \sigma_{c1}^{(e)}}{\partial \epsilon_{c1}} = \left.\frac{\partial \sigma_{c1}^{(e)}}{\partial \epsilon_{c1}}\right|_{E_d} + \frac{\partial \sigma_{c1}^{(e)}}{\partial E_d}\frac{\partial E_d}{\partial \mu}\frac{\partial \mu}{\partial \epsilon_{c1}} \tag{8.41}$$

where the first term on the right hand side symbolizes differentiation when E_d is kept constant. Thus, from Eq.(8.19/8.20)

Normal, $E_d \geq E_{dc}$:

$$\left.\frac{\partial \sigma_{c1}^{(e)}}{\partial \epsilon_{c1}}\right|_{E_d} = \begin{cases} E_c\left[1 - \left(\dfrac{\epsilon_{c1}}{\psi_t \epsilon_{cr}}\right)^2\right] & ; 0 \leq \epsilon_{c1} \leq \psi_t \epsilon_{cr} \\ -E_d + \dfrac{2A_2(\epsilon_{c1} - \psi_t\epsilon_{cr})}{1 - b_t} + \dfrac{3A_3(\epsilon_{c1} - \psi_t\epsilon_{cr})^2}{(1-b_t)^2} & ; \psi_t\epsilon_{cr} < \epsilon_{c1} \leq \epsilon_b \\ -E_d + \dfrac{2A_2(\epsilon_y - \epsilon_{c1})}{b_t} + \dfrac{3A_3(\epsilon_y - \epsilon_{c1})^2}{b_t^2} & ; \epsilon_b < \epsilon_{c1} \leq \epsilon_y \\ 0 & ; \epsilon_y < \epsilon_{c1} \end{cases} \tag{8.42}$$

Subcritical, $E_d < E_{dc}$:

$$\left.\frac{\partial \sigma_{c1}^{(e)}}{\partial \epsilon_{c1}}\right|_{E_d} = \begin{cases} E_c\left[1 - \left(\dfrac{\epsilon_{c1}}{\psi_t \epsilon_{cr}}\right)^2\right] & ; 0 \leq \epsilon_{c1} \leq \psi_t \epsilon_{cr} \\ -E_d & ; \psi_t\epsilon_{cr} < \epsilon_{c1} \leq \epsilon_y \\ 0 & ; \epsilon_y < \epsilon_{c1} \end{cases} \tag{8.43}$$

The chain of derivatives in Eq.(8.41) accounts for the dependency of ϵ_{c1} through E_d. Here the first derivative follows from Eq.(8.19/8.20), when also using Eq.(8.39) whenever appropriate

Normal, $E_d \geq E_{dc}$:

$$\frac{\partial \sigma_{c1}^{(e)}}{\partial E_d} = \begin{cases} 0 & ; 0 \leq \epsilon_{c1} \leq \psi_t \epsilon_{cr} \\ -(\epsilon_{c1} - \psi_t \epsilon_{cr}) + \dfrac{\partial A_2}{\partial E_d} \dfrac{(\epsilon_{c1} - \psi_t \epsilon_{cr})^2}{1 - b_t} + \dfrac{\partial A_3}{\partial E_d} \dfrac{(\epsilon_{c1} - \psi_t \epsilon_{cr})^3}{(1 - b_t)^2} & ; \psi_t \epsilon_{cr} < \epsilon_{c1} \leq \epsilon_b \\ -\epsilon_{c1} - \dfrac{\partial A_2}{\partial E_d} \dfrac{(\epsilon_y - \epsilon_{c1})^2}{b_t} + \dfrac{2A_2(\epsilon_y - \epsilon_{c1})\epsilon_y}{b_t E_d} & \\ \quad - \dfrac{\partial A_3}{\partial E_d} \dfrac{(\epsilon_y - \epsilon_{c1})^3}{b_t^2} + \dfrac{3A_3(\epsilon_y - \epsilon_{c1})^2 \epsilon_y}{b_t^2 E_d} & ; \epsilon_b < \epsilon_{c1} \leq \epsilon_y \\ 0 & ; \epsilon_y < \epsilon_{c1} \end{cases} \tag{8.44}$$

Subcritical, $E_d < E_{dc}$:

$$\frac{\partial \sigma_{c1}^{(e)}}{\partial E_d} = \begin{cases} 0 & ; 0 \leq \epsilon_{c1} \leq \psi_t \epsilon_{cr} \\ -\epsilon_{c1} & ; \psi_t \epsilon_{cr} < \epsilon_{c1} \leq \epsilon_y \\ 0 & ; \epsilon_y < \epsilon_{c1} \end{cases} \tag{8.45}$$

where from Eqs.(8.23,8.24), and still using Eq.(8.39) whenever appropriate

$$\frac{\partial A_2}{\partial E_d} = \frac{1}{\epsilon_y - \psi_t \epsilon_{cr}} \left(A_2 \frac{\epsilon_y}{E_d} + 2 + \frac{\partial E_b}{\partial E_d} - 3 \frac{\partial E_{dc}}{\partial E_d} \right) \tag{8.46}$$

$$\frac{\partial A_3}{\partial E_d} = \frac{1}{(\epsilon_y - \psi_t \epsilon_{cr})^2} \left(2A_3 \frac{(\epsilon_y - \psi_t \epsilon_{cr})\epsilon_y}{E_d} - 1 - \frac{\partial E_b}{\partial E_d} + 2 \frac{\partial E_{dc}}{\partial E_d} \right) \tag{8.47}$$

Here $\partial E_b / \partial E_d$ can be found from Eq.(8.26)

$$\frac{\partial E_b}{\partial E_d} = \begin{cases} 2 \dfrac{\partial E_{dc}}{\partial E_d} - 1 & ; E_{dc} \leq E_d \leq 2E_{dc} \\ 0 & ; 2E_{dc} < E_d \end{cases} \tag{8.48}$$

and finally $\partial E_{dc} / \partial E_d$ from Eqs.(8.25,8.39)

$$\frac{\partial E_{dc}}{\partial E_d} = \frac{E_{dc}\, \epsilon_y}{E_d (\epsilon_y - \psi_t \epsilon_{cr})} \tag{8.49}$$

The remaining two terms in the chain of derivatives in Eq.(8.41) read

$$\frac{\partial E_d}{\partial \mu} = \sum_{i=1}^{n} \begin{cases} \rho_i E_{si} \cos^2\Delta\beta_i \, \sin^2\Delta\beta_i & ; \mu \geq -\cot^2\Delta\beta_i \\ 0 & ; \mu < -\cot^2\Delta\beta_i \end{cases} \tag{8.50}$$

$$\frac{\partial \mu}{\partial \epsilon_{c1}} = -\frac{\epsilon_{c2}}{\epsilon_{c1}^2} \tag{8.51}$$

Here the former equation originates from Eqs.(8.35,8.36), while the latter follows from Eq.(8.34). The 'cross' modulus, that reflects the biaxial effects, may also be derived using the chain rule

$$\frac{\partial \sigma_{c1}^{(e)}}{\partial \epsilon_{c2}} = \frac{\partial \sigma_{c1}^{(e)}}{\partial \psi_t} \frac{\partial \psi_t}{\partial \epsilon_{c2}} + \frac{\partial \sigma_{c1}^{(e)}}{\partial E_d} \frac{\partial E_d}{\partial \mu} \frac{\partial \mu}{\partial \epsilon_{c2}} \tag{8.52}$$

Here the first chain is caused by the effect of degrading tensile strength in tension/compression states, in which the first derivative follows from Eq.(8.19/8.20), depending on the amount of reinforcement. Thus

Normal, $E_d \geq E_{dc}$:

$$\frac{\partial \sigma_{c1}^{(e)}}{\partial \psi_t} = \begin{cases} f_{ct} \left(\dfrac{\epsilon_{c1}}{\psi_t \epsilon_{cr}} \right)^3 & ; 0 \leq \epsilon_{c1} \leq \psi_t \epsilon_{cr} \\ f_{ct} + E_d \epsilon_{cr} + \dfrac{\partial A_2}{\partial \psi_t} \dfrac{(\epsilon_{c1} - \psi_t \epsilon_{cr})^2}{1 - b_t} - \dfrac{2A_2(\epsilon_{c1} - \psi_t \epsilon_{cr})\epsilon_{cr}}{1 - b_t} & \\ \qquad + \dfrac{\partial A_3}{\partial \psi_t} \dfrac{(\epsilon_{c1} - \psi_t \epsilon_{cr})^3}{(1 - b_t)^2} - \dfrac{3A_3(\epsilon_{c1} - \psi_t \epsilon_{cr})^2 \epsilon_{cr}}{(1 - b_t)^2} & ; \psi_t \epsilon_{cr} < \epsilon_{c1} \leq \epsilon_b \\ -\dfrac{\partial A_2}{\partial \psi_t} \dfrac{(\epsilon_y - \epsilon_{c1})^2}{b_t} - \dfrac{\partial A_3}{\partial \psi_t} \dfrac{(\epsilon_y - \epsilon_{c1})^3}{b_t^2} & ; \epsilon_b < \epsilon_{c1} \leq \epsilon_y \\ 0 & ; \epsilon_y < \epsilon_{c1} \end{cases} \tag{8.53}$$

Subcritical, $E_d < E_{dc}$:

$$\frac{\partial \sigma_{c1}^{(e)}}{\partial \psi_t} = \begin{cases} f_{ct} \left(\dfrac{\epsilon_{c1}}{\psi_t \epsilon_{cr}} \right)^3 & ; 0 \leq \epsilon_{c1} \leq \psi_t \epsilon_{cr} \\ 0 & ; \psi_t \epsilon_{cr} < \epsilon_{c1} \leq \epsilon_y \\ 0 & ; \epsilon_y < \epsilon_{c1} \end{cases} \tag{8.54}$$

where

$$\frac{\partial A_2}{\partial \psi_t} = \frac{1}{\epsilon_y - \psi_t \epsilon_{cr}} \left(A_2 \epsilon_{cr} + \frac{\partial E_b}{\partial \psi_t} - 3 \frac{\partial E_{dc}}{\partial \psi_t} \right) \tag{8.55}$$

$$\frac{\partial A_3}{\partial \psi_t} = \frac{1}{(\epsilon_y - \psi_t \epsilon_{cr})^2} \left(2A_3(\epsilon_y - \psi_t \epsilon_{cr})\epsilon_{cr} - \frac{\partial E_b}{\partial \psi_t} + 2\frac{\partial E_{dc}}{\partial \psi_t} \right) \tag{8.56}$$

and

$$\frac{\partial E_{dc}}{\partial \psi_t} = \frac{1}{\epsilon_y - \psi_t \epsilon_{cr}} \left(f_{ct} + E_{dc}\epsilon_{cr} \right) \tag{8.57}$$

$$\frac{\partial E_b}{\partial \psi_t} = \begin{cases} 2\dfrac{\partial E_{dc}}{\partial \psi_t} & ; E_{dc} \le E_d \le 2E_{dc} \\ 0 & ; 2E_{dc} < E_d \end{cases} \tag{8.58}$$

Here the last four equations follow, in their order of appearance, from Eqs.(8.23-8.26), respectively. The second term in the first chain of derivatives in Eq.(8.52) can be obtained from Eqs.(8.27-8.29), and reads

$$\frac{\partial \psi_t}{\partial \epsilon_{c2}} = \begin{cases} 0 & ; e_2 \le 0 \\ \dfrac{\partial f(e_2)}{\partial \epsilon_{c2}} & ; 0 < e_2 \le 1 \\ 0 & ; 1 < e_2 \end{cases} \tag{8.59}$$

where

$$\begin{aligned} \frac{\partial f(e_2)}{\partial \epsilon_{c2}} = \frac{2}{\eta_t^2(1-\eta_t)^2\epsilon_o} \Big\{ &\left[\gamma_t - 1 + \eta_t^3(4 - 3\eta_t) \right] e_2 - 3\left[\gamma_t - 1 + \eta_t^2(2 - \eta_t^2) \right] e_2^2 \\ &+ 2\left[\gamma_t - 1 + \eta_t^2(3 - 2\eta_t) \right] e_2^3 \Big\} \end{aligned} \tag{8.60}$$

In the remaining chain of derivatives in Eq.(8.52), the first two terms are already expressed by Eq.(8.44/8.45) and Eq.(8.50), while the last term follows from Eq.(8.34), i.e.

$$\frac{\partial \mu}{\partial \epsilon_{c2}} = \frac{1}{\epsilon_{c1}} \tag{8.61}$$

Also a simplifying option for the normal reinforcement case has been implemented in the computer program that will be reviewed in Chapter 11. Then the stress-strain relation after cracking is assumed to follow the same linear curve as shown in Fig. 8.3 for critical reinforcement, and thus the formulation becomes independent of the tension stiffening coefficient b_t. The final expressions for this option are summarized in the following.

Simplified Normal, $E_d \geq E_{dc}$:
Stress-strain relation

$$\sigma_{c1}^{(e)} = \begin{cases} \frac{3}{2} f_{ct} \frac{\epsilon_{c1}}{\epsilon_{cr}} \left[1 - \frac{1}{3} \left(\frac{\epsilon_{c1}}{\psi_t \epsilon_{cr}} \right)^2 \right] & ; 0 \leq \epsilon_{c1} \leq \psi_t \epsilon_{cr} \\ \psi_t f_{ct} \frac{\epsilon_y - \epsilon_{c1}}{\epsilon_y - \psi_t \epsilon_{cr}} & ; \psi_t \epsilon_{cr} < \epsilon_{c1} \leq \epsilon_y \\ 0 & ; \epsilon_y < \epsilon_{c1} \end{cases} \tag{8.62}$$

'Direct' modulus

$$\frac{\partial \sigma_{c1}^{(e)}}{\partial \epsilon_{c1}} = \left. \frac{\partial \sigma_{c1}^{(e)}}{\partial \epsilon_{c1}} \right|_{\epsilon_y} + \frac{\partial \sigma_{c1}^{(e)}}{\partial \epsilon_y} \frac{\partial \epsilon_y}{\partial E_d} \frac{\partial E_d}{\partial \mu} \frac{\partial \mu}{\partial \epsilon_{c1}} \tag{8.63}$$

where

$$\left. \frac{\partial \sigma_{c1}^{(e)}}{\partial \epsilon_{c1}} \right|_{\epsilon_y} = \begin{cases} E_c \left[1 - \left(\frac{\epsilon_{c1}}{\psi_t \epsilon_{cr}} \right)^2 \right] & ; 0 \leq \epsilon_{c1} \leq \psi_t \epsilon_{cr} \\ -\frac{\psi_t f_{ct}}{\epsilon_y - \psi_t \epsilon_{cr}} & ; \psi_t \epsilon_{cr} < \epsilon_{c1} \leq \epsilon_y \\ 0 & ; \epsilon_y < \epsilon_{c1} \end{cases} \tag{8.64}$$

$$\frac{\partial \sigma_{c1}^{(e)}}{\partial \epsilon_y} \frac{\partial \epsilon_y}{\partial E_d} \frac{\partial E_d}{\partial \mu} \frac{\partial \mu}{\partial \epsilon_{c1}} = \begin{cases} 0 & ; 0 \leq \epsilon_{c1} \leq \psi_t \epsilon_{cr} \\ \frac{\psi_t f_{ct}}{E_d} \frac{(\epsilon_{c1} - \psi_t \epsilon_{cr}) \epsilon_y \epsilon_{c2}}{(\epsilon_y - \psi_t \epsilon_{cr})^2 \epsilon_{c1}^2} \frac{\partial E_d}{\partial \mu} & ; \psi_t \epsilon_{cr} < \epsilon_{c1} \leq \epsilon_y \\ 0 & ; \epsilon_y < \epsilon_{c1} \end{cases} \tag{8.65}$$

and $\partial E_d / \partial \mu$ given by Eq.(8.50).
'Cross' modulus

$$\frac{\partial \sigma_{c1}^{(e)}}{\partial \epsilon_{c2}} = \frac{\partial \sigma_{c1}^{(e)}}{\partial \psi_t} \frac{\partial \psi_t}{\partial \epsilon_{c2}} + \frac{\partial \sigma_{c1}^{(e)}}{\partial \epsilon_y} \frac{\partial \epsilon_y}{\partial E_d} \frac{\partial E_d}{\partial \mu} \frac{\partial \mu}{\partial \epsilon_{c2}} \tag{8.66}$$

where $\partial \psi_t / \partial \epsilon_{c2}$ given by Eqs.(8.59,8.60), and

$$\frac{\partial \sigma_{c1}^{(e)}}{\partial \psi_t} = \begin{cases} f_{ct} \left(\frac{\epsilon_{c1}}{\psi_t \epsilon_{cr}} \right)^3 & ; 0 \leq \epsilon_{c1} \leq \psi_t \epsilon_{cr} \\ f_{ct} \frac{(\epsilon_y - \epsilon_{c1}) \epsilon_y}{(\epsilon_y - \psi_t \epsilon_{cr})^2} & ; \psi_t \epsilon_{cr} < \epsilon_{c1} \leq \epsilon_y \\ 0 & ; \epsilon_y < \epsilon_{c1} \end{cases} \tag{8.67}$$

$$\frac{\partial \sigma_{c1}^{(e)}}{\partial \epsilon_y}\,\frac{\partial \epsilon_y}{\partial E_d}\,\frac{\partial E_d}{\partial \mu}\,\frac{\partial \mu}{\partial \epsilon_{c2}} = \begin{cases} 0 & ;0 \le \epsilon_{c1} \le \psi_t \epsilon_{cr} \\ -\dfrac{\psi_t f_{ct}}{E_d}\,\dfrac{(\epsilon_{c1}-\psi_t\epsilon_{cr})\epsilon_y}{(\epsilon_y-\psi_t\epsilon_{cr})^2\epsilon_{c1}}\,\dfrac{\partial E_d}{\partial \mu} & ;\psi_t\epsilon_{cr} < \epsilon_{c1} \le \epsilon_y \\ 0 & ;\epsilon_y < \epsilon_{c1} \end{cases} \tag{8.68}$$

Finally note that the formulation presented in this subsection will be subjected to a simple modification in Section 9.1 in order to account for time dependent effects. This becomes necessary since tension stiffening results from interaction between concrete and reinforcement, which are two materials with completely different time dependent characteristics.

8.1.5 Unloading and Reloading under Fixed Principal Directions

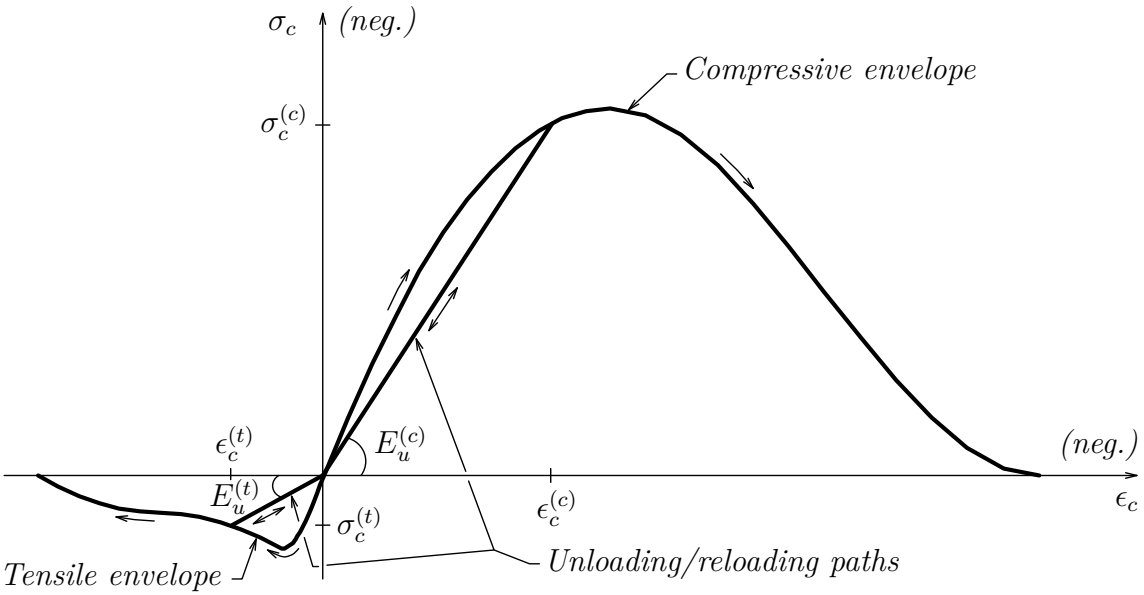

Figure 8.4: Generalized Stress-Strain Relationship for Concrete

Unloading and reloading in the sense *redistribution* of strains and stresses are almost inevitable in concrete structures, even for monotonic and sustained loading. Typically, such incidents may be caused by cracking and creep in concrete. Since concrete does not behave nonlinear elastic, distinction between the paths for loading and subsequent unloading and reloading should be made. However, actual *cyclic* behavior will not be a subject of primary concern in this work, and thus a very simple model for load reversals has been selected. As depicted in Fig. 8.4, unloading and reloading in both the compressive and tensile regimes are described by joint

linear paths that meet at the origin of the axis system. Indeed, this is a quite crude approximation, but compared to the test results of reinforced concrete panels subjected to cyclic shear, as reported in [32], this seems to be more adequate than the commonly seen alternative of adopting the initial modulus E_c as basis for unloading and reloading (e.g. [22],[23],[26],[27]). Besides, by letting the lines pass through the origin, no adjustments of the envelope relationships become necessary.

In principal compression the stress at the interior is then given by

$$\sigma_{c2}^{(i)} = E_{u2}^{(c)}\,\epsilon_{c2} \qquad ;\epsilon_{c2}^{(c)} \le \epsilon_{c2} \le 0 \tag{8.69}$$

where $\epsilon_{c2}^{(c)}$ denotes the strain at which the compressive stress reaches the envelope curve, and $E_{u2}^{(c)}$ is the slope of the joint unloading/reloading line in compression. The latter is determined by the strain and stress state $(\hat{\epsilon}_{c2}^{(c)}, \hat{\sigma}_{c2}^{(c)})$ when unloading took place, thus

$$E_{u2}^{(c)} = \begin{cases} \dfrac{\hat{\sigma}_{c2}^{(c)}}{\hat{\epsilon}_{c2}^{(c)}} & ;\hat{\epsilon}_{c2}^{(c)} < 0 \\ E_c & ;\hat{\epsilon}_{c2}^{(c)} = 0 \end{cases} \tag{8.70}$$

Note that $\hat{\epsilon}_{c2}^{(c)}$ in general is different from $\epsilon_{c2}^{(c)}$, since the location of the envelope curve is influenced by the value of the coexisting orthogonal strain ϵ_{c1} through the quantity ψ_c as explained in Subsection 8.1.2. In unloading/reloading no such biaxial effect is included, and thus the tangent moduli simply become

$$\frac{\partial \sigma_{c2}^{(i)}}{\partial \epsilon_{c2}} = E_{u2}^{(c)} \qquad ;\epsilon_{c2}^{(c)} \le \epsilon_{c2} \le 0 \tag{8.71}$$

$$\frac{\partial \sigma_{c2}^{(i)}}{\partial \epsilon_{c1}} = 0 \qquad ;\epsilon_{c2}^{(c)} \le \epsilon_{c2} \le 0 \tag{8.72}$$

In principal tension the corresponding expressions read

$$\sigma_{c1}^{(i)} = E_{u1}^{(t)}\,\epsilon_{c1} \qquad ;0 \le \epsilon_{c1} \le \epsilon_{c1}^{(t)} \tag{8.73}$$

$$E_{u1}^{(t)} = \begin{cases} \dfrac{\hat{\sigma}_{c1}^{(t)}}{\hat{\epsilon}_{c1}^{(t)}} & ;\hat{\epsilon}_{c1}^{(t)} > 0 \\ E_c & ;\hat{\epsilon}_{c1}^{(t)} = 0 \end{cases} \tag{8.74}$$

$$\frac{\partial \sigma_{c1}^{(i)}}{\partial \epsilon_{c1}} = E_{u1}^{(t)} \qquad ;0 \le \epsilon_{c1} \le \epsilon_{c1}^{(t)} \tag{8.75}$$

$$\frac{\partial \sigma_{c1}^{(i)}}{\partial \epsilon_{c2}} = 0 \qquad ;0 \le \epsilon_{c1} \le \epsilon_{c1}^{(t)} \tag{8.76}$$

Here $\epsilon_{c1}^{(t)}$ denotes the strain at which the tensile stress reaches the envelope curve, and $E_{u1}^{(t)}$ is the slope of the joint unloading/reloading line in tension. Furthermore, $(\hat{\epsilon}_{c1}^{(t)}, \hat{\sigma}_{c1}^{(t)})$ are the strain and stress when unloading took place. Again, $\hat{\epsilon}_{c1}^{(t)}$ is in general different from $\epsilon_{c1}^{(t)}$ due to biaxial effects in the envelope curve through the quantities ψ_t and μ, as dealt with in Subsection 8.1.4; while such effects are not included at the interior.

8.1.6 Stress State Search Procedure under Rotating Principal Directions

A consequence of abandoning the assumption of nonlinear elasticity for concrete, is that the stress-strain response now becomes history dependent. In the simple model for unloading/reloading that was introduced in the preceding subsection, the slopes $(E_u^{(c)}, E_u^{(t)})$ for each principal direction may serve as history parameters or state variables. This history effect is easy to deal with as long as the principal directions remain fixed. However, when they are allowed to rotate, the problem becomes much more obscure, and again simplifying assumptions must be called for. Probably simplest then is to assume that the history effect recorded at the previous equilibrium state for one principal direction also applies for the closest of the two current principal directions. In other words; the damage obtained in one direction is carried over to the next neighboring direction. Since it seems likely that some kind of damage influence must be present, this simple approach is believed to be acceptable, and thus it has been adopted in this work.

Based on these premises a search procedure for a new stress state has been derived. As demonstrated in the following, the steps are quite simple:

- For each principal direction j the following quantities are stored

$$E_{uj}^{(c)} \quad E_{uj}^{(t)} \qquad ; j = (\hat{1}, \hat{2})$$

  These are the recorded slopes for unloading/reloading in compression and tension. In addition, the angle $\beta_{c1}^{(p)}$ to the principal $\hat{1}$-direction at the previous equilibrium state is also stored. Note that the $(\hat{1}, \hat{2})$-directions correspond to the ordering of state variables. These directions are either identical to or the interchanged of the actual principal $(1, 2)$-directions at the previous equilibrium state. Initially, the slopes are set equal to E_c and the angle to zero.

- In each iteration the angle to the principal 1-direction is determined in the interval

$$-\frac{\pi}{2} \leq \beta_{c1} \leq \frac{\pi}{2}$$

  Then current and previous directions are compared through

  if

$$\beta_{c1}^{(p)} - \frac{\pi}{4} \leq \beta_{c1} \leq \beta_{c1}^{(p)} + \frac{\pi}{4}$$

then stored values for the previous directions j are valid for the current directions i

$$i/j \;=\; (1/\hat{1}, 2/\hat{2})$$

and the previous angle is updated by

$$\beta_{c1}^{(p)} \;=\; \beta_{c1}$$

else

then the correspondence between directions becomes

$$i/j \;=\; (1/\hat{2}, 2/\hat{1})$$

and the previous angle is updated by

$$\begin{aligned} \beta_{c1} > 0 \quad &\longrightarrow \quad \beta_{c1}^{(p)} \;=\; \beta_{c1} - \frac{\pi}{2} \\ \beta_{c1} \leq 0 \quad &\longrightarrow \quad \beta_{c1}^{(p)} \;=\; \beta_{c1} + \frac{\pi}{2} \end{aligned}$$

end if

- Now the new stress state $(\sigma_{ci}, (\partial\sigma_{ci}/\partial\epsilon_{ci}), (\partial\sigma_{ci}/\partial\epsilon_{cn}))$ in the principal i-direction can be evaluated based on the found combination of directions i/j and the known current principal strains $(\epsilon_{ci}, \epsilon_{cn})$, where n denotes the the normal (orthogonal) direction of i.

  if

  $$\epsilon_{ci} \;\geq\; 0$$

  then tensile regime
  compute stresses

  $$\begin{aligned} \sigma_{ci}^{(e)} \quad &- \quad \text{Eq.(8.19/8.20/8.62)} \\ \sigma_{ci}^{(i)} \quad &- \quad \text{Eq.(8.73)} \end{aligned}$$

  if

  $$\sigma_{ci}^{(e)} \;>\; \sigma_{ci}^{(i)}$$

  then at the interior
  new stress state becomes

  $$\begin{aligned} \sigma_{ci} \;&=\; \sigma_{ci}^{(i)} \\ \frac{\partial\sigma_{ci}}{\partial\epsilon_{ci}} \;&=\; \frac{\partial\sigma_{ci}^{(i)}}{\partial\epsilon_{ci}} \quad - \quad \text{Eq.(8.75)} \\ \frac{\partial\sigma_{ci}}{\partial\epsilon_{cn}} \;&=\; \frac{\partial\sigma_{ci}^{(i)}}{\partial\epsilon_{cn}} \quad - \quad \text{Eq.(8.76)} \end{aligned}$$

else

then at the envelope

new stress state becomes

$$\sigma_{ci} = \sigma_{ci}^{(e)}$$

$$\frac{\partial \sigma_{ci}}{\partial \epsilon_{ci}} = \frac{\partial \sigma_{ci}^{(e)}}{\partial \epsilon_{ci}} \quad - \quad \text{Eqs.(8.41ff./8.63ff.)}$$

$$\frac{\partial \sigma_{ci}}{\partial \epsilon_{cn}} = \frac{\partial \sigma_{ci}^{(e)}}{\partial \epsilon_{cn}} \quad - \quad \text{Eqs.(8.52ff./8.66ff.)}$$

and state variable is updated

$$E_{uj}^{(t)} \quad - \quad \text{Eq.(8.74)}$$

where

$$\hat{\epsilon}_{cj}^{(t)} = \epsilon_{ci}$$
$$\hat{\sigma}_{cj}^{(t)} = \sigma_{ci}^{(e)}$$

end if

else

then compressive regime

compute stresses

$$\sigma_{ci}^{(e)} \quad - \quad \text{Eq.(8.1)}$$
$$\sigma_{ci}^{(i)} \quad - \quad \text{Eq.(8.69)}$$

if

$$\sigma_{ci}^{(e)} < \sigma_{ci}^{(i)}$$

then at the interior

new stress state becomes

$$\sigma_{ci} = \sigma_{ci}^{(i)}$$

$$\frac{\partial \sigma_{ci}}{\partial \epsilon_{ci}} = \frac{\partial \sigma_{ci}^{(i)}}{\partial \epsilon_{ci}} \quad - \quad \text{Eq.(8.71)}$$

$$\frac{\partial \sigma_{ci}}{\partial \epsilon_{cn}} = \frac{\partial \sigma_{ci}^{(i)}}{\partial \epsilon_{cn}} \quad - \quad \text{Eq.(8.72)}$$

else

then at the envelope

new stress state becomes

$$\sigma_{ci} = \sigma_{ci}^{(e)}$$

$$\frac{\partial \sigma_{ci}}{\partial \epsilon_{ci}} = \frac{\partial \sigma_{ci}^{(e)}}{\partial \epsilon_{ci}} \quad - \quad \text{Eq.(8.6)}$$

$$\frac{\partial \sigma_{ci}}{\partial \epsilon_{cn}} = \frac{\partial \sigma_{ci}^{(e)}}{\partial \epsilon_{cn}} \quad - \quad \text{Eqs.(8.7ff.)}$$

and state variable is updated

$$E_{uj}^{(c)} \quad - \quad \text{Eq.(8.70)}$$

where

$$\hat{\epsilon}_{cj}^{(c)} = \epsilon_{ci}$$
$$\hat{\sigma}_{cj}^{(c)} = \sigma_{ci}^{(e)}$$

end if

end if

- Finally, if the found stress state belongs to a global equilibrium state, the updated combination of state variables is saved. Otherwise, the state variables pertaining to the previous equilibrium state are retained as basis for the stress state search in the next iteration cycle.

Note that the stress at the previous equilibrium state $\sigma_{cj}^{(p)}$ in addition is stored as a history parameter since this quantity enters into the computations of creep and aging strains in Sections 9.5 and 9.6, as well as the computation of strength under sustained loading in Subsection 9.3.3. For reasons that will become clear in Section 9.7, the stresses $(\hat{\sigma}_{cj}^{(c)}, \hat{\sigma}_{cj}^{(t)})$ corresponding to the extreme strains, are also stored.

8.1.7 Calibration of Biaxial Strength Parameters

The biaxial effect on strength in the stress-strain envelopes for compression and tension was introduced through the quantities (ψ_c, ψ_t), as expressed by Eqs.(8.4,8.27ff.), respectively. In these expressions the internal parameters $((\gamma_c, \eta_{c1}, \eta_{c2}), (\gamma_t, \eta_t))$ appeared. The objective now is to quantify these parameters by a fit to the experimental results of Kupfer et al. [34] on concrete strength under biaxial stresses.

From Eqs.(8.1,8.19/8.20/8.62) it follows that the apparent compressive and tensile strengths (f_{aci}, f_{ati}) in the principal i-direction and the biaxial effect quantities

(ψ_{ci}, ψ_{ti}) are related through

$$\frac{f_{aci}}{f_{cc}} = \psi_{ci}(\epsilon_{cn}) \tag{8.77}$$

$$\frac{f_{ati}}{f_{ct}} = \psi_{ti}(\epsilon_{cn}) \tag{8.78}$$

where ϵ_{cn} is the current principal strain in the normal (orthogonal) direction of i. Since the biaxial effects considered here are for states of combined compression/compression and tension/compression, the corresponding stress $\sigma_{cn}^{(e)}$ in the n-direction will be compressive only, and thus it may be expressed through Eq.(8.1). However, it is desirable now to have this stress on a purely normalized form, which is not possible with the adopted three-parameter expression for the ascending branch in Eq.(8.1). For this reason, the following simplified replacement is introduced

$$\frac{\sigma_{cn}^{(e)}}{f_{cc}} = \frac{\epsilon_{cn}}{\epsilon_o}\left[2 - \frac{\epsilon_{cn}}{\psi_{cn}(\epsilon_{ci})\,\epsilon_o}\right] \quad ; 0 \leq \frac{\epsilon_{cn}}{\psi_{cn}\epsilon_o} \leq 1 \tag{8.79}$$

This expression is similar to the one adopted in MCFT, but deviates in the respect that the biaxial effect here intervenes in both the stress and strain direction as demonstrated in Fig. 8.1. Note that Eq.(8.79) will only be employed for the purpose of calibrating the internal strength parameters. Beyond that, the more versatile ascending branch in Eq.(8.1) is adopted in this work. However, for ordinary concrete the practical differences between the two expressions are believed to be minor.

Now the calibration procedure can be addressed. This is basically a simple trial-and-comparison procedure, based on the main steps:

- Select a set of values for the internal parameters, i.e.

$$\begin{array}{llll} \gamma_c & \eta_{c1} \quad \eta_{c2} & - & \text{compression/compression} \\ \gamma_t & \eta_t & - & \text{tension/compression} \end{array}$$

- For the region of interest, compute pairs of apparent strength and coexisting orthogonal stress, i.e.

$$\begin{array}{lll} \dfrac{f_{aci}}{f_{cc}} \quad \dfrac{\sigma_{cn}^{(e)}}{f_{cc}} & - & \text{compression/compression} \\ \dfrac{f_{ati}}{f_{ct}} \quad \dfrac{\sigma_{cn}^{(e)}}{f_{cc}} & - & \text{tension/compression} \end{array}$$

- Compare computed results with experimental results by Kupfer et al. [34].

For the strength and stress computations further elaboration is needed. In combined compression/compression the substeps then consist of the loop:

1. Select values of the principal strain ratio e_{ni} in increasing order from the following interval, starting at the lower boundary

$$0 \leq e_{ni} = \frac{\epsilon_{cn}}{\epsilon_{ci}} \leq 1$$

2. Search for the strain state $(\tilde{\epsilon}_{ci}, \tilde{\epsilon}_{cn})$ corresponding to $(f_{aci}, \sigma_{cn}^{(e)})$ by iteration, applying $\tilde{\epsilon}_{cn} = e_{ni}\tilde{\epsilon}_{ci}$ and Eq.(8.4). This state is found when

$$\frac{f_{aci}}{f_{cc}} = \psi_{ci} \approx \frac{\tilde{\epsilon}_{ci}}{\epsilon_o}$$

3. Compute $\dfrac{\sigma_{cn}^{(e)}}{f_{cc}}$, using Eqs.(8.4,8.79).

4. Return to item 1. until the upper boundary for e_{ni} is reached.

The corresponding substeps in combined tension/compression become simpler, since the biaxial effect in the n-direction now is neglectable (i.e. $\psi_{cn} \approx 1$) due to the small tensile strain at cracking in the i-direction (ref. the second expression in Eq.(8.4)). Thus, the loop may then take the form:

1. Select values of the strain ratio e_n in increasing order from the following interval, starting at the lower boundary

$$0 \leq e_n = \frac{\epsilon_{cn}}{\epsilon_o} \leq 1$$

2. Compute $\dfrac{f_{ati}}{f_{ct}} = \psi_{ti}$, using Eq.(8.29).

3. Compute $\dfrac{\sigma_{cn}^{(e)}}{f_{cc}}$ by Eq.(8.79), assuming $\psi_{cn} = 1$.

4. Return to item 1. until the upper boundary for e_n is reached.

By running this calibration procedure for several sets of internal parameter values, good agreement with the results by Kupfer et al. was obtained at moderate to high combinations of biaxial compression and in the whole region of tension/compression, using the values

$$\begin{array}{llll} \gamma_c = 0.25 & \eta_{c1} = 0.4 & \eta_{c2} = 2.0 & - \text{ compression/compression} \\ \gamma_t = 0.4 & \eta_t = 0.5 & & - \text{ tension/compression} \end{array} \tag{8.80}$$

Then based on these parameter values, the complete biaxial strength envelope may be formed. The result becomes as depicted in Fig. 8.5. Here a ratio between the uniaxial strengths of $f_{ct}/f_{cc} = -0.1$ has been used. As indicated, only poor fit to the results by Kupfer et al. is obtained in the regions with low biaxial compression. However, this has been a necessary compromise to make in order to have smooth transitions into compression/tension, where the response basically is based on MCFT (ref. the two first expressions in Eq.(8.4)).

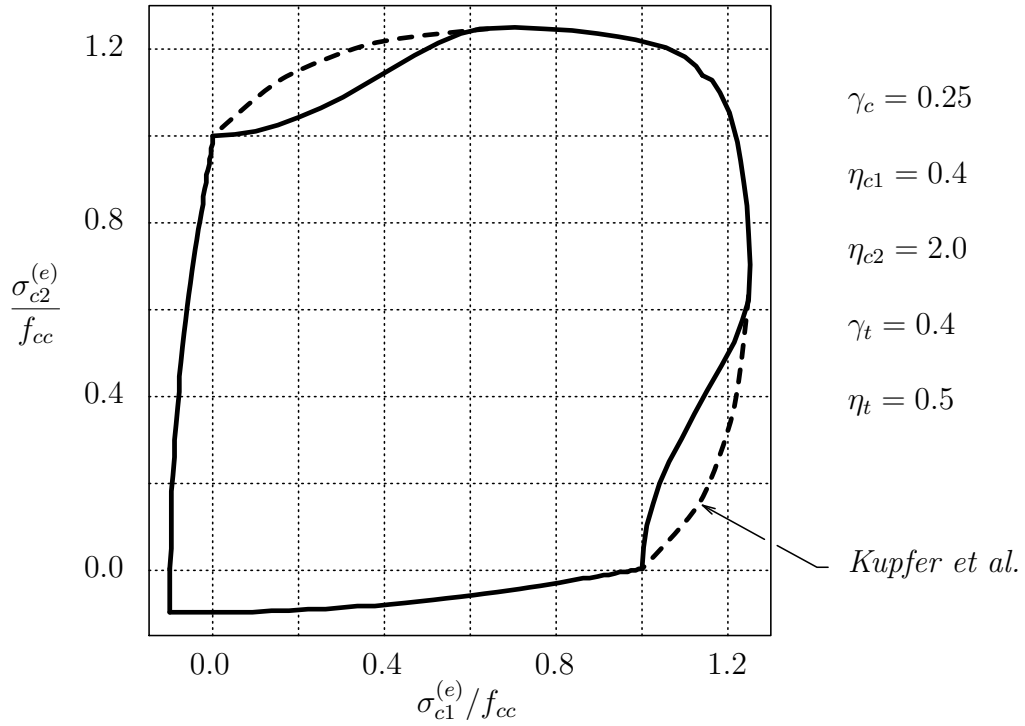

Figure 8.5: Derived Biaxial Strength Envelope

8.2 Reinforcing Steel

The adopted stress-strain relationship for reinforcing steel on 'smeared' form is depicted in Fig. 8.6. The response is piecewise linear, and as indicated, properties are assumed to be equal in tension and compression. Unloading and reloading are described by joint paths with slope as for initial elastic loading. The total elastic range is assumed to stay constant (kinematic hardening). Thus, the relationship is characterized by the three material parameters (f_y, E_s, E_y), which are the yield stress and the elastic and plastic hardening moduli, respectively. In addition, the steel to concrete area ratio ρ is introduced to attain the 'smeared' form. Finally, the history dependency is taken care of through the strain ϵ_r, corresponding to intersection between the unloading/reloading line and the parallel to the yield lines through the origin. Initially ϵ_r is set to zero. By using the current strain in excess of ϵ_r, i.e. $(\epsilon_s - \epsilon_r)$, as basis for the stress state search, the relationship takes the simple form

$$\sigma_s^{(s)} = \begin{cases} -\rho f_y + \rho E_y(\epsilon_s + \epsilon_y) & ; \epsilon_s - \epsilon_r < -\epsilon_y \\ \rho E_y \epsilon_r + \rho E_s(\epsilon_s - \epsilon_r) & ; -\epsilon_y \leq \epsilon_s - \epsilon_r \leq \epsilon_y \\ \rho f_y + \rho E_y(\epsilon_s - \epsilon_y) & ; \epsilon_y < \epsilon_s - \epsilon_r \end{cases} \tag{8.81}$$

where

$$\epsilon_y = \frac{f_y}{E_s} \tag{8.82}$$

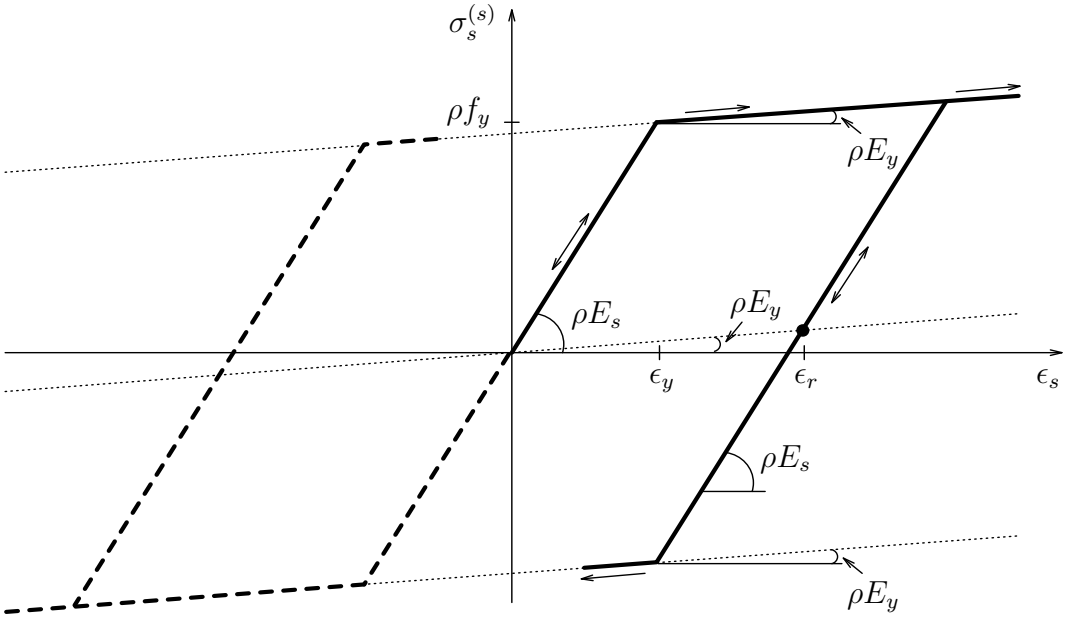

Figure 8.6: Stress-Strain Relationship for 'Smeared' Reinforcing Steel

The tangent modulus becomes

$$\frac{\partial \sigma_s^{(s)}}{\partial \epsilon_s} = \begin{cases} \rho E_y & ; \epsilon_s - \epsilon_r < -\epsilon_y \\ \rho E_s & ; -\epsilon_y \leq \epsilon_s - \epsilon_r \leq \epsilon_y \\ \rho E_y & ; \epsilon_y < \epsilon_s - \epsilon_r \end{cases} \tag{8.83}$$

and the history parameter is updated by

$$\tilde{\epsilon}_r = \begin{cases} \epsilon_s + \epsilon_y & ; \epsilon_s - \epsilon_r < -\epsilon_y \\ \epsilon_r & ; -\epsilon_y \leq \epsilon_s - \epsilon_r \leq \epsilon_y \\ \epsilon_s - \epsilon_y & ; \epsilon_y < \epsilon_s - \epsilon_r \end{cases} \tag{8.84}$$

If the found stress state belongs to a global equilibrium state, the updated history parameter is saved. Otherwise, the parameter pertaining to the previous equilibrium state is retained as basis for the stress state search in the next iteration cycle.

8.3 Prestressing Steel

8.3.1 Stress-Strain Relationship

As depicted in Fig. 8.7, only the tensile part of the stress-strain relationship for prestressing steel will be considered. Since cold-worked steel has no distinct yield limit, a smooth transition in terms of a cubic polynomial has been introduced between

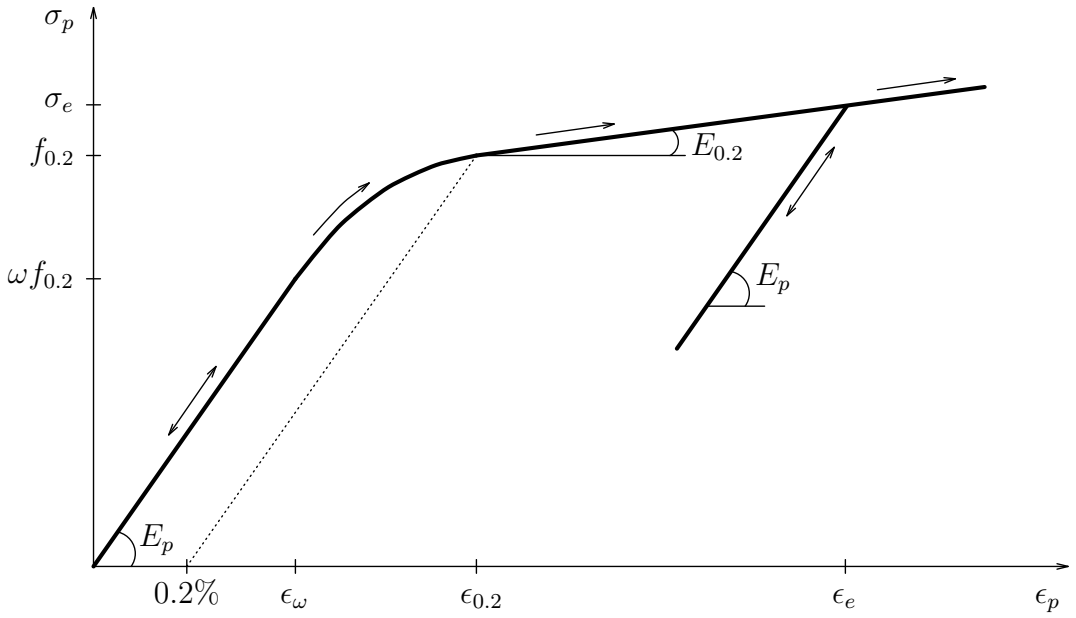

Figure 8.7: Stress-Strain Relationship for Prestressing Steel

the linear ranges of elastic and plastic hardening behavior. Consequently, the envelope curve becomes C^1-continuous in the entire domain. Unloading and reloading are described by joint linear paths with slope as for initial elastic loading. Thus, the relationship may be characterized by the four material parameters $(f_{0.2}, \omega, E_p, E_{0.2})$, which are the stress at 0.2% strain offset, the elasticity-limit factor, and the elastic and plastic hardening moduli, respectively. In addition, the maximum recorded strain ϵ_e is included as a history parameter. The expressions for the stress and the tangent modulus then become

Loading:

$$\sigma_p^{(e)} = \begin{cases} E_p\,\epsilon_p & ;\epsilon_p \le \epsilon_\omega \\ \omega f_{0.2} + E_p(\epsilon_p - \epsilon_\omega)\left[1 - \left(2 + \dfrac{E_{0.2}}{E_p} - \dfrac{3(1-\omega)f_{0.2}}{E_p(\epsilon_{0.2}-\epsilon_\omega)}\right)\dfrac{\epsilon_p - \epsilon_\omega}{\epsilon_{0.2}-\epsilon_\omega}\right. & \\ \qquad\qquad \left. + \left(1 + \dfrac{E_{0.2}}{E_p} - \dfrac{2(1-\omega)f_{0.2}}{E_p(\epsilon_{0.2}-\epsilon_\omega)}\right)\left(\dfrac{\epsilon_p - \epsilon_\omega}{\epsilon_{0.2}-\epsilon_\omega}\right)^2\right] & ;\epsilon_\omega < \epsilon_p \le \epsilon_{0.2} \\ f_{0.2} + E_{0.2}(\epsilon_p - \epsilon_{0.2}) & ;\epsilon_{0.2} < \epsilon_p \end{cases} \tag{8.85}$$

$$\frac{\partial \sigma_p^{(e)}}{\partial \epsilon_p} = \begin{cases} E_p & ; \epsilon_p \leq \epsilon_\omega \\ E_p \left[1 - 2 \left(2 + \dfrac{E_{0.2}}{E_p} - \dfrac{3(1-\omega) f_{0.2}}{E_p(\epsilon_{0.2} - \epsilon_\omega)} \right) \dfrac{\epsilon_p - \epsilon_\omega}{\epsilon_{0.2} - \epsilon_\omega} \right. & \\ \qquad \left. + 3 \left(1 + \dfrac{E_{0.2}}{E_p} - \dfrac{2(1-\omega) f_{0.2}}{E_p(\epsilon_{0.2} - \epsilon_\omega)} \right) \left(\dfrac{\epsilon_p - \epsilon_\omega}{\epsilon_{0.2} - \epsilon_\omega} \right)^2 \right] & ; \epsilon_\omega < \epsilon_p \leq \epsilon_{0.2} \\ E_{0.2} & ; \epsilon_{0.2} < \epsilon_p \end{cases} \tag{8.86}$$

where

$$\epsilon_\omega = \frac{\omega f_{0.2}}{E_p} \tag{8.87}$$

$$\epsilon_{0.2} = \frac{f_{0.2}}{E_p} + 0.002 \tag{8.88}$$

Unloading/reloading:

$$\sigma_p^{(i)} = \sigma_e - E_p(\epsilon_e - \epsilon_p) \quad ; \epsilon_p \leq \epsilon_e \tag{8.89}$$

$$\frac{\partial \sigma_p^{(i)}}{\partial \epsilon_p} = E_p \quad ; \epsilon_p \leq \epsilon_e \tag{8.90}$$

Here σ_e is the stress corresponding to ϵ_e, as determined by Eq.(8.85). Note that in order to secure a monotonic envelope curve, it may be shown that the elasticity-limit factor must satisfy the following constraint

$$\omega \leq 1 - \frac{E_p(E_p + 2E_{0.2})10^{-3}}{f_{0.2}(E_p - E_{0.2})} \tag{8.91}$$

The search procedure for a new stress state now takes the simple form:

if

$$\epsilon_p \geq \epsilon_e$$

then at the envelope

new stress state becomes

$$\sigma_p = \sigma_p^{(e)} \quad - \quad \text{Eq.(8.85)}$$

$$\frac{\partial \sigma_p}{\partial \epsilon_p} = \frac{\partial \sigma_p^{(e)}}{\partial \epsilon_p} \quad - \quad \text{Eq.(8.86)}$$

and history parameter is updated

$$\epsilon_e \;=\; \epsilon_p$$

else

then at the interior

new stress state becomes

$$\begin{aligned} \sigma_p &= \sigma_p^{(i)} \quad - \quad \text{Eq.(8.89)} \\ \frac{\partial \sigma_p}{\partial \epsilon_p} &= \frac{\partial \sigma_p^{(i)}}{\partial \epsilon_p} \quad - \quad \text{Eq.(8.90)} \end{aligned}$$

end if

Only if the found stress state belongs to a global equilibrium state, the updated history parameter ϵ_e is saved. Otherwise, the parameter pertaining to the previous equilibrium state is retained as basis for the stress state search in the next iteration cycle. Note that the stress at the previous equilibrium state enters into the computation of relaxation in prestressing steel, as dealt with in Section 9.8. Thus, this quantity is also stored as a history parameter.

So far, the presentation in this subsection has focused on plain prestressing steel modeling, as will be the selected formulation in conjunction with tendons. Pbars, however, are more conveniently treated as 'smeared' steel. Then conversion to the 'smeared' form is obtained through

$$\sigma_b^{(s)} = \rho\, \sigma_b \tag{8.92}$$

$$\frac{\partial \sigma_b^{(s)}}{\partial \epsilon_b} = \rho\, \frac{\partial \sigma_b}{\partial \epsilon_b} \tag{8.93}$$

Here ρ is the steel to concrete area ratio, and $((\sigma_b), (\partial \sigma_b / \partial \epsilon_b))$ are as expressed by Eqs.((8.85/8.89),(8.86/8.90)), respectively; now using 'b' as subscript instead of 'p'. Besides this, no further adjustments are necessary.

8.3.2 Steel Strain at the Tensioning State

The strain analysis at the tensioning state has already been covered in Subsection 6.4.5 and Section 7.5 for tendons and pbars, respectively. However, no specific expression was given with respect to the steel strain, ref. the general form of Eqs.(6.79,7.21). This problem is in fact the opposite of the one treated in the preceding subsection, i.e. find the strain for a given stress. Prior to loss due to anchorage slip the solution is to be sought on the envelope curve. Thus, the initial value of the

maximum recorded strain ϵ_{eo} may be found by inverting Eq.(8.85)

$$\epsilon_{eo} = \begin{cases} \dfrac{\sigma_{eo}}{E_p} & ;\sigma_{eo} \leq \omega f_{0.2} \\ g^{-1}(\sigma_{eo}) & ;\omega f_{0.2} < \sigma_{eo} \leq f_{0.2} \\ \epsilon_{0.2} + \dfrac{\sigma_{eo} - f_{0.2}}{E_{0.2}} & ; f_{0.2} < \sigma_{eo} \end{cases} \tag{8.94}$$

Here σ_{eo} is the tensioning stress prior to anchorage loss, and $g^{-1}()$ symbolizes the inverse of the second expression in Eq.(8.85). Since this expression is a cubic polynomial, no simple formula for the inverse exists. However, the problem can be solved in several ways, e.g. by Newton-Raphson iteration according to the scheme:

1. From a value $\epsilon_{eo}^{(i)}$, compute $\sigma_{eo}^{(i)}$ by the second expression in Eq.(8.85). With the actual shape of the curve, a 'safe' start value is

$$\epsilon_{eo}^{(1)} = \epsilon_{\omega} + \frac{\sigma_{eo} - \omega f_{0.2}}{E_p}$$

2. Compute the corresponding value of the tangent modulus $E_{eo}^{(i)}$ by applying the second expression in Eq.(8.86).

3. Compute the strain increment

$$\Delta\epsilon_{eo}^{(i+1)} = \frac{\sigma_{eo} - \sigma_{eo}^{(i)}}{E_{eo}^{(i)}}$$

4. Update the strain

$$\epsilon_{eo}^{(i+1)} = \epsilon_{eo}^{(i)} + \Delta\epsilon_{eo}^{(i+1)}$$

5. Check convergence

   if

$$\frac{|\Delta\epsilon_{eo}^{(i+1)}|}{\epsilon_{eo}^{(i+1)}} < C_{tol}$$

   where C_{tol} is a convergence tolerance parameter, say 10^{-3}

   then $\epsilon_{eo} \approx \epsilon_{eo}^{(i+1)}$, and stop

   else

   then return to item 1. with $\epsilon_{eo}^{(i+1)}$ as the current strain value

   end if

Having determined the strain ϵ_{eo} prior to loss due to anchorage slip, the steel strain $\epsilon_p^{(o)}$ at the final tensioning state (i.e. after slip) is then given by the inverse of Eq.(8.89). Thus

$$\epsilon_p^{(o)} = \epsilon_{eo} - \frac{\sigma_{eo} - \sigma_p^{(o)}}{E_p} \quad ; \sigma_p^{(o)} \leq \sigma_{eo} \tag{8.95}$$

where $\sigma_p^{(o)}$ is the stress at the final tensioning state.

Finally, the expressions for the tensioning stresses before and after anchorage loss will be resumed. For tendons these are given by

$$\sigma_{eo} = \frac{P_o}{A_p} \tag{8.96}$$

$$\sigma_p^{(o)} = \frac{P}{A_p} \tag{8.97}$$

Here A_p is the tendon cross section area, and P is the tendon force after anchorage slip, as summarized in Eq.(6.47). Prior to slip, the force P_o is composed of the two sub-expressions from Eqs.(6.31,6.32), that summarized reads

$$P_o = \begin{cases} P_1\, e^{-(\mu\bar{\kappa} + k)\, S} & ; 0 \leq S \leq S_r \\ P_2\, e^{-(\mu\bar{\kappa} + k)\,(S_t - S)} & ; S_r < S \leq S_t \end{cases} \tag{8.98}$$

See also Fig. 6.4 for clarification. For pbars the corresponding stress-expressions become (now again using 'b' as subscript instead of 'p')

$$\sigma_{eo} = \frac{p_o}{a_b} \tag{8.99}$$

$$\sigma_b^{(o)} = \frac{p}{a_b} \tag{8.100}$$

where (a_b, p_o, p) are the intensities of cross section and prestressing forces, applied from the jack and after anchorage loss, respectively; all quantities measured per unit length normal to the bar axis. The latter force is determined by Eqs.(7.4,7.1).

Chapter 9

Models for Time and Temperature Dependent Effects

9.1 The Concept of Mechanical and Nonmechanical Strains

Like other investigators, e.g. [22]-[27], the analysis of time dependent behavior of concrete structures will here be based on decomposition of the total strain ϵ into so-called *mechanical* strain $\epsilon^{(m)}$ and *nonmechanical* strain $\epsilon^{(n)}$, i.e.

$$\epsilon \;=\; \epsilon^{(m)} \;+\; \epsilon^{(n)} \tag{9.1}$$

Mechanical strain is understood to be the short-time or instantaneous stress-producing strain. Consequently, the independent variables in the stress-strain relationships in Chapter 8 are now taken as mechanical strains. Thus

$$\sigma \;=\; f(\epsilon^{(m)}) \tag{9.2}$$

where for the individual structural components, the strain reads

$$\epsilon^{(m)} \;=\; \begin{cases} \epsilon_c & - \quad \textit{concrete} \\ \epsilon_s & - \quad \textit{reinforcing bars (rebars)} \\ \epsilon_p & - \quad \textit{prestressing tendons} \\ \epsilon_b & - \quad \textit{prestressing bars (pbars)} \end{cases} \tag{9.3}$$

All other kinds of strain considered in this work, are classified as nonmechanical. These strains are

$$\epsilon^{(n)} \;=\; \begin{cases} \epsilon_{cT} + \epsilon_{cs} + \epsilon_{cc} + \epsilon_{ca} & - \quad \textit{concrete} \\ \epsilon_{sT} & - \quad \textit{all steel materials} \end{cases} \tag{9.4}$$

where $(\epsilon_{cT}, \epsilon_{sT})$ are the thermal strains, and $(\epsilon_{cs}, \epsilon_{cc}, \epsilon_{ca})$ are the time dependent strains due to shrinkage, creep and aging, respectively. Relaxation in prestressing steel is also included as a time dependent effect, based on a pure stress-formulation, and thus it is not accounted for through strain decomposition.

This simple procedure of first deriving the stress-strain relationship based on the short-time situation, and then include time and temperature effects through strain decomposition as an afterthought, works well for a constitutive model involving one material component only. When the stress-strain behavior depends on mixed properties of concrete and steel, as is the case for tension stiffening, special considerations should be taken. Obviously, the short-time stress-strain envelope formulation for concrete in principal tension, as presented in Subsection 8.1.4, could have been made with all strain components present. That would have led to a somewhat more complicated formulation. Instead, the following simple modification of the existing formulation will be made: In all pertinent expressions, substitute the yield strain ϵ_y of the equivalent reinforcement by the modified yield strain $\hat{\epsilon}_y$, given by

$$\hat{\epsilon}_y \;=\; \epsilon_y \;-\; \epsilon_{cs} \;-\; \epsilon_{cc} \;-\; \epsilon_{ca} \tag{9.5}$$

where ϵ_y is taken from Eq.(8.39); and then apply the preceding strain decomposition for concrete. With this modification the apparent extent of the stress-strain diagram along the mechanical strain axis is reduced. However, in a total strain reference, this implies that the strain 'stretching' due to long-time effects now is prevented, since such effects should not be placed on the yield strain of reinforcing steel. Furthermore, it is here also assumed that the thermal strains of concrete and steel are approximately equal, which normally holds true.

Finally note that an initial load correction due to nonmechanical strains, as e.g. addressed by Kang [22], will not be included in this work. The reason is that this load term automatically enters into the load residual in the succeeding equilibrium iteration of Eq.(5.49).

9.2 Thermal Strain in Concrete and Steel

The thermal strains for the concrete and steel components are given by

$$\epsilon_{cT} \;=\; \alpha_c\,(T - T_o) \tag{9.6}$$

$$\epsilon_{sT} \;=\; \alpha_s\,(T - T_o) \tag{9.7}$$

where (α_c, α_s) are the coefficients of thermal expansion for concrete and steel, respectively. These are normally taken to be equal. Furthermore, (T, T_o) are respectively the current temperature and the reference temperature at the location; both determined from Eq.(5.73). For concrete and rebars T_o may be taken as the temperature at which the pertaining element was included in a structural system for the first time, while for tendons and pbars the temperature at the tensioning state may apply[1].

[1]The latter suggestion is in fact already implemented in Eqs.(6.84,7.25); that otherwise should have taken the form (subscripts 'p'/'b' omitted): $\Delta\epsilon^{(o)} = \epsilon^{(o)} + \epsilon_{sT} - \epsilon_t$.

9.3 Effects on Concrete Stress-Strain Parameters

9.3.1 Aging

The expressions given in this subsection are basically taken from the final draft-version of Model Code 1990 (MC90) [35]. Deviations from MC90 that are made will be stated. Also the notation will differ somewhat from MC90 to better fit with notation used elsewhere in this work.

The development of mean concrete compressive strength f_{cm} with temperature adjusted age t_T is given by

$$f_{cm}(t_T) \;=\; \mathcal{B}_{cc}(t_T)\, f_{cm28} \tag{9.8}$$

where

$$\mathcal{B}_{cc}(t_T) \;=\; \exp\left\{ m \left[1 - \sqrt{\frac{28}{t_T/t_1}} \right] \right\} \tag{9.9}$$

$$t_T \;=\; \sum_{i=1}^{n} \Delta t_i \exp\left\{ -\left[\frac{4000}{273 + \overline{T}_i/T_1} - 13.65 \right] \right\} \tag{9.10}$$

and with the remaining quantities

f_{cm28} – mean compressive strength at the age $t_T = 28$ days

m – coefficient depending on the type of cement mix, i.e.

$$m \;=\; \begin{cases} 0.20 & - \text{ rapid hardening high strength cement} \\ 0.25 & - \text{ normal and rapid hardening cements} \\ 0.38 & - \text{ slowly hardening cement} \end{cases}$$

t_1 = 1 day

Δt_i – generic time step [days]

$\overline{T}_i$ – average temperature [^oC] during Δt_i

T_1 = 1 ^oC

Here $\overline{T}_i$ may be obtained by superimposing the corresponding time averages ($\overline{T}_{st}, \overline{\Delta T}$) from respectively the mean seasonal component and the deviation from the mean, i.e.

$$\overline{T}_i \;=\; \overline{T}_{st}(\Delta t_i) \;+\; \overline{\Delta T}(\Delta \lambda_i) \tag{9.11}$$

Since $\overline{T}_{st}$ originates from the periodic expression in Eq.(5.72), it may easily be determined analytically. Thus

$$\overline{T}_{st}(\Delta t_i) \;=\; \frac{1}{\Delta t_i} \int_{t_{i-1}}^{t_i} \overline{T}_s(t)\, dt \tag{9.12}$$

where

$$\Delta t_i \;=\; t_i \;-\; t_{i-1} \tag{9.13}$$

The solution becomes

$$\overline{T}_{st}(\Delta t_i) = \frac{\overline{T}_{max} + \overline{T}_{min}}{2} - \frac{\overline{T}_{max} - \overline{T}_{min}}{2} \frac{\Delta t_{yr}}{2\pi\, \Delta t_i} \left[\sin\left(\frac{2\pi}{\Delta t_{yr}}\, t_i \right) - \sin\left(\frac{2\pi}{\Delta t_{yr}}\, t_{i-1} \right) \right] \tag{9.14}$$

Here $(\overline{T}_{max}, \overline{T}_{min})$ are the mean values of maximum and minimum seasonal temperature, respectively, and Δt_{yr} is the duration of a year. The $\overline{\Delta T}$-contribution originates from the temperature deviation history, as dealt with in Subsection 5.3.6, and thus may not so easily be expressed on a simple exact form. Here this contribution is determined by taking the average of the values at the boundaries in the pertinent interval of λ, i.e.

$$\overline{\Delta T}(\Delta\lambda_i) \;\approx\; \frac{1}{2}\left[\Delta T(\lambda_i) \;+\; \Delta T(\lambda_{i-1})\right] \tag{9.15}$$

where $(\lambda_i, \lambda_{i-1})$ are the values of the history parameter that correspond to (t_i, t_{i-1}); as linked through the time history concept (Subsection 5.3.4). Note that the $\overline{\Delta T}$-contribution normally will vanish, since the temperature deviation component ΔT primarily is introduced for investigating extreme thermal effects at a certain instant of time.

Although not stated in MC90, the aging relation in Eq.(9.8) will be assumed valid for any statistical fractile of concrete compressive strength. Thus

$$f_{cc}(t_T) \;=\; \mathcal{B}_{cc}(t_T)\; f_{cc28} \tag{9.16}$$

where (f_{cc}, f_{cc28}) denote corresponding strength-values at a temperature adjusted age t_T and $t_T = 28$ days, respectively.

For the development of tensile strength with age, no explicit expression is given in MC90. Here for simplicity, a similar relationship to that of compressive strength will be applied up to $t_T = 28$ days. Beyond that, no further increase of strength will be accounted for. On the other hand, adverse effect due to sustained loading will also be left out (Subsection 9.3.3). Thus

$$f_{ct}(t_T) \;=\; \mathcal{B}_{ct}(t_T)\; f_{ct28} \tag{9.17}$$

where

$$\mathcal{B}_{ct}(t_T) \;\approx\; \begin{cases} \mathcal{B}_{cc}(t_T) & ;t_T < 28 \text{ days} \\ 1 & ;t_T \geq 28 \text{ days} \end{cases} \tag{9.18}$$

and (f_{ct}, f_{ct28}) denote corresponding strength-values at t_T and $t_T = 28$ days, respectively.

In MC90 the initial modulus of elasticity E_c at an age of t_T days may be estimated from

$$E_c(t_T) \;=\; \sqrt{\mathcal{B}_{cc}(t_T)}\; E_{c28} \tag{9.19}$$

where E_{c28} denotes the value at $t_T = 28$ days.

For the remaining two of the parameters that characterize the stress-strain behavior of concrete in compression, i.e. (ϵ_o, ϵ_h), no expressions for the development

with age are given in MC90. However, it may be reasonable to assume a similar dependency of age for the corresponding secant moduli (E_o, E_h), see Fig. 8.1, as for the initial modulus. Thus

$$E_o(t_T) \approx \sqrt{\mathcal{B}_{cc}(t_T)}\, E_{o28} \tag{9.20}$$

$$E_h(t_T) \approx \sqrt{\mathcal{B}_{cc}(t_T)}\, E_{h28} \tag{9.21}$$

This leads in turn, combined with Eq.(9.16), to a similar dependency for the strains (ϵ_o, ϵ_h), i.e.

$$\epsilon_o(t_T) = \frac{f_{cc}(t_T)}{E_o(t_T)} \approx \sqrt{\mathcal{B}_{cc}(t_T)}\, \epsilon_{o28} \tag{9.22}$$

$$\epsilon_h(t_T) = \frac{f_{cc}(t_T)}{2E_h(t_T)} \approx \sqrt{\mathcal{B}_{cc}(t_T)}\, \epsilon_{h28} \tag{9.23}$$

where $(\epsilon_{o28}, \epsilon_{h28})$ denote the values at $t_T = 28$ days.

9.3.2 Temperature

MC90 [35] is also providing expressions for the effect of temperature on concrete stress-strain parameters. These expressions are usually valid in the range of $0\,^oC < T < 80\,^oC$ and often limited to the case of no moisture exchange. However, when moisture exchange takes place, the effect of temperature on the compressive and tensile strengths (f_{cc}, f_{ct}) may be disregarded due to a counteracting effect from drying. Consequently, in this study it will be assumed that

$$f_{cc}(T) \approx f_{cc}^{(T20)} \tag{9.24}$$

$$f_{ct}(T) \approx f_{ct}^{(T20)} \tag{9.25}$$

where $(f_{cc}^{(T20)}, f_{ct}^{(T20)})$ denote the strength-values at $T = 20\,^oC$.

For the initial modulus of elasticity E_c the following dependency of temperature will be employed

$$E_c(T) = \mathcal{B}_T(T)\, E_c^{(T20)} \tag{9.26}$$

where $E_c^{(T20)}$ denotes the value at $T = 20\,^oC$, and

$$\mathcal{B}_T(T) = 1.06 - 0.003\, T/T_1 \tag{9.27}$$

Here T is measured in $[^oC]$ and $T_1 = 1\,^oC$. Eq.(9.27) agrees with MC90, but there the expression relates the moduli at an age of 28 days only, for the case of no moisture exchange. However, in contrast to strength, it is stated that moisture exchange now makes the effect of temperature more pronounced than in Eq.(9.27). Thus, for simplicity and in lack of better information, Eqs.(9.26,9.27) will here be applied to the initial modulus at any age and independent of drying conditions. Since no explicit range of validity is specified in MC90 for this case, the relation will also

be assumed adequate for temperatures below $0\,^oC$, corresponding to a Scandinavian winter climate. A possible upper bound of $80\,^oC$ is considered to be outside the range of interest for this study.

Again, by assuming a similar dependency for the secant moduli (E_o, E_h) as for E_c, i.e.

$$E_o(T) \approx \mathcal{B}_T(T)\, E_o^{(T20)} \tag{9.28}$$

$$E_h(T) \approx \mathcal{B}_T(T)\, E_h^{(T20)} \tag{9.29}$$

the temperature dependency for the remaining two stress-strain parameters (ϵ_o, ϵ_h) takes the form

$$\epsilon_o(T) = \frac{f_{cc}(T)}{E_o(T)} \approx \frac{1}{\mathcal{B}_T(T)}\, \epsilon_o^{(T20)} \tag{9.30}$$

$$\epsilon_h(T) = \frac{f_{cc}(T)}{2E_h(T)} \approx \frac{1}{\mathcal{B}_T(T)}\, \epsilon_h^{(T20)} \tag{9.31}$$

Here $(\epsilon_o^{(T20)}, \epsilon_h^{(T20)})$ denote the strain-values at $T = 20\,^oC$.

Finally note that temperature effects on the stress-strain parameters for steel materials will not be considered. Although these are severe effects, they take place at temperatures way above the range of interest for this study.

9.3.3 High Sustained Loading

It is known that high sustained loading has a detrimental effect on the compressive strength of concrete. In [39] Rüsch et al. reported testing of some 200 specimens subjected to a variety of high constant sustained stress levels. Once a specimen failed after some time, an identical companion specimen, stored free of load, was tested to obtain the corresponding short-time strength. Assuming the effect of aging to be the same in both specimens, the influence of sustained loading alone could then be expressed as the long-time to short-time strength ratio. Rüsch et al. found that this strength ratio was fairly independent of all other variables investigated than the duration of loading. The following expression for $\mathcal{B}_{sus}$ agrees well with the strength ratio variation proposed in [39]

$$\mathcal{B}_{sus}(t_f) = 1 - 0.135\sqrt[4]{\ln(720\, t_f/t_1)} \qquad ; t_f/t_1 \geq 1/720 \tag{9.32}$$

Here t_f is the time to failure [days], and $t_1 = 1$ day. Clearly, $\mathcal{B}_{sus}$ starts from value 1 when $t_f = 1/720$ day $= 2$ minutes, which corresponds to the standard test duration for short-time strength. Actually, Rüsch et al. also reported strength ratio variations based on 20 minute test duration for the short-time strength. When scaling these results against the standard 2 minute strength, a value of 0.96 at start of the sustained stress period (i.e. after 20 minutes) was obtained. In MC90 [35] an expression similar to Eq.(9.32) is given, but then based on the 20 minute short-time strength. However, the two expressions give practically identical results from a duration of loading of

about one day on. This alternative $\mathcal{B}_{sus}$-expression is in MC90 simply introduced as a correction factor on Eq.(9.8) to obtain the mean compressive strength of concrete, considering the combined effect of aging and sustained loading. This approach is believed to be an oversimplification of actual behavior, since experimental evidence reveals that the influence of sustained loading depends on the stress level, as well as the loading history in general. Thus, instead of complying with MC90 in this case, a more realistic approach mainly based on the work by Hellesland and Green [40], will be adopted. This approach rests on the three main assumptions:

1. When subjected to a stepwise varying stress history, the strength loss at one stress level is unaffected by the accumulated damage from previous stresses.

2. No detrimental effect occurs when the stress relative to the current short-time strength (i.e. the relative stress) is below the lower bound η of the $\mathcal{B}_{sus}$-curve from Eq.(9.32).

3. The strength loss due to a relative stress above η takes place at a constant rate of time.

In [40] detrimental effect is in addition restricted to stress states on the ascending branch of the stress-strain envelope only. Possibly best would have been to omit only the unstable descending branch. However, here for simplicity strength loss will be counted for all stress states (i.e. at the envelope or at the interior) as long as the relative stress is above η. Furthermore, this lower bound of the $\mathcal{B}_{sus}$-curve will be taken as the value corresponding to 100 years of sustained loading. Thus, from Eq.(9.32) by inserting $t_f = 3.65 \cdot 10^4$, yields

$$\eta \;=\; 0.725 \tag{9.33}$$

To find the strength loss due to a relative stress s_i, it is necessary first to determine the corresponding time to failure t_{fi}. This time is obtained from the equality

$$s_i \;=\; \mathcal{B}_{sus}(t_{fi}) \tag{9.34}$$

Then by inverting Eq.(9.32), the result becomes

$$t_{fi} \;=\; \frac{t_1}{720}\,\exp\left\{\left[\frac{1-s_i}{0.135}\right]^4\right\} \tag{9.35}$$

where

$$s_i \;=\; \frac{\bar{\sigma}_{ci}}{\psi_c f_{cc}(t_T)} \tag{9.36}$$

Here $\bar{\sigma}_{ci}$ is the sustained concrete stress in the principal direction in question for the time step considered; taken as the average of the current stress and the stress at the previous equilibrium state (i.e. at the previous time considered). Furthermore, ψ_c is the biaxial effect coefficient for the same principal direction, according to Eq.(8.4).

Finally, $f_{cc}(t_T)$ is the compressive strength at the time considered, given by Eq.(9.16). Then the corresponding constant rate of loss of relative strength γ_i may be expressed through

$$\gamma_i \;=\; \begin{cases} \dfrac{1-s_i}{t_{fi}-t_1/720} & ;\, s_i > \eta \\ 0 & ;\, s_i \le \eta \end{cases} \tag{9.37}$$

Now, by accumulating the losses $\gamma_i \Delta t_i$, the expression for the relative strength $\mathcal{B}_\sigma$ due to a stepwise varying stress history may take the form

$$\mathcal{B}_\sigma(t_s) \;=\; 1 \;-\; \sum_{i=1}^{n} \gamma_i \, \Delta t_i \;\ge\; \eta \tag{9.38}$$

Here t_s is the total time under sustained loading, and Δt_i is the time step corresponding to the stress $\bar{\sigma}_{ci}$; both times counted in days. Finally the total compressive strength, considering the combined effect of aging and sustained loading, then becomes

$$f_{cc}(t_s, t_T) \;=\; \mathcal{B}_\sigma(t_s)\, \mathcal{B}_{cc}(t_T)\, f_{cc28} \tag{9.39}$$

where $\mathcal{B}_{cc}$ is given by Eq.(9.9), and f_{cc28} is the strenght at $t_T = 28$ days. The biaxial effect coefficient ψ_c is of convenience omitted here, but will be included again in the stress-strain relationship. Due to the stress dependency, Eq.(9.39) (or $\mathcal{B}_\sigma$) needs to be evaluated at every integration point and for each principal direction.

As already mentioned, the sustained stress $\bar{\sigma}_{ci}$ is taken as the average of the stress at the previous equilibrium state and the current stress. However, the latter quantity is in general not known when the strength is adjusted for sustained loading, since this is done prior to entering the (short-time) constitutive model (where the current stress is computed). For this reason, an approximate value for the current stress, determined as outlined in Section 9.7, will be employed when evaluating $\bar{\sigma}_{ci}$. Also note that since the experimental basis for modeling strength dependency of sustained loading is restricted to uniaxial tests, an extension into biaxial stress states will necessarily involve additional uncertainties. For instance, should the current short-time reference strength have the biaxial effect included or not (see Eq.(9.36))? Here the former option is believed to be the more 'correct'. Finally note that the accuracy of this strength reduction model will in general depend on the time step size employed. Therefore, Δt_i should be made 'small' compared to the corresponding value of t_{fi} from Eq.(9.35) for the sustained stress level that is expected.

There is insufficient experimental basis to account for influence on the tensile strength of concrete due to high sustained loading [35].

9.3.4 Summary of Influence on Input-Parameters

Below is summarized the relationships that yield the influence on the stress-strain parameters due to aging, temperature and high sustained loading

$$f_{cc}(t_s, t_T) \;=\; \mathcal{B}_\sigma(t_s)\, \mathcal{B}_{cc}(t_T)\, f_{cc28} \tag{9.40}$$

$$f_{ct}(t_T) = \mathcal{B}_{ct}(t_T)\, f_{ct28} \tag{9.41}$$

$$E_c(T,t_T) = \mathcal{B}_T(T)\,\sqrt{\mathcal{B}_{cc}(t_T)}\, E_{c28} \tag{9.42}$$

$$\epsilon_o(T,t_T) = \frac{1}{\mathcal{B}_T(T)}\,\sqrt{\mathcal{B}_{cc}(t_T)}\,\epsilon_{o28} \tag{9.43}$$

$$\epsilon_h(T,t_T) = \frac{1}{\mathcal{B}_T(T)}\,\sqrt{\mathcal{B}_{cc}(t_T)}\,\epsilon_{h28} \tag{9.44}$$

where

$$\begin{aligned} \mathcal{B}_\sigma(t_s) &- \text{Eq.(9.38)} \\ \mathcal{B}_{cc}(t_T) &- \text{Eq.(9.9)} \\ \mathcal{B}_{ct}(t_T) &- \text{Eq.(9.18)} \\ \mathcal{B}_T(T) &- \text{Eq.(9.27)} \end{aligned}$$

and parameters with subscript '28' are the input-values that refer to the standard age of 28 days. Note that the expression for the compressive strength f_{cc} needs to be evaluated at every integration point and for each principal direction. The tension stiffening coefficient b_t is not subjected to adjustments.

9.3.5 Influence on History Parameters

As dealt with in Subsection 8.1.6, the selected history parameters or state variables in the short-time constitutive model are the unloading/reloading moduli $(E_u^{(c)}, E_u^{(t)})$ in compression and tension for each principal direction. These moduli may be subjected to aging and influence of temperature using expressions similar to Eq.(9.42) for the initial modulus, i.e.

$$E_u^{(c)}(T,t_T) = \mathcal{B}_T(T)\,\sqrt{\mathcal{B}_{cc}(t_T)}\, E_{u28}^{(c)} \tag{9.45}$$

$$E_u^{(t)}(T,t_T) = \mathcal{B}_T(T)\,\sqrt{\mathcal{B}_{cc}(t_T)}\, E_{u28}^{(t)} \tag{9.46}$$

Here $(E_{u28}^{(c)}, E_{u28}^{(t)})$ denote the equivalent 28 day-values, obtained by applying the inverse of the above relationships at the time t_u when unloading took place. Thus

$$E_{u28}^{(c)} = \frac{\hat{E}_u^{(c)}}{\mathcal{B}_T(T_u)\,\sqrt{\mathcal{B}_{cc}(t_{Tu})}} \tag{9.47}$$

$$E_{u28}^{(t)} = \frac{\hat{E}_u^{(t)}}{\mathcal{B}_T(T_u)\,\sqrt{\mathcal{B}_{cc}(t_{Tu})}} \tag{9.48}$$

where $(\hat{E}_u^{(c)}, \hat{E}_u^{(t)})$ are determined from Eqs.(8.70,8.74), while t_{Tu} is the temperature adjusted age according to Eq.(9.10) and T_u is the temperature, both at time t_u. In fact, the state variables will be stored on the form $(E_{u28}^{(c)}, E_{u28}^{(t)})$ and then recomputed by Eqs.(9.45,9.46) for the current time.

Adjusting the modulus in tension for aging and temperature may look questionable from the point of view that this quantity in the cracked regime more likely is a mixed property of concrete and steel. Disregarding this, however, makes the formulation consistent with the treatment of aging strain in Section 9.6 where no distinction between compression and tension is made either.

9.4 Shrinkage Strain in Concrete

The shrinkage prediction model will mainly be based on MC90 [35]. Thus, the total shrinkage or swelling strain ϵ_{cs} may be estimated from the product of the notional shrinkage strain ϵ_{cso} and the coefficient $\mathcal{B}_s$ that describes the development with time, i.e.

$$\epsilon_{cs}(t-t_o,\overline{T}_t) \;=\; \epsilon_{cso}(\overline{T}_t)\,\mathcal{B}_s(t-t_o,\overline{T}_t) \tag{9.49}$$

where

$$\mathcal{B}_s(t-t_o,\overline{T}_t) \;=\; \sqrt{\frac{(t-t_o)/t_1}{0.035(h/h_1)^2\exp[-0.06(\overline{T}_t/T_1-20)]\;+\;(t-t_o)/t_1}} \tag{9.50}$$

with

$$h \;=\; \frac{2A_c}{u} \tag{9.51}$$

$$\overline{T}_t \;=\; \frac{1}{t-t_o}\sum_{i=1}^{n}\overline{T}_i\,\Delta t_i \tag{9.52}$$

t – current time [days]

t_o – time at the beginning of shrinkage or swelling [days]

t_1 = 1 day

h – notional member size [mm]

h_1 = 1 mm

A_c – area of concrete section [mm^2]

u – perimeter in contact with the atmosphere [mm]

$\overline{T}_t$ – average temperature [^oC] during $(t-t_o)$

T_1 = 1 ^oC

Δt_i – generic time step [days]

$\overline{T}_i$ – average temperature [^oC] during Δt_i, Eqs.(9.11ff.)

and

$$\epsilon_{cso}(\overline{T}_t) \;=\; \beta_{HT}(\overline{T}_t)\,\beta_{RH}\;[160\;+\;\beta_m(90+f_{cm28}/f_1)]\,10^{-6} \tag{9.53}$$

with

$$\beta_{HT}(\overline{T}_t) \;=\; 1 \;+\; \frac{8}{103 - RH/RH_1}\,\frac{\overline{T}_t/T_1 - 20}{40} \tag{9.54}$$

$$\beta_{RH} \;=\; \begin{cases} -1.55\,C_{RH} & ;40\,\% \le RH < 99\,\% \\ +0.25 & ;RH \ge 99\,\% \end{cases} \tag{9.55}$$

$$C_{RH} \;=\; 1 \;-\; \left[\frac{RH}{100\,RH_1}\right]^3 \tag{9.56}$$

RH – relative humidity of the ambient atmosphere [%]

RH_1 = 1 %

β_m – coefficient depending on the type of cement mix, i.e.

$$\beta_m \;=\; \begin{cases} 8 & - \text{ rapid hardening high strength cement} \\ 5 & - \text{ normal and rapid hardening cements} \\ 4 & - \text{ slowly hardening cement} \end{cases}$$

f_{cm28} – mean compressive strength at the age of 28 days [MPa]

f_1 = 1 MPa

In MC90 the expressions that account for temperature different from 20 ^oC are based on a constant value T. Here this assumption is met by always using the average temperature $\overline{T}_t$ for the drying period in question. Also note that since compressive strengths in this work by definition are negative quantities, the sign in front of f_{cm28} in Eq.(9.53) is altered accordingly. In addition, some symbols and reference quantities (to obtain nondimensionalized expressions) differ from those in MC90. Finally note that the time at the beginning of shrinkage or swelling t_o in this work of convenience will be taken equal to the time of first inclusion of the pertaining element in a structural system.

9.5 Creep Strain in Concrete

9.5.1 Introduction

The creep strain ϵ_{cc} at time t_n, due to a constant stress σ_c applied at time t_a, may be expressed through

$$\epsilon_{cc}(t_n, t_a) \;=\; \phi(t_n, t_a)\,\frac{\sigma_c}{E_{c28}} \tag{9.57}$$

Here ϕ is the creep coefficient, and E_{c28} is the modulus of elasticity at the age of 28 days. When the stress history is stepwise varying, the corresponding creep strain may be predicted by several methods, like the *effective modulus method* (EMM), the *linear superposition method* (LSM) and the *rate of creep method* (RCM); to mention the most common ones. These methods are discussed by e.g. Åldstedt [21] and Neville

et al. [41]. The EMM is the oldest, simplest and most used method. However, it yields poor results for severe variations of stress. The LSM is usually considered the most accurate, but overestimates creep recovery upon stress removal. Besides, in its general form LSM requires storage of all previous stress-values in order to evaluate the creep strain increment for the next time step. From a computational point of view, this is a serious disadvantage. However, the problem may be circumvented by introducing a special form of the creep function [22]. The RCM on the other hand is computationally attractive since only the current stress is required when finding the next creep strain increment. A deficiency of RCM is that it does not consider any creep recovery upon stress removal. Also it is known to underestimate the creep deformation under increasing stresses. The mathematical statement of RCM may take the form

$$\epsilon_{cc}(t_n, t_a) \;=\; \frac{1}{E_{c28}} \sum_{i=1}^{n} \left[\phi(t_i, t_a) \;-\; \phi(t_{i-1}, t_a)\right] \bar{\sigma}_{ci} \tag{9.58}$$

where $\bar{\sigma}_{ci}$ is the stress corresponding to the time step $t_i - t_{i-1}$, and t_a is now the time at first load application. The remaining symbols are as explained in conjunction with Eq.(9.57).

9.5.2 Modified Rate of Creep Method (MRCM)

The deficiencies of RCM may be improved considerably by representing the creep phenomenon with a so-called summation model, i.e. by separating the creep coefficient ϕ into one (or more) recoverable delayed elastic component(s) ϕ_d and one (or more) irrecoverable flow component(s) ϕ_f. On this basis England and Illston [42] proposed an improved RCM, termed the *rate of flow method*. Also Roll [43] made a reformulation, by Hellesland [44] termed the *modified rate of creep method* (MRCM). The latter approach will be the adopted creep analysis method for this study. Here the irrecoverable flow component of the creep strain $\epsilon_{cc}^{(f)}$ is treated according to the original RCM. Thus

$$\epsilon_{cc}^{(f)}(t_n, t_a) \;=\; \frac{1}{E_{c28}} \sum_{i=1}^{n} \left[\phi_f(t_i, t_a) \;-\; \phi_f(t_{i-1}, t_a)\right] \bar{\sigma}_{ci} \tag{9.59}$$

Before arriving at the delayed elastic component, an expression for the corresponding creep coefficient must be introduced. Assuming now that the current stress is applied at time t_{n-1}, ϕ_d at time t_n may be expressed through

$$\phi_d(t_n, t_{n-1}) \;=\; \hat{\phi}_{do}(t_{n-1})\, \mathcal{B}_d(t_n, t_{n-1}) \tag{9.60}$$

Here $\hat{\phi}_{do}$ is the asymptote when $t_n \to \infty$, taken into account a possible effect of aging up to t_{n-1}, while $\mathcal{B}_d$ describes the development with time. In MRCM the recoverable delayed elastic component of the creep strain $\epsilon_{cc}^{(d)}$ at time t_n is now given by

$$\epsilon_{cc}^{(d)}(t_n, t_{n-1}) \;=\; \epsilon_{cc}^{(d)}(t_{n-1}) \;+\; \left[\hat{\phi}_{do}(t_{n-1})\, \frac{\bar{\sigma}_{cn}}{E_{c28}} \;-\; \epsilon_{cc}^{(d)}(t_{n-1})\right] \mathcal{B}_d(t_n, t_{n-1}) \tag{9.61}$$

Here $\epsilon_{cc}^{(d)}(t_{n-1})$ is the delayed elastic creep strain at time t_{n-1}, and the expression enclosed by brackets is the so-called recoverable strain yet to come. Furthermore, $\bar{\sigma}_{cn}$ is the stress corresponding to the time step $t_n - t_{n-1}$. Rearrangement of terms and introduction of Eq.(9.60) yield

$$\epsilon_{cc}^{(d)}(t_n, t_{n-1}) \;=\; \epsilon_{cc}^{(d)}(t_{n-1})\,[1 \;-\; \mathcal{B}_d(t_n, t_{n-1})] \;+\; \phi_d(t_n, t_{n-1})\,\frac{\bar{\sigma}_{cn}}{E_{c28}} \tag{9.62}$$

This is a simple recursion formula that starts from

$$\epsilon_{cc}^{(d)}(t_1, t_a) \;=\; \phi_d(t_1, t_a)\,\frac{\bar{\sigma}_{c1}}{E_{c28}} \tag{9.63}$$

From Eq.(9.62) it is seen that MRCM provides creep recovery upon stress removal. Compared to the original RCM, it will also give larger creep deformation under increasing stresses (and less under decreasing stresses). These beneficial effects are obtained still without having to save previous stress values. Thus, MRCM appears to be an attractive creep analysis method.

9.5.3 Revised Summation Model (RSM)

From the preceding subsection it became clear that MRCM requires the creep phenomenon to be characterized by a summation model (as opposed to a product model). Since the creep prediction model given in MC90 [35] is of the product kind, it is obviously not a candidate. However, in the CEB Information Bulletin No. 199 (B199) [45] a model termed the *revised summation model*[2] (RSM) is presented. It yields the same accuracy as the MC90-model when compared to a data bank of test results [45]. Consequently, RSM is considered to be a suitable creep prediction model for this study. Some deviations from B199 are however made. These will be summarized at the end of the subsection.

In RSM the resulting creep coefficient ϕ of concrete may be expressed by

$$\phi(\hat{t}_i, \hat{t}_{i-1}, \hat{t}_a) \;=\; \phi_d(\hat{t}_i, \hat{t}_{i-1}) \;+\; \phi_{fb}(\hat{t}_i, \hat{t}_a) \;+\; \phi_{fd}(\hat{t}_i, \hat{t}_a) \tag{9.64}$$

where $(\phi_d, \phi_{fb}, \phi_{fd})$ are the creep coefficients due to delayed elasticity, basic flow (i.e. at constant moisture content) and drying flow, respectively. Furthermore, $(\hat{t}_a, \hat{t}_{i-1}, \hat{t}_i)$ are respectively the concrete ages at first load application, at change to the generic stress $\bar{\sigma}_{ci}$ and at the generic time considered; adjusted for influence of type of cement and curing temperature as follows

$$\hat{t}_a \;=\; t_{Ta}\left[\frac{9}{2 + (t_{Ta}/t_1)^{1.2}} \;+\; 1\right]^{\alpha} \;\geq\; 0.5 \text{ day} \tag{9.65}$$

$$\hat{t}_{i-1} \;=\; t_{i-1} \;-\; t_a \;+\; \hat{t}_a \tag{9.66}$$

[2] Significantly 'revised' compared to the old MC78 summation model.

$$\hat{t}_i \;=\; t_i \;-\; t_a \;+\; \hat{t}_a \tag{9.67}$$

Here (t_a, t_{i-1}, t_i) are the corresponding actual times, while t_{Ta} is the temperature adjusted age at time t_a according to Eq.(9.10), and $t_1 = 1$ day. All ages/times are counted in days. Finally, α is a coefficient depending on the type of cement, i.e.

$$\alpha \;=\; \begin{cases} 1 & - \quad \text{rapid hardening high strength cement} \\ 0 & - \quad \text{normal and rapid hardening cements} \\ -1 & - \quad \text{slowly hardening cement} \end{cases}$$

The delayed elastic creep coefficient is further expressed by

$$\phi_d(\hat{t}_i, \hat{t}_{i-1}) \;=\; \phi_{d0}\, \phi_{d1}(\hat{t}_{i-1})\, \mathcal{B}_d(\hat{t}_i, \hat{t}_{i-1}) \tag{9.68}$$

where

$$\phi_{d0} \;=\; \frac{0.9}{\sqrt[5]{-f_{cm28}/f_1}} \tag{9.69}$$

$$\phi_{d1}(\hat{t}_{i-1}) \;=\; 0.25 \;+\; \frac{46}{60 + \sqrt{\hat{t}_{i-1}/t_1}} \tag{9.70}$$

$$\begin{aligned} \mathcal{B}_d(\hat{t}_i, \hat{t}_{i-1}) \;&=\; a_0 \left[1 - \exp\left\{-b_0\,(\hat{t}_i - \hat{t}_{i-1})/t_1\right\}\right] \\ &\quad + \sum_{j=1}^{4} a_j \left[1 - \exp\left\{-b_j\,(\hat{t}_i^{\,0.35} - \hat{t}_{i-1}^{\,0.35})/t_1^{0.35}\right\}\right] \end{aligned} \tag{9.71}$$

Here f_{cm28} is the mean compressive strength [MPa] at the age of 28 days, and $f_1 = 1$ MPa. The coefficients (a_j, b_j) follow from the succeeding table

j	0	1	2	3	4
a_j	0.24	0.23	0.22	0.19	0.12
b_j	9.2	1.3	2.9	8.8	42

The basic flow creep coefficient takes the form

$$\phi_{fb}(\hat{t}_i, \hat{t}_a) \;=\; \phi_{fb0}\, \phi_{fb1}\, \mathcal{B}_{fb}(\hat{t}_i, \hat{t}_a) \tag{9.72}$$

where

$$\phi_{fb0} \;=\; \frac{1.1}{\sqrt{-f_{cm28}/f_1}} \tag{9.73}$$

$$\phi_{fb1} \;=\; \begin{cases} \exp\left[1.3(s_{ai} - 0.4)\right] & ;\, s_{ai} > 0.4 \\ 1 & ;\, s_{ai} \le 0.4 \end{cases} \tag{9.74}$$

$$\mathcal{B}_{fb}(\hat{t}_i, \hat{t}_a) \;=\; \ln\left\{\left[\frac{-7 f_{cm28}/f_1}{10000} \;+\; \frac{7}{2 + (\hat{t}_a/t_1)^{1.2}}\right] \sqrt[3]{(\hat{t}_i - \hat{t}_a)^2/t_1^2} \;+\; 1\right\} \tag{9.75}$$

with the new quantity

$$s_{ai} \;=\; \frac{\bar{\sigma}_{ci}}{f_{cc}(t_{Ta})} \tag{9.76}$$

Here $f_{cc}(t_{Ta})$ is the compressive strength at the temperature adjusted age t_{Ta} according to Eq.(9.16). Finally, the drying flow creep coefficient follows from

$$\phi_{fd}(\hat{t}_i, \hat{t}_a) \;=\; \phi_{fd0}\, \phi_{fd1}\, \phi_{fd2}\, \mathcal{B}_{fd}(\hat{t}_i, \hat{t}_a) \tag{9.77}$$

where

$$\phi_{fd0} \;=\; \frac{38}{\sqrt{-f_{cm28}/f_1}} \tag{9.78}$$

$$\phi_{fd1} \;=\; 1 \;-\; \sqrt{\left[\frac{RH}{100\, RH_1}\right]^3} \tag{9.79}$$

$$\phi_{fd2} \;=\; \begin{cases} \exp\left[1.7(s_{ai} - 0.4)\right] & ;\, s_{ai} > 0.4 \\ 1 & ;\, s_{ai} \leq 0.4 \end{cases} \tag{9.80}$$

$$\mathcal{B}_{fd}(\hat{t}_i, \hat{t}_a) \;=\; \frac{\exp[-\hat{t}_a/(1000 t_1)] + 0.2}{(\hat{t}_a/t_1)^{0.15}} \left[\frac{(\hat{t}_i - \hat{t}_a)/t_1}{-0.35(f_{cm28}/f_1)(h/h_1) \;+\; (\hat{t}_i - \hat{t}_a)/t_1}\right]^{0.4} \tag{9.81}$$

Here RH is the relative humidity of the ambient atmosphere [%], and $RH_1 = 1$ %; while h is the notional member size [mm] according to Eq.(9.51), and $h_1 = 1$ mm.

Compared to B199, the following modifications are made:

- In Eq.(9.71) for $\mathcal{B}_d$ that expresses the development of the delayed elastic creep with time, the 'zeroth' term is here made rapid time dependent rather than being instantaneous as in B199. Then the effect of creep is avoided for problems that take place under constant time. The coefficient b_0 is determined so that 99 % of the rapid creep is developed during the first 0.5 day.

- The relative stress s_{ai} from Eq.(9.76) that enters the nonlinearity coefficients (ϕ_{fb1}, ϕ_{fd2}), is here based on the actual strength f_{cc} instead of the mean value f_{cm} as reference. Also the temperature adjusted age t_{Ta} is here used when evaluating the strength, rather than the temperature and cement adjusted age $\hat{t}_a$ from Eq.(9.65). The reason for the latter modification is that the influence of cement type is already accounted for in $\mathcal{B}_{cc}$ from Eq.(9.9) that expresses the dependency of strength with time.

- In B199 an upper bound for s_{ai} of 0.6 is introduced in the expressions similar to Eqs.(9.74,9.80) for the nonlinearity coefficients (ϕ_{fb1}, ϕ_{fd2}); i.e. the exponential-expressions are then valid only in the range of $0.4 < s_{ai} \leq 0.6$. However, omission of this upper bound yields coefficients in the order of $2-3$ when $s_{ai} = 1$. Such values are only moderate compared to results obtained by Hellesland [44], who reported values as high as 15 immediate to failure. Although $s_{ai} > 1$ may

theoretically occur, the values predicted by Eqs.(9.74,9.80) are still not believed to be excessive.

- A lower bound of 0.5 day is introduced in Eq.(9.65). The absence of this bound in B199 in conjunction with RSM is in fact believed to be a misprint, since it is included in a similar expression when presenting the product model that is selected for MC90. Thus, the same bound is also included in the MC90-document.

In addition, some symbols differ from those used in B199. Also reference quantities (with subscript '1') have been introduced to obtain a formally correct nondimensionalized form of the expressions. Finally note that since compressive strengths in this work by definition are negative quantities, the sign in front of f_{cm28} is altered accordingly in all expressions of pertinence.

9.5.4 Summary of MRCM Applied to RSM

Now, applying the modified rate of creep method (MRCM) to the revised summation model (RSM), the resulting creep strain ϵ_{cc} of concrete may read

$$\epsilon_{cc}(\hat{t}_n, \hat{t}_{n-1}, \hat{t}_a) \;=\; \epsilon_{cc}^{(d)}(\hat{t}_n, \hat{t}_{n-1}) \;+\; \epsilon_{cc}^{(fb)}(\hat{t}_n, \hat{t}_a) \;+\; \epsilon_{cc}^{(fd)}(\hat{t}_n, \hat{t}_a) \tag{9.82}$$

where $(\epsilon_{cc}^{(d)}, \epsilon_{cc}^{(fb)}, \epsilon_{cc}^{(fd)})$ are the creep strain components due to delayed elasticity, basic flow and drying flow, respectively. Furthermore, $(\hat{t}_a, \hat{t}_{n-1}, \hat{t}_n)$ are the temperature and cement adjusted ages at first load application, at change to the current stress $\bar{\sigma}_{cn}$ and at the time considered, according to Eqs.(9.65-9.67)[3] respectively. Then combination of Eq.(9.68)[3] and Eq.(9.62) yields for the delayed elastic component

$$\epsilon_{cc}^{(d)}(\hat{t}_n, \hat{t}_{n-1}) \;=\; \epsilon_{cc}^{(d)}(\hat{t}_{n-1}) \left[1 \;-\; \mathcal{B}_d(\hat{t}_n, \hat{t}_{n-1})\right] \;+\; \phi_{d0}\, \phi_{d1}(\hat{t}_{n-1})\, \mathcal{B}_d(\hat{t}_n, \hat{t}_{n-1})\, \frac{\bar{\sigma}_{cn}}{E_{c28}} \tag{9.83}$$

with the first expression of this recursion formula given by

$$\epsilon_{cc}^{(d)}(\hat{t}_1, \hat{t}_a) \;=\; \phi_{d0}\, \phi_{d1}(\hat{t}_a)\, \mathcal{B}_d(\hat{t}_1, \hat{t}_a)\, \frac{\bar{\sigma}_{c1}}{E_{c28}} \tag{9.84}$$

Here the entries $(\phi_{d0}, \phi_{d1}, \mathcal{B}_d)$ follow from Eqs.(9.69-9.71)[3], respectively, and E_{c28} is the modulus of elasticity at the age of 28 days. The basic flow strain component is obtained by inserting Eq.(9.72) into Eq.(9.59). Thus

$$\epsilon_{cc}^{(fb)}(\hat{t}_n, \hat{t}_a) \;=\; \frac{\phi_{fb0}}{E_{c28}} \sum_{i=1}^{n} \phi_{fb1} \left[\mathcal{B}_{fb}(\hat{t}_i, \hat{t}_a) \;-\; \mathcal{B}_{fb}(\hat{t}_{i-1}, \hat{t}_a)\right] \bar{\sigma}_{ci} \tag{9.85}$$

where $(\phi_{fb0}, \phi_{fb1}, \mathcal{B}_{fb})$ are given by Eqs.(9.73-9.75), respectively, and $\bar{\sigma}_{ci}$ is the stress corresponding to the generic time step $\hat{t}_i - \hat{t}_{i-1}$. Similarly, the drying flow strain component becomes by inserting Eq.(9.77) into Eq.(9.59)

$$\epsilon_{cc}^{(fd)}(\hat{t}_n, \hat{t}_a) \;=\; \frac{\phi_{fd0}\, \phi_{fd1}}{E_{c28}} \sum_{i=1}^{n} \phi_{fd2} \left[\mathcal{B}_{fd}(\hat{t}_i, \hat{t}_a) \;-\; \mathcal{B}_{fd}(\hat{t}_{i-1}, \hat{t}_a)\right] \bar{\sigma}_{ci} \tag{9.86}$$

[3] Altering subscript 'i' to 'n'.

Here $(\phi_{fd0}, \phi_{fd1}, \phi_{fd2}, \mathcal{B}_{fd})$ are given by Eqs.(9.78-9.81), respectively.

Note that the creep strain has to be evaluated for each principal direction at every integration point. As already pointed out in Subsection 9.3.3, the sustained stress $\bar{\sigma}_{ci}$ for the generic time step will be taken as the average of the stresses at the times t_{i-1} and t_i. Since the latter stress is not known yet when the creep strain is updated, an approximate value, determined as outlined in Section 9.7, will instead be employed. One exception is however made; the relative stress s_{ai} that enters the nonlinearity coefficients (ϕ_{fb1}, ϕ_{fd2}) in Eqs.(9.74,9.80), will for simplicity be based on the stress-value that pertain to time t_{i-1} only (i.e. at the previous equilibrium state). As becomes clear in Section 9.7, this inconsistency is necessary in order to avoid iteration at the integration point level when determining the creep strain contribution for the time step. Finally also note that s_{ai} in Eq.(9.76) is computed without the biaxial effect coefficient ψ_c included (as opposed to s_i in Eq.(9.36) when dealing with strength degradation due to sustained loading). Since the strength in this case refers to the age at first load application, it is here believed to be 'better' omitting rather than retaining the initial biaxial effect at all succeeding stress/strain states (that may differ significantly from the initial state). Irrespective of this, the nonlinear creep model must be considered as a crude approximation of actual behavior.

9.6 Aging Strain in Concrete

The aging strain is introduced to compensate for an inconsistency between the adopted time dependent solution procedure and the experimental basis of the creep prediction model. In the latter case, the stress dependent strain $\epsilon_{c\sigma}$ at time t_n due to a constant stress σ_c applied at time t_a, may be expressed on the form

$$\epsilon_{c\sigma}(t_n, t_a) \;=\; \frac{\sigma_c}{E_c(t_a)} \;+\; \phi(t_n, t_a)\,\frac{\sigma_c}{E_{c28}} \tag{9.87}$$

Here $E_c(t_a)$ is the modulus of elasticity at the time of load application, ϕ is the creep coefficient, and E_{c28} is the modulus of elasticity at the age of 28 days. Thus, the first term represents the instantaneous strain at load application, and the second term yields the creep strain. The creep coefficients given in the preceding section are based on this concept. In this study, however, the instantaneous stress-strain characteristics will instead be updated according to the current time in the solution process. Consequently, to comply with this, Eq.(9.87) may conveniently be rewritten to

$$\epsilon_{c\sigma}(t_n, t_a) \;=\; \frac{\sigma_c}{E_c(t_n)} \;+\; \phi(t_n, t_a)\,\frac{\sigma_c}{E_{c28}} \;+\; \frac{\sigma_c}{E_c(t_a)} \;-\; \frac{\sigma_c}{E_c(t_n)} \tag{9.88}$$

Or in terms of strain components

$$\epsilon_{c\sigma}(t_n, t_a) \;=\; \epsilon_c(t_n) \;+\; \epsilon_{cc}(t_n, t_a) \;+\; \epsilon_{ca}(t_n, t_a) \tag{9.89}$$

Here $(\epsilon_c(t_n), \epsilon_{cc}, \epsilon_{ca})$ are the instantaneous strain at the time considered, the creep strain and the aging strain, respectively. Thus, for a constant stress the aging strain

component may take the form

$$\epsilon_{ca}(t_n, t_a) \;=\; \phi_a(t_n, t_a)\,\frac{\sigma_c}{E_{c28}} \tag{9.90}$$

where ϕ_a is the aging coefficient, given by

$$\phi_a(t_n, t_a) \;=\; \frac{E_{c28}}{E_c(t_a)} \;-\; \frac{E_{c28}}{E_c(t_n)} \tag{9.91}$$

In other words, the aging strain may be considered as another irrecoverable creep strain component. Thus, when the stress is stepwise varying, the corresponding aging strain on rate form becomes (ref. Eq.(9.58))

$$\epsilon_{ca}(t_n, t_a) \;=\; \frac{1}{E_{c28}} \sum_{i=1}^{n} \left[\phi_a(t_i, t_a) \;-\; \phi_a(t_{i-1}, t_a)\right] \bar{\sigma}_{ci} \tag{9.92}$$

where $\bar{\sigma}_{ci}$ is the stress corresponding to the time step $t_i - t_{i-1}$, and t_a is now the time at first load application. Application of Eq.(9.91) by altering subscript 'n' to 'i' and '$i-1$' in turn, yields for the increment of the aging coefficient

$$\phi_a(t_i, t_a) \;-\; \phi_a(t_{i-1}, t_a) \;=\; \frac{E_{c28}}{E_c(t_{i-1})} \;-\; \frac{E_{c28}}{E_c(t_i)} \tag{9.93}$$

By also introducing Eq.(9.42), the aging strain component enters its final form

$$\epsilon_{ca}(t_{Tn}, T_n) \;=\; \frac{1}{E_{c28}} \sum_{i=1}^{n} \left[\frac{1}{\mathcal{B}_T(T_{i-1})\sqrt{\mathcal{B}_{cc}(t_{Ti-1})}} \;-\; \frac{1}{\mathcal{B}_T(T_i)\sqrt{\mathcal{B}_{cc}(t_{Ti})}}\right] \bar{\sigma}_{ci} \tag{9.94}$$

Here $(\mathcal{B}_T, \mathcal{B}_{cc})$ are given by Eqs.(9.27,9.9), respectively; while (t_T, T) are the temperature adjusted age according to Eq.(9.10) and the temperature, respectively, at times indicated by the subscripts ('n','i','$i-1$'). Like creep, the aging strain has to be evaluated for each principal direction at every integration point. As already pointed out in Subsections 9.3.3 and 9.5.4, the sustained stress $\bar{\sigma}_{ci}$ for the generic time step will be taken as the average of the stresses at the times t_{i-1} and t_i. Since the latter stress is not known yet when the aging strain is updated, an approximate value, determined as outlined in the next section, will instead be employed.

9.7 Computing Mechanical Strain in Concrete

So far, the stress $\bar{\sigma}_c$ that enters the creep and aging strain increments for the time step considered is said to represent an average of the stress at the previous equilibrium state and the current stress. Since the latter stress in return is a function of the current instantaneous or mechanical strain ϵ_c, it follows from the strain decomposition in Eq.(9.1) that some kind of iteration in general becomes necessary in order to determine ϵ_c. However, iteration at the integration point level is not desirable from

a computational point of view, and thus an approximate procedure to solve for ϵ_c without iteration will be outlined in this section.

By inserting the concrete strains from Eqs.(9.3,9.4) into Eq.(9.1) and rearranging terms, the following expression may result

$$\epsilon_c + \Delta\epsilon_{cc} + \Delta\epsilon_{ca} \;=\; \epsilon - \epsilon_{cT} - \epsilon_{cs} - \epsilon_{cc}^{(p)} - \epsilon_{ca}^{(p)} \tag{9.95}$$

Here ϵ is the total strain, as derived from the nodal displacements, and strains with subscripts ('cT','cs','cc','ca') are the thermal, shrinkage, creep and aging strains, respectively. Furthermore, superscript '(p)' refers to the previous equilibrium state, and Δ denotes increment for the time step considered. All quantities on the right hand side are known. The strain increments on the left hand side may be expressed through

$$\Delta\epsilon_{cc} \;=\; \Delta\phi_c \,\frac{\bar{\sigma}_c}{E_{c28}} \;-\; \epsilon_{ccd}^{(p)}\,\mathcal{B}_d \tag{9.96}$$

$$\Delta\epsilon_{ca} \;=\; \Delta\phi_a \,\frac{\bar{\sigma}_c}{E_{c28}} \tag{9.97}$$

where Eq.(9.96) follows from Eqs.(9.83,9.85,9.86). Here $\Delta\phi_c$ is the incremental creep coefficient for the time step, as a sum of the delayed elastic, basic flow and drying flow contributions, while the term $-\epsilon_{ccd}^{(p)}\mathcal{B}_d$ expresses the recovery with time of the delayed elastic creep strain component at the previous equilibrium state. Furthermore, Eq.(9.97) follows from Eq.(9.94), and here $\Delta\phi_a$ is the incremental aging coefficient. Finally, E_{c28} is the initial modulus of elasticity at the age of 28 days. Now the expression for the corresponding stress $\bar{\sigma}_c$ may conveniently be introduced, i.e.

$$\bar{\sigma}_c \;=\; \frac{1}{2}\left(\breve{\sigma}_c \,+\, \sigma_c^{(p)}\right) \tag{9.98}$$

where $(\breve{\sigma}_c, \sigma_c^{(p)})$ are the current stress and the stress at the previous equilibrium state, respectively. The former is now equipped with an accent '$\breve{}$' to signify that it is a preliminary estimate of the current stress σ_c, used here in the creep and aging strain computations. Note that $\bar{\sigma}_c$ is also entering the nonlinear creep coefficients (ϕ_{fb1}, ϕ_{fd2}) in Eqs.(9.74,9.80) through the relative stress s_a from Eq.(9.76). However, in these expressions $\sigma_c^{(p)}$ will now instead be employed, so that $\Delta\phi_c$ in Eq.(9.96) can be considered as a known quantity. To proceed further, a stress-strain relationship has to be introduced. The initial assumption made here is that the redistribution of stresses due to combined creep and aging implies *unloading* in concrete (and loading in reinforcing steel). Thus, the bilinear stress-strain relationship valid for concrete in unloading/reloading may be adopted, i.e.

$$\breve{\sigma}_c \;=\; E_u\,\epsilon_c \qquad ;\tilde{\epsilon}_c^{(c)} \le \epsilon_c \le \tilde{\epsilon}_c^{(t)} \tag{9.99}$$

where

$$E_u \;=\; \begin{cases} E_u^{(c)} & ;\tilde{\epsilon}_c^{(c)} \le \epsilon_c < 0 \\ E_u^{(t)} & ;0 \le \epsilon_c \le \tilde{\epsilon}_c^{(t)} \end{cases} \tag{9.100}$$

Here $(E_u^{(c)}, E_u^{(t)})$ are respectively the unloading/reloading moduli in compression and tension, as given by Eqs.(8.70,8.74) when unloading took place, and then adjusted for aging and temperature at the current time according to Eqs.(9.45,9.46). The strain limits $(\tilde{\epsilon}_c^{(c)}, \tilde{\epsilon}_c^{(t)})$ are approximations for the unknown actual strains at which the stress reaches the envelope curves in compression and tension. The following expressions for these limits are employed

$$\tilde{\epsilon}_c^{(c)} = \frac{\hat{\sigma}_c^{(c)}}{E_u^{(c)}} \tag{9.101}$$

$$\tilde{\epsilon}_c^{(t)} = \frac{\hat{\sigma}_c^{(t)}}{E_u^{(t)}} \tag{9.102}$$

where $(\hat{\sigma}_c^{(c)}, \hat{\sigma}_c^{(t)})$ are the envelope stresses that correspond to the previously experienced extreme strains $(\hat{\epsilon}_c^{(c)}, \hat{\epsilon}_c^{(t)})$ in compression and tension, respectively. Note that $(\tilde{\epsilon}_c^{(c)}, \tilde{\epsilon}_c^{(t)})$ become different from $(\hat{\epsilon}_c^{(c)}, \hat{\epsilon}_c^{(t)})$ since $(E_u^{(c)}, E_u^{(t)})$ are adjusted for aging and temperature as mentioned. Now, by combining Eqs.(9.95-9.99), the following expression for the current mechanical strain results

$$\epsilon_c = \frac{\epsilon - \epsilon_{cT} - \epsilon_{cs} - \epsilon_{cc}^{(p)} - \epsilon_{ca}^{(p)} - \frac{1}{2}(\Delta\phi_c + \Delta\phi_a)\frac{\sigma_c^{(p)}}{E_{c28}} + \epsilon_{ccd}^{(p)}\mathcal{B}_d}{1 + \frac{1}{2}(\Delta\phi_c + \Delta\phi_a)\frac{E_u}{E_{c28}}} \quad ; \tilde{\epsilon}_c^{(c)} \leq \epsilon_c \leq \tilde{\epsilon}_c^{(t)} \tag{9.103}$$

Thus, this expression is valid as long as ϵ_c falls within the range $\tilde{\epsilon}_c^{(c)} \leq \epsilon_c \leq \tilde{\epsilon}_c^{(t)}$. In (rare) cases that do not fulfill this condition, the $\breve{\sigma}_c$-value has to be selected. Then the expression for ϵ_c becomes, using Eqs.(9.95-9.98) only

$$\epsilon_c = \epsilon - \epsilon_{cT} - \epsilon_{cs} - \epsilon_{cc}^{(p)} - \epsilon_{ca}^{(p)} - \frac{1}{2}(\Delta\phi_c + \Delta\phi_a)\frac{\breve{\sigma}_c + \sigma_c^{(p)}}{E_{c28}} + \epsilon_{ccd}^{(p)}\mathcal{B}_d \tag{9.104}$$

Based on the preceding expressions, a search procedure for finding the mechanical strain in each principal direction at an integration point has been developed. The steps are outlined in the following:

- For each principal direction j that pertain to the previous equilibrium state, the following quantities are stored

$$\epsilon_{ccfj}^{(p)} \quad \epsilon_{ccdj}^{(p)} \quad \epsilon_{caj}^{(p)} \quad \mathcal{B}_{\sigma j}^{(p)} \quad \sigma_{cj}^{(p)} \quad E_{u28j}^{(c)} \quad E_{u28j}^{(t)} \quad \hat{\sigma}_{cj}^{(c)} \quad \hat{\sigma}_{cj}^{(t)} \qquad ; j = (\hat{1}, \hat{2})$$

  Thus, the creep strain components due to irrecoverable flow (basic plus drying) and delayed elasticity are stored separately, while the unloading/reloading moduli are represented by their equivalent 28 day-values. Furthermore, $\mathcal{B}_\sigma$ accounts for the detrimental effect on compressive strength due to high sustained loading. The remaining quantities are explained previously in this section. In addition, the angle $\beta_{c1}^{(p)}$ to the principal $\hat{1}$-direction is also stored.

- Prior to entering the algorithm, the following quantities have been computed

$$\epsilon_i \qquad ; i = (1, 2)$$

$$\beta_{c1} \quad \epsilon_{cT} \quad \epsilon_{cs} \quad \Delta\phi_{cd} \quad \mathcal{B}_d \quad \Delta\phi_a$$

$$\Delta\phi_{cfj} \quad E_{uj}^{(c)} \quad E_{uj}^{(t)} \quad \tilde{\epsilon}_{cj}^{(c)} \quad \tilde{\epsilon}_{cj}^{(t)} \qquad ; j = (\hat{1}, \hat{2})$$

  Here i refers to the current principal directions, and β_{c1} is the angle to the first of these. Similar to strains, the incremental creep coefficients are now characterized by irrecoverable flow and delayed elastic components. The remaining quantities are explained previously in this section.

- Then compare current and previous directions according to the procedure in Subsection 8.1.6, i.e.

  if

$$\beta_{c1}^{(p)} - \frac{\pi}{4} \leq \beta_{c1} \leq \beta_{c1}^{(p)} + \frac{\pi}{4}$$

  then stored values for the previous directions j are valid for the current directions i

$$i/j \; = \; (1/\hat{1}, 2/\hat{2})$$

  else

  then the correspondence between directions becomes

$$i/j \; = \; (1/\hat{2}, 2/\hat{1})$$

  end if

- Now search for the current mechanical strain ϵ_{ci} in the principal i-direction and the corresponding stress $\breve{\sigma}_{ci}$ by following the algorithm:

  At start, assume tension state by computing ϵ_{ci} from Eq.(9.103), inserting $E_{uj} \; = \; E_{uj}^{(t)}$.

  if

$$0 \leq \epsilon_{ci} \leq \tilde{\epsilon}_{cj}^{(t)}$$

  then

$$\breve{\sigma}_{ci} \; = \; E_{uj}^{(t)} \, \epsilon_{ci}$$

  else if

$$\epsilon_{ci} \; > \; \tilde{\epsilon}_{cj}^{(t)}$$

then select

$$\breve{\sigma}_{ci} \;=\; \hat{\sigma}_{cj}^{(t)}$$

and recompute ϵ_{ci}, using Eq.(9.104)

else passed to compression state

then recompute ϵ_{ci} from Eq.(9.103), now inserting $E_{uj} = E_{uj}^{(c)}$

if

$$\tilde{\epsilon}_{cj}^{(c)} \;\leq\; \epsilon_{ci} \;\leq\; 0$$

then

$$\breve{\sigma}_{ci} \;=\; E_{uj}^{(c)}\,\epsilon_{ci}$$

else if

$$\epsilon_{ci} \;<\; \tilde{\epsilon}_{cj}^{(c)}$$

then select

$$\breve{\sigma}_{ci} \;=\; \hat{\sigma}_{cj}^{(c)}$$

and recompute ϵ_{ci}, using Eq.(9.104)

else passed to neutral state

then select

$$\breve{\sigma}_{ci} \;=\; 0$$

and recompute ϵ_{ci}, using Eq.(9.104)

end if

end if

- Having determined $\breve{\sigma}_{ci}$, the time dependent quantities $(\epsilon_{ccfj}, \epsilon_{ccdj}, \epsilon_{caj}, \mathcal{B}_{\sigma j})$ can now be updated for the time step considered.

- Based on the computed mechanical strain ϵ_{ci}, the final current stress σ_{ci} is then found according to the search procedure outlined in Section 8.1.6. If this stress belongs to a global equilibrium state, the aforementioned updated quantities are saved. Otherwise the values pertaining to the previous equilibrium state are retained for the mechanical strain computation in the next iteration cycle.

A consequence of adopting the form in Eq.(9.98) for the sustained stress $\bar{\sigma}_c$, is that the values $(\sigma_c^{(p)}, \breve{\sigma}_c)$ at the beginning and end of the time step should refer to the same external load level. To comply with this, as already mentioned in Section 5.4, the prescribed sequence of the 'neutral time'-parameter λ will here be chosen so that typical short-time and long-time phenomena are handled in separate solution steps. To be more specific; take a structure subjected to a sustained load A, followed by an additional load B. In this case two separate solutions should be made regarding the introduction of load B; one immediate to application that yields the long-time effect

of load A, and one shortly after that includes the short-time response due to load B. Also note that the introduction of $(\hat{\sigma}_c^{(c)}, \hat{\sigma}_c^{(t)})$ as limit-values for $\breve{\sigma}_c$, implies that this procedure in possible loading phases reduces to a simple step forward procedure, as adopted by e.g. Kang [22]. There the stress at the previous equilibrium state is used for the succeeding time step (i.e. $\bar{\sigma}_c = \sigma_c^{(p)}$). In general, such a procedure requires 'small' time steps in order to achieve acceptable accuracy.

9.8 Stress Relaxation in Prestressing Steel

9.8.1 Relaxation under Constant Action

Relaxation is by definition loss of stress under constant strain. Thus, the total or final stress σ_f at time t_n due to a constant strain imposed at time t_e, may be expressed through the stress components

$$\sigma_f(t_n, t_e) \;=\; \sigma_p(t_e) \;+\; \sigma_r(t_n, t_e) \tag{9.105}$$

where σ_p is the initial (instantaneous) stress, and σ_r is the relaxation stress (i.e. a negative quantity). Numerous experiments have been carried out to quantify the stress development with time for this situation. Magura et al. [46] proposed the following relationship

$$\frac{\sigma_f}{\sigma_p} \;=\; 1 \;-\; \left(\frac{\sigma_p}{f_{0.1}} - 0.55\right) \frac{\log\left[24\,(t_n - t_e)/t_1\right]}{C_r} \qquad ; \frac{\sigma_p}{f_{0.1}} \geq 0.55 \tag{9.106}$$

Here $f_{0.1}$ is the stress at 0.1% strain offset, and C_r is a coefficient depending on the relaxation characteristics of the prestressing steel. Originally, C_r was set to 10. However, by fitting the expression to loss data for the three relaxation classes given in MC90 [35], the following average values were found

$$C_r \;=\; \begin{cases} 10 & - \quad \text{normal relaxation for wires and strands (class 1)} \\ 36 & - \quad \text{improved relaxation for wires and strands (class 2)} \\ 20 & - \quad \text{relaxation for bars (class 3)} \end{cases}$$

While C_r was found to be almost constant with stress level for class 1, and fairly constant for class 3, the coefficient varied from about 46 to 23 for a stress level $\sigma_p/f_{0.1}$ ranging from 0.7 to 0.95 in the case of class 2. Note that the above averages are for the stress range mentioned. Further, with reference to Eq.(9.106), the elapsed time $t_n - t_e$ is counted in days, and $t_1 = 1$ day. In order to yield losses, the value of the logarithm in Eq.(9.106) has to become positive, and thus $t_n - t_e \geq 1/24$ day $= 1$ hour. For shorter duration, no loss will be accounted for. Now, by combining Eqs.(9.105,9.106), the relaxation stress may take the form

$$\sigma_r \;=\; \begin{cases} 0 & ; \dfrac{\sigma_p}{f_{0.1}} \leq 0.55 \\[2ex] -\sigma_p \left(\dfrac{\sigma_p}{f_{0.1}} - 0.55\right) \dfrac{\log\left[24\,(t_n - t_e)/t_1\right]}{C_r} & ; \dfrac{\sigma_p}{f_{0.1}} > 0.55 \end{cases} \tag{9.107}$$

9.8.2 Rate of Relaxation Method

To this author's knowledge, very little experimental data exist on stress relaxation due to a stepwise varying strain, or in other words; due to a stepwise varying instantaneous stress. Consequently, an analysis method that covers this situation will mainly be 'hypothesis-based', and thus simplicity should take preference over complexity. A suitable and very simple method is obtained by applying a pure rate formulation. Since this method is similar to that of the rate of creep in Subsection 9.5.1, the term *rate of relaxation method* (RRM) will be introduced. Here the relaxation stress σ_r at time t_n may be expressed on the form

$$\begin{aligned} \sigma_r(t_n, t_e) &= -\sum_{i=1}^{n} \left[R(t_i - t_e) - R(t_{i-1} - t_e)\right] \bar{\sigma}_{pi} \\ &= -\sum_{i=1}^{n} R_o \left[\mathcal{B}_r(t_i - t_e) - \mathcal{B}_r(t_{i-1} - t_e)\right] \bar{\sigma}_{pi} \end{aligned} \tag{9.108}$$

where

$$R_o = \begin{cases} 0 & ; \dfrac{\bar{\sigma}_{pi}}{f_{0.1}} \leq 0.55 \\ \left(\dfrac{\bar{\sigma}_{pi}}{f_{0.1}} - 0.55\right) \dfrac{1}{C_r} & ; \dfrac{\bar{\sigma}_{pi}}{f_{0.1}} > 0.55 \end{cases} \tag{9.109}$$

$$\mathcal{B}_r(t_i - t_e) = \begin{cases} 0 & ; (t_i - t_e)/t_1 \leq 1/24 \\ \log\left[24\,(t_i - t_e)/t_1\right] & ; (t_i - t_e)/t_1 > 1/24 \end{cases} \tag{9.110}$$

Here $(R_o, \mathcal{B}_r)$ follow from Eq.(9.107), t_e is the time at the tensioning state, and $\bar{\sigma}_{pi}$ is the instantaneous stress corresponding to the time step $t_i - t_{i-1}$. In order to account for redistribution between concrete and steel during the time step, $\bar{\sigma}_{pi}$ will be taken as the average of the stresses at times t_i and t_{i-1}, i.e.

$$\bar{\sigma}_{pi} = \frac{1}{2}\left[\sigma_p(t_i) + \sigma_p(t_{i-1})\right] \tag{9.111}$$

This form is consistent with the treatment of the various stress dependent time effects in concrete. However, no approximation is necessary in this case since $\sigma_p(t_i)$ is readily available when computation of $\bar{\sigma}_{pi}$ is needed. Finally, the total or final stress σ_f at the time considered t_n is given by

$$\sigma_f(t_n, t_e) = \sigma_p(t_n) + \sigma_r(t_n, t_e) \tag{9.112}$$

So far, the presentation has focused on plain prestressing steel, as will be the selected formulation in conjunction with tendons. Pbars, however, are more conveniently treated as 'smeared' steel. Then a 'smeared' stress $f_{0.1}^{(s)}$ at 0.1% strain offset may be introduced

$$f_{0.1}^{(s)} = \rho\, f_{0.1} \tag{9.113}$$

where ρ is the steel to concrete area ratio. Now by using $f_{0.1}^{(s)}$ instead of $f_{0.1}$, the format works equally well for 'smeared' steel.

From Section 8.3 it is seen that the stress $f_{0.2}$ at 0.2% strain offset is among the material parameters employed for the short-time constitutive model. Since $f_{0.1}$ is used in this section, two input-parameters that basically characterize the same property, are now introduced; a circumstance that is impractical. Therefore, an approximate conversion formula

$$f_{0.1} \approx 0.95\, f_{0.2} \tag{9.114}$$

has been adopted in the computer program that is developed as a part of this work (Chapter 11), rendering $f_{0.2}$ as the only input-value. This approximate expression is based on data taken from MC90 [35].

9.8.3 Fictitious Initial Stress Method

First, a method proposed by Glodowski and Lorenzetti [47] will be mentioned briefly. This method is quite similar to RRM, but deviates by letting the starting time on the relaxation curve be adjusted for each new time step in order to comply with the previous accumulated relaxation stress. In this manner, an effect of stress history is taken into account. However, the far most popular method seems to be one originally introduced by Hernandez and Gamble [48], and later adopted by several other investigators [22]-[27]. Also this method is close to RRM, but now the instantaneous stress for each new time step is adjusted to comply with the previous total or final stress. Thus, an effect of stress history is again accounted for. Since an adjusted stress is employed instead of the actual instantaneous stress, this method will here be termed the *fictitious initial stress method* (FISM). The details on how to arrive at this fictitious stress will be given in the following. Note that in order to account for redistribution during the time step, the instantaneous stress will here still be based on the average value $\bar{\sigma}_{pi}$ according to Eq.(9.111). This is in contrast to the original FISM that employs the instantaneous stress $\sigma_p(t_{i-1})$. Thus, instead of using the final stress σ_f at time t_{i-1} as basis, a modified value $\hat{\sigma}_{fi-1}$ will now be defined

$$\hat{\sigma}_{fi-1} = \bar{\sigma}_{pi} + \sigma_r(t_{i-1}, t_e) \tag{9.115}$$

Then the fictitious initial stress $\hat{\sigma}_{pi}$ is here determined as the stress applied at time t_e that relaxes to $\hat{\sigma}_{fi-1}$ at t_{i-1}. This relationship is described by Eq.(9.106), that now reads

$$\hat{\sigma}_{fi-1} = \hat{\sigma}_{pi} - \hat{\sigma}_{pi}\left(\frac{\hat{\sigma}_{pi}}{f_{0.1}} - 0.55\right)\frac{\log\left[24\,(t_{i-1} - t_e)/t_1\right]}{C_r} \tag{9.116}$$

Solving for $\hat{\sigma}_{pi}$ implies finding the solution of a quadratic equation. The result becomes

$$\frac{\hat{\sigma}_{pi}}{f_{0.1}} = \begin{cases} \dfrac{0.55\,\dfrac{\log \hat{t}}{C_r} + 1}{2\,\dfrac{\log \hat{t}}{C_r}} \left[1 - \sqrt{1 - \dfrac{4\,\dfrac{\log \hat{t}}{C_r}\,\dfrac{\hat{\sigma}_{fi-1}}{f_{0.1}}}{\left(0.55\,\dfrac{\log \hat{t}}{C_r} + 1 \right)^2}} \right] & ;\hat{t} > 1 \\ \dfrac{\bar{\sigma}_{pi}}{f_{0.1}} & ;\hat{t} \leq 1 \end{cases} \tag{9.117}$$

where

$$\hat{t} = 24\,(t_{i-1} - t_e)/t_1 \tag{9.118}$$

The remaining steps using FISM are now identical to RRM. Thus, the relaxation stress σ_r at time t_n follows from Eqs.(9.108-9.110), inserting $\hat{\sigma}_{pi}$ instead of $\bar{\sigma}_{pi}$, while the corresponding final stress σ_f is given by Eq.(9.112). Again the format works equally well for 'smeared' steel through the correction made in Eq.(9.113). Compared to RRM, FISM will give more relaxation for an increasing instantaneous stress history, and less for the more typical decreasing history (i.e. highest stress at the tensioning state). These observations follow from the adopted form of Eq.(9.106). Although FISM has an effect of stress history embedded, it may not necessarily be the most accurate for that reason. Both methods are implemented in the computer program reviewed in Chapter 11.

9.9 Influence on Tangent Moduli of Concrete and Prestressing Steel

A consequence of introducing the average stress for the time step in the expressions for the stress dependent time effects in concrete and prestressing steel, is that these effects now also intervene in the tangent moduli formulations. For concrete the moduli that contribute to the material stiffness matrix of the element, are those obtained by differentiation of stresses σ_c with respect to total strains ϵ, as derived from the nodal displacements. Through the chain rule, however, a connection to the corresponding mechanical or instantaneous strains ϵ_c may be established. Thus, for the 'direct' modulus in the principal i-direction

$$\frac{\partial \sigma_{ci}}{\partial \epsilon_i} = \frac{\partial \sigma_{ci}}{\partial \epsilon_{ci}} \frac{\partial \epsilon_{ci}}{\partial \epsilon_i} \tag{9.119}$$

where the various expressions for $\partial\sigma_{ci}/\partial\epsilon_{ci}$ are derived in Section 8.1, while $\partial\epsilon_{ci}/\partial\epsilon_i$ follows from Eqs.(9.103,9.104), i.e.

$$\frac{\partial\epsilon_{ci}}{\partial\epsilon_i} = \begin{cases} \dfrac{1}{1+\dfrac{1}{2}(\Delta\phi_{cj}+\Delta\phi_a)\dfrac{E_{uj}}{E_{c28}}} & ;\tilde{\epsilon}_{cj}^{(c)} \le \epsilon_{ci} \le \tilde{\epsilon}_{cj}^{(t)} \\ 1 & ;\epsilon_{ci} < \tilde{\epsilon}_{cj}^{(c)} \ \vee \ \epsilon_{ci} > \tilde{\epsilon}_{cj}^{(t)} \end{cases} \tag{9.120}$$

Here $(\Delta\phi_c, \Delta\phi_a)$ are respectively the incremental creep and aging coefficients for the time step, E_u is the unloading/reloading modulus according to Eq.(9.100), and E_{c28} is the initial modulus of elasticity at the age of 28 days. Furthermore, $(\tilde{\epsilon}_c^{(c)}, \tilde{\epsilon}_c^{(t)})$, as expressed by Eqs.(9.101,9.102), are approximations for the unknown strains at which the stress reaches the envelope curves in compression and tension, respectively. Finally, subscript 'j' implies that the quantities pertain to the principal direction at the previous equilibrium state that now is closest to the current i-direction. For the 'cross' modulus that accounts for coupling to the coexisting normal n-direction, no corresponding time effect intervenes, and the relation simply becomes

$$\frac{\partial\sigma_{ci}}{\partial\epsilon_n} = \frac{\partial\sigma_{ci}}{\partial\epsilon_{cn}} \tag{9.121}$$

Again, the various expressions for $\partial\sigma_{ci}/\partial\epsilon_{cn}$ are given in Section 8.1.

Prestressing steel is in some respect special compared to concrete and ordinary reinforcing steel, since one part of the arising forces is treated as applied loading (that from the tensioning state), and the remaining part as internal resisting forces. The details of this procedure will be covered in Section 10.5 and 10.2 for tendons and pbars, respectively. To introduce the time effect on the tangent modulus of prestressing steel, however, it is here sufficient to consider only the derivative of the total or final stress σ_f with respect to the mechanical strain ϵ_p. By applying the stress decomposition from Eq.(9.112), and also using the chain rule, the following expression results

$$\frac{\partial\sigma_f}{\partial\epsilon_p} = \frac{\partial\sigma_p}{\partial\epsilon_p}\left(1 + \frac{\partial\sigma_r}{\partial\sigma_p}\right) \tag{9.122}$$

Here (σ_p, σ_r) are the instantaneous stress and relaxation stress, respectively. Expressions for $\partial\sigma_p/\partial\epsilon_p$ are given in Subsection 8.3.1. To proceed further now, a more specific relation for the relaxation stress has to be introduced. By assuming the rate of relaxation method (RRM), the selected relation is given by Eq.(9.108) that may be expressed on the partitioned form

$$\sigma_r = \sigma_r^{(p)} - \Delta R\,\bar{\sigma}_p \tag{9.123}$$

Here $\sigma_r^{(p)}$ is the relaxation stress at the previous equilibrium state, while $(\bar{\sigma}_p, \Delta R)$ pertain to the current time step; respectively the average stress and what here is termed the incremental relaxation coefficient (i.e. the difference enclosed by brackets

in the first part of Eq.(9.108)). Indeed, ΔR is also a function of $\bar{\sigma}_p$, and thus the derivative of σ_r with respect to σ_p takes the form

$$\frac{\partial \sigma_r}{\partial \sigma_p} = \frac{\partial \sigma_r}{\partial \bar{\sigma}_p}\frac{\partial \bar{\sigma}_p}{\partial \sigma_p} = -\left(\frac{\partial \Delta R}{\partial \bar{\sigma}_p}\bar{\sigma}_p + \Delta R\right)\frac{\partial \bar{\sigma}_p}{\partial \sigma_p} \tag{9.124}$$

The part of this expression in parentheses may be developed further by introducing Eqs.(9.109,9.110). However, correct differentiation will yield a quite severe discontinuity at $\bar{\sigma}_p/f_{0.1} = 0.55$, which is not desirable numerically. To avoid this problem, it has been decided to introduce the following simple approximation that is reasonably accurate and has the advantage of being continuous

$$\frac{\partial \Delta R}{\partial \bar{\sigma}_p}\bar{\sigma}_p + \Delta R \approx 3\,\Delta R \tag{9.125}$$

Furthermore, from Eq.(9.111) it follows

$$\frac{\partial \bar{\sigma}_p}{\partial \sigma_p} = \frac{1}{2} \tag{9.126}$$

Then by combining the last three equations, Eq.(9.122) converts to the simple form

$$\frac{\partial \sigma_f}{\partial \epsilon_p} \approx \frac{\partial \sigma_p}{\partial \epsilon_p}\left(1 - \frac{3}{2}\Delta R\right) \tag{9.127}$$

As stated, this expression is based on RRM. The fictitious initial stress method (FISM) will also yield a similar time effect on the tangent modulus, since the fictitious initial stress $\hat{\sigma}_p$ again is a function of the average stress for the time step. In fact, the only difference is that the value 1/2 from Eq.(9.126) now would have been replaced by an expression obtained through $\partial \hat{\sigma}_p/\partial \sigma_p$, which may be determined using Eqs.(9.117,9.115,9.111). Due to the nonlinear relation, the result becomes $\geq 1/2$. However, as a simplification, Eq.(9.127) will here be adopted for FISM as well.

Chapter 10

Cross Section Analysis

10.1 Introduction

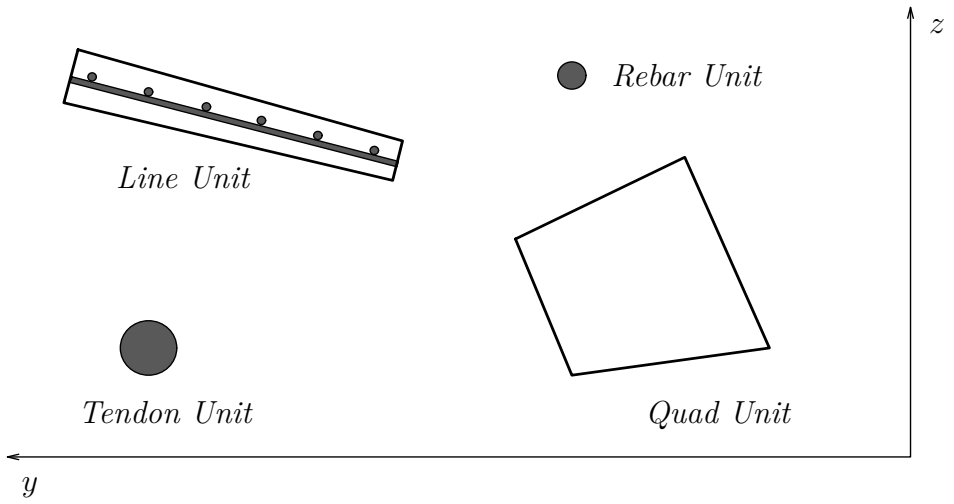

Figure 10.1: Elementary Section Units

Briefly speaking, the cross section analysis is the part that links the constitutive models presented in Chapters 8 and 9 to the finite element formulation in Chapter 4. Often a beam cross section is idealized into horizontal layers for 2D structural problems ([22],[27]), while some grid subdivision technique is common for 3D cases ([23],[26]). In this work, an approach based on defining elementary units or 'building blocks' for the total section, has instead been selected. The two typical units of this kind are the *line unit* consisting of concrete with 'smeared' reinforcement, and the *quad unit* of plain concrete. Since the analysis of these units relies on numerical integration, the actual layout is a choice between size and number of integration points. With 'large' units a corresponding saving on input-data results. In some problems, however, reinforcement may be better represented on discrete form. Thus, to cover individual bars, a *rebar unit* has been added to the list. Finally, the internal resistance from bonded prestressing tendons is taken care of through a separate *tendon*

unit. The selected elementary units may look as depicted in Fig. 10.1. Besides the inherent restriction that the modeling of a beam cross section can only be based on these four constituent units, the actual combination of units may be rather arbitrary, and there is e.g. no symmetry requirements for the resulting section.

10.2 Line Unit

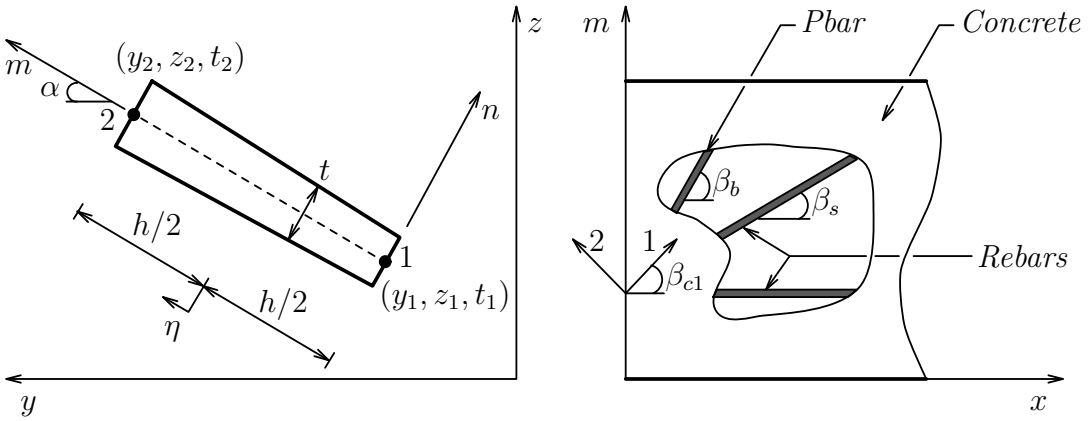

Figure 10.2: Line Unit

A line unit (Fig. 10.2) is the cross section part of a reinforced concrete panel that spans the entire length of an element. Its exterior geometry is defined by the (y, z)-coordinates and the thickness t at the endpoints, while embedded reinforcement is characterized by the angle of orientation β with the x-axis (the longitudinal element axis) and the cross section intensity a, measured per unit length normal to the bar axis. Three components of reinforcement are allowed; rebars in the (x, s)-directions and pbar in the b-direction. The latter is imported from the pbar panel (Chapter 7) that is assigned to the line unit. As mentioned, the analysis of line units relies on numerical integration, and thus the value of the natural coordinate η follows from the integration scheme. Then the corresponding (y, z, t)-values at the integration or sample point may be found from the parametric expression

$$\begin{Bmatrix} y \\ z \\ t \end{Bmatrix} = \begin{bmatrix} y_1 & y_2 \\ z_1 & z_2 \\ t_1 & t_2 \end{bmatrix} \begin{Bmatrix} \varphi_1 \\ \varphi_2 \end{Bmatrix} \tag{10.1}$$

where the linear shape functions read

$$\begin{Bmatrix} \varphi_1 \\ \varphi_2 \end{Bmatrix} = \frac{1}{2} \begin{Bmatrix} 1 - \eta \\ 1 + \eta \end{Bmatrix} \tag{10.2}$$

Thus, the (y, z, t)-values at the endpoints $(1, 2)$ are recovered from $\eta = (-1, 1)$, respectively. Now the vector of strains $\boldsymbol{\epsilon}$ at the sample point can be determined from the nodal displacements using Eq.(4.52). Of convenience, the ordering of the strain components will be repeated here

$$\boldsymbol{\epsilon}^T = \begin{bmatrix} \epsilon_x & \gamma_{xy} & \gamma_{xz} & \epsilon_y & \epsilon_z & \gamma_{yz} \end{bmatrix} \tag{10.3}$$

The analysis will be based on the assumption that a line unit can carry only in-plane forces. Thus, the out-of-plane strain components are not stress-producing and will be disregarded. The vector of in-plane strains $\boldsymbol{\epsilon}_m$ follows from the transformation

$$\boldsymbol{\epsilon}_m = \boldsymbol{A}_m \boldsymbol{\epsilon} \tag{10.4}$$

where $\boldsymbol{\epsilon}_m$ has the ordering

$$\boldsymbol{\epsilon}_m^T = \begin{bmatrix} \epsilon_x & \epsilon_m & \gamma_{xm} \end{bmatrix} \tag{10.5}$$

and $\boldsymbol{A}_m$ is the transformation matrix given by[1]

$$\boldsymbol{A}_m = \begin{bmatrix} 1 & 0 & 0 & 0 & 0 & 0 \\ 0 & 0 & 0 & \cos^2\alpha & \sin^2\alpha & \sin\alpha\cos\alpha \\ 0 & \cos\alpha & \sin\alpha & 0 & 0 & 0 \end{bmatrix} \tag{10.6}$$

Here α is the angle between the y-axis and the m-axis (the in-plane transverse axis), and thus $(\sin\alpha, \cos\alpha)$ are easily derivable from the (y, z)-coordinates at the endpoints of the line unit. Transformation further to the in-plane principal strains $\boldsymbol{\epsilon}_c$ takes place through

$$\boldsymbol{\epsilon}_c = \boldsymbol{A}_{cm} \boldsymbol{\epsilon}_m \tag{10.7}$$

where

$$\boldsymbol{\epsilon}_c^T = \begin{bmatrix} \epsilon_1 & \epsilon_2 \end{bmatrix} \tag{10.8}$$

$$\boldsymbol{A}_{cm} = \begin{bmatrix} \cos^2\beta_{c1} & \sin^2\beta_{c1} & \sin\beta_{c1}\cos\beta_{c1} \\ \sin^2\beta_{c1} & \cos^2\beta_{c1} & -\sin\beta_{c1}\cos\beta_{c1} \end{bmatrix} \tag{10.9}$$

Here β_{c1} is the angle between the x-axis and the principal 1-direction. A commonly used expression for this angle is

$$\beta_c = \frac{1}{2}\arctan\left[\frac{\gamma_{xm}}{\epsilon_x - \epsilon_m}\right] \tag{10.10}$$

However, care must be exercised here when retrieving β_{c1}, since this expression will yield the angle to the principal 2-direction when $\epsilon_x < \epsilon_m$. Besides, in order to make

[1] For transformation of strains, see e.g. [10].

sure that the comparison between previous and current directions, as needed in the search procedures in Subsection 8.1.6 and Section 9.7, is always based on angles in same semicircle, β_{c1} will here be determined in the interval $-\pi/2 \leq \beta_{c1} \leq \pi/2$. Thus

$$\beta_{c1} = \begin{cases} \beta_c & ; \epsilon_x \geq \epsilon_m \\ \beta_c + \dfrac{\pi}{2} & ; \epsilon_x < \epsilon_m \ \wedge \ \gamma_{xm} \geq 0 \\ \beta_c - \dfrac{\pi}{2} & ; \epsilon_x < \epsilon_m \ \wedge \ \gamma_{xm} < 0 \end{cases} \tag{10.11}$$

where β_c is given by Eq.(10.10). For hydrostatic strain states (i.e. $\epsilon_x = \epsilon_m$ and $\gamma_{xm} = 0$), however, the principal directions are not defined, and a value $\beta_{c1} = 0$ is instead employed. Note that the procedure for finding β_{c1} indeed assumes the arctan-function to yield values in the interval $(-\pi/2, \pi/2)$, which should be standard on computers. Having determined the total principal strains, computation of corresponding mechanical strains, as outlined in Section 9.7, may now take place. Then principal concrete stresses $\boldsymbol{\sigma}_c$ are found through the search procedure in Subsection 8.1.6, and finally transformation back to stresses $\boldsymbol{\sigma}_{mc}$ in the (x, m)-system follows from

$$\boldsymbol{\sigma}_{mc} = \boldsymbol{A}_{cm}^T \boldsymbol{\sigma}_c \tag{10.12}$$

where

$$\boldsymbol{\sigma}_c^T = \begin{bmatrix} \sigma_{c1} & \sigma_{c2} \end{bmatrix} \tag{10.13}$$

$$\boldsymbol{\sigma}_{mc}^T = \begin{bmatrix} \sigma_x & \sigma_m & \tau_{xm} \end{bmatrix}_c \tag{10.14}$$

and $\boldsymbol{A}_{cm}$ is given by Eq.(10.9). For reinforcement, the normal strain ϵ_t in the direction of a bar may be obtained from transformation of the in-plain strains $\boldsymbol{\epsilon}_m$. Thus

$$\epsilon_t = \boldsymbol{a}_{tm} \boldsymbol{\epsilon}_m \tag{10.15}$$

where $\boldsymbol{a}_{tm}$ is the transformation vector that takes the form

$$\boldsymbol{a}_{tm} = \begin{bmatrix} \cos^2\beta & \sin^2\beta & \sin\beta\cos\beta \end{bmatrix} \tag{10.16}$$

Here β is the angle between the x-axis and the bar direction (i.e. ($\beta_x \equiv 0, \beta_s$) for rebars and β_b for pbar). The mechanical rebar-strain ϵ_s is now given by

$$\epsilon_s = \epsilon_t - \epsilon_{sT} \tag{10.17}$$

while the mechanical pbar-strain ϵ_b reads

$$\epsilon_b = \epsilon_t + \Delta\epsilon_b^{(o)} - \epsilon_{sT} \tag{10.18}$$

Here ϵ_{sT} is the thermal strain from Eq.(9.7), and $\Delta\epsilon_b^{(o)}$ is the additional pbar-strain at the final tensioning state (when bond is established) according to Eq.(7.25). Furthermore, the steel to concrete area ratio ρ, introduced to convert reinforcement stresses to 'smeared' or 'equivalent concrete' form, is expressed by

$$\rho \;=\; \frac{a}{t} \tag{10.19}$$

where a is the area intensity of the reinforcement in question, and t is the concrete thickness at the sample point, as taken from Eq.(10.1). Then the stress-strain relationships in Sections 8.2 and 8.3 may be applied to obtain the 'smeared' stresses $(\sigma_s^{(s)}, \sigma_b^{(s)})$ for rebars and pbar, respectively. The latter is again corrected for stress relaxation, as dealt with in Section 9.8, before arriving at the total or final stress $\sigma_f^{(s)}$. Thus

$$\sigma_f^{(s)} \;=\; \sigma_b^{(s)} \,+\, \sigma_r^{(s)} \tag{10.20}$$

where $\sigma_r^{(s)}$ is the relaxation stress. However, remembering that the pbar-forces at the final tensioning state are still retained as applied loading (Section 7.6), only the change of stress since that state is here treated as the internal resistance-contributing stress $\sigma_{ir}^{(s)}$, i.e.

$$\sigma_{ir}^{(s)} \;=\; \sigma_f^{(s)} \,-\, \rho_b\, \sigma_b^{(o)} \tag{10.21}$$

Here $\sigma_b^{(o)}$ is the steel stress at the final tensioning state according to Eq.(8.100), and ρ_b is the pbar area ratio. Now the 'smeared' stress for the reinforcement in question may be transformed to stresses $\boldsymbol{\sigma}_m^{(s)}$ in the (x, m)-system using the relation

$$\boldsymbol{\sigma}_m^{(s)} \;=\; \boldsymbol{a}_{tm}^T\, \sigma^{(s)} \tag{10.22}$$

where $\boldsymbol{a}_{tm}$ is given by Eq.(10.16), and $\sigma^{(s)}$ symbolizes $(\sigma_s^{(s)}, \sigma_{ir}^{(s)})$ for rebars and pbar, respectively. The components of $\boldsymbol{\sigma}_m^{(s)}$ have the same ordering as in Eq.(10.14) for $\boldsymbol{\sigma}_{mc}$ that comes from the concrete. The resulting (x, m)-stresses $\boldsymbol{\sigma}_m$ are then obtained by adding the individual contributions. Thus

$$\boldsymbol{\sigma}_m \;=\; \boldsymbol{\sigma}_{mc} \,+\, \boldsymbol{\sigma}_{mx}^{(s)} \,+\, \boldsymbol{\sigma}_{ms}^{(s)} \,+\, \boldsymbol{\sigma}_{mb}^{(s)} \tag{10.23}$$

The varying second subscript here on 'smeared' stresses signify the contributions from rebars in the (x, s)-directions and pbar in the b-direction. Finally, the resulting stresses $\boldsymbol{\sigma}$ in the (x, y, z)-system (the element coordinate system) follow from the transformation

$$\boldsymbol{\sigma} \;=\; \boldsymbol{A}_m^T\, \boldsymbol{\sigma}_m \tag{10.24}$$

where $\boldsymbol{A}_m$ is given by Eq.(10.6), and $\boldsymbol{\sigma}$ is as presented in Eq.(4.67), but will of convenience be repeated here

$$\boldsymbol{\sigma}^T \;=\; \begin{bmatrix} \sigma_x & \tau_{xy} & \tau_{xz} & \sigma_y & \sigma_z & \tau_{yz} \end{bmatrix} \tag{10.25}$$

Having established $\boldsymbol{\sigma}$ and (y, z, t) from Eq.(10.1), all information necessary is then available for computing the sample point contribution through the area integrals in Eqs.(4.72-4.81,4.140) to the internal node-force vector $\boldsymbol{r}$ and the geometric stiffness matrix $\boldsymbol{k}_g$ of the element.

In parallel with the stress computation, the corresponding tangent moduli may also be evaluated. For the principal directions the moduli of concrete are here collected into a tangent constitutive or modular matrix $\boldsymbol{C}_c$, defined as follows

$$\boldsymbol{C}_c \;=\; \frac{\partial \boldsymbol{\sigma}_c}{\partial \boldsymbol{\epsilon}_c} \;=\; \begin{bmatrix} \dfrac{\partial \sigma_{c1}}{\partial \epsilon_1} & \dfrac{\partial \sigma_{c1}}{\partial \epsilon_2} \\ \dfrac{\partial \sigma_{c2}}{\partial \epsilon_1} & \dfrac{\partial \sigma_{c2}}{\partial \epsilon_2} \end{bmatrix} \tag{10.26}$$

where expressions for the entries are given in Sections 9.9 and 8.1. The tangent constitutive matrix $\boldsymbol{C}_{mc}$ of concrete in the (x, m)-system is defined similarly, i.e.

$$\boldsymbol{C}_{mc} \;=\; \frac{\partial \boldsymbol{\sigma}_{mc}}{\partial \boldsymbol{\epsilon}_m} \tag{10.27}$$

These derivatives may be developed further by first assuming the principal directions fixed, yielding the matrix $\boldsymbol{C}_{mc}^{(C)}$, and then differentiate with respect to the angle β_{c1} to obtain the contribution $\boldsymbol{C}_{mc}^{(\beta)}$ due to rotating principal directions. Thus

$$\boldsymbol{C}_{mc} \;=\; \boldsymbol{C}_{mc}^{(C)} \,+\, \boldsymbol{C}_{mc}^{(\beta)} \tag{10.28}$$

Then $\boldsymbol{C}_{mc}^{(C)}$ becomes using the chain rule

$$\boldsymbol{C}_{mc}^{(C)} \;=\; \frac{\partial \boldsymbol{\sigma}_{mc}}{\partial \boldsymbol{\sigma}_c}\, \frac{\partial \boldsymbol{\sigma}_c}{\partial \boldsymbol{\epsilon}_c}\, \frac{\partial \boldsymbol{\epsilon}_c}{\partial \boldsymbol{\epsilon}_m} \;=\; \boldsymbol{A}_{cm}^T\, \boldsymbol{C}_c\, \boldsymbol{A}_{cm} \tag{10.29}$$

Here $\boldsymbol{A}_{cm}$ is given by Eq.(10.9), and Eqs.(10.12,10.26,10.7) have been employed in turn to arrive at the familiar final relation. Again, using Eq.(10.12), the $\boldsymbol{C}_{mc}^{(\beta)}$-matrix takes the form

$$\boldsymbol{C}_{mc}^{(\beta)} = \frac{\partial\big(\boldsymbol{A}_{cm}^T\, \boldsymbol{\sigma}_c\big)}{\partial \beta_{c1}}\, \frac{\partial \beta_{c1}}{\partial \boldsymbol{\epsilon}_m} = \left(\frac{\partial \boldsymbol{A}_{cm}^T}{\partial \beta_{c1}}\, \boldsymbol{\sigma}_c \,+\, \boldsymbol{A}_{cm}^T\, \frac{\partial \boldsymbol{\sigma}_c}{\partial \beta_{c1}} \right) \frac{\partial \beta_{c1}}{\partial \boldsymbol{\epsilon}_m} = \boldsymbol{C}_{mc}^{(A(\beta))} + \boldsymbol{C}_{mc}^{(\sigma(\beta))} \tag{10.30}$$

where

$$\boldsymbol{C}_{mc}^{(A(\beta))} \;=\; \frac{\partial \boldsymbol{A}_{cm}^T}{\partial \beta_{c1}}\, \boldsymbol{\sigma}_c\, \frac{\partial \beta_{c1}}{\partial \boldsymbol{\epsilon}_m} \tag{10.31}$$

$$\boldsymbol{C}_{mc}^{(\sigma(\beta))} \;=\; \boldsymbol{A}_{cm}^T\, \frac{\partial \boldsymbol{\sigma}_c}{\partial \beta_{c1}}\, \frac{\partial \beta_{c1}}{\partial \boldsymbol{\epsilon}_m} \tag{10.32}$$

Thus, the tangent constitutive matrix of concrete in the (x, m)-system may now more conveniently be rewritten as a sum of three matrices, of which the last two originate from the effect of rotating principal directions

$$\boldsymbol{C}_{mc} \;=\; \boldsymbol{C}_{mc}^{(C)} \,+\, \boldsymbol{C}_{mc}^{(A(\beta))} \,+\, \boldsymbol{C}_{mc}^{(\sigma(\beta))} \tag{10.33}$$

While $\boldsymbol{C}_{mc}^{(A(\beta))}$ is an inherent part of the rotating crack concept, $\boldsymbol{C}_{mc}^{(\sigma(\beta))}$ is usually zero. However, it becomes nonvanishing here in the postcracking regime due to the equivalent reinforcement formulation that makes the stress-strain envelope in principal tension dependent on its orientation in relation to the reinforcement. The evaluation of the two matrices will here concentrate on $\boldsymbol{C}_{mc}^{(A(\beta))}$ first. Then differentiation of $\boldsymbol{A}_{cm}$ from Eq.(10.9) with respect to β_{c1} yields

$$\frac{\partial \boldsymbol{A}_{cm}^{T}}{\partial \beta_{c1}} = \begin{bmatrix} -\sin 2\beta_{c1} & \sin 2\beta_{c1} \\ \sin 2\beta_{c1} & -\sin 2\beta_{c1} \\ \cos 2\beta_{c1} & -\cos 2\beta_{c1} \end{bmatrix} = \frac{1}{\sqrt{(\epsilon_x - \epsilon_m)^2 + \gamma_{xm}^2}} \begin{bmatrix} -\gamma_{xm} & \gamma_{xm} \\ \gamma_{xm} & -\gamma_{xm} \\ (\epsilon_x - \epsilon_m) & -(\epsilon_x - \epsilon_m) \end{bmatrix} \tag{10.34}$$

where the last passage is easily derivable from the Mohr's circle approach. Furthermore, $\partial \beta_{c1} / \partial \boldsymbol{\epsilon}_m$ is defined as the row vector

$$\frac{\partial \beta_{c1}}{\partial \boldsymbol{\epsilon}_m} = \begin{bmatrix} \dfrac{\partial \beta_{c1}}{\partial \epsilon_x} & \dfrac{\partial \beta_{c1}}{\partial \epsilon_m} & \dfrac{\partial \beta_{c1}}{\partial \gamma_{xm}} \end{bmatrix} \tag{10.35}$$

Using Eqs.(10.11,10.10), the derivatives become

$$\frac{\partial \beta_{c1}}{\partial \boldsymbol{\epsilon}_m} = \frac{1}{2\left\{(\epsilon_x - \epsilon_m)^2 + \gamma_{xm}^2\right\}} \begin{bmatrix} -\gamma_{xm} & \gamma_{xm} & (\epsilon_x - \epsilon_m) \end{bmatrix} \tag{10.36}$$

By also employing Eq.(10.13) and carrying out the product sequence in Eq.(10.31), $\boldsymbol{C}_{mc}^{(A(\beta))}$ gets into final form

$$\boldsymbol{C}_{mc}^{(A(\beta))} = \frac{\sigma_{c1} - \sigma_{c2}}{2\left\{(\epsilon_x - \epsilon_m)^2 + \gamma_{xm}^2\right\}^{3/2}} \begin{bmatrix} \gamma_{xm}^2 & -\gamma_{xm}^2 & -\gamma_{xm}(\epsilon_x - \epsilon_m) \\ -\gamma_{xm}^2 & \gamma_{xm}^2 & \gamma_{xm}(\epsilon_x - \epsilon_m) \\ -\gamma_{xm}(\epsilon_x - \epsilon_m) & \gamma_{xm}(\epsilon_x - \epsilon_m) & (\epsilon_x - \epsilon_m)^2 \end{bmatrix} \tag{10.37}$$

It is interesting to notice here that $\boldsymbol{C}_{mc}^{(A(\beta))}$ is left with a shear modulus term when $\gamma_{xm} = 0$. Then the principal directions coincide with the (x, m)-axes, and consequently, $\boldsymbol{C}_{mc}^{(C)}$ from Eq.(10.29) will be without nonzero shear terms. Thus, neglection of the $\boldsymbol{C}_{mc}^{(A(\beta))}$-contribution may lead to the undesirable situation of attaining a singular stiffness matrix. The evaluation of the second matrix $\boldsymbol{C}_{mc}^{(\sigma(\beta))}$ that originates from the effect of rotating principal directions, will start by first addressing the entries of $\partial \boldsymbol{\sigma}_c / \partial \beta_{c1}$, i.e.

$$\frac{\partial \boldsymbol{\sigma}_c}{\partial \beta_{c1}} = \begin{Bmatrix} \dfrac{\partial \sigma_{c1}}{\partial \beta_{c1}} \\ \dfrac{\partial \sigma_{c2}}{\partial \beta_{c1}} \end{Bmatrix} \tag{10.38}$$

As mentioned, these derivatives become nonzero only at the envelope curve of the stress-strain relationship in principal tension through the presence of the equivalent

reinforcement. This reinforcement is characterized by the quantities (E_d, f_d, ϵ_y), i.e. the equivalent values of 'smeared' modulus of elasticity, 'smeared' yield stress and yield strain, respectively. The first entry of Eq.(10.38) may then be expressed on the form (using superscript '(e)' for envelope)

$$\frac{\partial \sigma_{c1}^{(e)}}{\partial \beta_{c1}} = \frac{\partial \sigma_{c1}^{(e)}}{\partial E_d}\frac{\partial E_d}{\partial \beta_{c1}} + \frac{\partial \sigma_{c1}^{(e)}}{\partial f_d}\frac{\partial f_d}{\partial \beta_{c1}} \tag{10.39}$$

Here $\sigma_{c1}^{(e)}$ is given by Eq.(8.19/8.20) for the two reinforcement cases, termed 'normal' and 'subcritical' respectively (ref. Fig. 8.3). Note that when evaluating $\partial\sigma_{c1}^{(e)}/\partial E_d$ and $\partial\sigma_{c1}^{(e)}/\partial f_d$, the interconnecting relation for (E_d, f_d, ϵ_y) in Eq.(8.39) needs to be employed whenever appropriate. However, $\partial\sigma_{c1}^{(e)}/\partial E_d$ has already been determined and is given by Eq.(8.44/8.45) for the two reinforcement cases. A similar evaluation of $\partial\sigma_{c1}^{(e)}/\partial f_d$ yields

Normal, $E_d \geq E_{dc}$:

$$\frac{\partial \sigma_{c1}^{(e)}}{\partial f_d} = \begin{cases} 0 & ;0 \leq \epsilon_{c1} \leq \psi_t \epsilon_{cr} \\ \dfrac{\partial A_2}{\partial f_d}\dfrac{(\epsilon_{c1}-\psi_t\epsilon_{cr})^2}{1-b_t} + \dfrac{\partial A_3}{\partial f_d}\dfrac{(\epsilon_{c1}-\psi_t\epsilon_{cr})^3}{(1-b_t)^2} & ;\psi_t\epsilon_{cr} < \epsilon_{c1} \leq \epsilon_b \\ 1 - \dfrac{\partial A_2}{\partial f_d}\dfrac{(\epsilon_y-\epsilon_{c1})^2}{b_t} - \dfrac{2A_2(\epsilon_y-\epsilon_{c1})}{b_t E_d} & \\ \quad - \dfrac{\partial A_3}{\partial f_d}\dfrac{(\epsilon_y-\epsilon_{c1})^3}{b_t^2} - \dfrac{3A_3(\epsilon_y-\epsilon_{c1})^2}{b_t^2 E_d} & ;\epsilon_b < \epsilon_{c1} \leq \epsilon_y \\ 0 & ;\epsilon_y < \epsilon_{c1} \end{cases} \tag{10.40}$$

Subcritical, $E_d < E_{dc}$:

$$\frac{\partial \sigma_{c1}^{(e)}}{\partial f_d} = \begin{cases} 0 & ;0 \leq \epsilon_{c1} \leq \psi_t \epsilon_{cr} \\ 1 & ;\psi_t\epsilon_{cr} < \epsilon_{c1} \leq \epsilon_y \\ 0 & ;\epsilon_y < \epsilon_{c1} \end{cases} \tag{10.41}$$

where from Eqs.(8.23,8.24), and still using Eq.(8.39) whenever appropriate

$$\frac{\partial A_2}{\partial f_d} = -\frac{1}{\epsilon_y - \psi_t\epsilon_{cr}}\left(\frac{A_2}{E_d} - \frac{\partial E_b}{\partial f_d} + 3\frac{\partial E_{dc}}{\partial f_d}\right) \tag{10.42}$$

$$\frac{\partial A_3}{\partial f_d} = -\frac{1}{(\epsilon_y - \psi_t\epsilon_{cr})^2}\left(2\frac{A_3(\epsilon_y - \psi_t\epsilon_{cr})}{E_d} + \frac{\partial E_b}{\partial f_d} - 2\frac{\partial E_{dc}}{\partial f_d}\right) \tag{10.43}$$

Here $\partial E_b/\partial f_d$ can be found from Eq.(8.26)

$$\frac{\partial E_b}{\partial f_d} = \begin{cases} 2\dfrac{\partial E_{dc}}{\partial f_d} & ; E_{dc} \leq E_d \leq 2E_{dc} \\ 0 & ; 2E_{dc} < E_d \end{cases} \tag{10.44}$$

and finally $\partial E_{dc}/\partial f_d$ from Eqs.(8.25,8.39)

$$\frac{\partial E_{dc}}{\partial f_d} = -\frac{E_{dc}}{E_d(\epsilon_y - \psi_t \epsilon_{cr})} \tag{10.45}$$

The remaining two derivatives in Eq.(10.39) that are with respect to β_{c1}, read

$$\frac{\partial E_d}{\partial \beta_{c1}} = \sum_{i=1}^{n} \begin{cases} 2\rho_i E_{si} \sin\Delta\beta_i \cos\Delta\beta_i \left[2\cos^2\Delta\beta_i + \mu\left(\sin^2\Delta\beta_i - \cos^2\Delta\beta_i\right)\right] & \\ & ; \mu \geq -\cot^2\Delta\beta_i \\ 0 & ; \mu < -\cot^2\Delta\beta_i \end{cases} \tag{10.46}$$

$$\frac{\partial f_d}{\partial \beta_{c1}} = \sum_{i=1}^{n} \begin{cases} 2\rho_i f_{yi} \sin\Delta\beta_i \cos\Delta\beta_i & ; \mu \geq -\cot^2\Delta\beta_i \\ 0 & ; \mu < -\cot^2\Delta\beta_i \end{cases} \tag{10.47}$$

Here the former equation originates from Eqs.(8.35,8.36), while the latter follows from Eqs.(8.37,8.38). The angle $\Delta\beta_i$ between the principal 1-direction and the reinforcement direction is given by Eq.(8.31). Also the simplifying option for the normal reinforcement case when the stress-strain envelope after cracking is assumed linear, will be covered. Then the chain of derivatives that expresses $\partial\sigma_{c1}^{(e)}/\partial\beta_{c1}$ is more conveniently rewritten

$$\frac{\partial \sigma_{c1}^{(e)}}{\partial \beta_{c1}} = \frac{\partial \sigma_{c1}^{(e)}}{\partial \epsilon_y}\left(\frac{\partial \epsilon_y}{\partial E_d}\frac{\partial E_d}{\partial \beta_{c1}} + \frac{\partial \epsilon_y}{\partial f_d}\frac{\partial f_d}{\partial \beta_{c1}}\right) \tag{10.48}$$

Now $\sigma_{c1}^{(e)}$ is given by Eq.(8.62), while the new terms $\partial\epsilon_y/\partial E_d$ and $\partial\epsilon_y/\partial f_d$ follow immediatedly from Eq.(8.39). The final result becomes

Simplified Normal, $E_d \geq E_{dc}$:

$$\frac{\partial \sigma_{c1}^{(e)}}{\partial \beta_{c1}} = \begin{cases} 0 & ; 0 \leq \epsilon_{c1} \leq \psi_t \epsilon_{cr} \\ \dfrac{\psi_t f_{ct}}{E_d}\dfrac{\epsilon_{c1} - \psi_t\epsilon_{cr}}{(\epsilon_y - \psi_t\epsilon_{cr})^2}\left(-\epsilon_y\dfrac{\partial E_d}{\partial \beta_{c1}} + \dfrac{\partial f_d}{\partial \beta_{c1}}\right) & ; \psi_t\epsilon_{cr} < \epsilon_{c1} \leq \epsilon_y \\ 0 & ; \epsilon_y < \epsilon_{c1} \end{cases} \tag{10.49}$$

In the case of a tension/tension-state the second entry of Eq.(10.38) may also become nonzero. However, the preceding expressions for $\partial\sigma_{c1}^{(e)}/\partial\beta_{c1}$ apply for this entry too.

The only difference is that the angle $\Delta\beta_i$ now refers to the principal 2-direction. Furthermore, the result is unaffected of specifying the derivative with respect to β_{c1} or β_{c2}. Thus, Eq.(10.38) may take the optional form

$$\frac{\partial \boldsymbol{\sigma}_c}{\partial \beta_{c1}} = \left\{ \begin{array}{c} \dfrac{\partial \sigma_{c1}}{\partial \beta_{c1}} \\ \dfrac{\partial \sigma_{c2}}{\partial \beta_{c1}} \end{array} \right\} \equiv \left\{ \begin{array}{c} \dfrac{\partial \sigma_{c1}}{\partial \beta_{c1}} \\ \dfrac{\partial \sigma_{c2}}{\partial \beta_{c2}} \end{array} \right\} \tag{10.50}$$

Before carrying out the product sequence in Eq.(10.32) for the $\boldsymbol{C}_{mc}^{(\sigma(\beta))}$-matrix, an optional form of $\boldsymbol{A}_{cm}$ from Eq.(10.9) will also be introduced, i.e.

$$\boldsymbol{A}_{cm} = \left[\begin{array}{ccc} \cos^2\beta_{c1} & \sin^2\beta_{c1} & \sin\beta_{c1}\cos\beta_{c1} \\ \cos^2\beta_{c2} & \sin^2\beta_{c2} & \sin\beta_{c2}\cos\beta_{c2} \end{array} \right] \tag{10.51}$$

Now, by using in addition Eq.(10.36), $\boldsymbol{C}_{mc}^{(\sigma(\beta))}$ may finally read

$$\boldsymbol{C}_{mc}^{(\sigma(\beta))} = \sum_{i=1}^{2} \frac{\dfrac{\partial \sigma_{ci}}{\partial \beta_{ci}}}{2\left\{(\epsilon_x - \epsilon_m)^2 + \gamma_{xm}^2\right\}} \cdot \left[\begin{array}{ccc} -\gamma_{xm}\cos^2\beta_{ci} & \gamma_{xm}\cos^2\beta_{ci} & (\epsilon_x - \epsilon_m)\cos^2\beta_{ci} \\ -\gamma_{xm}\sin^2\beta_{ci} & \gamma_{xm}\sin^2\beta_{ci} & (\epsilon_x - \epsilon_m)\sin^2\beta_{ci} \\ -\gamma_{xm}\sin\beta_{ci}\cos\beta_{ci} & \gamma_{xm}\sin\beta_{ci}\cos\beta_{ci} & (\epsilon_x - \epsilon_m)\sin\beta_{ci}\cos\beta_{ci} \end{array} \right] \tag{10.52}$$

For hydrostatic strain states (i.e. $\epsilon_x = \epsilon_m$ and $\gamma_{xm} = 0$) the principal directions are not defined, and consequently, the matrices $\boldsymbol{C}_{mc}^{(A(\beta))}$ and $\boldsymbol{C}_{mc}^{(\sigma(\beta))}$ will also suffer from lack of uniqueness. As mentioned, a value $\beta_{c1} = 0$ is employed at such events, which implies that $\boldsymbol{C}_{mc}^{(C)}$ from Eq.(10.29) will be without nonzero shear terms. To avoid numerical difficulties, the resulting matrix $\boldsymbol{C}_{mc}$ in Eq.(10.33) will be replaced by the following special expression when hydrostatic strain states occur

$$\boldsymbol{C}_{mc} = \boldsymbol{C}_{mc}^{(hyd)} \approx \left[\begin{array}{cc} \boldsymbol{C}_c & \boldsymbol{0} \\ \boldsymbol{0} & G \end{array} \right] \tag{10.53}$$

where $\boldsymbol{C}_c$ is from Eq.(10.26), and the shear modulus G is taken as

$$G = \left\{ \begin{array}{ll} \dfrac{1}{4}\left(\dfrac{\sigma_{c1}}{\epsilon_1} + \dfrac{\sigma_{c2}}{\epsilon_2}\right) & ;\epsilon_1 = \epsilon_2 \neq 0 \\ \dfrac{1}{4}\left(\dfrac{\partial \sigma_{c1}}{\partial \epsilon_1} + \dfrac{\partial \sigma_{c2}}{\partial \epsilon_2}\right) & ;\epsilon_1 = \epsilon_2 = 0 \end{array} \right. \tag{10.54}$$

This suggestion for G may be regarded as a generalization of the diagonal shear term of $\boldsymbol{C}_{mc}^{(A(\beta))}$ in Eq.(10.37) when $\gamma_{xm} = 0$, but is by no means claimed to be rigorously correct. Note that the initial state is also covered by $\boldsymbol{C}_{mc}^{(hyd)}$. Now returning to reinforcement again. For rebars, the 'smeared' tangent modulus in the bar direction that contribute to the material stiffness of the element, becomes

$$\frac{\partial \sigma_s^{(s)}}{\partial \epsilon_t} = \frac{\partial \sigma_s^{(s)}}{\partial \epsilon_s} \frac{\partial \epsilon_s}{\partial \epsilon_t} = \frac{\partial \sigma_s^{(s)}}{\partial \epsilon_s} \tag{10.55}$$

Here ϵ_t is the strain derived from the nodal displacements, while ϵ_s is the mechanical strain according to Eq.(10.17), and $\partial \sigma_s^{(s)}/\partial \epsilon_s$ is expressed by Eq.(8.83) in Section 8.2. The corresponding stiffness-contributing modulus for pbar is obtained by taking the derivative of the internal resistance stress $\sigma_{ir}^{(s)}$ from Eq.(10.21) with respect to ϵ_t. Thus

$$\frac{\partial \sigma_{ir}^{(s)}}{\partial \epsilon_t} = \frac{\partial \sigma_{ir}^{(s)}}{\partial \epsilon_b} \frac{\partial \epsilon_b}{\partial \epsilon_t} = \frac{\partial \sigma_f^{(s)}}{\partial \epsilon_b} \tag{10.56}$$

where $\sigma_f^{(s)}$ is the total or final stress, and ϵ_b is the mechanical strain according to Eq.(10.18). Furthermore, $\partial \sigma_f^{(s)}/\partial \epsilon_b$ is in turn related through Eq.(9.127) to the instantaneous modulus $\partial \sigma_b^{(s)}/\partial \epsilon_b$, that finally is determined in Subsection 8.3.1. For the reinforcement in question, the 'smeared' tangent constitutive matrix $\boldsymbol{C}_m^{(s)}$ in the (x, m)-system may then be defined similar to Eq.(10.27) for concrete, i.e.

$$\boldsymbol{C}_m^{(s)} = \frac{\partial \boldsymbol{\sigma}_m^{(s)}}{\partial \boldsymbol{\epsilon}_m} \tag{10.57}$$

By using the chain rule, $\boldsymbol{C}_m^{(s)}$ becomes

$$\boldsymbol{C}_m^{(s)} = \frac{\partial \boldsymbol{\sigma}_m^{(s)}}{\partial \sigma^{(s)}} \frac{\partial \sigma^{(s)}}{\partial \epsilon_t} \frac{\partial \epsilon_t}{\partial \boldsymbol{\epsilon}_m} = \boldsymbol{a}_{tm}^T \frac{\partial \sigma^{(s)}}{\partial \epsilon_t} \boldsymbol{a}_{tm} \tag{10.58}$$

Here Eqs.(10.22,10.15) have been employed to arrive at the final form, while $\boldsymbol{a}_{tm}$ is given by Eq.(10.16), and $\sigma^{(s)}$ symbolizes $(\sigma_s^{(s)}, \sigma_{ir}^{(s)})$ for rebars and pbar, respectively. Now the resulting tangent constitutive matrix $\boldsymbol{C}_m$ in the (x, m)-system may be obtained by superimposing the contributions from concrete and reinforcement. Thus

$$\boldsymbol{C}_m = \boldsymbol{C}_{mc} + \boldsymbol{C}_{mx}^{(s)} + \boldsymbol{C}_{ms}^{(s)} + \boldsymbol{C}_{mb}^{(s)} \tag{10.59}$$

where the second subscript on 'smeared' quantities signifies the contributions from rebars in the (x, s)-directions and pbar in the b-direction. The concrete component $\boldsymbol{C}_{mc}$ consists again of the contributions in Eq.(10.33) for general strain states, while Eq.(10.53) covers the special hydrostatic case. Note that an alternative way of deriving $\boldsymbol{C}_m$ is to start with the definition, i.e.

$$\boldsymbol{C}_m = \frac{\partial \boldsymbol{\sigma}_m}{\partial \boldsymbol{\epsilon}_m} \tag{10.60}$$

Then introduce $\boldsymbol{\sigma}_m$ from Eq.(10.23), and finally apply Eq.(10.27/10.57) for the individual components. Left now is to determine the tangent constitutive matrix $\boldsymbol{C}$ in the element (x, y, z)-system, as defined through Eq.(4.85)[2]. Again application of the chain rule yields

$$\boldsymbol{C} = \frac{\partial \boldsymbol{\sigma}}{\partial \boldsymbol{\sigma}_m} \frac{\partial \boldsymbol{\sigma}_m}{\partial \boldsymbol{\epsilon}_m} \frac{\partial \boldsymbol{\epsilon}_m}{\partial \boldsymbol{\epsilon}} = \boldsymbol{A}_m^T \boldsymbol{C}_m \boldsymbol{A}_m \tag{10.61}$$

where $\boldsymbol{A}_m$ is given by Eq.(10.6). Here Eqs.(10.24,10.60,10.4) have been employed in turn to arrive at the final relation. Having established $\boldsymbol{C}$ and (y, z, t) from Eq.(10.1), all information necessary is then available for computing the sample point contribution to the area integrals of the material stiffness matrix $\boldsymbol{k}_m$ of the element, as given by Eqs.(4.87-4.122).

10.3 Quad Unit

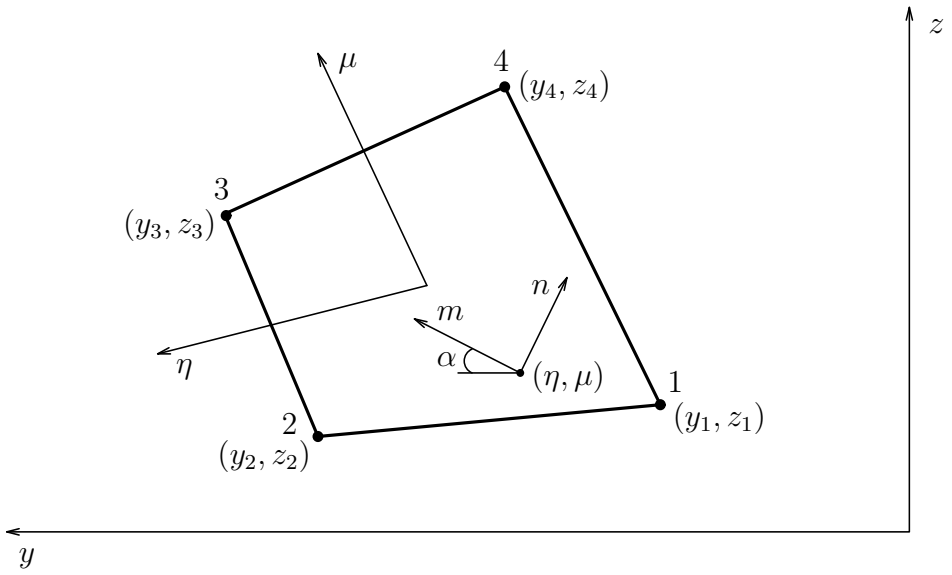

Figure 10.3: Quad Unit

A quad unit (Fig. 10.3) is the quadrilateral cross section of a uniform plain concrete beam component that spans the entire length of an element. Thus the quad unit geometry is defined by the (y, z)-coordinates of its four corners. Since the analysis of quad units relies on numerical integration, the sample point values of the natural coordinates (η, μ) follow from the integration scheme. Then the corresponding

[2]Subscript 't' on $\boldsymbol{C}$ now suppressed.

(y, z)-location is conveniently retrieved using the parametric representation

$$\left\{ \begin{array}{c} y \\ z \end{array} \right\} = \left[\begin{array}{cccc} y_1 & y_2 & y_3 & y_4 \\ z_1 & z_2 & z_3 & z_4 \end{array} \right] \left\{ \begin{array}{c} \varphi_1 \\ \varphi_2 \\ \varphi_3 \\ \varphi_4 \end{array} \right\} \tag{10.62}$$

where the shape functions read

$$\left\{ \begin{array}{c} \varphi_1 \\ \varphi_2 \\ \varphi_3 \\ \varphi_4 \end{array} \right\} = \frac{1}{4} \left\{ \begin{array}{c} (1-\eta)\,(1-\mu) \\ (1+\eta)\,(1-\mu) \\ (1+\eta)\,(1+\mu) \\ (1-\eta)\,(1+\mu) \end{array} \right\} \tag{10.63}$$

Thus, the (y, z)-coordinates at the corners $(1, 2, 3, 4)$ are recovered from $((\eta, \mu) = (-1, -1), (1, -1), (1, 1), (-1, 1))$, respectively. Having localized the sample point, the strain vector $\boldsymbol{\epsilon}$ may then be determined from the nodal displacements using Eq.(4.52). Due to its 'solid' shape, a quad unit may exhibit a typical 3D stress response when subjected to general action. However, the concrete constitutive model can only accommodate 2D stress states, and hence, some kind of simplification must be made. Here a plane stress response is assumed in the (x, m)-system (Fig. 10.3), where the the m-axis is determined 'free of transverse shear'. In other words, the angle α follows from the condition

$$\gamma_{xn} \;=\; -\sin\!\alpha\, \gamma_{xy} \;+\; \cos\!\alpha\, \gamma_{xz} \;=\; 0 \tag{10.64}$$

Thus

$$\alpha \;=\; \arctan\left[\frac{\gamma_{xz}}{\gamma_{xy}} \right] \tag{10.65}$$

This simplification implies that the stress components $(\sigma_n, \tau_{mn}, \tau_{xn})$ now are abandoned. However, of the surviving components $(\sigma_x, \sigma_m, \tau_{xm})$, the first and third are believed to be the most significant for the concrete response in a beam. Note that the orientation of the m-axis will vary to match the resulting shear strain direction for each sample point. In case of a 'shear free state', i.e. $\gamma_{xy} = \gamma_{xz} = 0$, the preceding expression for α becomes indefinite. Then a value $\alpha = \pi/4$ is instead employed. Having determined α, the succeeding procedure for computing the sample point contribution of a quad unit to the internal node-force vector and the geometric stiffness matrix is basically the same as for the concrete part of a line unit. Thus, only a brief step-by-step summary will be given:

- Compute strains $\boldsymbol{\epsilon}_m$ in the (x, m)-system using Eq.(10.4).
- Compute principal strains $\boldsymbol{\epsilon}_c$ from Eq.(10.7).

- Determine mechanical strains as outlined in Section 9.7, and then compute principal concrete stresses $\boldsymbol{\sigma}_c$ according to the search procedure in Subsection 8.1.6.
- Compute concrete stresses[3] $\boldsymbol{\sigma}_m$ in the (x, m)-system applying Eq.(10.12).
- Finally, obtain the (x, y, z)-stresses $\boldsymbol{\sigma}$ from Eq.(10.24).

Also the procedure for computing the sample point contribution to the material stiffness matrix is in several respects the same for a quad unit as for the concrete part of a line unit. The analogous steps are:

- Compute the tangent constitutive matrix $\boldsymbol{C}_c$ for the principal directions based on expressions in Section 9.9 and the search procedure in Subsection 8.1.6.
- Compute the tangent constitutive matrix[3] $\boldsymbol{C}_m$ of concrete in the (x, m)-system based on the contributions in Eq.(10.33) for general strain states or Eq.(10.53) for the hydrostatic case. Note that the $\boldsymbol{C}_m^{(\sigma(\beta))}$-matrix that originates from the equivalent reinforcement formulation, now vanishes.

When it comes to the final step of determining the tangent constitutive matrix in the (x, y, z)-system, the quad unit needs special attention. The reason is that the angle α is strain dependent (ref. Eq.(10.65)), which gives rise to a separate contribution to the resulting $\boldsymbol{C}$-matrix, i.e.

$$\boldsymbol{C} \;=\; \boldsymbol{C}^{(C)} \;+\; \boldsymbol{C}^{(\alpha)} \tag{10.66}$$

Here the first matrix is that derived in Eq.(10.61) by keeping α fixed. Thus

$$\boldsymbol{C}^{(C)} \;=\; \boldsymbol{A}_m^T\, \boldsymbol{C}_m\, \boldsymbol{A}_m \tag{10.67}$$

The second matrix is obtained by inserting Eq.(10.24) into the general expression for $\boldsymbol{C}$ in Eq.(4.85), and then apply the chain rule with respect to α, i.e.

$$\boldsymbol{C}^{(\alpha)} \;=\; \frac{\partial\big(\boldsymbol{A}_m^T\, \boldsymbol{\sigma}_m\big)}{\partial \alpha}\, \frac{\partial \alpha}{\partial \boldsymbol{\epsilon}} \;=\; \frac{\partial \boldsymbol{A}_m^T}{\partial \alpha}\, \boldsymbol{\sigma}_m\, \frac{\partial \alpha}{\partial \boldsymbol{\epsilon}} \tag{10.68}$$

Further differentiation of $\boldsymbol{A}_m$ from Eq.(10.6) with respect to α yields

$$\frac{\partial \boldsymbol{A}_m^T}{\partial \alpha} \;=\; \begin{bmatrix} 0 & 0 & 0 \\ 0 & 0 & -\sin\alpha \\ 0 & 0 & \cos\alpha \\ 0 & -\sin 2\alpha & 0 \\ 0 & \sin 2\alpha & 0 \\ 0 & \cos 2\alpha & 0 \end{bmatrix} \tag{10.69}$$

[3] Subscript 'c' suppressed.

The entries of $\partial\alpha/\partial\boldsymbol{\epsilon}$ are defined through the row vector

$$\frac{\partial\alpha}{\partial\boldsymbol{\epsilon}} = \left[\begin{array}{cccccc} \dfrac{\partial\alpha}{\partial\epsilon_x} & \dfrac{\partial\alpha}{\partial\gamma_{xy}} & \dfrac{\partial\alpha}{\partial\gamma_{xz}} & \dfrac{\partial\alpha}{\partial\epsilon_y} & \dfrac{\partial\alpha}{\partial\epsilon_z} & \dfrac{\partial\alpha}{\partial\gamma_{yz}} \end{array}\right] \tag{10.70}$$

Using Eq.(10.65), the derivatives become

$$\frac{\partial\alpha}{\partial\boldsymbol{\epsilon}} = \frac{1}{\gamma_{xy}^2 + \gamma_{xz}^2}\left[\begin{array}{cccccc} 0 & -\gamma_{xz} & \gamma_{xy} & 0 & 0 & 0 \end{array}\right] \tag{10.71}$$

By also introducing the components of $\boldsymbol{\sigma}_m$ according to Eq.(10.14) and then carry out the product sequence in Eq.(10.68), $\boldsymbol{C}^{(\alpha)}$ takes the final form

$$\boldsymbol{C}^{(\alpha)} = \frac{1}{\gamma_{xy}^2 + \gamma_{xz}^2}\left[\begin{array}{cccccc} 0 & 0 & 0 & 0 & 0 & 0 \\ 0 & \gamma_{xz}\tau_{xm}\sin\alpha & -\gamma_{xy}\tau_{xm}\sin\alpha & 0 & 0 & 0 \\ 0 & -\gamma_{xz}\tau_{xm}\cos\alpha & \gamma_{xy}\tau_{xm}\cos\alpha & 0 & 0 & 0 \\ 0 & \gamma_{xz}\sigma_m\sin 2\alpha & -\gamma_{xy}\sigma_m\sin 2\alpha & 0 & 0 & 0 \\ 0 & -\gamma_{xz}\sigma_m\sin 2\alpha & \gamma_{xy}\sigma_m\sin 2\alpha & 0 & 0 & 0 \\ 0 & -\gamma_{xz}\sigma_m\cos 2\alpha & \gamma_{xy}\sigma_m\cos 2\alpha & 0 & 0 & 0 \end{array}\right] \tag{10.72}$$

In case of a 'shear free state', i.e. $\gamma_{xy} = \gamma_{xz} = 0$, no $\boldsymbol{C}^{(\alpha)}$-contribution is computed. Finally note that the numerical integration of a quad unit also involves evaluating the determinant of the Jacobian matrix $\boldsymbol{J} = \partial(y,z)/\partial(\eta,\mu)$ at the sample point. The expressions necessary are then derived from Eqs.(10.62,10.63). However, in this respect a quad unit is identical to the bilinear isoparametric quadrilateral plane stress element, and thus this operation will not be covered further.

10.4 Rebar Unit

A rebar unit represents the cross section of an individual rebar oriented along the longitudinal element axis (i.e. the x-axis). Its location and geometry are characterized by the (y,z)-coordinates and the cross section area A_s. Thus, no transformation and numerical integration become necessary in order to evaluate the rebar unit-contribution to the internal element quantities $(\boldsymbol{r}, \boldsymbol{k}_g, \boldsymbol{k}_m)$. Since the analysis of a rebar unit becomes very simple, it will be summarized only briefly through the following steps:

- Evaluate ϵ_x from the first relation in Eq.(4.52).
- Obtain the mechanical strain ϵ_s by subtracting from ϵ_x the thermal strain ϵ_{sT}, as given by Eq.(9.7).

- Determine σ_x and the corresponding entry c_{11} of $\boldsymbol{C}$ in Eq.(4.85) by applying Eqs.(8.81,8.83), respectively; now inserting $\rho = 1$ for the reinforcement ratio to obtain pure steel quantities.

- Compute the contribution to the pertinent area integrals of $(\boldsymbol{r}, \boldsymbol{k}_g, \boldsymbol{k}_m)$.

10.5 Tendon Unit

A tendon unit represents the cross section of a prestressing tendon. Like the rebar unit, its location and geometry are characterized by the (y, z)-coordinates and the cross section area A_p. However, unlike the other three units, the tendon unit has a varying (y, z)-location along the element. This location is given by the last two relations of the parametric representation in Eq.(6.50). The parameter there is the natural tendon coordinate ρ that again relates to the natural beam coordinate ξ through Eq.(6.56/6.57); the latter being the quantity selected from the numerical integration scheme. Having determined the tendon unit localization, the vector of concrete (x, y, z)-strains $\boldsymbol{\epsilon}$ may then be retrieved using Eq.(4.52). Further transformation to normal strain ϵ_t in the tangential tendon direction takes place according to Eq.(6.82), i.e.

$$\epsilon_t \;=\; \boldsymbol{a}_t\, \boldsymbol{\epsilon} \tag{10.73}$$

where the transformation vector $\boldsymbol{a}_t$ is expressed by Eq.(6.83). Now the procedure follows closely that for pbar in the line unit. Thus, the mechanical tendon-strain ϵ_p reads

$$\epsilon_p \;=\; \epsilon_t \;+\; \Delta\epsilon_p^{(o)} \;-\; \epsilon_{sT} \tag{10.74}$$

Here ϵ_{sT} is the thermal strain from Eq.(9.7), and $\Delta\epsilon_p^{(o)}$ is the additional tendon-strain at the final tensioning state, as determined in Eq.(6.84). Then the stress-strain relationship in Subsection 8.3.1 may be applied to obtain the instantaneous tendon stress σ_p, whereupon the relaxation stress σ_r is computed based on one of the two methods in Section 9.8, yielding the total or final stress σ_f on the form

$$\sigma_f \;=\; \sigma_p \;+\; \sigma_r \tag{10.75}$$

However, since the prestressing forces at the final tensioning state are still retained as applied loading (Subsection 6.4.6), only the change of stress since that state is here treated as the internal resistance-contributing stress σ_{ir}, i.e.

$$\sigma_{ir} \;=\; \sigma_f \;-\; \sigma_p^{(o)} \tag{10.76}$$

Here $\sigma_p^{(o)}$ is the stress at the final tensioning state according to Eq.(6.77). Then transformation back to stresses $\boldsymbol{\sigma}$ in the (x, y, z)-system follows from

$$\boldsymbol{\sigma} \;=\; \boldsymbol{a}_t^T\, \sigma_{ir} \tag{10.77}$$

The stiffness-contributing modulus is obtained by taking the derivative of σ_{ir} with respect to ϵ_t. Application of the chain rule and Eqs.(10.76,10.74) yield

$$\frac{\partial \sigma_{ir}}{\partial \epsilon_t} = \frac{\partial \sigma_{ir}}{\partial \epsilon_p} \frac{\partial \epsilon_p}{\partial \epsilon_t} = \frac{\partial \sigma_f}{\partial \epsilon_p} \tag{10.78}$$

Here $\partial \sigma_f / \partial \epsilon_p$ is in turn related through Eq.(9.127) to the instantaneous modulus $\partial \sigma_p / \partial \epsilon_p$, that finally is determined in Subsection 8.3.1. The tangent constitutive matrix $\boldsymbol{C}$ in the (x, y, z)-system is defined according to Eq.(4.85). Again by using the chain rule, $\boldsymbol{C}$ becomes

$$\boldsymbol{C} = \frac{\partial \boldsymbol{\sigma}}{\partial \sigma_{ir}} \frac{\partial \sigma_{ir}}{\partial \epsilon_t} \frac{\partial \epsilon_t}{\partial \boldsymbol{\epsilon}} = \boldsymbol{a}_t^T \frac{\partial \sigma_{ir}}{\partial \epsilon_t} \boldsymbol{a}_t \tag{10.79}$$

Here Eqs.(10.77,10.73) have been employed to arrive at the final form. Having evaluated (y, z) by Eq.(6.50) and $(\boldsymbol{\sigma}, \boldsymbol{C})$, all information necessary is then available to compute the tendon unit-contribution to the internal element quantities $(\boldsymbol{r}, \boldsymbol{k}_g, \boldsymbol{k}_m)$.

Chapter 11

Review of Computer Program DARC

Before the validity of the various formulations/models presented in the preceding chapters may be confirmed, a considerable amount of programming work lies between. For this purpose a 'self-supported' computer program DARC[1] has been made, coded in the FORTRAN 77-language. It was found preferable to write a separate finite element code, rather than trying to modify an existing one, since in either case the computer implementation would have involved quite extensive work at all levels in the program hierarchy. In what follows is a brief review of the input-data to DARC. The intention is not to define each single datum in user's manual-style, but to give the reader information about the data-arrangement and program capabilities. However, data that appear for the first time will be explained. For previously defined data, the symbols are consistent with those adopted in the preceding chapters. The complete set of data is divided into subsets, ordered in agreement with the presentation that follows. The introduction of a new data subset is in general identified with a characterizing codeword, that mainly has the purpose of making the data-file more readable for the user. Then next in each subset comes usually a line containing information about the number of data-lines of various kinds that are to be read in the sequel. The first item on a data-line is typically the identification number. Data are read in free-field format and with units in $(\mathrm{MN}, \mathrm{m}, \mathrm{days}, {}^{o}C, -)$. The remaining part of the chapter deals with the layout of the individual subsets:

1. **Nodal coordinates**

NODEDATA									
numsep		*numgen*							
nn	*X*	*Y*	*Z*						$(1, numsep)$
$nn(1)$	$X(1)$	$Y(1)$	$Z(1)$	Δnn	ΔX	ΔY	ΔZ	$nn(n)$	$(1, numgen)$

[1] Deterministic Analysis of Reinforced Concrete; the name was selected with a probabilistic follow-up program PARC in mind.

Here the global coordinates of each system node are specified. Coordinates along a straight line may be generated.

2. **Materials**

MATERIAL													
numcon		*numrei*		*numpre*									
cm	f_{cc28}	E_{c28}	ϵ_{o28}	ϵ_{h28}	f_{ct28}	b_t	γ_c	α_c	*mix*	f_{cm28}	*RH*	*h*	$(1, numcon)$
rm	f_y	E_s	E_y	γ_s	α_s								$(1, numrei)$
pm	$f_{0.2}$	ω	E_p	$E_{0.2}$	μ	k	u_s	γ_s	α_s	C_r			$(1, numpre)$

Among the material parameters, the specific weights (γ_c, γ_s) of concrete and steel are now included. This is done to enable automatic computation of the structural dead weight. The *mix*-parameter is also new. It reflects the type of cement through the values

$$mix = \begin{cases} 1 & - \text{ rapid hardening high strength cement} \\ 0 & - \text{ normal and rapid hardening cements} \\ -1 & - \text{ slowly hardening cement} \end{cases}$$

Of convenience, relative humidity *RH* of the ambient atmosphere and notional member size h of concrete (ref. Eq.(9.51)), as well as the friction coefficients (μ, k) and anchorage slip u_s for prestressing steel are also listed here, although they hardly can be considered as material properties in a strict sense.

3. **Cross sections**

CROSSDAT											
numcro											
cc	*nlin*(*cc*)			*nqua*(*cc*)			*nreb*(*cc*)			*npba*(*cc*)		$(1, numcro)$
	lu	y_1	z_1	t_1	y_2	z_2	t_2	*cm*	t_{To}	a_x	rm_x	
								a_s	rm_s	β_s	*pp*	$(1, nlin(cc))$
	qu	y_1	z_1	y_2	z_2	y_3	z_3	y_4	z_4	*cm*	t_{To}	$(1, nqua(cc))$
	ru	y	z	A_s	*rm*							$(1, nreb(cc))$
	pp	y_1	z_1	y_2	z_2	a_b	*pm*	β_b	p_o			$(1, npba(cc))$

For each cross section number *cc* the data of pertaining line, quad and rebar units, as well as pbar panels, are read. A pbar panel is in turn assigned to a line unit through its pbar panel number *pp* (a zero value means no assignment). Furthermore, t_{To} denotes the temperature adjusted age of concrete according to Eq.(9.10) at the time of first inclusion of the pertaining element in a structural system (i.e. the initial effective age). This quantity is placed on the 'unit-level' rather than the cross section or element-level

to account for possible differences in the time at casting of the individual sectional parts. Note also that the material properties are assigned to the unit-level.

4. **Element orientation**

ELORIENT				
numori				
or	ΔX_{Q1}	ΔY_{Q1}	ΔZ_{Q1}	$(1, numori)$

For each data-line the global components of a vector pointing from element node 1 to an auxiliary point Q, lying in the first or second quadrant of the (x, y)-plane of a local element system, are specified. From this vector ${}_a\boldsymbol{i}$ and the global position vectors $({}^o\boldsymbol{X}^{(1)}, {}^o\boldsymbol{X}^{(2)})$ of node 1 and 2 the initial orientation in space of a local element system will be defined. Then the components of the initial transformation matrix ${}_o\boldsymbol{T}$ may be derived in a similar manner as outlined in Subsection 5.1.3 for the updated matrix ${}_{on}\boldsymbol{T}$.

5. **Eccentricities**

ECCENTRI				
numecc				
ee	e_x	e_y	e_z	$(1, numecc)$

Each eccentricity is specified in terms of the initial global components of a vector pointing from a system node to the attached element node. A set of zero values is assigned to non-eccentric element nodes.

Note that the program also automatically transfers the local (x, y, z)-system of each element from the user's reference point to the centroid of the beam cross section. The local eccentricity arising from this operation are transformed to the global system and then added to the above specified nodal eccentricities that is assigned to the element.

6. **Element connectivity-data**

ELEMDATA								
numsep		*numgen*						
ele	nn_1	nn_2	*cc*	*lh*	*or*	ee_1	ee_2	$(1, numsep)$
ele(1)	$nn_1(1)$	$nn_2(1)$	*cc*(1)	*lh*(1)	*or*	ee_1	ee_2	
			Δele	Δnn	Δcc	Δlh	*ele*(*n*)	$(1, numgen)$

Here identification numbers for system nodes, cross section, dead weight/pbar load history, element orientation and eccentricities are assigned to each element. Also an option for generating these assignments is specified. The decision of activating pbars (if any) through the same history as dead weight is made purely for simplification.

7. **Tendons**

TENDDATA											
numten			*numsep*								
te	X_1	Y_1	Z_1	X_2	Y_2	Z_2	X_3	Y_3	Z_3	A_p	
	pm	P_1	P_2	te_1	te_2	*lh*	*n*	*ele*(1)	...	*ele*(n)	(1, *numsep*)
te	X_1	Y_1	Z_1	X_2	Y_2	Z_2	X_3	Y_3	Z_3	A_p	
	pm	P_1	P_2	te_1	te_2	*lh*	*ele*(1)	Δ*ele*	*ele*(n)	(*numsep*+1, *numten*)	

The data of a tendon curve consist of the global coordinates at the three 'nodal' points, cross section area, material identification number, forces applied from the jack, identification numbers for the adjacent parts of a 'multiple-curve' tendon (a zero value means no continuation), tendon load history number and finally the identification numbers for the elements the tendon curve is passing through. An option that enables generation of these element numbers is also included.

8. **Direction of gravity**

GRAVIDIR		
$\cos(G, X)$	$\cos(G, Y)$	$\cos(G, Z)$

The direction of gravity G is defined through its direction cosines with the global (X, Y, Z)-axes. For instance, if Z is positive upwards and parallel to G, then the data set becomes $(0.0, 0.0, -1.0)$.

9. **Element loads**

ELEMLOAD											
numelo			*numsep*								
elo	q_x	q_y	q_z	y_q	z_q	*lh*	*n*	*ele*(1)	...	*ele*(n)	(1, *numsep*)
elo	q_x	q_y	q_z	y_q	z_q	*lh*	*ele*(1)	Δ*ele*	*ele*(n)	(*numsep*+1, *numelo*)	

Here uniform loads per unit axial element length are specified. The reference load for each case is given in terms of its initial components and position in the local element system. By putting a minus sign in front of the identification number *elo*, the corresponding load will be taken as corotational. Otherwise it is considered as unidirectional. Again, an option is included that enables generation of the assigned elements.

10. **Nodal loads**

NODELOAD							
numnlo							
nlo	F_x	F_y	F_z	e_x	e_y	e_z	$(1, numnlo)$

In this subset reference values of discrete nodal loads with eccentricities are specified in global components for the initial configuration. Again, by putting a minus sign in front of the identification number *nlo*, the corresponding load will be taken as corotational. Otherwise it is considered as unidirectional.

11. **Load-node-history connectivity**

NLOADHIS						
numpos		*numneg*				
$\|nlo\|$	$nn(1)$	$lh(1)$	Δnn	Δlh	$ncomb$	$(1, numpos)$
$\|nlo\|$	$nn(1)$	$lh(1)$	Δnn	Δlh	$ncomb$	$(1, numneg)$

This type of construction is introduced in order to simulate moving nodal loads, like e.g. a traveling formwork. Both positive nodal loads, with values of (F_x, F_y, F_z) as read in Subset 10, and their negative counterparts may 'travel'. Thus, removal of a load may take place by either letting the scaling factor in the pertaining load history become zero, or by adding the negative load counterpart for cancellation. Note that the nodal load numbers now are given as positive numbers only.

12. **Nodal displacements**

NODEDISP											
numndi											
ndi	$\check{v}_x$	$\check{v}_y$	$\check{v}_z$	$\check{\theta}_x$	$\check{\theta}_y$	$\check{\theta}_z$	dh	n	$nn(1)$	...	$nn(n)$	$(1, numndi)$

Here prescribed displacements at selected system nodes are read. The components of each reference case are in global system and scaled to correct level in accordance with the displacement history specified.

13. **Mean seasonal temperature**

TEMPMEAN	
$\overline{T}_{max}$	$\overline{T}_{min}$

The mean seasonal temperature variation is defined through the periodic expression in Eq.(5.72). In this subset the amplitudes are specified.

14. **Element temperature deviations**

ELTEMPDE									
numetp			*numsep*						
tpd	ΔT_1	g_{Tx}	g_{Ty}	g_{Tz}	*th*	*n*	*ele*(1)	...	*ele*(*n*)
tpd	ΔT_1	g_{Tx}	g_{Ty}	g_{Tz}	*th*	*ele*(1)	Δele	*ele*(*n*)	

(1, *numsep*)

(*numsep*+1, *numetp*)

Temperature deviation (from the mean) is determined by the product of a reference value, according to Eq.(5.75), and a scaling factor, given by the temperature deviation history. Here the reference value at node 1 and the gradients in the local (x, y, z)-directions, as well as the identification number for the pertaining history, are read for selected elements. Also an option is included for generation of these elements.

15. **Systems**

SYSTDATA								
numsep		*numgen*	*numcan*		*numspa*		*nummer*	
S	*n*	*ele*(1)	...	*ele*(*n*)				(1, *numsep*)
S	*ele*(1)	Δele	*ele*(*n*)					(1, *numgen*)
S(1)	S_{ref}	$ele_1(1)$	$ele_2(1)$	ΔS	Δele_1	Δele_2	*S*(*n*)	(1, *numcan*)
S(1)	S_{ref}	*n*	$ele_1(1)$	...	$ele_n(1)$	ΔS	Δele	*S*(*n*) (1, *numspa*)
S	$S_{ref}(1)$	$S_{ref}(2)$						(1, *nummer*)

This subset defines the assembly of elements that pertains to each system, identified by its number S. The elements may be introduced in several ways; through one-by-one reading (*sep*), by generation (*gen*), according to a 'double cantilever' construction sequence (*can*), 'span-by-span' construction (*spa*) and by merging the elements of two previously defined systems (*mer*). For the last option the reference systems may contain joint elements. The 'span-by-span' option may also be applied to a 'single cantilever' construction sequence.

16. **Boundary condition codes**

BOUNCODE						
numbco						
bco	tg_{vx}	tg_{vy}	tg_{vz}	$tg_{\theta x}$	$tg_{\theta y}$	$tg_{\theta z}$

(1, *numbco*)

A nonzero boundary condition tag *tg* implies that the corresponding displacement component is constrained (i.e. fixed or prescribed).

17. **Boundary code-node-system connectivity**

BNODESYS									
numbns									
$S(1)$	ΔS	$S(m)$	n	$nn(1)$	$bco(1)$	...	$nn(n)$	$bco(n)$	$(1, numbns)$

Here combinations of constrained system nodes and boundary codes are assigned to the structural systems in question. Also nodes subjected to prescribed displacements need to be included. All nodes/codes pertaining to the same system have to be specified on one data-line.

18. **Internal constraint code**

INCONSTR						
$tg_{\tilde{v}x3}$	$tg_{\tilde{\theta}y3}$	$tg_{\tilde{\theta}z3}$	$tg_{\tilde{\epsilon}yo}$	$tg_{\tilde{\epsilon}zo}$	$tg_{\tilde{g}ey}$	$tg_{\tilde{g}ez}$

Also a constraint code for the internal hierarchical DOFs is included. These DOFs are defined in Section 4.2. The constraint code applies to all elements. Now a nonzero tag tg implies that the corresponding component is fixed. With all DOFs constrained the ordinary Bernoulli-Euler beam element will be recovered.

19. **Load histories**

LOADHIST							
numsep		*numgen*					
lh	n	$\lambda(1)$	$h_l(1)$	...	$\lambda(n)$	$h_l(n)$	$(1, numsep)$
lh_{ref}	Δlh	$\Delta\lambda$	$lh(n)$				$(1, numgen)$

Each load history is characterized by its identification number lh and a sequence of discrete curve points of the 'neutral time'-measure λ and the scaling factor h_l. The rules for interpreting the history function from these curve points are given in Subsection 5.3.1. Also an option is included where new load histories are generated from a previously defined one through shifts of λ (while h_l is retained).

20. **Displacement histories**

DISPHIST							
numdhi							
dh	n	$\lambda(1)$	$h_d(1)$	...	$\lambda(n)$	$h_d(n)$	$(1, numdhi)$

Displacement histories are characterized and interpreted in the same way as load histories. No option for generation is included.

21. **Temperature deviation histories**

TEMPHIST							
numteh							
th	*n*	$\lambda(1)$	$h_T(1)$	...	$\lambda(n)$	$h_T(n)$	$(1, numteh)$

Also temperature deviation histories are characterized and interpreted in the same way as load histories. Again, no generation is included.

22. **System history**

SYSTHIST							
numsep		*numgen*					
seq	*n*	$\lambda(1)$	$S(1)$	...	$\lambda(n)$	$S(n)$	$(1, numsep)$
seq	seq_{ref}	$\Delta\lambda$	ΔS				$(1, numgen)$

The system history is characterized by a sequence of discrete curve points of λ and the corresponding system identification number S. The rules for interpreting the history function from these curve points are given in Subsection 5.3.3. Of convenience, the system history data are here divided into subsequences *seq* that are to be numbered (but not read) in increasing order with respect to increasing λ-values. Also a new subsequence may be generated from an already existing one by making shifts of λ and S.

23. **Time history**

TIMEHIST							
numsep		*numgen*					
seq	*n*	$\lambda(1)$	$t(1)$	...	$\lambda(n)$	$t(n)$	$(1, numsep)$
seq	seq_{ref}	$\Delta\lambda$	Δt				$(1, numgen)$

The time history relates the actual time t to the parameter λ. It is characterized in a similar manner as the system history, but the rules for interpreting the history function from the discrete curve points are now given in Subsection 5.3.4. The data input is arranged in the same way as described for the system history.

24. **Solution**

SOLUTION					
'*type*'	'*imet*'	'*file*'	C_{tol}		
numsep		*numgen*			
seq	*n*	$\lambda(1)$	...	$\lambda(n)$	$(1, numsep)$
seq	seq_{ref}	$\Delta\lambda$			$(1, numgen)$

The solution strategy is outlined in Section 5.4. In this subset the three character strings (enclosed in quotes) identify the type of solution, the iteration method and the file-name to read/write history parameters from/on, respectively. The following identifiers are accepted

$$'type' = \begin{cases} \text{'new'} & - \text{ new solution} \\ \text{'old'} & - \text{ restart run} \end{cases}$$

$$'imet' = \begin{cases} \text{'tnr'} & - \text{ true Newton-Raphson} \\ \text{'mnr'} & - \text{ modified Newton-Raphson} \end{cases}$$

Furthermore, C_{tol} is the convergence tolerance parameter. The solution advances according to a prescribed sequence of λ. Here this sequence is divided into subsequences *seq* that are to be numbered (but not read) in increasing order with respect to increasing λ-values. Also a new subsequence may be generated from an already existing one by making a shift of λ.

25. **Element results**

ELRESULT				
numsep		*numgen*		
n	*ele*(1)	...	*ele*(n)	$(1, numsep)$
ele(1)	Δele	*ele*(n)		$(1, numgen)$

First the (y, z)-location of the centroid of each element cross section is printed. Then for each solution step DARC automatically prints results of global translations and reaction forces at, respectively, every element endnode and constrained system node of the system in question. Besides, for the elements specified under this subset also additional results at the local element level are provided. These results consist of member forces at the endnodes, as well as strains and stresses at the sample points. For concrete the latter implies angle to the principal 1-direction and principal total strains and stresses, while total strains and pure total stresses (i.e. not 'smeared' and with relaxation when appropriate) in the bar/tendon direction are provided for all steel components. Note that among the elements specified, only those pertaining to the system in question will be listed.

Chapter 12

Numerical Studies

12.1 Introductory Remarks

The main objective for the numerical studies is to demonstrate the validity of the various formulations/models presented in the preceding chapters of this work. Consequently, emphasis is put on selecting application examples that are verifyable through experimental or theoretical results in the literature. For this reason it is also found necessary to investigate some linear elastic problems, although the intention of this work is to deal with reinforced concrete structures.

All succeeding examples are analyzed using true Newton-Raphson iteration. Unless otherwise noted, a convergence tolerance parameter $C_{tol} = 10^{-4}$ is employed in conjunction with the criterion in Eq.(5.76) for the termination of iteration. Furthermore, Gauss quadrature is the adopted numerical integration method. A three point rule is used as standard in the longitudinal element direction and for line units, as well as in each direction of quad units. Finally note that the number of units in the subdivision of the beam cross section is selected on judgement for each example case. Thus, no optimization in this respect is attempted.

12.2 Linear Elastic Problems Involving Large Displacements

12.2.1 Postbuckling of Tip-Loaded Cantilever Column (the Elastica)

The postbuckling response of an elastic cantilever column is one of the truly classical problems in solid mechanics. An analytical solution may be found in the textbook by Timoshenko and Gere [49]. In recent years the problem has been investigated numerically by several authors, e.g. Mathisen [5]. The motive for including the problem in this work is to demonstrate both that the 3D shear-beam element works satisfactorily in the slender beam regime, and that the large rotation and displacement formulation

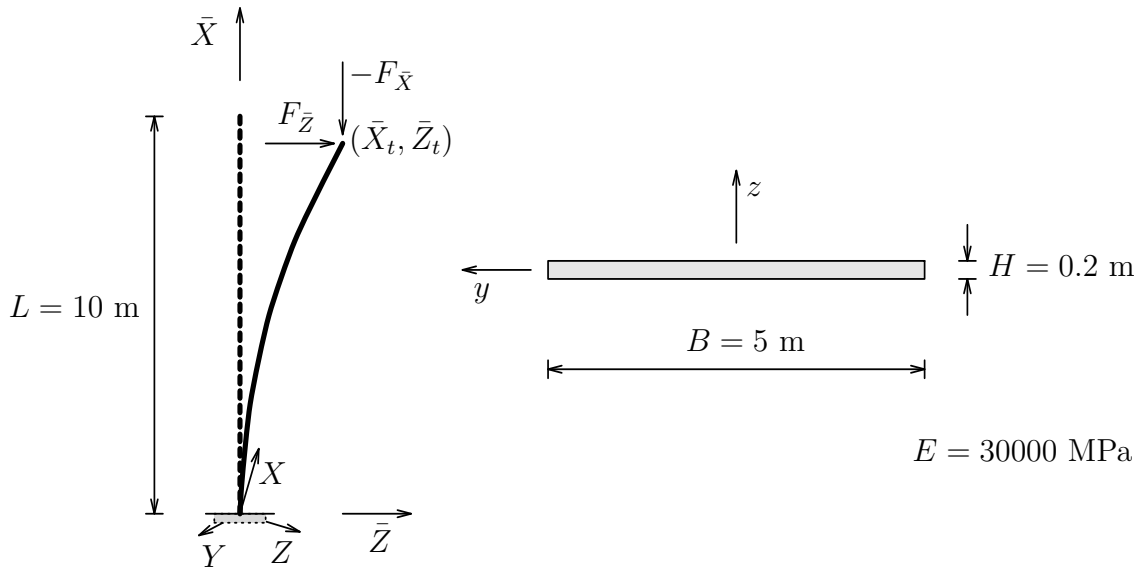

Figure 12.1: Unidirectionally Tip-Loaded Cantilever Column

is correctly implemented in the computer program DARC. To put the latter on a true test, the column is here oriented 'arbitrarily' in space.[1] This has been achieved by introducing an auxiliary $(\bar{X}, \bar{Y}, \bar{Z})$-system that is related to the global (X, Y, Z)-axes through the coordinate transformation

$$\bar{\boldsymbol{X}} \;=\; \boldsymbol{T}\,\boldsymbol{X} \tag{12.1}$$

The following entries have been selected for the 'arbitrary' $\boldsymbol{T}$

$$\boldsymbol{T} \;=\; \frac{1}{7}\begin{bmatrix} 6 & -2 & -3 \\ 3 & 6 & 2 \\ 2 & -3 & 6 \end{bmatrix} \tag{12.2}$$

As depicted in Fig. 12.1, the column is oriented along the $\bar{X}$-axis and buckles in the $(\bar{X}, \bar{Z})$-plane. However, the actual structural modeling and computations are carried out in the global (X, Y, Z)-system. Then the global nodal coordinates and forces follow from the transformations

$$\boldsymbol{X} \;=\; \boldsymbol{T}^T\bar{\boldsymbol{X}} \tag{12.3}$$

$$\boldsymbol{F} \;=\; \boldsymbol{T}^T\bar{\boldsymbol{F}} \tag{12.4}$$

Finally, for presentation of results the computed nodal translations are transformed back to the auxiliary $(\bar{X}, \bar{Y}, \bar{Z})$-system using

$$\bar{\boldsymbol{v}}_t \;=\; \boldsymbol{T}\,\boldsymbol{v}_t \tag{12.5}$$

[1] Usually buckling involving only one rotational component has been studied.

The cantilever length, cross section geometry and modulus of elasticity are given in Fig. 12.1. These values correspond to a slenderness ratio of $\lambda_s \approx 350$. The finite element mesh consists of 10 equally spaced elements, and 1 quad unit is used to model the cross section. In order to let the column sway into the sideway mode, a small horizontal force $F_{\bar{Z}}$ of magnitude 1 % of the buckling load F_{cr}, is initially applied. Thus

$$F_{cr} \;=\; \frac{\pi^2 EI}{4L^2} \;=\; 2.4674 \text{ MN} \tag{12.6}$$

$$F_{\bar{Z}} \;=\; 0.01\, F_{cr} \;=\; 0.0247 \text{ MN} \tag{12.7}$$

Then next is applied the vertical (negative) force in the following 11 steps, as ratios of the critical load

$$\begin{array}{lcccccc} \dfrac{|F_{\bar{X}}|}{F_{cr}} & : & 0.8 & 0.95 & 1.015 & 1.063 & 1.152 & 1.293 \\ & & 1.518 & 1.884 & 2.541 & 4.029 & 9.116 & \end{array} \tag{12.8}$$

For the postbuckling range these steps are chosen in accordance with [49], in which the displaced position of the tip is tabulated based on an analytical solution for the

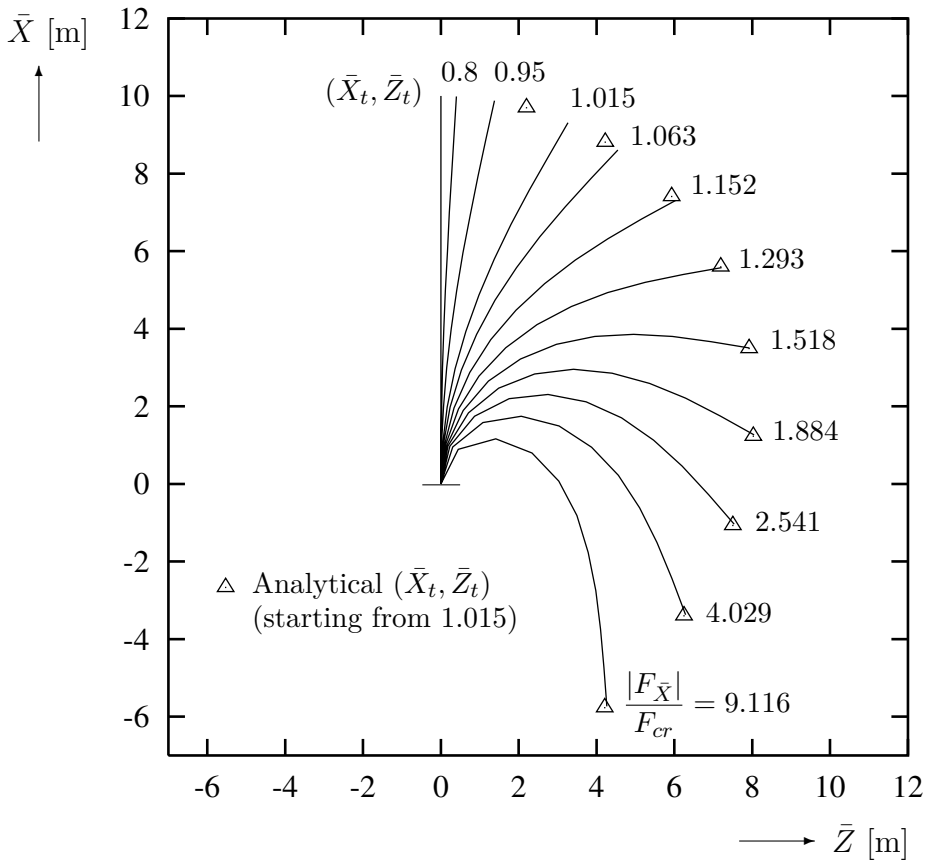

Figure 12.2: Deformed Shapes at Load Levels 0.8 − 9.116 of Critical

column subjected to vertical force only. The results of the computations in terms of deformed shapes are shown in Fig. 12.2. Here are also the analytical values for the tip plotted. Apart from the load levels following immediately upon buckling where the numerical solution is highly influenced by the horizontal force, close agreement is obtained. Furthermore, the total number of equilibrium iterations required to achieve convergence throughout the 11 load steps, amounts to 72. For the postbuckling range the typical value per load step is 6. These numbers correspond very well with the values reported in [5] for a quite similar solution. However, in [5] the convergence criterion was based on energy-norms (as opposed to displacement-norms in this work), although the value for the tolerance parameter was the same (i.e. 10^{-4}). Finally, a separate run is also carried out where the column buckles in the global (X, Z)-plane. Compared to the 'arbitrarily' oriented column, the results obtained in this in-plane test are the same both with respect to displacements (within roundoff) and iterations as well.

12.2.2 Cantilever Beam Subjected to Uniformly Distributed Pressure Loading

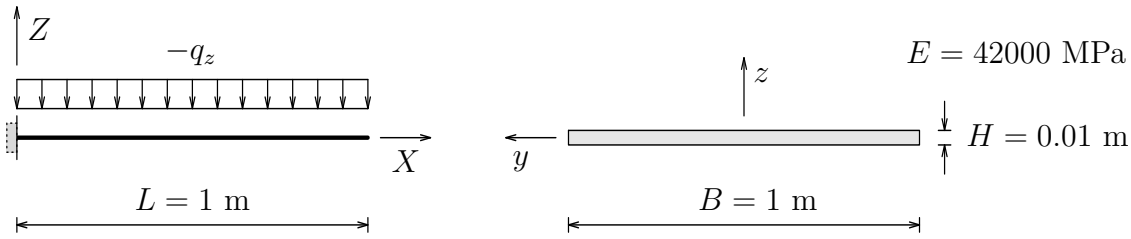

Figure 12.3: Corotationally Pressure-Loaded Cantilever Beam

This test is included to demonstrate the significance of the stiffness terms from corotational loading for a problem involving large displacements and rotations. The problem data are shown in Fig. 12.3. Here the (negative) loading is applied gradually in 10 equal increments corresponding to a (absolute) load level ranging from 10 to 100 kN/m. The finite element discretization consists of 16 equally spaced elements, and again 1 quad unit is used for modeling the cross section. The convergence tolerance parameter is now set to $C_{tol} = 10^{-3}$. The results in terms of deformed shape at each load level are depicted in Fig. 12.4. This run is made with the load correction contribution to the tangent stiffness included. In another run without this contribution the structure failed to converge beyond $|q_z| = 40$ kN/m. Also at this load level the number of iterations required for convergence now becomes tripled compared to the solution with load correction stiffness included. As can be seen from Tab. 12.1, no difference is experienced below this load level. Such a comparison has also been made by Mathisen [5] for the same example.[2] His results show the

[2]The load level given in [5] is (by a misprint?) only one hundredth of that presented here.

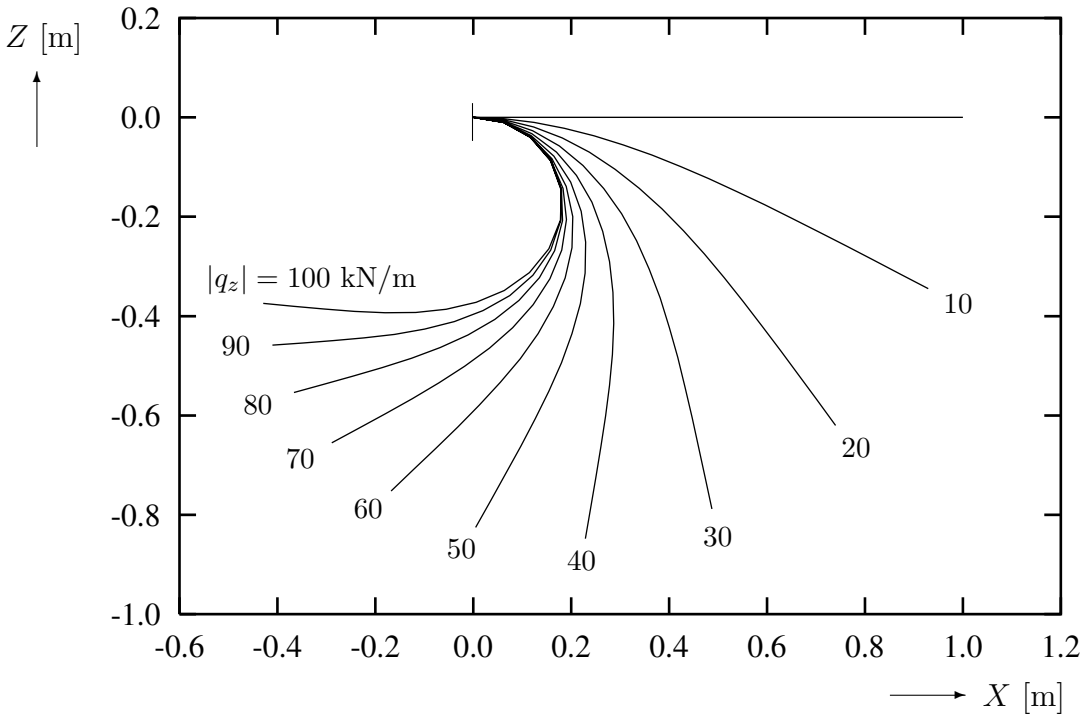

Figure 12.4: Deformed Shapes at Load Levels $10 - 100$ kN/m

same features as found here, although the numbers of iterations there are generally somewhat higher. This discrepancy may possibly be attributed to differences in the stiffness matrix formulation for corotational loading and/or in the convergence criterion (energy-norms versus displacement-norms) although the tolerances are the same. The deformed shapes reported in [5] appear to be in good agreement with those in Fig. 12.4.

$\|q_z\|$ [kN/m]	10	20	30	40	50	60	70	80	90	100
With $\boldsymbol{k}_{lc}^{(CL)}$	4	4	4	4	4	4	4	4	3	4
Without	4	4	4	12	–	–	–	–	–	–

Table 12.1: Number of Equilibrium Iterations in Dependence of Load Level

12.3 Semicircular Hinged Arch Subjected to Uniformly Distributed Loading

Fig. 12.5 depicts the geometry and load for this test problem in which the uniform pressure will be treated both as unidirectional and corotational loadings. The main

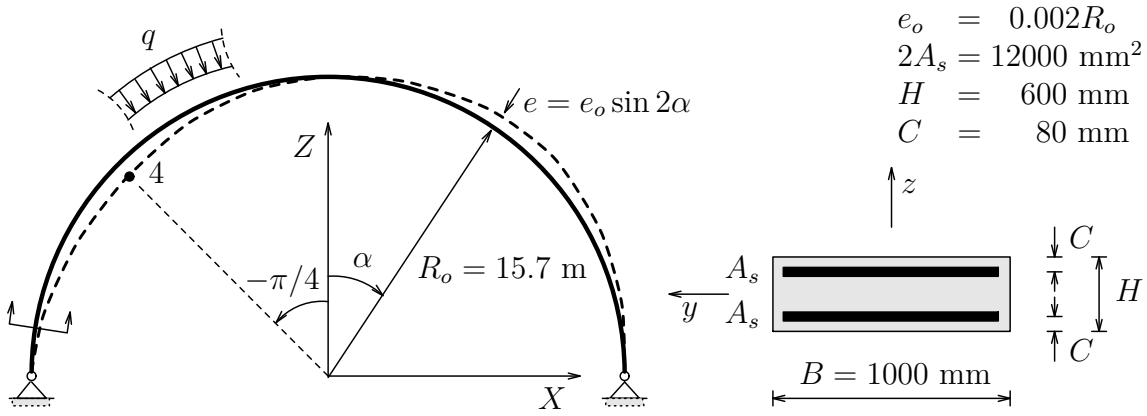

Figure 12.5: Pressure-Loaded Semicircular Hinged Arch

reason for including this problem here is to pursue the investigation regarding the significance of load correction stiffnesses in a large displacement setting. The structure has previously been analyzed by Åldstedt [21]. Like in his work, both linear elastic material with modulus $E = 30920$ MPa and reinforced concrete properties for short-time loading will be considered. In the latter case, the adopted parameter-values are given in Tab. 12.2. Although these values intend to represent the same

Concrete					Reinforcement			f [MPa]
f_{cc}	E_c	ϵ_o	ϵ_h	f_{ct}	f_y	E_s	E_y	E [MPa]
-34	30920	-2.2	-4.0	0	400	210000	0	ϵ [10^{-3}]

Table 12.2: Reinforced Concrete Material Properties for Arch

properties as employed in [21], full agreement can not be accomplished for the concrete due to differences in the stress-strain relationship. Since the tensile strength of concrete is set to zero, the shear-beam element is for this case reduced to an ordinary Bernoulli-Euler element by constraining all internal hierarchical DOFs except for the axial translation. Thus, a possible premature failure due to lacking shear resistance will be avoided. For the linear elastic case however, the full shear formulation is retained. Also the cross section model is different for the two cases; 1 quad unit is used in conjunction with linear elastic material, while 2 quad and 2 rebar units are employed for modeling the cross sections of concrete and reinforcement, respectively. Like in [21], the finite element mesh consists of 12 equally spaced elements irrespective of material case. As indicated on Fig. 12.5, a geometric imperfection defined through $e = e_o \sin 2\alpha$ is introduced to initiate the sideway deformation mode. This relation and the value adopted for e_o are both in accordance with [21]. Moreover, the structure is restrained from moving in the out-of-plane direction. For

each type of material (elastic/reinforced concrete) and assumption for the loading (unidirectional/corotational) two comparative runs are made; with and without the corresponding load correction stiffness terms included. Thus, a total of 8 runs are carried out.

The elastic solutions with load correction stiffnesses included where successfully terminated at the load levels of 500 and 480 N/mm for unidirectional and corotational loadings, respectively. However, for corotational loading convergence was barely attained at the load level of 435 N/mm. In fact, to pass this point within 50 iterations it was necessary to take an extra load increment, narrowed down from 5 to 2.5 N/mm. Apart from that, convergence was achieved after a few iterations. No corresponding incident occurred for unidirectional loading. The deformed shapes at termination of the two runs are shown in Fig. 12.6. Clearly, even with less load applied the coro-

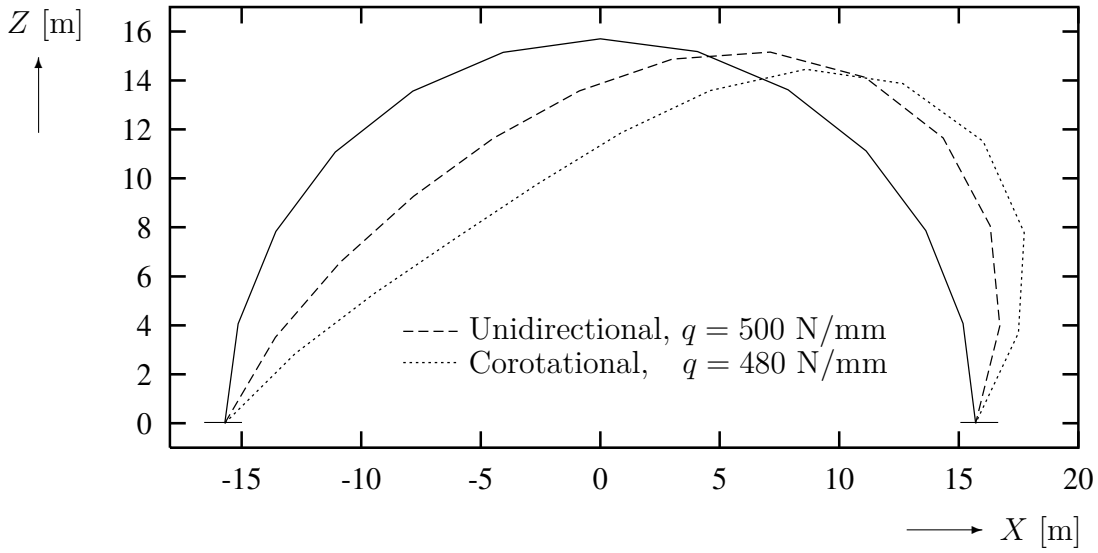

Figure 12.6: Deformed Shapes of Linear Elastic Arch

tationally loaded arch exhibits the softer response. Next the same runs but without load correction stiffness terms were carried out. Then the solution with unidirectional loading failed to converge beyond a load level of 476 N/mm. For corotational loading the run was still successfully terminated at 480 N/mm, but this time no critical behavior around 435 N/mm was experienced. These solutions converged somewhat slower compared to the companion-runs with load correction stiffnesses included. While for unidirectional loading this became really pronounced only in the ultimate range from 470 and up to 476 N/mm, the difference was more general for corotational loading. By considering the whole load history, the solutions without load correction required about 107 % and 43 % more iterations for unidirectional and corotational loadings, respectively; compared to the corresponding solutions with these stiffness terms included. Note that in this comparison three load steps in the range $432.5 - 440$ N/mm have been left out for corotational loading. The response curves for load versus horizontal translation of node 4 are shown in Fig. 12.7. This node is located at the

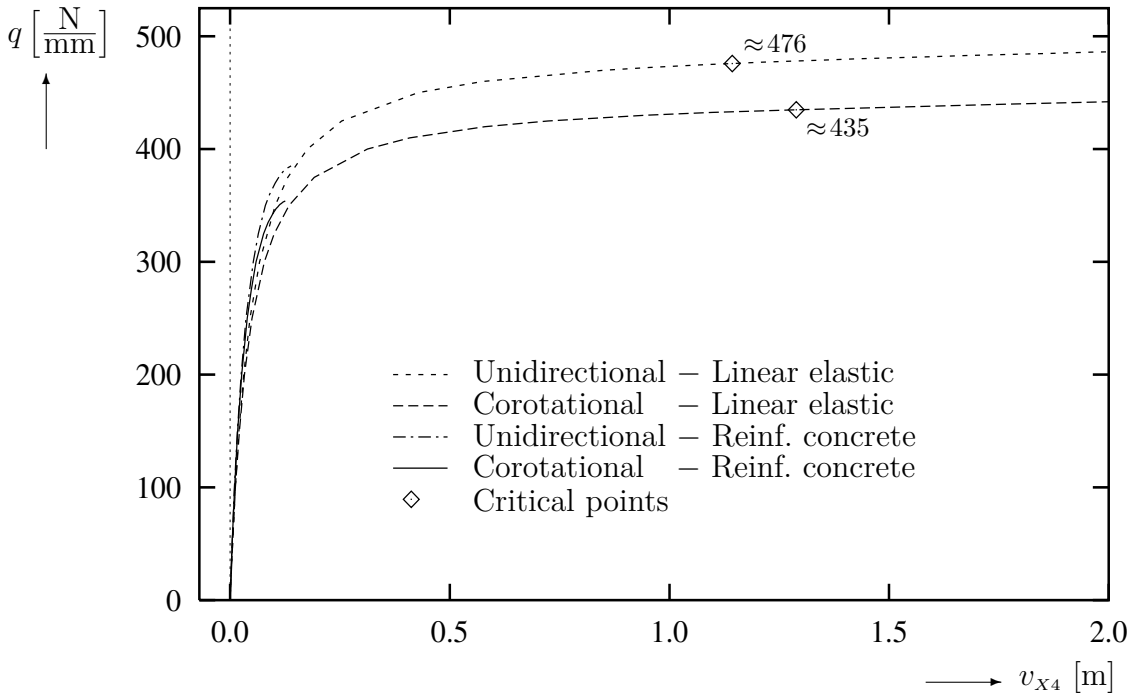

Figure 12.7: Load versus Horizontal Translation of Node 4

left quarter-point of the arch as indicated on Fig. 12.5. The curves are all referring to solutions with load correction stiffness terms included. Those without are however coincident (for the range with convergence) and are thus not displayed. It is believed that the convergence problem encountered around the 'critical points' may be attributed to bifurcational solution paths in these regions. The elastic solutions without the load correction stiffnesses are directly comparable to those reported in [21]. The results there confirm that very close agreement is obtained. An eigenvalue solution for unidirectional loading was also carried out in [21], yielding a critical load of 481 N/mm. Moreover, for corotational loading a critical load of 431 N/mm based on linearized buckling of a circular ring, is referred to there. Both values are close to the critical points mentioned.

The load-deformation curves for the reinforced concrete solutions are also shown in Fig. 12.7. The increase in stiffness, compared to the corresponding elastic solutions, is likely due to the reinforcement. For the reinforced concrete case no differences in the load capacities and deformational behavior, with and without load correction stiffnesses, were experienced. The structure reached the maximum loads of 385 and 354 N/mm for unidirectional and corotational loadings, respectively. The convergence however, is still somewhat slower when load correction stiffnesses are suppressed. By taking the whole load history, the solutions without load correction now required about 36 % more iterations for corotational loading and only 3 % more for unidirectional loading, compared to the solutions when these terms are included. In [21] the reinforced concrete solutions are traced through the peak points where

stability failure occurs, and down again to a load level corresponding to material failure. With the numerical solution procedure adopted here the descending part of the response can not be captured. For unidirectional loading the maximum load in [21] was found to be 395 N/mm, which is 10 N/mm above the value computed here. This slight discrepancy may be attributed to the differences in the numerical solution procedure. Also differences in the stress-strain relationship for concrete, the cross section modeling and the numerical integration technique are other possible causes. No solution for the corresponding case of corotational loading was reported in [21]. However, for another set of reinforced concrete material properties treated there the curves representing corotational loading were found to be located about 8 % lower than those for unidirectional loading. This reduction agrees very well with the aforementioned values for maximum load computed here. Also deformations seem to be in good agreement. In [21] a typical value for the horizontal translation of node 4 at peak load was $v_{X4} \approx 0.13\,\text{m}$. Here the corresponding computed values are 0.139 m and 0.126 m for unidirectional and corotational loadings, respectively.

12.4 Simply Supported Beams Tested by Bresler and Scordelis

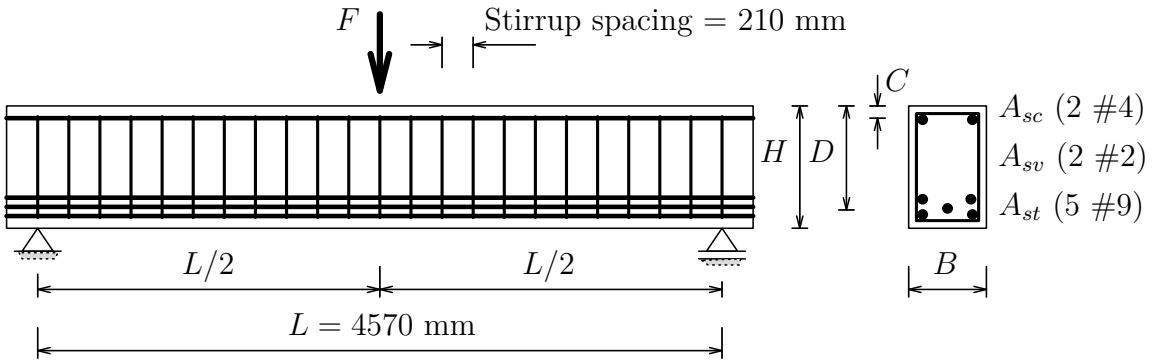

Beam	B [mm]	H [mm]	D [mm]	C [mm]	A_{st} [mm^2]	A_{sc} [mm^2]	A_{sv} [mm^2]
A-2	305	560	465	50	3290	252	64.5
OA-2	305	560	465	–	3290	–	–

Figure 12.8: Main Dimensions of Bresler/Scordelis Beams A-2 and OA-2

In 1963 Bresler and Scordelis [50] reported an experimental program designed for investigating the shear strength of reinforced concrete beams. A total of 12 simply supported beams were tested, among them the two companions denoted A-2 and OA-2 will be considered here. These beams were aimed to be identical in every respect, except for the shear reinforcement. While OA-2 was without stirrups, A-2

had a relatively light web reinforcement of about 0.1 % steel to concrete area ratio. In addition, A-2 had also longitudinal (compressive) reinforcement at the top of the beam to provide sufficient anchoring of the stirrups. The main dimensions of the two beams are summarized in Fig. 12.8. Despite the small amount of stirrups in beam A-2, the tests revealed that this reinforcement had a significant influence on the load capacity as well as the ductility of the beam. Thus, an adequate recreation of these differences with and without stirrups will be a severe test for the shear-beam element formulation. Since beams A-2 and OA-2 were not cast from the same batch, their concrete material properties are also slightly different. Only values for compressive cylinder strength and modulus of rupture are reported in [50]. Of these, the former is here employed as the compressive structural strength. Moreover, the direct tensile strength is taken as 50 % of the modulus of rupture. With this conversion good agreement is obtained for the load level at which diagonal tension cracks start to develop in the beams. Note that the tensile strength is a crucial parameter in these tests. For instance, adopting the full value of the modulus of rupture would have lead to a significantly different structural response. The remaining concrete material properties used for the analyses are derived from MC90 [35] based on the assumed values for the compressive strengths in the two beams. A summary of parameter-values for concrete is given in Tab. 12.3. The material properties for the various reinforcing steel bar sizes are taken from the tension tests in [50]. Since a bilinear stress-strain relationship is used in this work, the plastic hardening modulus E_y has been adjusted to obtain reasonably good fit to the experimental diagrams given in [50]. The values employed are summarized in Tab. 12.4. By introducing symmetry conditions at the

Beam	f_{cc} [MPa]	E_c [MPa]	ϵ_o [10^{-3}]	ϵ_h [10^{-3}]	f_{ct} [MPa]
A-2	-24.3	29000	-2.2	-4.6	1.85
OA-2	-23.7	28700	-2.2	-4.6	2.15

Table 12.3: Material Properties of Concrete

Bar size	f_y [MPa]	E_s [MPa]	E_y [MPa]
#9	555	218000	10000
#4	345	201400	2000
#2	325	189700	2000

Table 12.4: Material Properties of Reinforcing Steel Bars

midspan, only half of the beam is modeled in each case. However, discretizations

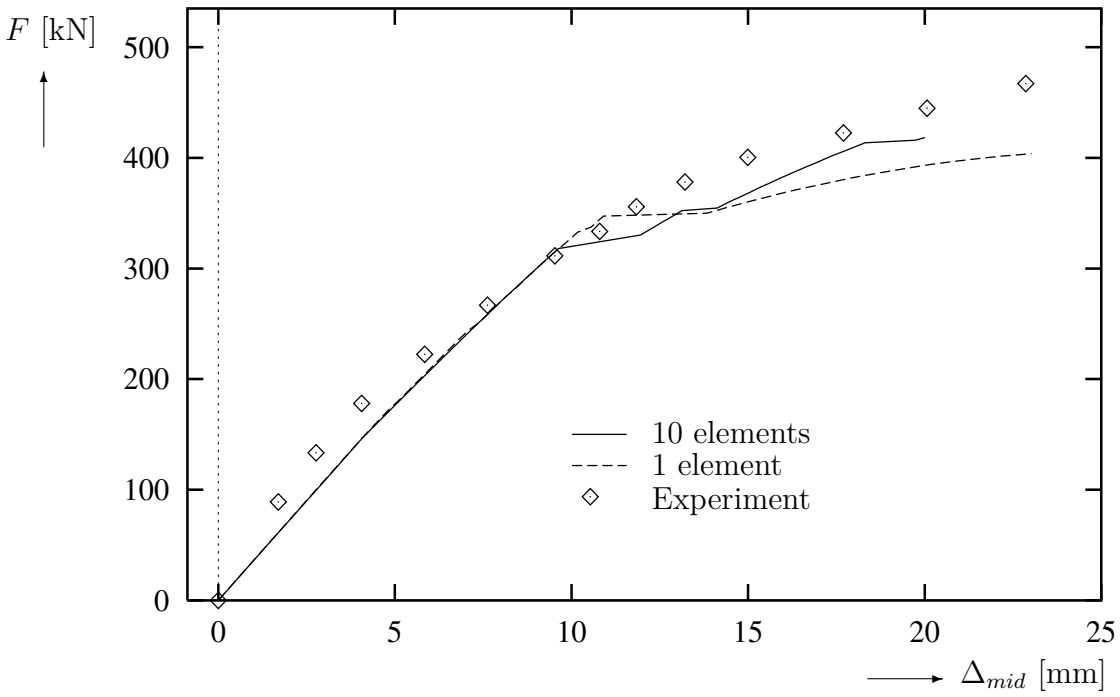

Figure 12.9: Load versus Midspan Deflection of Beam A-2

based on both 10 equally spaced elements and 1 element are considered. The structure is restrained from moving in the out-of-plane direction. Moreover, the cross section is subdivided into 3 line units over the height. Here the stirrups in beam A-2 are included as 'smeared' reinforcement. The longitudinal reinforcement is on the other hand treated on discrete form by employing a rebar unit for each layer. Thus, the total amount is 4 and 3 rebar units for beam A-2 and OA-2, respectively. Note that this modeling of the longitudinal reinforcement excludes the tension stiffening effect. The loading is applied according to a similar procedure as in the tests: First comes the dead weight. Next the midspan load is applied up to 30 % of the ultimate value from the test and is then removed. Finally, the load is reapplied monotonically until failure occurs. Only deformations computed during the final cycle of loading are included in the results presented in the sequel.

Fig. 12.9 shows a comparison between computed and observed load-deflection responses at midspan of beam A-2. Clearly, the computed response is somewhat too soft. The discrepancy in the initial range is possibly attributed to a less severe formation of flexural cracks than computed may actually have taken place in the test during the preloading phase, and that the tension stiffening effect, as mentioned, has been neglected. The good agreement at the intermediate stage corresponds to the load level at which diagonal tension cracks start to develop. Below this level the two element solutions are practically coincident. The response beyond onset of diagonal cracks is perhaps best illustrated in Fig. 12.10. Once cracking occurs, the beam expands laterally in that region and thereby causes the stirrups to get into action.

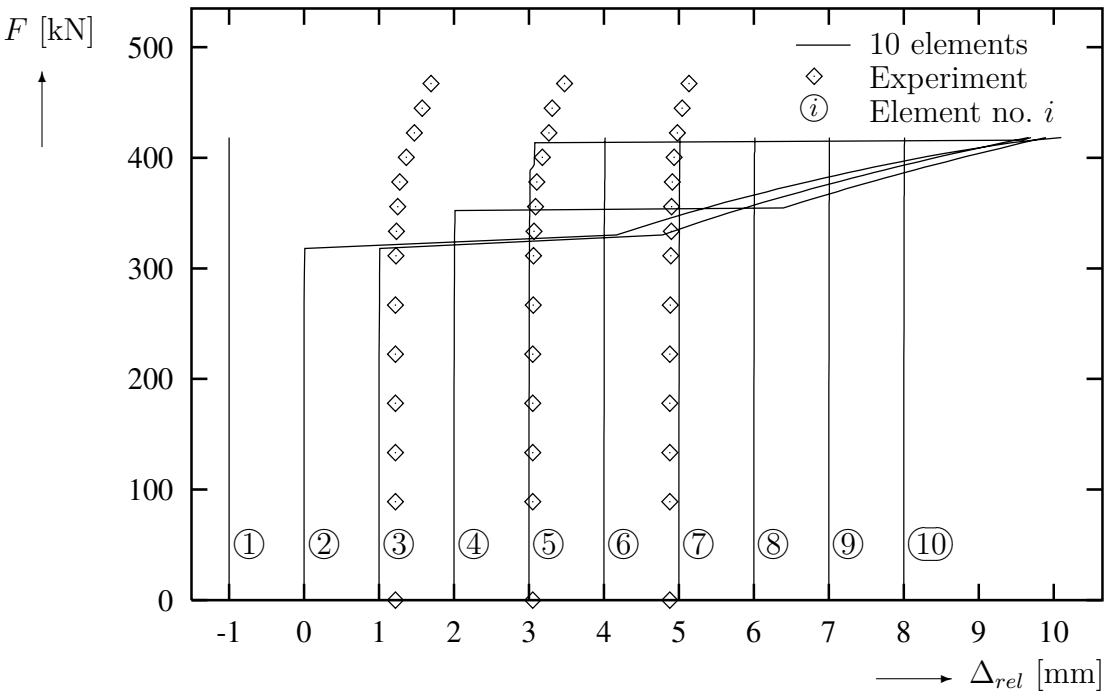

Figure 12.10: Load versus Relative Displacement of Beam A-2

Although the same happens in both test and analysis, this redistribution is much more pronounced in the latter case. For the 10 element solution it is evident that the stirrups are yielding immediately upon the occurrence of diagonal cracking in the element. This process starts in element no. 2 next to the support and propagates towards the center of the beam. A quite similar response can be read from the test results. In Fig. 12.10 the three reading stations for these measurements are in true position along the beam, compared to the element locations. To avoid overloading the figure, the 1 element solution is not shown here. However, the relative displacements for this case are about 30 % of those computed for element no. 2 in the 10 element solution. These excessive values from the finite element solutions may be attributed to the following two circumstances: The effect of so-called *aggregate interlock*, which yields an ability to transfer shear stresses across cracks, has been neglected. Otherwise the basic (and very convenient) assumption in the rotating crack concept that the directions of principal strains and stresses coincide, would have been violated. Probably more important, however, is the omission of the *dowel action*-effect in the longitudinal reinforcement. In this case the amount of shear that is carried by the heavy three-layered tensile reinforcement, is likely substantial; especially when the critical section appears not to be that of maximum moment. A similar consideration was also made in [50] as the main explanation for the high reserve strength exhibited by the beams compared to empirical expressions. For the case of beam A-2 this reserve strength varied from 43 % to 50 %. The ultimate load from the test was about 489 kN (110 kips). Note that the highest value shown in Figs. 12.9 and 12.10 are

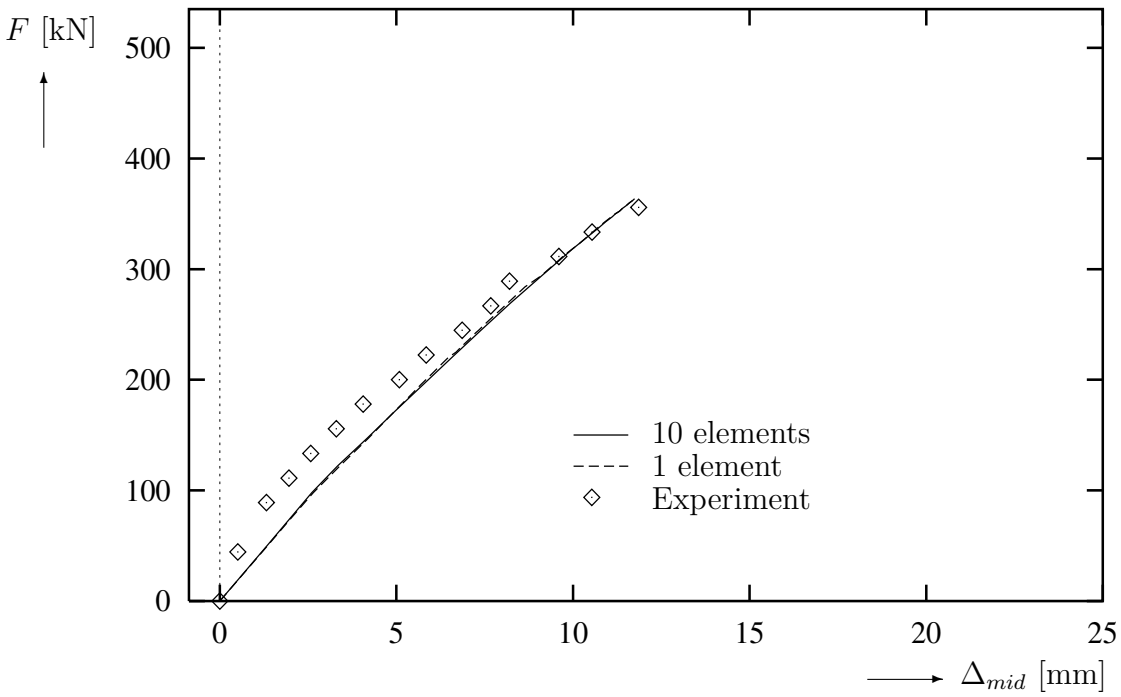

Figure 12.11: Load versus Midspan Deflection of Beam OA-2

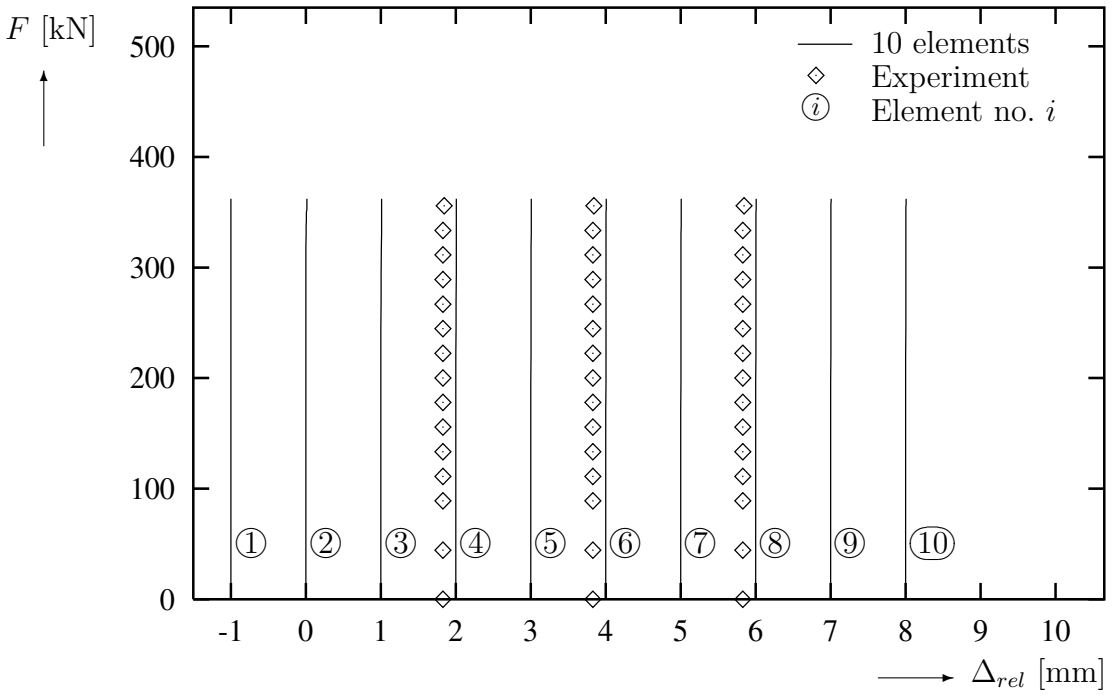

Figure 12.12: Load versus Relative Displacement of Beam OA-2

467 kN (105 kips) since deformations were not recorded for the ultimate load. In this work the computed failure loads are about 418 kN and 404 kN for the solutions with 10 elements and 1 element, respectively; implying corresponding reserve strengths of 17 % and 21 %. For both solutions the final failure was governed by crushing in the concrete, which agrees with the observed in the test. Moreover, from Fig.12.9 it is seen that the solution with 1 element develops the greater ductility of the two and is also in best agreement with the observed. Note again that the ultimate deflection of this beam was not recorded in the test.

The corresponding results for beam OA-2 are shown in Figs. 12.11 and 12.12. As can be seen, the response is much more brittle in this case, and the beam fails immediately upon the opening of diagonal tension cracks. Thus, this failure is almost exclusively governed by the direct tensile strength of concrete. The two finite element solutions become practically coincident, and very close agreement with the test is obtained for the load as well as displacement at ultimate. The discrepancy in the initial range may, as already pointed out for beam A-2, be attributed to differences in the extent of flexural cracking that has taken place during the preloading phase, and to the fact that tension stiffening is neglected.

12.5 Purely Twisted Box Beams Tested by Lampert and Thürlimann

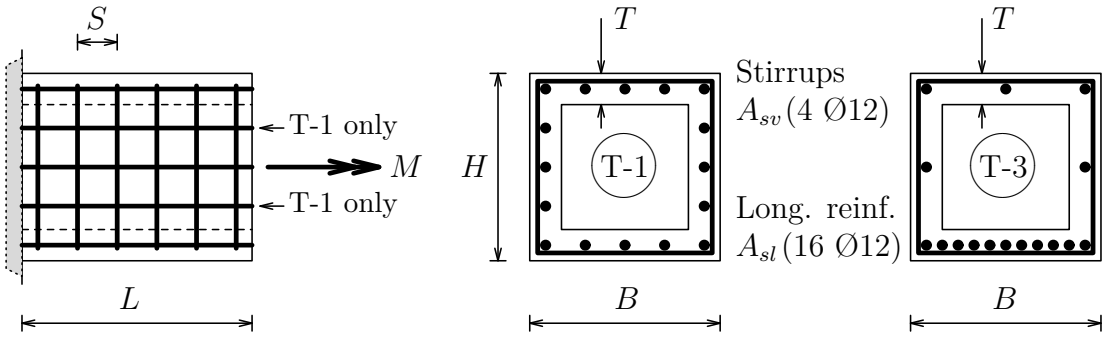

L [mm]	B [mm]	H [mm]	T [mm]	S [mm]	A_{sl} [mm^2]	A_{sv} [mm^2]
600	500	500	80	110	1808	452

Figure 12.13: Simplified Layout of Lampert/Thürlimann Box Beams T-1 and T-3

Lampert and Thürlimann [51] tested a series of box beams subjected to pure torsion, from which the two denoted T-1 and T-3 will be analyzed here. Since reference [51] has not been accessible, the background information is instead taken from the work by Jakobsen [52] who also studied the same beams. Although the total specimen length was about 4 m, the twisting angles were recorded over a region of 0.6 m. As

indicated in Fig. 12.13, only this part is modeled here. The two beams are identical with respect to concrete dimensions and the total amount of reinforcement. However, while beam T-1 is equally reinforced in all four walls with almost the same intensity in both directions, T-3 has most of its longitudinal reinforcement concentrated in the bottom flange. Since the material properties of the reinforcing steels were reported to be the same in the two directions, the simple layout of beam T-1 will provide a good opportunity to demonstrate that the tension stiffening formulation based on the concept of equivalent reinforcement (Subsection 8.1.4) works as intended under biaxial strain/stress-conditions. In pure torsion this beam will theoretically have almost constant orientation of principal directions close to 45° in relation to the reinforcement, throughout the entire response domain. Thus, the shape of the torque-twist relationship should become similar to that of a uniaxially loaded reinforced concrete bar, as was the starting point for the proposed tension stiffening formulation. To investigate the response further, the tension stiffening coefficient b_t will be varied in the range $0.4 - 0.0$ for both beams, and also the simplified formulation based on a linear stress-strain relationship for concrete after cracking will be included. For the remaining material parameters the values employed are summarized in Tab. 12.5. Here (E_c, f_y, E_s) are in accordance with reported values, while f_{cc} is taken as about

Concrete						Reinforcement			f [MPa]
f_{cc}	E_c	ϵ_o	ϵ_h	f_{ct} (T-1)	f_{ct} (T-3)	f_y	E_s	E_y	E [MPa]
-29	31000	-2.2	-4.2	1.6	2.0	364	210000	1500	ϵ [10^{-3}]

Table 12.5: Reinforced Concrete Material Properties for Box Beams T-1 and T-3

80 % of the tested cube strength. Furthermore, (ϵ_o, ϵ_h) are based on MC90 [35], and E_y is adjusted to the experimental curve. The values of f_{ct} for the two beams are those chosen by Jakobsen. With these values good agreement is obtained with the observed torque at which diagonal tension cracks start to develop. Note that a modulus of rupture as high as 5.8 MPa was reported. Also in these tests the tensile strength is a sensitive parameter, and apparently also in particular an uncertain one. For both beams the cross section is subdivided into 4 line units along the 'middle-surface', one for each wall. Here the reinforcement is included on 'smeared' form. All computations refer to a 1 element model, clamped at one end and with all DOFs free at the other, except for the prescribed twisting angle. Thus, the runs are carried out in displacement control. The convergence criterion Eq.(5.76), involving only translational DOFs, is in principle unsuitable for studying pure twist problems. However, the dead weight is here applied gradually while the beam is in the the precracking and early postcracking stages. Beyond onset of diagonal cracks, translations due to activation of the reinforcement will accompany the twisting mode. These secondary translations are considered to be sufficient to secure a reliable convergence at each solution step. At least, no spurious behavior has been experienced.

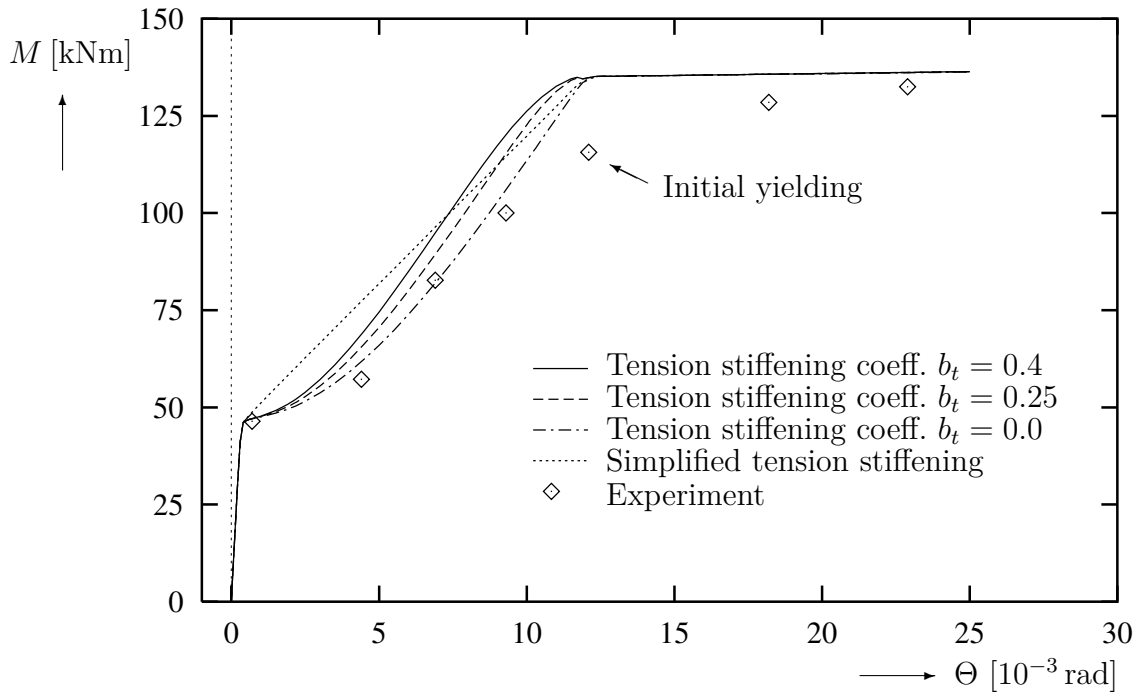

Figure 12.14: Torque versus Twisting Angle of Box Beam T-1

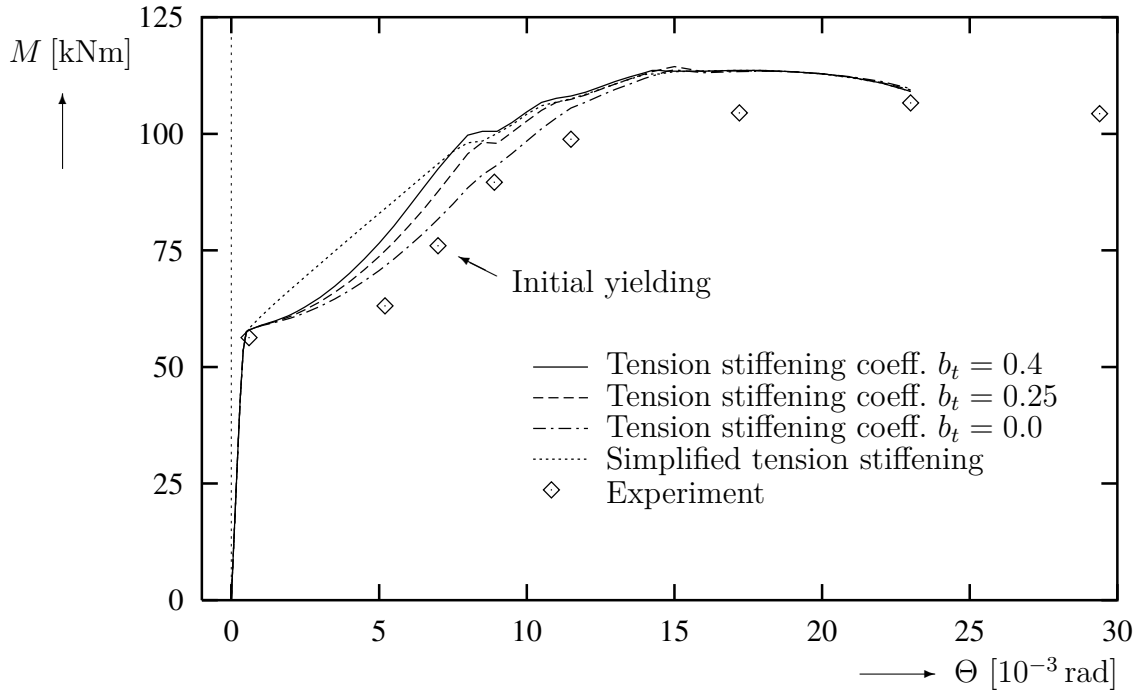

Figure 12.15: Torque versus Twisting Angle of Box Beam T-3

Fig. 12.14 shows the torque-twist relationships for beam T-1. By comparing the curves for various values of the tension stiffening coefficient with the response of the uniaxially loaded bar in Fig. 8.2, taken into account the smoothing of the abrupt transitions made for concrete in the postcracking range as indicated in Fig. 8.3 (compare the two 'normal'-curves), it is seen that the same type of behavior is now recovered. Thus, the concept of equivalent reinforcement works as intended in this case. Clearly, the same holds true for the simplified tension stiffening formulation since the linear curve between cracking and yielding is recovered. Jakobsen also compared various tension stiffening formulations for this beam. His results cover mainly the same band as here in the range between cracking and yielding. Besides, good agreement for the location of these two events is found. On the other hand, the test exhibits a much softer response beyond the intermediate stage of postcracking, as seen in Fig. 12.14. The main reason for this is probably the premature yielding indicated. Also in the early postcracking stage the test results are well below the computed curve based on a tension stiffening coefficient $b_t = 0.4$, which is the recommended value in MC90 for short-term loading. In fact, the curve corresponding to $b_t = 0.0$ agrees best with the test. Note that also this curve includes some effect of tension stiffening in early postcracking due to the aforementioned smoothing.

The torque-twist relationships for beam T-3 are shown in Fig. 12.15. Computed initial yielding occurred at a torque ranging from about 90 kNm to about 100 kNm, corresponding to solutions with $b_t = 0.0$ and $b_t = 0.4$, respectively. Here the longitudinal reinforcement in the top flange and the upper part of the side walls yielded. Then the remaining reinforcement in these three walls yielded gradually until the apex was reached. The final failure took place by concrete crushing in the lower part of the side walls. The reduction of compressive strength due to the orthogonal tensile strain was here substantial. Again the observed response is softer and now also exhibiting greater ductility than those computed. However, the shapes are in reasonable agreement. As shown, initial yielding took place in the test at a torque of about 75 kNm. This quite severe discrepancy may again indicate a premature yielding. Nevertheless, also this beam displays very little effect of tension stiffening in the early postcracking stage. What at least may be stated then, based on these two tests, is that the tension stiffening coefficient should have a smaller value than under uniaxial conditions for cases where the orientations of cracks and reinforcement are not orthogonal.

12.6 Box Beam Revisited, but Reinforced with Prestressing Bars

In order to demonstrate the effect of using prestressing bars (pbars) as shear reinforcement, a brief revisit of box beam T-1 from the preceding example will be made. The only difference introduced here is that the ordinary reinforcing bars (rebars) in the orthogonal grid now are exchanged with pbars oriented 'antisymmetrically' in 45°

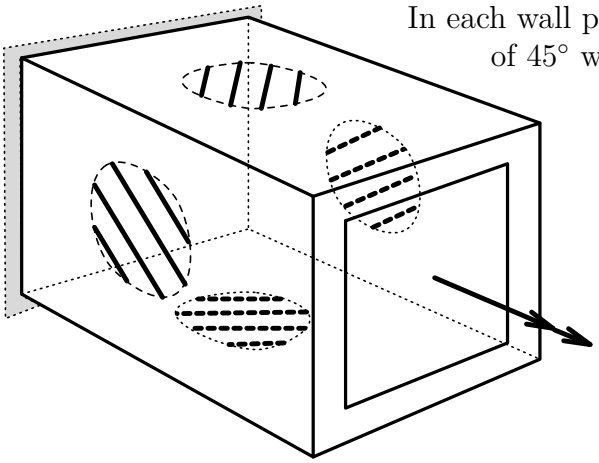

Figure 12.16: Arrangement of Pbars in Twisted Box Beam

with the longitudinal axis, as indicated in Fig. 12.16. Note that with this odd arrangement the beam can only resist torsion beyond the limit of cracking in the direction considered. The amount of pbars is determined so that the corresponding force at yielding becomes the same as in the stirrups of beam T-1, i.e. $a_b f_{0.2} = a_{sv} f_y$. Here, (a_b, a_{sv}) are the cross sections per unit length normal to the bar axis for pbars and stirrups, respectively. Then approximately[3] the same torque at yielding is achieved for the two beams. The fact that this 45°-arrangement of pbars will give a stiffer response in the range between cracking and yielding than reinforcement in an orthogonal grid, has also been compensated for to some extent by taking the value of $f_{0.2}$ higher than f_y (and thus reducing a_b compared to a_{sv}). The values employed are summarized in Tab. 12.6. As for rebars, a pure bilinear stress-strain relationship has

a_b [mm]	$f_{0.2}$ [MPa]	E_b [MPa]	$E_{0.2}$ [MPa]
0.468	800	210000	1500

Table 12.6: Cross Section and Material Properties of Pbars

been adopted for pbars. This is obtained here by first applying an initial tensioning stress of $\sigma_{eo} = f_{0.2}$, and then unload to the target value $\sigma_b^{(o)}$ through the introduction of a corresponding anchorage slip. Four different levels of prestress are considered

$$r = \frac{\sigma_b^{(o)}}{f_{0.2}} : \quad 0.0 \quad 0.3 \quad 0.6 \quad 0.9$$

The material properties of concrete are the same as those valid for beam T-1 in Tab. 12.5. In addition, a tension stiffening coefficient of $b_t = 0.4$ is employed for all

[3] Approximately only, since the intensity of the longitudinal reinforcement of beam T-1 is about 5 % larger than that of the stirrups.

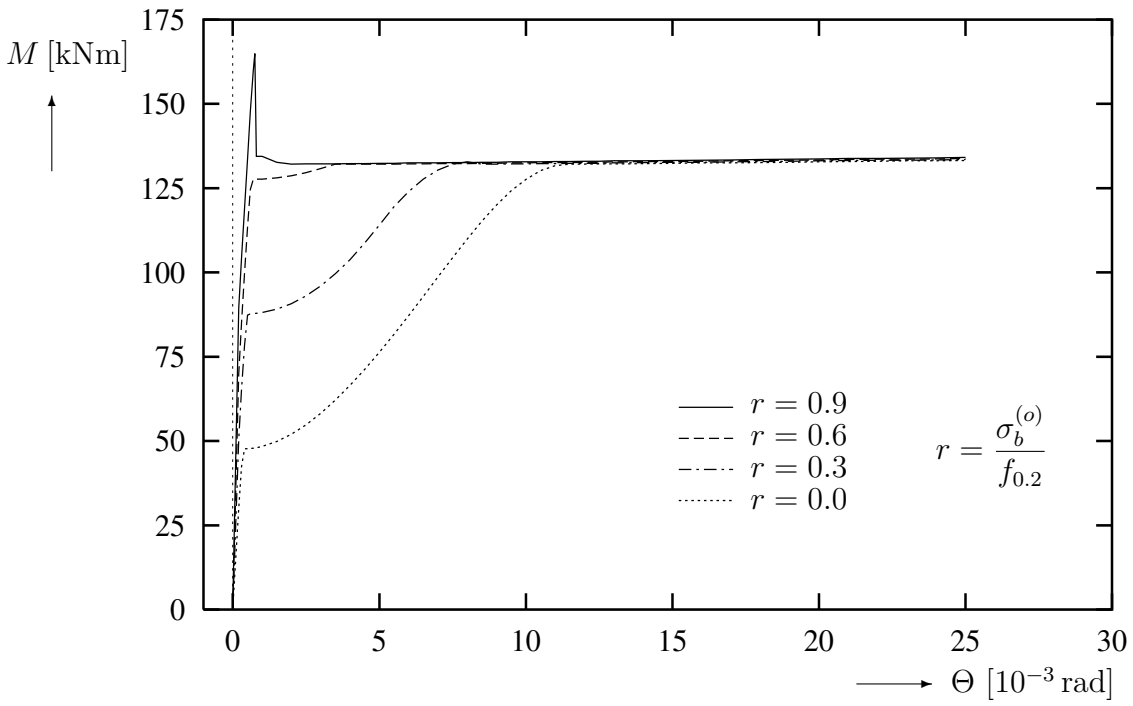

Figure 12.17: Torque versus Twisting Angle in Dependence of Prestress Level

runs. Also the finite element and cross section models are similar to those adopted in the preceding example.

Fig. 12.17 shows the torque-twist relationships obtained. Here the curve pertaining to zero prestress corresponds to that for $b_t = 0.4$ in Fig. 12.14. Of reasons mentioned, the two curves are not completely identical. Moreover, it is seen that the range between cracking and yielding gradually diminishes as prestress is applied, until an almost ideal elastic-plastic behavior is reached shortly above a ratio of $r = 0.6$. Beyond that, the maximum torque that can be resisted by the beam is governed by the tensile strength of concrete. Then follows a sudden drop to the yield plateau of increasing magnitude as more prestress is applied. This type of behavior is like one could expect to find, and it confirms that the shear-beam element formulation works satisfactorily under conditions of lateral (and longitudinal) prestressing.

12.7 Partially Sustained and Short-Time Loaded Column Tested by Hellesland

Hellesland [44] tested a series of seven hinged columns subjected to eccentric, time dependent axial loading. Here, column C-4 from this series with main dimensions as given in Fig. 12.18, will be considered. The load history of this column consisted of:

1. Initial short-time loading at 14 days after casting to about 101 kN (22.8 kips), which is approximately 50 % of the ultimate load.

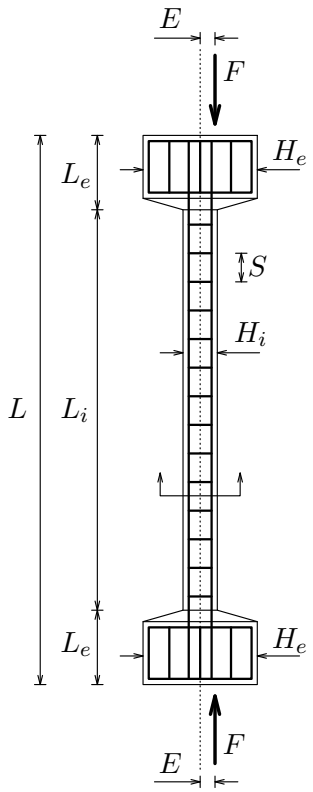

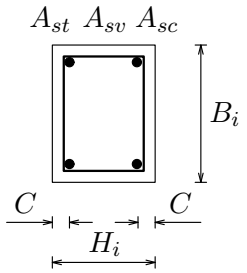

A_{st} (2 #3)
A_{sc} (2 #3)
A_{sv} (2 #1)

L [mm]	L_i [mm]	L_e [mm]	B_i [mm]	[1] B_e [mm]
1905	1375	265	180	230

H_i [mm]	H_e [mm]	E [mm]	C [mm]	S [mm]
130	410	50	20	100

A_{st} [mm^2]	A_{sc} [mm^2]	A_{sv} [mm^2]
143	143	16

[1] Width for end sections

Figure 12.18: Main Dimensions of Hellesland Column C-4

2. Constant loading at this level for another 128 days.

3. Then 1428 load cycles during 1 day in the range between that level and about 156 kN (35 kips).

4. Subsequent short-time loading to failure.

Companion tests on standard cylinder specimens were also carried out to record the corresponding histories of compressive strength, creep and shrinkage. The strength values at initial loading (14 days) and final loading (142 days) were reported to 29.0 MPa (4.20 ksi) and 39.4 MPa (5.72 ksi), respectively. The creep and shrinkage recordings will not be utilized for the analysis in this work, since the models employed here are characterized mainly by environmental parameters (temperature and relative humidity) and strength properties of concrete. The thermostat regulated temperature had little variation throughout the test period. A constant value of $23\,^oC$ is adopted here. The relative humidity was on the other hand not controlled, and for the first important 50 days after casting not measured. However, a relative humidity of $RH = 25\,\%$ is assumed here based on monthly averages for the remaining part of the loading period and for the same months the following year for the period missing. Note that this value is actually below the recommended range of applicability for the creep and shrinkage prediction models employed ($40\,\% < RH < 100\,\%$). For the

concrete parameters the values adopted are summarized in Tab. 12.7. Here the *mix*-parameter has been assigned a value that corresponds to slowly hardening cement.

f_{cc28} [MPa]	E_{c28} [MPa]	ϵ_{o28} [10^{-3}]	ϵ_{h28} [10^{-3}]	f_{ct28} [MPa]	mix [−]	f_{cm28} [MPa]	h [mm]
−27.3	30100	−2.2	−4.3	2.7	−1	−27.3	75

Table 12.7: Concrete Parameters for Column C-4

Then reasonably good agreement with the reported increase of strength between 14 and 142 days has been obtained. In [53] Hellesland et al. analyzed column C-4 using the computer program developed by Kang [22]. In that analysis the structural compressive strength was taken to be 0.85 times the cylinder strength. The same conversion factor is employed here, also for the mean strength f_{cm}. Moreover, h is the notional member size determined according to Eq.(9.51). The values of the remaining parameters in Tab. 12.7 are derived from MC90 [35]. For the longitudinal reinforcement the material properties are given in Tab. 12.8. These values are adopted from [53]. Since values for the very light lateral reinforcement were not reported,

Side	f_y [MPa]	E_s [MPa]	E_y [MPa]
Compression	434	234400	10800
Tension	400	234400	10800

Table 12.8: Material Properties of Longitudinal Reinforcement

these bars are for simplicity assigned the same properties as the longitudinal tensile reinforcement. Due to symmetry only half the column is considered. This part is modeled as a cantilever clamped at the column midheight. The finite element discretization consists of 8 elements; 7 of equal length and 1 with half this length next to the midheight. Moreover, the structure is restrained from moving in the out-of-plane direction. This model is equivalent to that employed in [53]. Both types of cross section, the typical and the enlarged at the loaded end, are subdivided into 2 line units. Here the lateral reinforcement is included on 'smeared' form. For the longitudinal reinforcement 2 rebar units are used; 1 on each side. The loading is in accordance with the aforementioned load history. However, the 1428 load cycles are here represented with 1 cycle only. The dead weight of the column is included. Like in [53], the sustained load period of 128 days is subdivided into time steps of increasingly larger duration: 3, 7, 12, 18, 40 and 48 days.

Fig. 12.19 shows computed[4] and observed load-deflection responses at midheight of the column. In the analysis tension cracking took place in the course of the initial

[4]Due to the cantilever model employed, these values are actually computed for the tip.

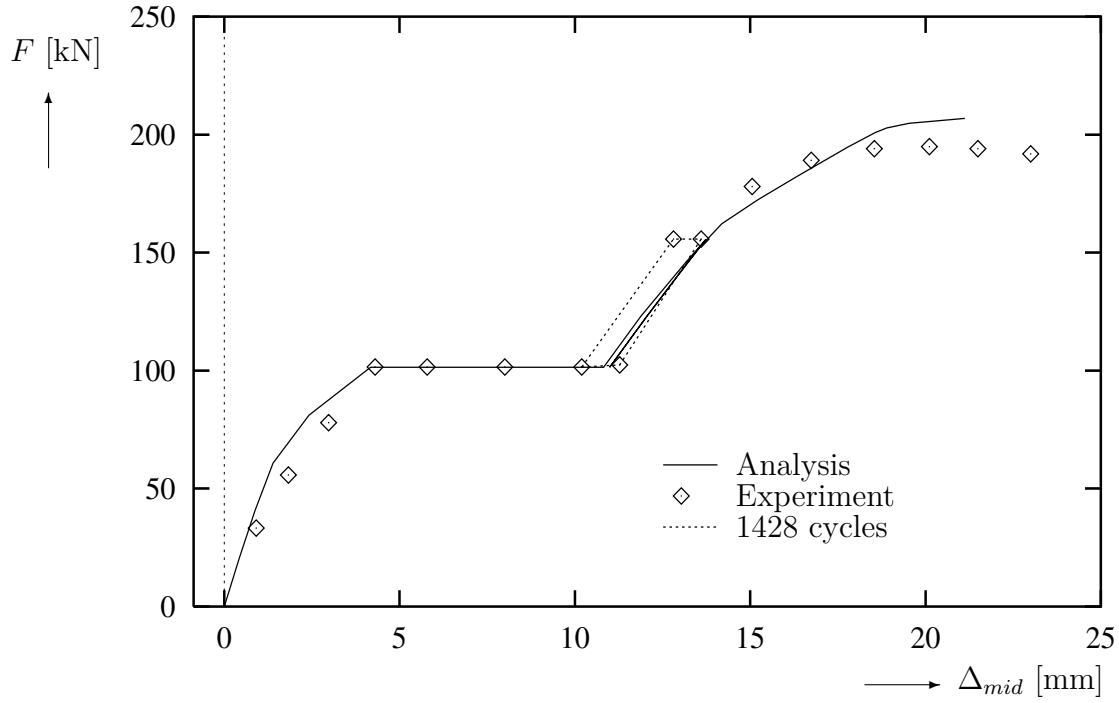

Figure 12.19: Load versus Midheight Deflection of Column C-4

short-time loading. During the sustained load period a severe increase in compressive steel stresses and a corresponding unloading of concrete were experienced. The first yielding in compressive steel was encountered in the only load cycle that replaced the 1428 cycles from the test. The ultimate stage (around 200 kN) was initiated by yielding in the tensile reinforcement. At the very ultimate load the maximum compressive stress in the concrete was about 93 % of the uniaxial strength, indicating that a material failure was close when instability occurred. A similar failure mode was recorded in the test. Also note the increase in tangent stiffness that apparently has taken place during the sustained load period. This is likely attributed to the effect of aging and also to the redistribution mentioned. As a whole, quite good agreement between computed and observed responses is obtained. The discrepancy in the initial load range is probably attributed to the tensile strength of concrete that may have been smaller in the test than assumed here. Clearly, the creep deformation during the sustained load period is somewhat excessive in the analysis. However, this is compensated for by less deformation due to cyclic loading. The approximate ultimate loads are 207 kN and 195 kN (43.8 kips) for analysis and test, respectively. Although such a discrepancy ($\approx 6\,\%$) should lie well within the natural scatter for reinforced concrete, a more specific reason for this overestimated capacity could be that some deterioration owing to the load cycling may have taken place in the test, like reduction of bond effectiveness between concrete and steel bars. On the other hand, the computed failure load in [53] was about 197 kN, which is in excellent agreement with the test value.

12.8 'Interior' Bridge Span Built by Cantilever Construction

The final example addresses a single cast-in-place and posttensioned bridge span built by cantilever construction. As indicated in Fig. 12.20, this structure may be interpreted as an 'interior' span of a multi-span bridge system. Moreover, due to assumed symmetry, only half the span is analyzed. Despite its limited size, the problem considered contains most features of a full bridge, and as such is a suitable example for demonstrating the applicability of the analysis-model developed in this work. All dimensions are taken from the work by Ketchum [24]. He made a detailed investigation of the time dependent behavior of this span considering three different girder profiles and three different creep models. The girder employed here is the one with the larger haunch, of greatest interest for longer span. Also the construction sequence and the service life analysis are in accordance with [24]. Each segment is cast and tensioned on a weekly schedule. The details are: When a new segment is introduced, it is assigned an initial effective age of $t_{To} = 3$ days. Immediate upon the introduction, the dead weight of the segment and the prestressing force of the corresponding cantilever tendon (see Fig. 12.20) are applied in a joint short-time operation. Then a 7 day step is made until the next segment is introduced, and so on. The weight of the traveling formwork is disregarded. After the midspan segment (the closure segment) is introduced, the prestressing forces of the continuity tendons and a nonstructural dead weight of 36.5 kN/m, accounting for guard rails and pavement, are applied in a single short-time operation that completes the construction of the girder. With the 11 segments this results in a construction period of 77 days. Then the analysis for the service life of 27 years (10000 days) following construction is subdivided into 22 time steps: First 5 time steps are used between day 77 and day 100. Next 7 steps are adopted in the range from day 100 to day 200, and finally 10 steps for the remaining period up to day 10000. Over each of these three main intervals, equal time step lengths on a logarithmic scale are employed. No live loads are considered. Also like in [24], each segment is modeled with one element and with dimensions for the cross section determined at its midlength. When the closure segment is introduced, the system changes from a cantilever to one with only the vertical and axial translations free at the midspan, as indicated in Fig. 12.20. Note that the axial midspan continuity is here relaxed in order to represent the expansion capability provided in all bridges. In this work, each cross section is subdivided into 4 line units; one for each of the top slab, bottom slab and the two webs. In the base case model no reinforcing steel is included. For a comparative run such reinforcement has been added on 'smeared' form in all line units based on a 2 % steel to concrete area ratio. Then the whole amount is taken in the longitudinal direction for the two slabs, while an equal split on both directions is used for the webs. The cantilever tendons are located in the top slab and are straight over their entire length. Four tendons are actively anchored (i.e. jacked) at the front of each segment, excepting that of closure. In the model each such quartet is grouped into one tendon of the

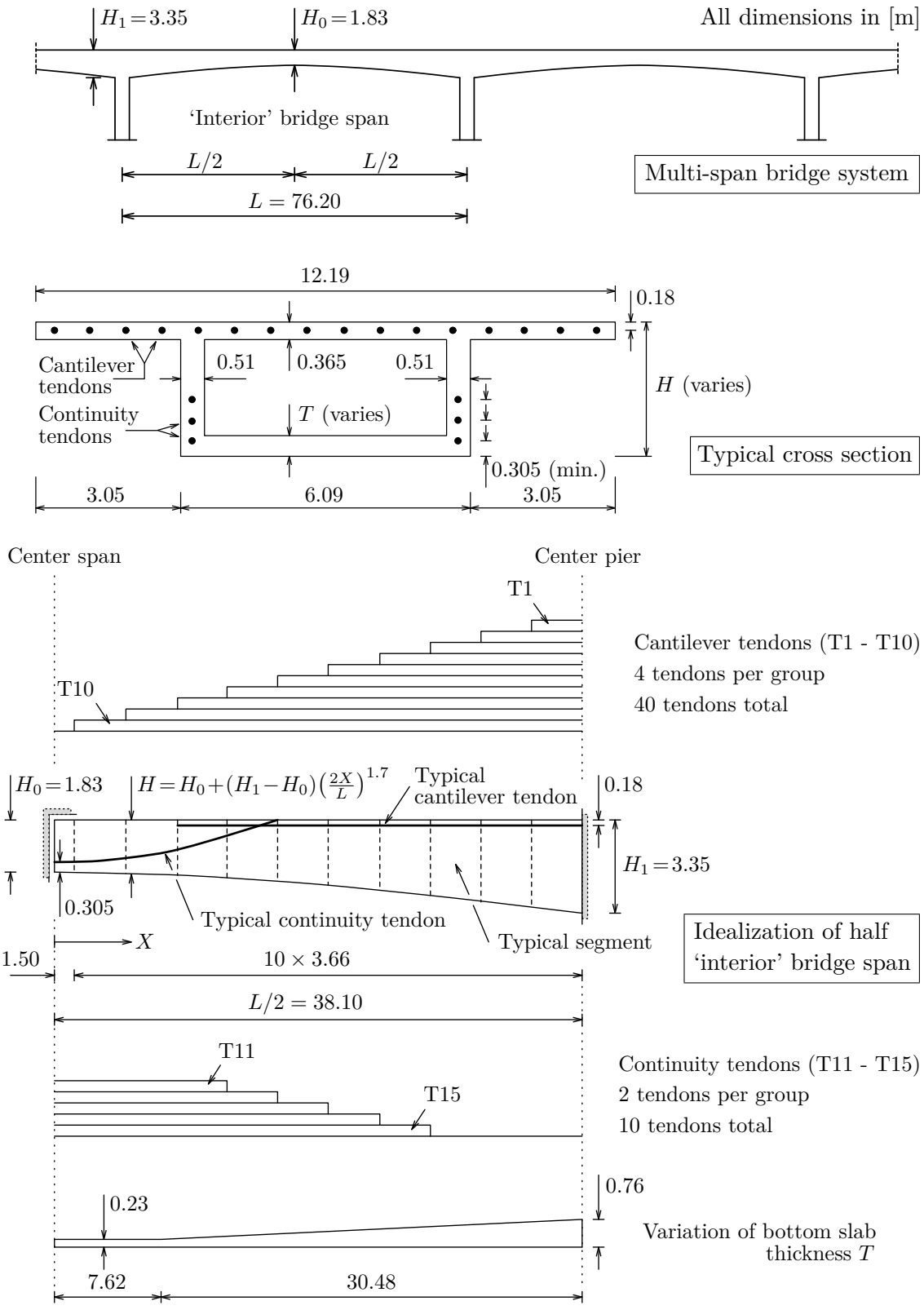

Figure 12.20: Main Dimensions of 'Interior' Bridge Span

kind denoted T1 through T10. The continuity tendons are parabolically draped in the webs, actively anchored at the top face of the girder and with a minimum distance to the bottom face at the midspan. In the model each pair is grouped into one tendon of the kind denoted T11 through T15. The tendon data employed for the cross section area A_p, jacking force P_0, curvature friction coefficient μ, wobble friction coefficient k and the anchorage slip u_s, all according to [24], are summarized in Tab. 12.9. Moreover, the values of the material parameters adopted for all prestressing steel are

Tendon	A_p [mm^2]	P_0 [MN]	μ [1/rad]	k [1/km]	u_s [mm]
T1 - T10	7900	10.35	0.25	1.31	6.35
T11 - T15	2370	3.10	0.25	1.31	6.35

Table 12.9: Tendon Specifications

$f_{0.2}$ [MPa]	ω [–]	E_p [MPa]	$E_{0.2}$ [MPa]	C_r [–]
1650	0.83	193000	4400	10

Table 12.10: Material Properties of Prestressing Steel

given in Tab. 12.10. In their order of appearance, these parameters are the stress at 0.2 % strain offset, the elasticity-limit factor, the elastic and plastic hardening moduli, and finally the relaxation coefficient. Only the values of E_p and C_r are in direct agreement with Ketchum's analysis since that was restricted to linear elastic short-time behavior. However, based on the ultimate strength also specified there (1860 MPa), the remaining values in Tab. 12.10 are derived from data in [53] for a similar steel. As mentioned, three different time dependent concrete models were considered by Ketchum. In common, they were all based on a compressive cylinder strength at the age of 28 days of about 35 MPa (5000 psi), a ultimate creep factor[5] of 3.0, and a ultimate shrinkage strain of $0.8 \cdot 10^{-3}$. Here this strength is taken as the characteristic value for the concrete grade and also as the structural compressive strength. Based on these assumptions the 28 day values given in Tab. 12.11 have been derived from MC90 [35]. In addition, with the values adopted for the *mix*-parameter (normal and rapid hardening cements) and the relative humidity RH, reasonably good agreement with the specified ultimate creep factor has been obtained. Also the specific weight of concrete γ_c is according to [24]. Here this value is assumed to include the weight of all steel (i.e. tendons and also rebars in the comparative run). Note that the notional member size h is taken to be the same for all cross sections. Since no seasonal temperature variation was reported in [24], a constant year-round

[5]Defined as the ratio between creep strain at infinity and elastic strain at time of loading.

f_{cc28} [MPa]	E_{c28} [MPa]	ϵ_{o28} [10^{-3}]	ϵ_{h28} [10^{-3}]	f_{ct28} [MPa]	b_t [−]	γ_c [kN/m^3]	mix [−]	f_{cm28} [MPa]	RH [%]	h [mm]
−35	35000	−2.2	−4.0	3.2	0.4	24.3	0	−43	70	500

Table 12.11: Concrete Parameters

value of $20\,^oC$ is employed here. Finally, the material properties adopted for the reinforcing steel in the comparative run are given in Tab. 12.12.

f_y [MPa]	E_s [MPa]	E_y [MPa]
400	200000	1000

Table 12.12: Material Properties of Reinforcing Steel

Figs. 12.21 and 12.22 show respectively the bending moments and shear forces computed in the girder at completion of construction and after 27 years. Note that the applied or primary prestress contribution has been subtracted here, and consequently, these are the member forces due to externally applied loading and secondary prestress contribution (i.e. the deformation part). As can be seen, practically no redistribution of forces between the two observation times has taken place. This important characteristic agrees well with that found by Ketchum for the same girder. Also his moment[6] values are close to those computed here. Despite the agreement, this author would like to emphasize, based on several years of personal bridge design experience, that this lack of redistribution by far is a conventional result for such structures. It may be argued that the half 'interior' span considered here, is not a representative case. However, Ketchum analyzed in addition a full three-span bridge that also showed almost insignificant redistribution, and thus indicating a more general trend when adopting refined analyses. In Fig. 12.23 girder deflections at completion of construction and after 27 years for various models are summarized. These are the deflections recorded for each element, and due to the segmental construction procedure, they are discontinuous at interelement boundaries. However, during the actual construction the girder will be precambered to eliminate discontinuities and to obtain the elevation specified. The information necessary for these adjustments is found from the computed deflections. In this figure the first legend 'no reinforcing steel' identifies the base case model, while the second represents that of 2 % steel to concrete area ratio, distributed as explained. The third one is identical to the base case model, except that the shear-beam element now is reduced to an ordinary Bernoulli-Euler formulation by constraining all internal hierarchical DOFs other than the axial translation. Clearly, the contribution from shear deformations

[6]Shear forces and deflections were not reported for this example in [24].

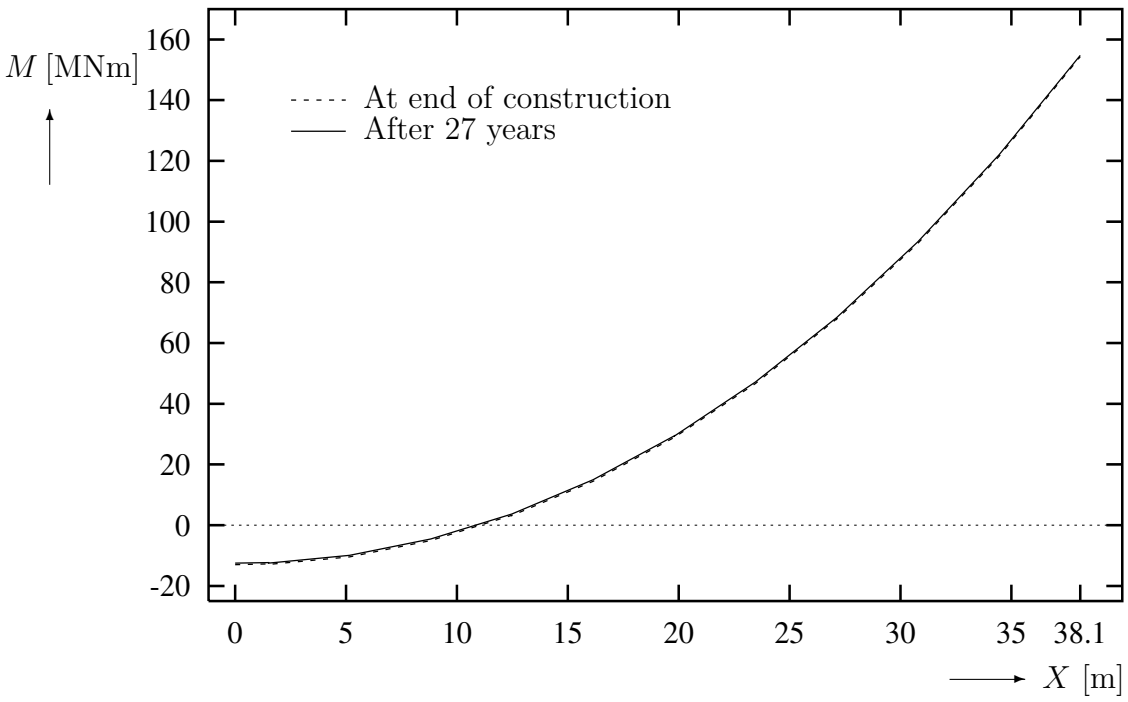

Figure 12.21: Girder Bending Moments

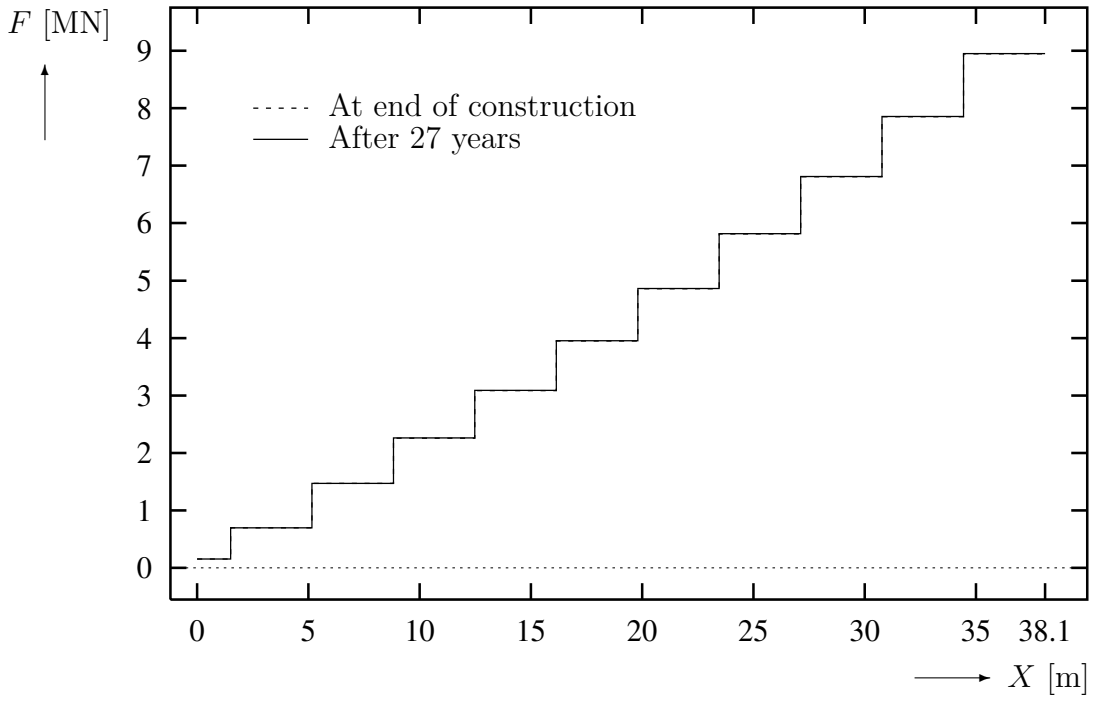

Figure 12.22: Girder Shear Forces

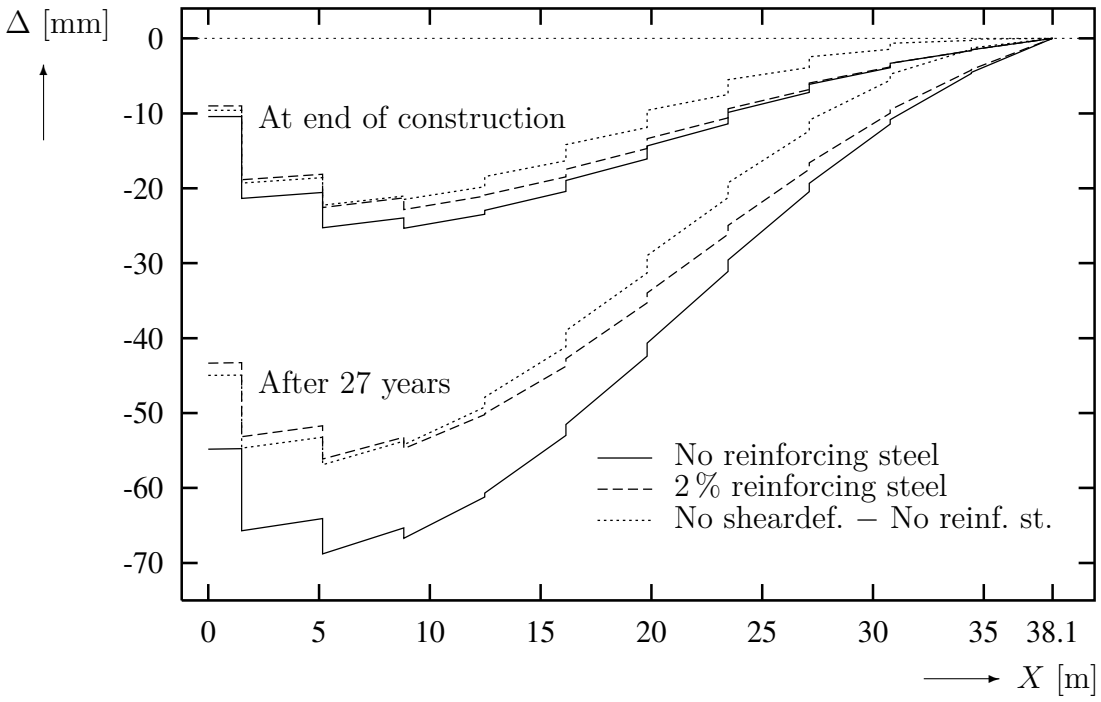

Figure 12.23: Girder Deflections

to the resulting deflections is significant along the entire span, although it varies from being the main component closest to the support to about a 15 % share in the central part. The relative importance is roughly the same at the two observation times. Adding 2 % reinforcing steel yields an almost equal adverse contribution in the central part of the span and gradually less towards the support. Here the long-time effect is the more pronounced. Finally, tendon force profiles at the tensioning state and after 27 years for various models are compared in Fig. 12.24. The two tendons considered, T10 and T15, are the longest of the cantilever and continuity kinds, respectively (see Fig. 12.20). The force profiles vary with respect to both the assumption made for the anchorage slip and the stress relaxation method employed. As already specified, the base case model uses an anchorage slip of $u_s = 6.35$ mm (1/4 inch). In a comparative run the slip is now set to zero. From Fig. 12.24 it is seen that the original value in fact influences the force variation over a considerable length, especially for the straight tendon T10. Although not mentioned before, the base case model also employs the rate of relaxation method (RRM), as proposed in this work, for computing the corresponding stress losses in the prestressing steel. The commonly adopted and more complex fictitious initial stress method (FISM) is now used in another comparative run. As shown in the figure, practically the same long-time forces result ('WAS − RRM' versus 'WAS − FISM'). Moreover, the resulting time dependent prestress losses taken place during the 27 year period are fairly constant over each length. For the runs with anchorage slip the averages are around 20 % and 18 % for tendons T10 and T15, respectively. Note that this fairly uniform

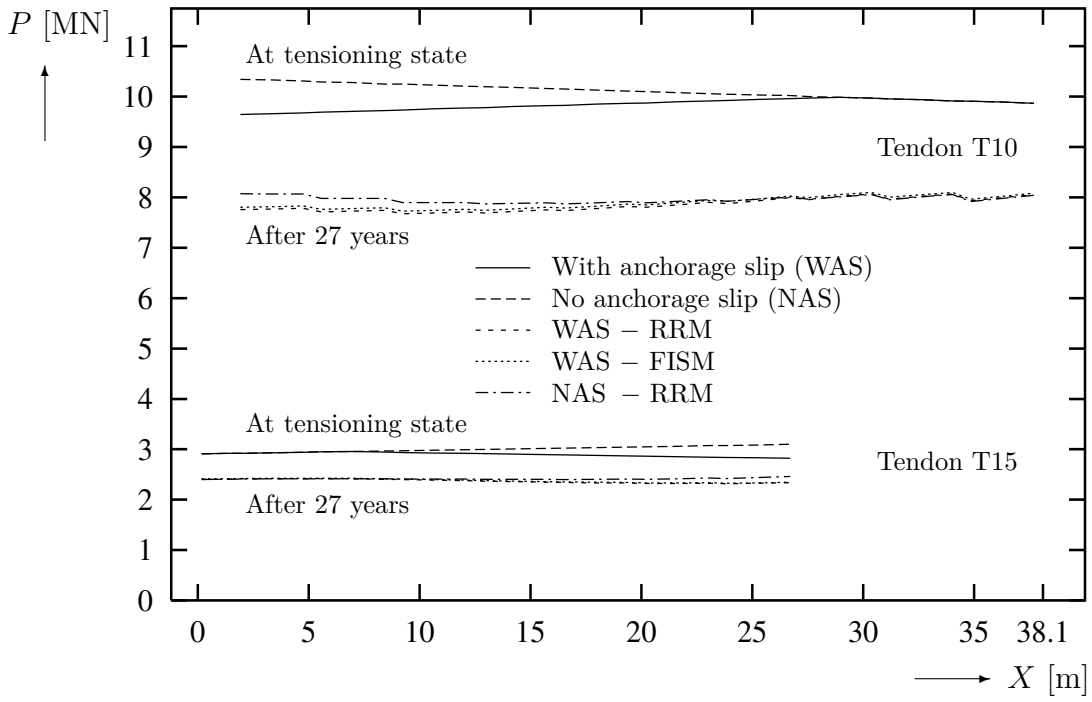

Figure 12.24: Forces in Tendons T10 and T15

distribution is in some contrast to what was reported by Ketchum. There the losses were found to be higher in the central part of the span with younger concrete at the tensioning state. However, for the ACI-model with the fastest aging function of the three concrete models investigated there, the distribution as well as the loss-values are in quite good agreement with the results obtained here. In this work the aging function employed, based on MC90 [35], is even faster than for the ACI-model. For instance, the compressive strength after 3 days, the age at first load application, is about 30 % higher here than using the ACI-model. This is probably the main reason for the discrepancy mentioned.

Chapter 13

Summary, Conclusions and Recommendations for Future Research

13.1 Summary and Conclusions

In the present work an analysis-model applicable to large scale 3D beam structures of reinforced and prestressed concrete, has been developed. The model is based on the finite element method and allows for large displacements through the Corotated Lagrangian description of motion and a variety of material nonlinearities in the short-time as well as the long-time regime. The loading may be both unidirectional and corotational. By relating all changes in loads, prescribed displacements, temperature, time and static system to a common history parameter, the response of a structure may be traced from the very start of construction to its completion, throughout the service life and finally into the ultimate load range.

The key ingredient of the analysis-model is considered to be the new shear-beam element formulation. Initially, for linear elastic behavior in pure bending-shear a 2D version with five DOFs was developed; both on conventional as well as hierarchical form. This element can model problems with linear moment variation and constant shear exactly. Also for higher order force variations the nodal displacements are very accurately represented. That was demonstrated through closed form solutions of a cantilevered beam modeled with one element and subjected to various loading. As expected, results were identical in every respect with the conventional and the hierarchical forms of the element. Then based on the hierarchical form, an extension to a general nonlinear 3D version with fifteen displacement DOFs and four strain DOFs was undertaken. Different from previous beam elements for reinforced concrete, this element can model the behavior in each one and combinations of the axial, bending, shear and torsion modes. Through numerical examples it was demonstrated that the element successfully handles the severe redistribution of strains and stresses that takes place in a shear reinforced beam when the concrete cracks and the stirrups

get into action. Also it was shown that the effect of lateral prestressing is correctly modeled. These effects are attributed to the strain DOFs in the element formulation. In addition, the 3D shear-beam element was tested with linear elastic material properties for problems involving large displacements. Again the element proved excellent performance. A spin off of the element formulation has been the derivation of load correction stiffness matrices for corotational and unidirectional body attached distributed loading. Also corresponding matrices have been presented for discrete nodal loading. To this author's knowledge, such contribution from unidirectional loading has not been proposed before, while for corotational loading the expressions given here differ somewhat from those reported in [5]. For the problems investigated involving large displacements, these load corrections have typically lead to more rapid convergence[1], and also enhanced load capacity has been experienced.

Among the various types of prestressed concrete structures, only the most common 'posttensioned and bonded' has been considered in this work. However, both tensioning by tendons and bars are studied. For the prestressing tendon modeling, the geometry has been defined using parametric representation of quadratic curves in space. From this geometry the force variation at the tensioning state is then consistently derived. This implies the tendon force profile considering losses due to friction and anchorage slip, and the corresponding distributed loading on the concrete structure. When bonded, the tendon has been treated as an integral part of the beam cross section, and thus current strains in excess of those from the tensioning state are derived from the displacement field of the element. This procedure differs in several respects from that adopted by previous investigators [22]-[27]. An additional advantage of the parametrized form is the saving on the amount of input-data. Also a closed form solution for the loss of tensioning force due to anchorage slip has been presented. Prestressing bars (pbars) have been included mainly to impose lateral prestressing in conjunction with shear dominated problems. As demonstrated through numerical examples, the precracking range may be considerably extended using pbars compared to ordinary shear reinforcement. A 'smeared' form has been adopted for the pbar modeling. Loss of prestress due to anchorage slip is included, while friction loss is not since pbars are straight and 'short'. Nevertheless, the pbar and tendon models are based on the same principles. Although the main intention has been to utilize pbars as shear reinforcement, the formulation works for any bar orientation. Inclusion of lateral prestressing in beam elements is definitely believed to be a new contribution.

For the constitutive modeling of short-time or instantaneous material behavior, a so-called 2D rotating 'smeared' crack model has been adopted for concrete. This is a popular approach in conjunction with membrane element implementations. The most common model of this kind today is probably the modified compression field theory (MCFT) [31]. Although, the model adopted in this work share many of MCFT's features, several extensions are also made:

- The shape of the stress-strain relationship in compression is now described by

[1]For corotational loading there is one exception at a certain load level for the arch in Section 12.3.

a four-parameter expression (two in MCFT).

- The tension stiffening formulation is made dependent on the amount and the orientation of reinforcement. In addition, the need for a separate stress control at cracks is eliminated.

- Introduction of increased compressive strength in biaxial compression and reduced tensile strength in tension/compression, both effects expressed in terms of the coexisting orthogonal strain.

- Unloading and reloading are accounted for.

For reinforcing and prestressing steels, nonlinear uniaxial stress-strain relationships representative for hot-rolled and cold-worked steels, respectively, have been adopted. Again, unloading and reloading are accounted for. The biaxial tension stiffening formulation has been extended from uniaxial observations through the introduction of an 'equivalent reinforcement' in the principal tensile strain direction. Numerical examples have confirmed that this formulation works conceptually correct. However, compared to test results, it appears that the tension stiffening coefficient should be smaller than that recommended in e.g. [35] for cases where the orientations of cracks and reinforcement are not orthogonal. Also the numerical analyses have revealed that the direct tensile strength of concrete is a parameter which significantly influences the structural deformational response. Unfortunately, this is in particular an uncertain parameter. Effects of dowel action and aggregate interlock have not been included. The underestimation of ultimate load in the shear reinforced simply supported beam example may be attributed to these circumstances.

The material models for time and temperature dependent effects have mainly been based on established relationships from the literature, in particular from [35]. Among the time dependent effects considered, are creep, shrinkage, aging and strength reduction due to high sustained loading for concrete, and stress relaxation for prestressing steel. For the creep analysis the so-called modified rate of creep method has been adopted. This is an attractive method since it allows for creep recovery without saving more of the stress history than the value at the previous equilibrium state. Nevertheless, the method has to this author's knowledge not been applied in a finite element framework before. The same is probably also true for the strength reduction model due to high sustained loading. A general feature of the stress and time dependent models for concrete is that these originally are uniaxial formulations. The extensions here to biaxial conditions have rendered necessary certain assumptions that are difficult to verify since very few relevant experiments seem to exist. For stress relaxation a method termed the rate of relaxation method, has been proposed. This is a simpler method than the commonly adopted fictitious initial stress method. However, comparative runs for the bridge span example gave practically the same results using the two methods. In this work, all stress and time dependent effects have been analyzed based on applying the mean stress (or an approximation thereof) for the current time step when computing the next incremental contributions. This has

been achieved without relying on iteration at the integration point level. In contrast, most previous investigators [21]-[27] have either adopted some kind of iteration or simply applied the stress at the previous equilibrium state for the current time step. However, in [20] a procedure that in certain respects are similar to the one outlined in this work, has been employed.

The beam cross section analysis has been based on subdividing the total section into generic units or 'building blocks'. The following units are defined:

- Line unit consisting of concrete and 'smeared' reinforcement in three directions; two directions for rebars (axial and arbitrary) and one for pbars (arbitrary).
- Quad unit consisting of plain concrete.
- Rebar unit representing the cross section of an individual reinforcing bar in the axial direction.
- Tendon unit representing the cross section of an arbitrarily oriented prestressing tendon.

With these units, large freedom in composing various cross sectional configurations has been obtained. Since the subanalyses of line and quad units rely on numerical integration, relatively 'large' and 'input-saving' units may be employed. The beam element formulation does not place any symmetry requirements on the resulting cross section.

So far in this section, results from the numerical studies have been focused on in conjunction with the various modeling aspects. However, one additional result should be addressed for the bridge span example. Here the member forces due to externally applied loading showed practically no redistribution between completion of construction and after 27 years. This result is in agreement with that reported in [24], but seems surprising when comparing with established design practice. Thus, it may be good reason to pursue the numerical investigations, and eventually also to revise the present practice in this field.

13.2 Recommendations for Future Research

In the future research on nonlinear analysis with application to large scale concrete structures the following three areas should be addressed:

- Since the 3D shear-beam element has proved to work successfully, development of plate and shell elements based on a similar approach should be attempted. This may however be a more demanding task due to the general difficulties in meeting the continuity requirements for such elements.
- The rotating 'smeared' crack model should be extended to 3D stress conditions. Since the experimental basis for a full 3D formulation still seems inadequate, more such work is also deemed necessary. The Poisson effect should be accounted for.

- All loads, material parameters and geometric quantities that define a structural problem, are by nature random variables. In order to design safe and economic structures, it is essential to take the uncertainties arising from this random nature into account. To no surprise, a rapid growing area of research today is the development of structural analysis methods involving theory of probability and statistics. One such method that is well suited for implementation in a nonlinear analysis concept, is the so-called probabilistic finite element method. Previously, this method has successfully been applied to concrete structures in [54, 55]. However, much work is still left in order to develop this approach into a mature structural safety assessment method.

References

[1] Malvern, L.E., *Introduction to the Mechanics of a Continuous Medium*, Prentice-Hall, 1969.

[2] Fung, Y.C., *Foundations of Solid Mechanics*, Prentice-Hall, 1965.

[3] Bergan, P.G., *Lecture Notes in Nonlinear Finite Element Analysis* (in Norwegian), Division of Structural Mechanics, The Norwegian Institute of Technology, Trondheim, 1981.

[4] Nygård, M.K., *The Free Formulation for Nonlinear Finite Elements with Applications to Shells*, Report No. 86-2, Division of Structural Mechanics, The Norwegian Institute of Technology, Trondheim, 1986.

[5] Mathisen, K.M., *Large Displacement Analysis of Flexible and Rigid Systems Considering Displacement-Dependent Loads and Nonlinear Constraints*, Dr.Ing. Thesis 1990:33, Division of Structural Engineering, The Norwegian Institute of Technology, Trondheim, 1990.

[6] *FENRIS - Finite Element NonlineaR Integrated System*, System Manual, Theory - Program Outline - Data Input, Developed by NTH - SINTEF - VERITAS, Veritas Sesam Systems, Høvik, Norway, 1987.

[7] Cowper, G.R., *The Shear Coefficient in Timoshenko's Beam Theory*, Journal of Applied Mechanics, pp. 335-340, June 1966.

[8] Archer, J.S., *Consistent Matrix Formulations for Structural Analysis Using Finite-Element Techniques*, AIAA Journal, Vol. 3, No. 10, pp. 1910-1918, 1965.

[9] Narayanaswami, R. and Adelman, H.M., *Inclusion of Transverse Shear Deformation in Finite Element Displacement Formulations*, AIAA Journal, Vol. 12, No. 11, pp. 1613-1614, 1974.

[10] Cook, R.D., Malkus, D.S. and Plesha, M.E., *Concepts and Applications of Finite Element Analysis*, Wiley, 3rd ed., 1989.

[11] Severn, R.T., *Inclusion of Shear Deflection in the Stiffness Matrix for a Beam Element*, Journal of Strain Analysis, Vol. 5, No. 4, pp. 239-241, 1970.

[12] Oral, S., *Anisoparametric Interpolation in Hybrid-Stress Timoshenko Beam Element*, Journal of Structural Engineering, Vol. 117, No. 4, pp. 1070-1078, 1991.

[13] Carol, I. and Murcia, J., *Nonlinear Time-Dependent Analysis of Planar Frames Using an 'Exact' Formulation - I. Theory*, Computers and Structures, Vol. 33, No. 1, pp. 79-87, 1989.

[14] Carol, I. and Murcia, J., *Nonlinear Time-Dependent Analysis of Planar Frames Using an 'Exact' Formulation - II. Computer Implementation for R.C. Structures and Examples*, Computers and Structures, Vol. 33, No. 1, pp. 89-102, 1989.

[15] Tessler, A. and Dong, S.B., *On a Hierarchy of Conforming Timoshenko Beam Elements*, Computers and Structures, Vol. 14, No. 3-4, pp. 335-344, 1981.

[16] Kreyszig, E., *Advanced Engineering Mathematics*, Wiley, 2nd ed., 1967.

[17] *COBE - Version 85* (computer program for segmentally constructed concrete bridges), User's Manual (in Norwegian), Public Roads Administration, Bridge Department, Norway, 1985.

[18] Mollestad, E., *Techniques for Static and Dynamic Solution of Nonlinear Finite Element Problems*, Report No. 83-1, Division of Structural Mechanics, The Norwegian Institute of Technology, Trondheim, 1983.

[19] Bjærum, R.O., *Finite Element Formulations and Solution Algorithms for Buckling and Collapse Analysis of Thin Shells*, Dr.Ing. Thesis 1992:30, Division of Structural Engineering, The Norwegian Institute of Technology, Trondheim, 1992.

[20] Aas-Jakobsen, K., *Design of Slender Reinforced Concrete Frames*, Bericht Nr. 48, Institut für Baustatik, ETH, Zürich, 1973.

[21] Åldstedt, E., *Nonlinear Analysis of Reinforced Concrete Frames*, Report No. 75-1, Division of Structural Mechanics, The Norwegian Institute of Technology, Trondheim, 1975.

[22] Kang, Y.J., *Nonlinear Geometric, Material and Time Dependent Analysis of Reinforced and Prestressed Concrete Frames*, Report No. UC-SESM 77-1, Division of Structural Engineering and Structural Mechanics, University of California, Berkeley, 1977.

[23] Mari, A.R., *Nonlinear Geometric, Material and Time Dependent Analysis of Three Dimensional Reinforced and Prestressed Concrete Frames*, Report No. UCB/SESM-84/12, Division of Structural Engineering and Structural Mechanics, University of California, Berkeley, 1984.

[24] Ketchum, M.A., *Redistribution of Stresses in Segmentally Erected Prestressed Concrete Bridges*, Report No. UCB/SESM-86/07, Division of Structural Engineering and Structural Mechanics, University of California, Berkeley, 1986.

[25] Kang, Y.J., *SPCFRAME - Computer Program for Nonlinear Segmental Analysis of Planar Prestressed Concrete Frames*, Report No. UCB/SEMM-89/07, Division of Structural Engineering and Structural Mechanics, University of California, Berkeley, 1989.

[26] Kasti, F.A., *Nonlinear Material and Time Dependent Analysis of Segmentally Erected Reinforced and Prestressed Concrete Composite 3D Frame Structures*, Report No. UCB/SEMM-90/03, Division of Structural Engineering and Structural Mechanics, University of California, Berkeley, 1990.

[27] Kanstad, T., *Nonlinear Analysis Considering Timedependent Deformations and Capacity of Reinforced and Prestressed Concrete*, Dr.Ing. Thesis 1990:26, Division of Concrete Structures, The Norwegian Institute of Technology, Trondheim, 1990.

[28] Ryshik, I.M. and Gradstein, I.S., *Tables of Series, Products, and Integrals*, Deutscher Verlag der Wissenschaften, 1957.

[29] Collins, M.P., Vecchio, F.J. and Mehlhorn, G., *An International Competition to Predict the Response of Reinforced Concrete Panels*, Canadian Journal of Civil Engineering, Vol. 12, No. 3, pp. 624-644, 1985.

[30] Crisfield, M.A. and Wills, J., *Analysis of R/C Panels Using Different Concrete Models*, Journal of Engineering Mechanics, Vol. 115, No. 3, pp. 578-597, 1989.

[31] Vecchio, F.J. and Collins, M.P., *The Modified Compression-Field Theory for Reinforced Concrete Elements Subjected to Shear*, ACI Journal, Vol. 83, No. 2, pp. 219-231, 1986.

[32] Stevens, N.J., Uzumeri, S.M. and Collins, M.P., *Analytical Modelling of Reinforced Concrete Subjected to Monotonic and Reversed Loadings*, Publication No. 87-1, Department of Civil Engineering, University of Toronto, 1987.

[33] Vecchio, F.J., *Nonlinear Finite Element Analysis of Reinforced Concrete Membranes*, ACI Structural Journal, Vol. 86, No. 1, pp. 26-35, 1989.

[34] Kupfer, H., Hilsdorf, H.K. and Rüsch, H., *Behavior of Concrete Under Biaxial Stresses*, ACI Journal, Vol. 66, No. 8, pp. 656-666, 1969.

[35] *CEB-FIP Model Code 1990*, Final Draft, Information Bulletins Nos. 203-205, Euro-International Committee for Concrete (CEB), 1991.

[36] Park, R. and Paulay, T., *Reinforced Concrete Structures*, Wiley, 1975.

[37] Noakowski, P. and Krawinkler, H., *Modeling of the Deformation Behavior of Concrete Structures. Importance, Procedures, and Tasks*, in: 'New Directions in Structural System Reliability', by D.M. Frangopol (Ed.), Proc., Int. Workshop on Structural System Reliability, University of Colorado, Boulder, pp. 200-210, 1989.

[38] Dahlblom, O. and Ottosen, N.S., *Smeared Crack Analysis Using Generalized Fictitious Crack Model*, Journal of Engineering Mechanics, Vol. 116, No. 1, pp. 55-76, 1990.

[39] Rüsch, H., Grasser, E. and Rao, P.S., *Principles of Calculation of Reinforced Concrete under Uniaxial Stress* (in French), Information Bulletin No. 36, Euro-International Committee for Concrete (CEB), 1962.

[40] Hellesland, J. and Green, R., *A Stress and Time Dependent Strength Law for Concrete*, Cement and Concrete Research, Vol. 2, No. 3, pp. 261-275, 1972.

[41] Neville, A.M., Dilger, W.H. and Brooks, J.J, *Creep of Plain and Structural Concrete*, Construction Press, 1983.

[42] England, G.L. and Illston, J.M., *Methods of Computing Stress in Concrete from a History of Measured Strain*, Civil Engineering and Public Works Review, Vol. 60, Nos. 705-707, 1965.

[43] Roll, F., *Long-Time Creep-Recovery of Highly Stressed Concrete Cylinders*, Symposium on Creep of Concrete, ACI Publication, SP-9, 1964.

[44] Hellesland, J., *A Study into the Sustained and Cyclic Load Behaviour of Reinforced Concrete Columns*, Ph.D. Thesis, Department of Civil Engineering, University of Waterloo, Canada, 1970.

[45] *Evaluation of the Time Dependent Behavior of Concrete*, Information Bulletin No. 199, Euro-International Committee for Concrete (CEB), 1990.

[46] Magura, D.D., Sozen, M.A. and Siess, C.P., *A Study of Stress Relaxation in Prestressing Reinforcement*, PCI Journal, Vol. 9, No. 2, pp. 13-57, 1964.

[47] Glodowski, R.J. and Lorenzetti, J.J., *A Method for Predicting Prestress Losses in a Prestressed Concrete Structure*, PCI Journal, Vol. 17, No. 2, pp. 17-31, 1972.

[48] Hernandez, H.D. and Gamble, W.L., *Time-Dependent Prestress Losses in Pretensioned Concrete Construction*, Structural Research Series No. 417, Civil Engineering Studies, University of Illinois, Urbana, 1975.

[49] Timoshenko, S.P. and Gere, J.M., *Theory of Elastic Stability*, McGraw-Hill, 2nd ed., 1961.

[50] Bresler, B. and Scordelis, A.C., *Shear Strength of Reinforced Concrete Beams*, ACI Journal, Vol. 60, No. 1, pp. 51-74, 1963.

[51] Lampert, P. and Thürlimann, B., *Torsionsversuche in Stahlbetonbalken*, Bericht Nr. 6506-2, Institut für Baustatik, ETH, Zürich, 1968.

[52] Jakobsen, B., *Nonlinear Static and Dynamic Analysis of Thin-Walled Concrete Members*, Report No. 80-3, Division of Structural Mechanics, The Norwegian Institute of Technology, Trondheim, 1980.

[53] Hellesland, J., Choudhury, D. and Scordelis, A.C., *Nonlinear Analysis and Design of RC Bridge Columns Subjected to Imposed Deformations*, Report No. UCB/SESM-85/03, Division of Structural Engineering and Structural Mechanics, University of California, Berkeley, 1985.

[54] Teigen, J.G., Frangopol, D.M., Sture, S. and Felippa, C.A., *Probabilistic FEM for Nonlinear Concrete Structures. I: Theory*, Journal of Structural Engineering, Vol. 117, No. 9, pp. 2674-2689, 1991.

[55] Teigen, J.G., Frangopol, D.M., Sture, S. and Felippa, C.A., *Probabilistic FEM for Nonlinear Concrete Structures. II: Applications*, Journal of Structural Engineering, Vol. 117, No. 9, pp. 2690-2707, 1991.


UNIVERSITAS OSLOENSIS
MDCCCXI